Dynamical modelling of Kara Sea land-fast ice

Dissertation

Zur Erlangung des Doktorgrades der Naturwissenschaften
im Department Geowissenschaften
der Universität Hamburg

vorgelegt von

Einar Örn Ólason

aus

Island

Hamburg
2012

Als Dissertation angenommen vom
Department Geowissenschaften der Universität Hamburg

Auf Grund der Gutachten
von Jun. Prof. Dr. Lars Kaleschke
und Dr. Ingo Harms

Hamburg, den 30. Januar, 2012

Prof. Dr. Jürgen Oßenbrügger
Leiter des Department Geowissenschaften

Abstract

In this thesis land-fast ice is modelled based on the internal dynamics of sea ice. The region of interest is the Kara Sea, which has a well documented semi-permanent fast-ice cover. The Kara Sea fast ice is especially interesting because it forms over relatively deep waters compared to the maximum thickness of pressure ridges. This means that internal ice stresses must play an important role, in addition to the well-known grounding of pressure ridges. The main objective here is therefore to model the internal stresses of the ice well enough to reproduce the observed fast-ice cover. This has not been done successfully before. The model and methods developed here are general and should be applicable to other areas of fast-ice growth.

In order to accurately model land-fast ice an improved version of the well-known viscous-plastic model is used. To produce a more physically realistic model material different yield curves are proposed while some numerical properties of the model are improved. The transition from plasticity to viscosity and the role of linear viscosity is also reconsidered. In an idealised stand-alone setup the model is used to investigate some general properties of polynya formation in the model. Coupling the ice model to an ocean model, realistic decadal simulations of the ice and ocean in the Kara Sea are then carried out testing some dynamic and thermodynamic properties of the model. Having thus confirmed that the model produces realistic results attempts are made to model land-fast ice. First the winter of 1997–98 is considered in which various model parametrisations are tested and evaluated. Utilising the improved model and correct parametrisations the observed fast-ice cover can be reproduced during the height of the fast-ice season. After further tuning the fast-ice cover in 1967–74 and 1997–2005 could also be reproduced. The longer runs allow us to give an estimate of the minimum ice thickness required for fast ice to form over the deeper areas of the Kara Sea.

Contents

Chapter 1

Introduction

Sea ice is an important part of the climate system and clearly an integral part of the ocean-atmosphere system at high latitudes. This is mainly because the ice acts as an insulating layer between the atmosphere and ocean influencing any exchange between the two. The ocean-atmosphere heat exchange is severely dampened by the presence of sea ice, as well as the atmosphere-ocean momentum transfer. The surface albedo of ice is also much larger than that of water causing the majority of incoming solar radiation to be reflected back into space. The latent heat stored in the ice also causes a delay in the seasonal temperature cycle. Finally the formation of ice alters the sea surface salinity, possibly causing dense or deep water formation and a redistribution of salinity in the upper ocean through sea ice drift.

One of the many forms sea ice takes is that of land-fast ice. According to the World Meteorological Organization (1970) land fast ice is "sea ice which remains fast along the coast, where it is attached to the shore, to an ice wall, to an ice front, or over shoals, or between grounded icebergs". Here "fast" should be taken to mean "not easily moved, firm ... fixed, stable" (Webster and McKechnie, 1979). Although some ambiguity exists when comparing different definitions (see e.g. Weaver, 1951, Barry et al., 1979) two main criteria appear to be used to define fast ice: It should be attached to the shore and it should be stationary.

Land-fast ice can be found all around the Arctic rim, but it is an especially prominent feature of the Siberian winter ice cover. While the largest fast-ice extent is probably to be found in the Laptev Sea, the Kara Sea has an extensive and well documented fast-ice cover. There land-fast ice may extend as far as 300 km off shore in certain areas. In particular the Vilkitsky Strait, separating the Laptev and Kara Seas is closed by fast ice for about seven months of the year. This is arguably the most difficult road block for the north-east passage shipping route.

In general fast ice can have considerable effects on navigation. With increasing interest in shipping and offshore exploration in the Arctic, un-

derstanding the behaviour of land-fast ice is becoming more important in an economic context. Aside from that, land-fast ice also has a considerable effect on the ocean and atmosphere at a regional scale. With ever increasing computing powers these effects may soon be of interest to researchers running basin-scale or even global models.

Despite this the dynamical modelling of land-fast ice has not garnered much interest in the sea-ice modelling community. As of yet dynamic sea-ice models have not been able to reproduce land-fast ice in a realistic setting. The reason for this appears to be mainly the focus on pan-Arctic and global models, rather than regional ones for the model design. In particular large scale models should assume that very little cohesion exists in the ice on the scale of one grid cell. This is a suitable assumption for resolutions greater than about 100 km. However, when the grid resolution is increased to, for example 10 km this assumption may need reconsidering, especially where land-fast ice is concerned.

This thesis focuses on the Severozemelsky region in the eastern Kara Sea. The fast ice there extends up to 300 km off shore over waters deeper than 100 m. Fast ice is known to attach itself to grounded pressure ridges, but this is impossible over deep waters. Such grounding cannot be expected to be important at much more than 25 m depth. Some other dynamical process must therefore be involved and we assume here that this is sea-ice cohesion.

By adding cohesive strength to the ice in a high resolution regional model we have the potential to model land-fast ice in a dynamic sea-ice model. This does not require a radically different approach to sea-ice modelling and the model proposed here is closely based on the viscous-plastic model published by Hibler (1979), although some changes still have to be made, as outlined below. The model developed is intended to both allow for accurate simulation of the fast-ice cover and the associated polynyas, as well as to enrich our understanding of the large fast-ice massifs seen both in the Kara and Laptev Seas.

The mechanism for fast-ice formation appears to mostly depend on local geography. According to Volkov et al. (2002) there are two basic mechanisms at work in the Kara Sea. Firstly, grounded pressure ridges stabilise the ice sheet facilitating fast ice growth in shallow regions. The spatial extent of this ice is then presumably limited by the thickness of the pressure ridge and the ocean depth. This explains why the fast ice edge tends to follow isobaths in shallow areas. Secondly, further fast ice growth may occur as ice floes drift onshore and attach themselves onto the coast or fast ice. During periods of offshore winds grounded pressure ridges and, more importantly, off-shore islands then prevent the ice drift allowing fast ice to form over deep water. The islands in the Severozemelsky region of the Kara Sea appear to play a large role in stabilising the fast ice (Divine et al., 2005).

The ice behaviour in between the stabilising ridges and islands is therefore of interest here. Goldstein et al. (2004) made a study of the shape of the fast ice boundary in the Bothnian Bay in the Baltic Sea. An interesting conclusion of theirs is that the "fast ice boundary is formed of piecewise curved sections" (Goldstein et al., 2004) or arches. Arching is a well known phenomenon, both in soil mechanics and structural engineering, as well as sea-ice modelling (see e.g. Hibler et al., 2006). From there we know that a well constructed arch can carry great loads almost entirely through the material's shear and compressive strength, relying only weakly on its tensile strength. Examples abound, but the best known ones are probably the stone arches made by Roman builders.

While sea ice cannot be expected to form well constructed arches, the arching mechanism may help explain how vast extents of fast ice can form given the apparently relatively low cohesive strength of sea ice. The tensile strength is frequently quoted at about $1/20^{\text{th}}$ of the compressive strength (see e.g. Hibler and Schulson, 2000, Wang, 2007, and references therein). In this context it is interesting to note that when Tremblay and Hakakian (2006) tried to estimate the strength of fast ice from satellite images and reanalysis data they found the tensile strength to be comparable to the compressive strength. The reason for this discrepancy may be that Tremblay and Hakakian (2006) did not measure the tensile strength of the ice, but rather the total strength of the arched structure.

The formation of land-fast ice has so far been poorly represented in large scale numerical ice models. While ice arching and ice bridges in convergent channels have been modelled (see e.g. Hibler et al., 2006, Dumont et al., 2009), these ice formations can only be considered remotely related to the land-fast ice modelled here. Zyryanov and Korsnes (2003) simulated fast-ice formation in the Kara Sea under idealised wind stress using a cohesive discrete element model. This model shares some very basic rheological characteristics with the current model; however, their approach is still considerably different to the current one. Aside from these examples, no dynamic fast-ice modelling in a realistic setup has yet been successful.

Cohesive strength has been included in sea-ice models on a number of occasions. In a modification of the classical elliptic yield curve Hibler and Schulson (2000) include a small amount of cohesion in their modified Coulombic yield curve. This was done in accordance with laboratory results and to ensure energy dissipation, but without any reference to fast ice. Zhang and Rothrock (2005) also include cohesion in some of the yield curves they tested, but again no reference was made to fast ice. König Beatty and Holland (2010) on the other hand modified the elliptic yield curve to include cohesive stress expressly to model land-fast ice. They then proceed to show how their formulation allows them to model fast ice in one dimension using the viscous-plastic approach of Hibler (1979), but not as effectively when using the elastic-viscous-plastic approach suggested by Hunke and Dukowicz

(1997).

Dumont et al. (2009) point out that even though the elliptic yield curve has no cohesive strength under isotropic divergence it does possess cohesive strength because of the curve's uniaxial compressive strength. This is a key parameter in defining the strength of static arches and is controlled by the ellipse eccentricity. They then proceed to show that an elastic-viscous-plastic model with an elliptic yield curve can be used to model ice bridges, both in an ideal and semi-realistic setting. Their model domain consisted of a converging channel (for the ideal case) and Nares Strait (for the realistic case), where the North Water Polynya forms. In both the ideal and realistic cases, land-fast ice forms where drifting ice floes form an arch in a converging channel. That situation may be considered remotely related to fast ice formation in the Kara Sea where the fast ice is presumably held at the shore by a chain of islands and a series of arches.

Static arching occurs in plastic materials, but not viscous ones. In the viscous-plastic model a phase transition occurs at small strain rates where the formerly plastic model material turns linear viscous. Here this transition should occur at either small enough strain rates so as not to affect the fast ice or in such a way that the viscosity of the linear viscous ice is high enough so that it is essentially immobile. Both of these goals are reached by raising the maximum viscosity allowed in the model. It will be shown that this needs to be several orders of magnitude larger than the commonly used values for fast ice to form. Using such a high maximum viscosity value the linear viscous phase is barely present in the land-fast ice, casting some doubt on the applicability of the linear viscous approximation. The resulting creep flow speed is also so small as to be meaningless in the current context. This topic has received little attention in the literature, but will be shown to be very important here.

In this thesis it will be shown that fast ice can be modelled using a viscous-plastic ice model. To achieve this it is necessary to take a closer look at the yield curve shape and, to this end, new formulations for older yield curves, as well as one new one, are suggested. These yield curves all have uniaxial compressive strength and adjustable cohesive strength. This is necessary to reproduce the static arching expected to play a role in the fast-ice formation.

In addition to modifying the yield curve the model features an improved non-linear solver for the ice momentum equation. This is important to the accurate prediction of ice velocity. Errors in the velocity field may cause the fast ice to break up or even prevent a sensible definition of what ice is moving slowly enough to be considered land-fast. The limit for the viscous assumption also needs to be reviewed so that the ice remains in a plastic state under smaller strain rates. Finally some improvements are made to the algorithm describing new-ice formation in order to improve the

representation of flaw polynyas.

This model is then used to model land-fast ice in the Kara Sea; first only during the winter 1997–98 and then for longer periods. Tests of the 1997–98 winter involve testing all the different yield curves available in the model, as well as the momentum solver and the role of the viscous limit. The model results are compared to observed fast-ice extent and flaw polynyas. In these tests it becomes clear that using high maximum viscosity is crucial for a realistic fast-ice simulation. The accuracy of the momentum solver plays an important role, as well as the shape of the yield curve. Some flexibility in the yield curve is, however, permitted and all yield curves used in the "Hibler type" model can be tuned to give realistic fast-ice extent, although some give better results than others. The granular model, which introduces an extra pressure term solver, does not produce realistic land-fast ice in these tests.

Having modelled the land-fast ice in the Kara Sea in 1998 the best yield curves are used in experiments run for the years 1967–74 and 1998–2005. The initial results of these tests were not promising and it became clear that the role of pressure ridge grounding was underestimated. By making more extensive use of the grounding scheme already introduced, realistic fast-ice extent can be obtained for all modelled years. These results are then used to give an estimate of the critical thickness for fast-ice formation, i.e. how thick the ice needs to grow before fast-ice formation is possible.

This thesis is set up in 7 chapters, including an Introduction and Conclusion. First the ice model used is described. This is then followed by an idealised study of polynya formation done using the model. Chapter 4 describes the setup of the coupled ice-ocean model in the Kara Sea as well as discussing initial dynamical and thermodynamical tests performed using the coupled model. In chapter 5 the winter of 1997–98 is modelled using the coupled model and the model is tuned to give the best possible land-fast ice and drift ice results. The model results are analysed with the aim of increasing our understanding of both fast-ice modelling and land-fast ice itself. This is then followed by chapter 6 in which longer simulations are considered. The ability of the model to simulate fast ice on a longer time-scale is discussed along with the main factors affecting the model performance. Finally an estimate of the critical thickness for fast-ice formation is given.

Chapter 2

Model description

2.1 Introduction

Sea ice is an important component in coupled models since the ice model can have considerable effects on the ocean and atmosphere. It is clearly important to model this component properly, but sea-ice modellers are faced with the difficulty of modelling a complex and poorly understood system under sometimes severe computational restrains. One way to approach this problem is to restrain the model subject and here the focus is on polynya formation and land-fast ice. This helps in deciding what the model requirements are; i.e. which aspects of the ice model are important and which are not.

In the following discussion the ice model implemented here is described and the design choices made are justified. As such it is meant to give an overview of the model, going only into details when required by the thesis' focus. First of all section 2.2 introduces the fundamental equations of a sea-ice model, including a brief discussion of some details of the numerical implementation. The model thermodynamics are then discussed in section 2.3, describing briefly the three layer Semtner (1976) model used and discussing the way new ice forms, as well as the problem of lateral melt. Section 2.4 discusses the model rheology, going into considerable details about the different yield curves considered here. The latter half of that section discusses yield curves that may potentially be used for modelling fast ice.

2.2 The fundamental sea ice equations

The model presented here is a two class (ice and open water) dynamic-thermodynamic sea-ice model, written to be coupled with the Vector Ocean Model (Backhaus, 2008). With the exception of the momentum equation the fundamental equations that follow are the same as in Hibler (1979).

The focus of this study is on fast ice and the associated flaw polynyas.

Land-fast ice is in general level and multiple thickness classes should therefore not be needed to describe it. Using only two ice classes simplifies the model construction considerably, making it an attractive simplification. There are known cases of fast ice with a complex morphology (see e.g. Volkov et al., 2002) and this may cause problems later on. As a first approximation, however, using two ice classes is considered good enough here. For modelling the flaw polynyas two classes; of ice and open water should also be sufficient.

The ice is modelled as a continuum using an Eulerian perspective. It moves in a horizontal plane, subject to both external and internal forces. Temporal evolution of the sea ice cover is described using two continuity equations and the momentum equation. The continuity equation for mass is

$$\frac{\partial m}{\partial t} + \vec{\nabla} \cdot (\vec{v} m) = S_m \,, \tag{2.1}$$

where m is the sea ice mass per unit area, S_m is a thermodynamic source/sink term and $\vec{v}$ is velocity.

An equation for the evolution of the ice thickness distribution within each cell is also needed. The model uses two ice classes; i.e. ice and open water and so this becomes an equation of conservation of sea ice concentration. That takes the same basic form;

$$\frac{\partial A}{\partial t} + \vec{\nabla} \cdot (\vec{v} A) = S_A \,, \tag{2.2}$$

with S_A being a source/sink term. The average ice thickness over ice-covered area, h can be derived using $m{=}Ah\rho_{\mathrm{i}}$. The source/sink terms S_A and S_m will be discussed in section 2.3. In addition the condition $A{\leq}1$ is imposed. This can be interpreted as a ridging condition since m (and thus h) can increase even if A does not (Hibler, 1979). Together these equations describe the advection of the ice in a given velocity field.

The momentum equation used is (Connolley et al., 2004)

$$0 = A(\vec{\tau}_{\mathrm{a}} + \vec{\tau}_{\mathrm{w}}) - mf\vec{k} \times \vec{v} - mg\vec{\nabla}H - \boldsymbol{\nabla \cdot \sigma}. \tag{2.3}$$

Here $\vec{k}$ is a unit vector normal to the surface, $\vec{\tau}_{\mathrm{a}}$ and $\vec{\tau}_{\mathrm{w}}$ are air and water stresses, f is the Coriolis factor, g is the gravitational acceleration, $\vec{\nabla}H$ is the gradient of the sea surface height and $\boldsymbol{\sigma}$ is the sea ice stress tensor. The last term on the right hand side; $\boldsymbol{\nabla \cdot \sigma}$, describes forces due to internal stress while the other terms are all external factors. Hibler (1979) included the material derivative $\mathrm{D}m/\mathrm{D}t$ on the left hand side, but that has been set to zero here. This simplification will be discussed further in chapter 3. The momentum equation is solved using a semi-implicit approach described in section 2.2.1.

Wind and water stresses are modelled as quadratic drag (McPhee, 1975);

$$\tau_{\mathrm{a}} = \rho_{\mathrm{a}} C_{\mathrm{da}} |\vec{v}_{\mathrm{a}}| \vec{v}_{\mathrm{a}} \tag{2.4}$$

$$\tau_{\mathrm{w}} = \rho_{\mathrm{w}} C_{\mathrm{dw}} |\vec{v} - \vec{v}_{\mathrm{w}}| (\vec{v} - \vec{v}_{\mathrm{w}}) \,, \tag{2.5}$$

where C_{dw} and C_{da} are drag coefficients, ρ_{w} and ρ_{a} are air and water densities and $\vec{v}_{\mathrm{w}}$ and $\vec{v}_{\mathrm{a}}$ are the near surface water and wind velocities. This assumes that the wind velocity is much larger than the ice velocity; i.e. that $|\vec{v}-\vec{v}_{\mathrm{a}}| \approx |\vec{v}_{\mathrm{a}}|$. The drag coefficients are assumed to have the values $C_{\mathrm{da}} = 1.2 \times 10^{-3}$ (Hibler, 1979, Tremblay and Hakakian, 2006) and $C_{\mathrm{dw}} = 5.5 \times 10^{-3}$ (Hibler, 1979, Woods Hole Oceanographic Institution, 2010).

The last term in equation (2.3) is the force due to the divergence of the internal stress tensor $\boldsymbol{\sigma}$. Stress and strain rate (and thus ice velocity) are related through the sea-ice rheology, but the correct definition of the rheology is a central point in sea-ice dynamics research. Sea-ice rheologies will be discussed in detail in section 2.4.

2.2.1 Time stepping of the momentum equation

In his paper Hibler (1979) described a method for solving the momentum equation. This method consists of two separate solutions to the linearised version of the equation. First the viscosities needed to linearise the non-linear term $\boldsymbol{\nabla \cdot \sigma}$ are calculated. For this the velocities from the previous time step are used. The Coriolis term must also be calculated using velocities from the previous time step. Once the viscosities have been calculated the equation can be linearised and solved using a linear solver.

However, since velocities from the previous time step are used to calculate the viscosities and the Coriolis term this solution is not exact. To address this Hibler added a single pseudo-time step so that during each model time-step the momentum equation is solved twice. The first time it is solved using the velocities from the previous time step to calculate the semi-implicit terms as described earlier. This is the pseudo-time step. The final solution is then found by using the velocities from the pseudo-time step solution to calculate the semi-implicit terms and solving the linear equation again.

On closer consideration it is not immediately clear how much improvement a single pseudo-time step makes, but Hibler (1979) cites stability reasons for using a pseudo-time step at all. In general using too few pseudo-time steps means that the ice internal stress depends more on the previous time step than the current one. Consider, for instance a uniform block of stationary ice subject to no forcing. In this case the internal stresses are zero. Now let a sudden increase in wind forcing compress the ice. Using no pseudo-time steps the ice will compress considerably during the first time step, since the internal stresses are based on the previous time step and are therefore zero. Conversely, if a steady wind has been blowing but then suddenly slows down internal stresses in the ice will cause it to expand when the wind slows. Such an "overreaction" to changes in the forcing may cause instabilities. It is also

possible that they may prevent fast ice formation or cause the fast ice to break up early.

Lemieux and Tremblay (2009) showed that for a 10 km resolution model one pseudo-time step is far from being sufficient to reach an acceptably accurate solution and they suggest using between 200 and 1000 pseudo-time steps, or outer-loop iterations, using their nomenclature. What is considered to be an "acceptably accurate solution" will be discussed in more detail below.

The algorithm used here is based on the one presented by Lemieux and Tremblay (2009). They use a general minimum residual method to solve the linearised problem while here a successive over relaxation method is used. This results in some minor differences in focus. The implementation of the outer-loop solver used here is as follows:

for $k = 1$ to n_{OL} **do**
  Calculate viscosities based on $\vec{v}^{k-1}$
  $\vec{v}^{k} \leftarrow$ solution to the linear system (using an SOR solver)
  if $k > 1$ **then**
    $\vec{v}^{k} \leftarrow (\vec{v}^{k} + \vec{v}^{k-1})/2$
  end if
  $\epsilon \leftarrow \max(|u^k - u^{k-1}|, |v^k - v^{k-1}|)$
  if $\epsilon < \epsilon_{\mathrm{OL}}$ **then**
    exit loop
  end if
  $\epsilon_{\mathrm{SOR}} \leftarrow \alpha\epsilon$
end for
$\epsilon_{\mathrm{SOR}} \leftarrow \max(\epsilon_{\mathrm{OL}}, |u^k - u^0|, |v^k - v^0|)$

First of all this algorithm assumes an upper limit on the number of outer loops, n_{OL}. This is necessary since the condition $\epsilon < \epsilon_{\mathrm{OL}}$ may not be met within a reasonable number of outer loops. Here $\epsilon = 10^{-4}$ m/s, which is a somewhat stricter definition of convergence than Lemieux and Tremblay (2009) suggest. They require that no more than 1% of ice-covered cells have outer-loop errors larger than $\epsilon_{\mathrm{OL}} = 10^{-4}$ m/s, while the current definition demands that every cell meets the convergence condition. Section 4.4 will discuss more closely what value for n_{OL} should be used in the Kara Sea model, as well as outlining the model's convergence properties in more detail.

Viscosities are calculated based on the chosen yield curve and the yield curves considered here are discussed in section 2.4. When $k = 1$ velocities from the previous time step, $\vec{v}^0$, are used.

The SOR solver is a basic tool, which will not be discussed in detail here. An important point, though, is the exit condition for the SOR solver. In this implementation the SOR solver is considered to have converged when the maximum change in velocity between consecutive SOR steps is less than

ϵ_{SOR}. In traditional SOR implementations ϵ_{SOR} is a constant, but here it is always proportional to the outer-loop error, with a constant of proportionality $\alpha = 1/10$. For the first SOR solve the outer-loop error is unknown and so the maximum velocity difference between the two previous time steps is used. Using a variable exit condition both increases stability of the method and also vastly decreases the computing time, compared to using a constant ϵ_{SOR}. Using this approach the first few outer loop iterations may be considered as preconditioning steps.

The matrix constants of the SOR method are recalculated during each outer loop and for completeness the equations for these are included here. Firstly the SOR iterates as

while $\max(r^u, r^v) > \epsilon_{\text{SOR}}$ **do**
$r^u \leftarrow e^u u_{10} + w^u u_{-10} + n^u u_{01} + s^u u_{0-1} + c^u u_{00} - b^u$
$u \leftarrow u - \omega r^u / c^u$
$r^v \leftarrow e^v u_{10} + w^v u_{-10} + n^v u_{01} + s^v u_{0-1} + c^v v_{00} - b^v$
$v \leftarrow v - \omega r^v / c^v$
end while

where $\omega \in]1, 2[$ is the over-relaxation constant, $u_{00} = u_{i,j}$, $u_{11} = u_{i+1,j+1}$ etc. and e^u is a short hand for e^u_{00} etc. The above pseudo-code omits to include a maximum on the number of SOR iterations, the appropriate masking which prevents division by zero and the checker board scheme that's used in the actual implementation (see e.g. Press et al., 1992). The matrix constants, appropriate for all formulations except the granular model (which is discussed in section 2.4.3) follow. For the appropriate constants for the granular model any occurrences of $P/2$ are simply replaced by P and ζ is set to zero.

For the u-component the constants are:

$$c^u = \tau'_{\text{w}} + (\zeta_{10} + \zeta_{00} + \eta_{10} + \eta_{00})/\Delta x^2 + (\eta^B_{00} + \eta^B_{0-1})/\Delta y^2 \tag{2.6}$$

$$n^u = -\eta^B_{00}/\Delta y^2 \tag{2.7}$$

$$s^u = -\eta^B_{0-1}/\Delta y^2 \tag{2.8}$$

$$e^u = -(\zeta_{10} + \eta_{10})/\Delta x^2 \tag{2.9}$$

$$w^u = -(\zeta_{00} + \eta_{00})/\Delta x^2 \tag{2.10}$$

and

$$\begin{aligned} b^u = u_{\text{a}}\tau'_{\text{a}} + u_{\text{w}}\tau'_{\text{w}} + (mfv)^u + m^u g(H_{10} - H_{00})/\Delta x - (P_{10} - P_{00})/2\Delta x \\ + [(\zeta_{10} - \eta_{10})(v_{10} - v_{1-1}) - (\zeta_{00} - \eta_{00})(v_{00} - v_{0-1}) \\ + \eta^B_{00}(v_{10} - v_{00}) - \eta^B_{0-1}(v_{1-1} - v_{0-1})]/\Delta x \Delta y. \end{aligned} \tag{2.11}$$

For the v-component the constants are:

$$c^v = \tau'_{\rm w} + (\eta^B_{00} + \eta^B_{-10})/\Delta x^2 + (\zeta_{01} + \zeta_{00} + \eta_{01} + \eta_{00})/\Delta y^2 \quad (2.12)$$

$$n^v = -(\zeta_{01} + \eta_{01})/\Delta y^2 \quad (2.13)$$

$$s^v = -(\zeta_{00} + \eta_{00})/\Delta y^2 \quad (2.14)$$

$$e^v = -\eta^B_{00}/\Delta x^2 \quad (2.15)$$

$$w^v = -\eta^B_{-10}/\Delta x^2 \quad (2.16)$$

and

$$\begin{aligned} b^v = v_{\rm a}\tau'_{\rm a} + v_{\rm w}\tau'_{\rm w} - (mfu)^v + m^v g(H_{01} - H_{00})/\Delta y - (P_{01} - P_{00})/2\Delta y \\ + [(\zeta_{01} - \eta_{01})(u_{01} - u_{-11}) - (\zeta_{00} - \eta_{00})(u_{00} - u_{-10}) \\ + \eta^B_{00}(u_{01} - u_{00}) - \eta^B_{-10}(u_{-11} - u_{-10})]/\Delta x \Delta y. \end{aligned} \quad (2.17)$$

The model is solved on a C-grid where the velocity points are situated at $i+1/2$ and $j+1/2$. The Coriolis term must therefore be calculated using mfu in the v point and mfv in the u point, which is written as $(mfu)^v$ and $(mfv)^u$ respectively. The surface stress terms are

$$\tau'_{\rm w} = \rho_{\rm w} C_{\rm dw} |\vec{v} - \vec{v}_{\rm w}| \quad (2.18)$$

$$\tau'_{\rm a} = \rho_{\rm a} C_{\rm da} |\vec{v}_{\rm a}| \quad (2.19)$$

and they should be calculated on the u point when calculating the u-components and on the v-point for the v-component. In addition it greatly simplifies the equations to first calculate η also on the B-grid, shown here as η^B. This means that $4\eta^B_{-10} = \eta_{00} + \eta_{01} + \eta_{-11} + \eta_{-10}$ and $4\eta^B_{00} = \eta_{10} + \eta_{11} + \eta_{01} + \eta_{00}$.

2.3 Thermodynamics

We have already mentioned how sea ice may effect the ocean and atmosphere, as well as any exchange between the two. Most of these effects should in essence be modelled within the thermodynamic portion of a sea ice model, the dynamic part only coming into play when wind or ocean currents transport the ice and thus changing its thickness distribution. The relative importance of thermodynamics led early investigators to try modelling sea ice in a global context using only very limited (or no) dynamics and focusing on thermodynamics (see e.g. Bryan et al. (1975), Washington et al. (1976), Manabe et al. (1979)). These models were relatively successful at the time but today a thermodynamics-only approach is considered insufficient.

The first truly successful thermodynamic model of sea ice was compiled by Maykut and Untersteiner (1971). This is a one dimensional model which

describes the thermodynamical growth and melt of a snow covered sea-ice slab due to prescribed external forcing. The model was very successful in describing the seasonal variations of sea-ice thickness. The Maykut and Untersteiner (1971) model is of course not perfect and Ebert and Curry (1993) made some noteworthy improvements to it. Further steps towards a detailed understanding of sea ice thermodynamics on a small scale have been made (see e.g. Feltham et al. (2006)), but the focus here is on the simplified thermodynamic models which have resulted and are applicable to coupled model experiments.

Such a model was first introduced by Semtner (1976) and it remains a popular choice among modellers. Semtner (1976) made a number of simplifications to the model proposed by Maykut and Untersteiner (1971)—the most important of which is a greatly reduced number of vertical layers in the ice. Maykut and Untersteiner (1971) modelled the heat conduction through the ice using a grid with a constant vertical spacing of 10 cm while Semtner (1976) used a grid with a variable vertical spacing. He showed that his model gave good results with only three grid points, one in the snow layer and two in the ice. Fewer points are needed when modelling thin ice.

For very thin ice Semtner (1976) suggested using a "zero-layer" model that only predicts the snow thickness, ice thickness and the surface temperature. He also noted that users strained for computational resources could use the zero-layer model alone when running climate simulations. With a few adjustments in the parametrisation Semtner (1976) could reach remarkably good results using the zero-layer model, given the model's simplicity. He did however note that the zero-layer model would not be well suited for climate studies and reiterated this conclusion in a later paper (Semtner, 1984). Despite these warnings the zero-layer model remained a popular choice in climate modelling and the model is still widely used today.

More advanced thermodynamic models for use in coupled modelling studies have of course been developed since the Semtner-model. These include for example the models by Bitz and Libscomb (1999), Ukita and Martinson (2001) and Huwald et al. (2005). In their model Bitz and Libscomb (1999) focus on solving the energy imbalance present in the previously mentioned models due to inappropriate treatment of internal brine-pocket melting. Ukita and Martinson (2001) and Huwald et al. (2005) focus on ways to improve the modelling of processes within the ice. Ukita and Martinson (2001) propose a multilayer model which determines the optimum number of levels for each time step while Huwald et al. (2005) propose a multilayer sigma-coordinate model. These latest improvements in modelling of the thermodynamics of sea ice are likely to result in considerable improvements in the sea ice component of global climate models.

Most of the problems being addressed by latest thermodynamic models are of little concern here, where our main goal is to model fast ice and flaw polynyas. The thin ice forming out of polynyas can be adequately described

using a Semtner zero layer model, although the transition from frazil ice to level ice is poorly parametrised in most ice models. This will be addressed in more detail in chapter 3. The fast ice is fairly thick first year ice which could probably be modelled using a zero layer model, although a three-layer model would be preferable. A three layer model, with variable albedo should give a good simulation of the ice growth and melt, which are of main concern here. Other concerns, such as imbalance in energy and the lack of proper salt content formulation are of minor importance and are ignored.

In the three layer Semtner model the ice is modelled using two model layers and the snow is modelled in one model layer. The temperature in each layer is governed by the one dimensional heat equation;

$$(\rho c)_{\mathrm{i/s}} \frac{\partial T}{\partial t} = k_{\mathrm{i/s}} \frac{\partial^2 T}{\partial z^2}, \tag{2.20}$$

where $(\rho c)_{\mathrm{i}} = 1.88 \times 10^6$ J/m^3/K is the heat capacity of ice, $(\rho c)_{\mathrm{s}} = 6.90 \times 10^5$ J/m^3/K the heat capacity of snow, $k_{\mathrm{i}} = 2.03$ W/m/K is the conductivity of ice and $k_{\mathrm{s}} = 0.310$ W/m/K the conductivity of snow. These values are adopted from Semtner (1976).

Additionally the three layer model includes an energy reservoir for collecting the penetrating solar radiation. In reality penetrating solar radiation initiates melting of high salinity patches within the ice, before the surface starts melting. This has the effect that brine pockets within the ice grow larger, but they remain trapped in the ice until considerable amount of melting takes place. These brine pockets may be considered to represent a storage of energy not yet used to melt the ice.

This behaviour is simulated in the model using a simple energy reservoir. The energy in the reservoir is used to prevent the temperature of the uppermost layer from dropping below the freezing point. Semtner (1976) prevented the reservoir arbitrarily from accumulating more than 30% of the heat needed to melt all the ice. According to him the net effect of the reservoir is that penetrating solar radiation does not cause immediate surface melting in summer while internal cooling in the fall is retarded.

The model implementation here follows Semtner (1976) very closely and for further detail the reader is directed to the original publication. One notable exception, however, is the treatment of thin ice. If the layer thickness falls below a critical threshold the numerical method becomes unstable and the number of layers is reduced by one. This means that the three layer model can be any combination of zero to two layers of ice and zero or one layer of snow. The critical threshold depends on the model time step so that the grid box thickness cannot fall below $\sqrt{2k_{\mathrm{s}}\Delta t/(\rho c)_{\mathrm{s}}} \approx 2.3$ cm in the snow and $\sqrt{2k_{\mathrm{i}}\Delta t/(\rho c)_{\mathrm{i}}} \approx 3.6$ cm in the ice, with $\Delta t = 600$ s, an appropriate time step for 10 km horizontal resolution.

The thinnest ice a two (ice) layer model can simulate is therefore approximately 5 cm thick. If we were to use an 8-hour time step, like Semtner

(1976) did the thinnest allowed grid thickness in the ice would be 25 cm and so we assume the zero layer model can be safely used for all ice thinner than that. We can therefore use the two layer setup until the ice becomes approximately 5 cm thick and then switch directly to a zero layer model. In fact for any time step shorter than 2 hours the two layer setup can be used for ice thicker than 25 cm. This simplifies the model formulation somewhat. We'll see later that it also makes sense to demand that the ice is never much thinner than somewhere between 5 and 10 cm and so, for short time steps, there is no need for switching to a zero layer model as the ice melts.

The models suggested by Semtner (1976) were stand-alone ice models with prescribed forcing. In a coupled model some additional considerations come into play. First of all Semtner (1976) prescribed a constant oceanic heat flux, but in a coupled model this should be calculated based on the ocean state. The oceanic heat flux (Q_{oi}) is calculated using the bulk formula

$$Q_{\mathrm{oi}} = C_{\mathrm{oi}}\rho_{\mathrm{o}}c_{\mathrm{o}}(T_{\mathrm{f}} - T_{\mathrm{o}})|\vec{v}_{\mathrm{i}} - \vec{v}_{\mathrm{w}}|/H, \tag{2.21}$$

where C_{oi} is the sensible heat transfer coefficient, ρ_{o} is the ocean density, c_{o} is its heat capacity, H is the thickness of the surface ocean layer, T_{f} is the freezing temperature and T_{o} is the ocean temperature. Finally $|\vec{v}_{\mathrm{i}} - \vec{v}_{\mathrm{w}}|$ is the speed of the water flow relative to the ice speed. The freezing temperature of sea water T_{f} is calculated using the relationship

$$T_{\mathrm{f}} = S_{\mathrm{o}}(c_a + c_b\sqrt{S_{\mathrm{o}}} + c_c S_{\mathrm{o}}) \tag{2.22}$$

where S_{o} is the ocean surface salinity, $c_a = -0.0575$, $c_b = 1.710523 \times 10^{-3}$ psu$^{-1/2}$, $c_c = -2.154996 \times 10^{-4}$ psu^{-1} (Millero, 1978).

Surface fluxes in Semtner (1976) were prescribed depending on the month of the year. In the current model the surface fluxes are calculated based on the 2 m temperature, cloud cover, wind speed and relative humidity given by the forcing data. The incoming short wave radiation is supplied by the ocean model thermodynamics routines, but other fluxes are calculated using the equations of Idso and Jackson (1969) and Liu et al. (1979). The implementation of these calculations is the same as in Günzel (2003). Using these formulations the change in surface temperature (T_{s}) is ΔT_{s}, where

$$\sum_j F_j + \Delta T_{\mathrm{s}} \sum_j \frac{\partial F_j}{\partial T_{\mathrm{s}}} = \begin{cases} (1-\alpha_{\mathrm{s}})F_{\mathrm{sw}} - k_{\mathrm{s}}\frac{T_0 - T_{\mathrm{s}} - \Delta T_{\mathrm{s}}}{h_{\mathrm{s}}/2} & \text{snow covered} \\ (1-\alpha_{\mathrm{i}})(1-I_0)F_{\mathrm{sw}} - k_{\mathrm{i}}\frac{T_1 - T_{\mathrm{s}} - \Delta T_{\mathrm{s}}}{h/4} & \text{else,} \end{cases} \tag{2.23}$$

and F_{sw} is the incoming solar radiation, α_{s} and α_{i} are the snow and ice albedos, respectively, I_0 is the fraction of penetrating short wave radiation, F_j denotes the long wave radiation and the sensible and latent heat fluxes and T_0 is the temperature of the snow layer while T_1 is the temperature of the uppermost ice layer.

Semtner (1976) also prescribes ice and snow albedos that change depending on the month of the year. In the current model a varying albedo is used, based on the albedo scheme of the NCAR Community Sea Ice Model (Briegleb et al., 2004), in which the albedo depends on spectral band, snow thickness and surface temperature. The total surface albedo may range from 0.83 for dry snow to 0.48 for melting and bare ice. For a detailed description of the scheme the reader is referred to Briegleb et al. (2004).

Finally advection of ice must be taken into account and it is important to advect heat rather than temperature. This cannot be done for the surface temperature, so it must be calculated by iterating equation (2.23) a sufficient number of times. The initial condition for this iteration should be the prescribed 2 m temperature. In the current implementation the iteration continues as long as the change in surface temperature between successive iterations is greater then 10^{-4} K.

Ice formation in open water is modelled in a relatively simple fashion, based on the formulation by Hibler (1979). In reality, when the temperature of the ocean surface falls below the freezing point frazil ice forms. The ice model simply assumes this ice is immediately transported to the surface forming a layer of thin ice. No frazil ice is formed in deeper layers of the ocean model. The amount of ice formed is calculated from the energy needed to bring the ocean surface from its supercooled state to freezing, i.e.

$$Q_{\mathrm{ow}} = \rho_{\mathrm{o}} c_{\mathrm{o}} H (T_{\mathrm{f}} - T_{\mathrm{o}}). \tag{2.24}$$

The amount of ice formed in the open water is then

$$\Delta h_{\mathrm{ow}} = \frac{Q_{\mathrm{ow}}}{\rho_{\mathrm{i}} q_{\mathrm{i}}}, \tag{2.25}$$

where q_{i} and ρ_{i} are the latent heat of fusion and density for sea ice respectively.

These changes in h now need to be related to the continuity equations (2.1) and (2.2) via the source/sink terms S_m and S_A. Deriving an equation for S_m is not difficult since it is a mass conservation formula. Assuming ρ_{i} is a constant, which is a reasonable approximation, this term can be written out simply as

$$S_m = \rho_{\mathrm{i}} [A \Delta h + (1 - A) \Delta h_{\mathrm{ow}}], \tag{2.26}$$

where Δh is the change in level ice thickness. Another mass conservation equation that should be kept in mind is that of salt flux to and from the ice. In the model no freshwater flux is associated with ice melt, only salt flux and so the change in ocean salt contents during one time step is simply

$$\Delta S = (S_{\mathrm{o}} - S_{\mathrm{i}}) \frac{S_m}{\rho_{\mathrm{o}} H - S_m}, \tag{2.27}$$

where S_{o} is the salinity of the surface ocean layer and S_{i} is the (constant) ice salinity.

It is, however, not possible to derive an equation for S_A in such simple terms and the equation for it must be empirical. Two common methods for calculating S_A are due to Hibler (1979) and Mellor and Kantha (1989). Hibler devised his method using fixed thermodynamic growth rates instead of calculating Δh and Δh_{ow}, but the resulting equation is the same;

$$S_A = (1 - A)\max(\Delta h_{\mathrm{ow}}, 0)/h_0 + A\min(S_m, 0)/2m, \tag{2.28}$$

where h_0 is the demarcation thickness between thick and thin ice, also known as the lead closing parameter. To see how this equation works we will now consider the two obvious cases of freezing and melting.

When freezing $\Delta h_{\mathrm{ow}} > 0$ and $S_m > 0$ so equation (2.28) becomes simply

$$S_A h_0 = (1 - A)\Delta h_{\mathrm{ow}}. \tag{2.29}$$

This means that the new ice covers an area S_A so that its thickness is greater than or equal to h_0. Hibler (1979) states that h_0 should be chosen to be small compared to mean ice thickness but large enough so that heat flux through ice with thickness h_0 is substantially less than through open water. Based on this and an idealised experiment, he chooses $h_0 = 0.5$ m for a pan-Arctic sea ice simulation. In contrast Bjornsson et al. (2001) used $h_0 = 0.3$ m in their polynya simulation. They argued that h_0 should be considered a measure of the thickness of the initial ice forming in the polynya and that the thickness of pancake ice would be a good measure of that, giving 10 cm $\lesssim h_0 \lesssim$ 30 cm. They noted also that a higher value of h_0 is needed for a proper simulation of the seasonal cycle of the central Arctic. It appears therefore that this simple model is not able to model both the central ice pack and the marginal ice zone. This is of little concern here since the focus is on the marginal ice zone and first-year ice, but the choice of h_0 remains difficult.

When the ice starts melting $\Delta h_{\mathrm{ow}} = 0$ and $S_m < 0$ and following Tremblay and Mysak (1997) we let incoming heat flux warm the ocean. Hibler (1979) stipulates that the ocean should stay at freezing while ice is present and calculates a negative Δh_{ow}, which then contributes to the melting of the ice through S_m. But, as Tremblay and Mysak (1997) point out, incident energy warms up the mixed layer, despite the presence of ice so allowing the ocean to warm up beyond T_{f} is more realistic.

During melt equation (2.28) then becomes

$$S_A = AS_m/2m = A\Delta h/2h. \tag{2.30}$$

The reasoning behind this formulation is as follows: Let us assume that the ice thickness in the grid box is uniformly distributed between 0 and $2h$ and all the ice melts at the same rate. Then at time Δt all ice that is thinner than Δh will have melted away creating open water. Having assumed uniform distribution this means that the open water now covers

an area equal to $\Delta hA/2h$, giving the sink term S_A in equation (2.30). This assumption works very well for most situations, but not for land-fast ice. If one uses equation (2.30) for fast ice one may expect that the fast ice starts breaking up as soon as melting begins.

Another approach to calculating S_A is due to Mellor and Kantha (1989). They formulate S_A as

$$S_A = \Phi(1 - A)\frac{Q_{\text{ow}}}{\rho_{\text{i}} q_{\text{i}} h}\Delta t, \tag{2.31}$$

where Φ is an empirically determined function. This equation describes both melting and freezing and the ocean surface temperature is therefore kept at freezing as long as there is ice in the grid cell. Mellor and Kantha (1989) differentiate between melting and freezing by giving Φ different constant values;

$$\Phi = \begin{cases} \Phi_{\text{F}} = 4 & \text{if } Q_{\text{ow}} < 0 \\ \Phi_{\text{M}} = 0.5 & \text{otherwise.} \end{cases} \tag{2.32}$$

To better understand the difference between the two approaches we first compare the two during freezing. We can easily recover equation (2.29) from equation (2.31) by setting $\Phi_{\text{F}} = h/h_0$, which gives $h_0 = h/\Phi_{\text{F}}$. Equation (2.31) therefore states that during freezing the newly formed ice will have a thickness equal to h/Φ_{F}. This means that when ice forms in a grid cell that had no ice before this cell will become fully covered with thin ice. This is reasonable under calm conditions, but wind and wave action will tend to create streaks of ice leaving large areas of open ocean, despite continuous ice formation in the area (Bjornsson et al., 2001, and refrences therein). Under these conditions a constant h_0 gives better results. Ideally therefore h_0 (or Φ_{F}) should be a function of at least wind speed and possibly ice thickness and/or compactness. We are unaware of any studies regarding such parametrisations, but in chapter 3 an attempt is made to parametrise h_0 based on wind speed and ice thickness.

Mellor and Kantha (1989) handle melting somewhat differently to the approaches by Hibler (1979) and Tremblay and Mysak (1997) in that open water only forms due to negative Q_{ow} and the ice thickness within the cell is assumed to be constant. In the original implementation the ocean temperature is kept at freezing while ice exists in the grid cell, the same as in the Hibler (1979) model. It is, however, easy to modify the Mellor and Kantha (1989) model so that the ocean temperature rises before all the ice is melted, similar to what Tremblay and Mysak (1997) do.

To do this we note that if the ocean temperature is always kept at the freezing point when ice is present then the oceanic heat flux in equation (2.21) is always zero. All basal melt (Δh_{b}) that occurs in the model must therefore be due to the negative Δh_{ow} in equation (2.26). If we allow the ocean to heat up above the freezing point basal melt occurs because of the

resulting oceanic heat flux and we can therefore replace $(1 - A)Q_{\mathrm{ow}}/(\rho_{\mathrm{i}} q_{\mathrm{i}})$ in equation (2.31) with the total basal melt; $A\Delta h_b$. Equation (2.31) then becomes

$$S_A = \Phi_{\mathrm{M}} A \frac{\Delta h_b}{h} \Delta t. \tag{2.33}$$

Compared to Hibler's formulation in equation (2.28) this formulation is much better suited for modelling fast ice. In this formulation no open water forms unless the ocean temperature rises above the freezing temperature. Under normal circumstances this does not happen unless there's an opening in the ice cover and incoming short wave radiation warms the water in that opening. It is possible that the ocean be heated from below, e.g. by the advection of warmer river water. In such a case it is not unreasonable to demand that S_A remains zero as long as $A = 1$.

2.4 Rheology

Rheology is the study of the deformation and flow of matter under the influence of applied stress. Mathematically the study of sea-ice rheology revolves around finding an appropriate formulation for the stress tensor $\boldsymbol{\sigma}$ as a function of the applied strain rate $\dot{\boldsymbol{\varepsilon}}$, sea-ice thickness, concentration and possibly other parameters.

In the following sections we will discuss some viscous-plastic rheologies, which have been the most widely used methods for modelling sea ice on the large scale. The most common of these is without doubt the viscous-plastic rheology of Hibler (1979) which is discussed in section 2.4.2, but the granular model of Tremblay and Mysak (1997), the modified Coulomb yield curve of Hibler and Schulson (2000) and the curved diamond yield curve of Wang (2007) are also discussed. The discussion also includes new derivatives of these yield curves, specifically designed to allow for tensile strength necessary for land-fast ice modelling.

The first truly successful sea-ice rheology was the isotropic elastic-plastic rheology, introduced in the AIDJEX sea ice model (Coon et al., 1974). In it sea ice was described primarily as plastic material which deforms irreversibly once a critical stress state in the ice is reached. While the stress is sub-critical, however, the ice is modelled as an elastic material which deforms under stress, but returns back to its original shape when the stress is removed. Conceptually then the model describes a material which acts like a stiff rubber sheet under sub-critical stress but breaks when the stress becomes too large. The critical stress threshold is in general a surface in stress space but assuming isotropy allows it to be expressed as a (yield) curve in the plane of the principle stresses σ_1 and σ_2 or through the stress invariants σ_{I} and σ_{II} (which will be discussed in the following section).

A plastic description of sea ice is highly intuitive since the formation of ice ridges and leads can obviously be described as an irreversible deforma-

tion which occurs at a critical stress. The sub-critical elastic deformation was however mostly chosen for mathematical convenience. A purely plastic model does not allow sub-critical stresses to be calculated so it's impossible to decide whether the stress is critical or sub-critical. It is therefore necessary to apply a different model for sub-critical stresses and Coon et al. (1974) argued for an elastic response.

Hibler (1979) based his ice model on the AIDJEX model, except that he replaced the elastic response with a viscous one. He also replaced the thickness distribution of the AIDJEX model with a simple two class model as described earlier. This model became the standard reference for sea-ice modellers, commonly known as "Hibler-type" models. In replacing the elastic behaviour with a viscous one Hibler (1979) attempted to avoid complexities involved in the elastic formulation and also to improve the model performance in terms of computing resources. He chose an elliptic yield curve because it gives a mathematically simple and numerically stable formulation while also giving a reasonable representation of the physical processes involved. This model is therefore often also referred to as a viscous-plastic model with an elliptical yield curve.

In this model the ice is still modelled as a plastic for large strain rates, but at smaller strain rates it becomes linearly viscous. Hibler (1979) argues that this simulates the behaviour of a large number of jostling plastic floes. A viscous-plastic model can however not maintain high stress without any ice motion, like the elastic-plastic formulation can. So while ice subject to sub-critical stress will remain stationary in the elastic-plastic model it will flow very slowly, or creep, in the viscous-plastic model.

2.4.1 Yield curves of viscous-plastic rheologies

The viscous-plastic models discussed here are isotropic and thus have a yield surface that is a curve in the $\{\sigma_{\mathrm{I}}, \sigma_{\mathrm{II}}\}$ plane, i.e. $F(\sigma_{\mathrm{I}}, \sigma_{\mathrm{II}}, \text{scalars}) = 0$. For stresses inside the yield curve viscous deformation occurs, while for stresses on the yield curve plastic deformation takes place. In addition a flow rule is needed to determine the direction of the plastic strain rate.

Both plastic and viscous behaviour can be represented using the standard (reduced) Reiner-Rivlin form of the stress tensor

$$\sigma_{ij} = 2\eta\dot{\varepsilon}_{ij} + [\zeta - \eta]\dot{\varepsilon}_{kk}\delta_{ij} - P\delta_{ij}/2, \tag{2.34}$$

using the Einstein summation convention. Here ζ and η are the non-linear bulk and shear viscosities, P is a pressure term and $\dot{\boldsymbol{\varepsilon}}$ is the strain rate tensor given by

$$\dot{\varepsilon}_{ij} = \frac{1}{2}\left(\frac{\partial u_i}{\partial x_j} + \frac{\partial u_j}{\partial x_i}\right). \tag{2.35}$$

The viscosities may be functions of the strain rate $\dot{\boldsymbol{\varepsilon}}$ and some scalars representing the ice state. In the following they always depend on the strain

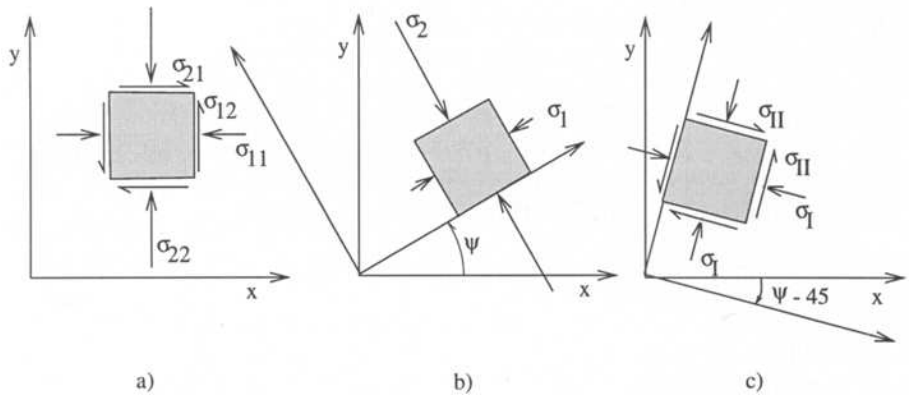

Figure 2.1: State of stress at a point in: a) model coordinates, b) principle stress coordinates and c) stress invariant coordinates (figure from Tremblay (1999)).

rate and hydrostatic ice pressure alone. The formulation of the viscosities determines the shape of the yield curve.

Since the stress tensor is symmetric, it can be diagonalized with a pure rotation of the coordinate axes. A certain rotation aligns the co-ordinate axes with the so called stress invariant axes. The stress invariants can be interpreted as the average normal stress at a point (σ_{I}) and the maximum shear stress at that same point (σ_{II}). The stress invariants are:

$$\sigma_{\mathrm{I}} = \frac{1}{2}(\sigma_{11} + \sigma_{22}) \tag{2.36}$$

$$\sigma_{\mathrm{II}} = \sqrt{(\sigma_{11} - \sigma_{22})^2 + 4\sigma_{12}^2}. \tag{2.37}$$

Another useful frame of reference are the principle stress axes. When aligned with these the stresses acting on the rotated element are the maximum and minimum normal stresses acting at a point. The shear stresses acting on the rotated element vanish identically. The principle stress axes are related to the stress invariant axis via:

$$\sigma_1 = \sigma_{\mathrm{I}} - \sigma_{\mathrm{II}} \tag{2.38}$$

$$\sigma_2 = \sigma_{\mathrm{I}} + \sigma_{\mathrm{II}}. \tag{2.39}$$

Figure 2.1 gives a graphical view of these three representations of the stress tensor.

Similar to the principle and invariant stresses principle and invariant strain rates can be defined. In the present context only the strain rate

invariants are important, and they are:

$$\dot{\varepsilon}_{\mathrm{I}} = \dot{\varepsilon}_{11} + \dot{\varepsilon}_{22} \tag{2.40}$$

$$\dot{\varepsilon}_{\mathrm{II}} = \sqrt{(\dot{\varepsilon}_{11} - \dot{\varepsilon}_{22})^2 + 4\dot{\varepsilon}_{12}^2}. \tag{2.41}$$

It is assumed that the invariant and principle axes of stress coincide with the invariant and principle axes of strain. This means that where the average normal stress and maximum shear stress occur, the average normal strain rate and maximum shear strain rate will occur. Also, where maximum (minimum) axial stress occurs, there the maximum (minimum) axial strain rate will also occur.

2.4.2 Elliptic yield curve

In his 1979 paper, Hibler suggested a model where the viscosities are formulated such that the resulting yield curve is an ellipse and that for typical strain rates normal plastic flow applies. The chosen yield curve reproduces basic sea ice characteristics, i.e. the ice is weak in tension, strong in shear and strongest in compression. It is at the same time mathematically very simple. The viscosities are given by

$$\zeta = P/2\Delta \quad \text{and} \quad \eta = \zeta/e^2, \tag{2.42}$$

where P is the hydrostatic ice pressure,

$$\Delta = \sqrt{\dot{\varepsilon}_{\mathrm{I}}^2 + \dot{\varepsilon}_{\mathrm{II}}^2/e^2} \tag{2.43}$$

and e is the ratio of the ellipse axes. It is clear that for small strain rates the viscosity tends to infinity so an upper bound must be set for ζ and η. Hibler (1979) chose the limiting values to depend on the pressure term as

$$\zeta_{\max} = (2.5 \times 10^8 \text{ s})P, \tag{2.44}$$

$$\eta_{\max} = \zeta_{\max}/e^2. \tag{2.45}$$

In addition minimum values on ζ and η were imposed to improve numerical stability. Hibler (1979) chose

$$\zeta_{\min} = 4 \times 10^8 \text{ kg/s} \tag{2.46}$$

$$\eta_{\min} = \zeta_{\min}/e^2, \tag{2.47}$$

arguing that this value is several orders of magnitude below typical strong ice interaction values, effectively yielding free drift results.

Finally the pressure term itself must depend on the ice thickness and concentration. The form chosen by Hibler (1979) was

$$P = P^* h \exp(-C[1 - A]), \tag{2.48}$$

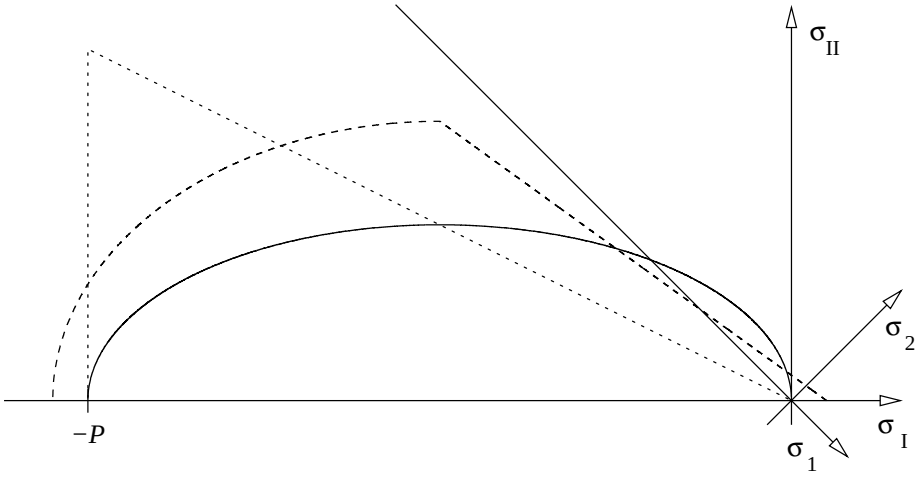

Figure 2.2: The first three yield curves discussed in the text plotted in stress invariant space scaled against P (the principle stress axes are also shown); the elliptic yield curve (solid line), the yield curve of the granular model (dotted line) and the modified Coulombic yield curve (dashed line).

where P^*, the ice strength and C are constants, h is the ice thickness and A the concentration. The constants must be chosen empirically, but $P^* \approx 30$ kN/m^2 and $C = 20$ are common choices (Hibler, 1979, Hibler and Walsh, 1982, Feltham, 2008, Tremblay and Hakakian, 2006). Here $C = 30$ and $e = 2$ are used based on Bjornsson et al. (2001) and Hibler (1979) respectively.

Ip et al. (1991) noted that this formulation for P gives non-zero stress at zero strain rates, but this can be remedied by setting

$$P' = 2\Delta\zeta, \tag{2.49}$$

and replace P in equation (2.34) with P'. This only has an effect when the viscosity is capped via equation (2.47). Figure 2.2 shows this yield curve in the $\{\sigma_\mathrm{I}, \sigma_\mathrm{II}\}$ plane.

By way of further refinement Lemieux and Tremblay (2009) suggest using a continuously differentiable form of the maximum and minimum conditions in equations (2.45) and (2.47). They show that this improves the outer-loop iteration convergence speed (see section 2.2.1) and suggest that it may prevent the appearance of multiple solutions. The form Lemieux and Tremblay (2009) suggest for ζ is

$$\zeta = \zeta_\mathrm{max} \tanh\left(\frac{P}{2\Delta\zeta_\mathrm{max}}\right) + \zeta_\mathrm{min}. \tag{2.50}$$

This form proved problematic when used in conjunction with the modifications of König Beatty and Holland (2010) (see section 2.4.5 and following

sections) and a variation of it is used here, where Δ is capped in stead of ζ. Using this approach

$$\Delta = \Delta_{\min} / \tanh \left(\frac{\Delta_{\min}}{\sqrt{\dot{\varepsilon}_{\mathrm{I}}^2 + \dot{\varepsilon}_{\mathrm{II}}^2 / e^2}} \right), \tag{2.51}$$

where $\Delta_{\min} = P/(2\zeta_{\max})$. We then calculate ζ as

$$\zeta = \frac{P}{2\Delta} + \zeta_{\min}. \tag{2.52}$$

This approach is equivalent to the one suggested by Lemieux and Tremblay (2009) when using the unmodified ellipse, but suites the modified approach by König Beatty and Holland (2010) better.

Despite being probably the most widely used sea ice model the Hibler-type model is not without faults. A notable flaw is the fact that the pressure term can cause the ice to flow, even if there are no external forces acting. This happens when there are no, or negligible winds and ocean currents acting on the ice, but there exists however a thickness gradient in the ice cover. This gets translated into a pressure gradient which causes the ice to flow. Tremblay (1999) shows that the pressure gradient term is of the same order of magnitude as the wind stress term for a 1 m thickness gradient over 100 km, compared to a wind speed of 10 m/s. It is also worth mentioning that although the pressure term parametrisation in equation (2.48) gives qualitatively reasonable sea ice strength little other justification has been given for its precise form.

The shape of the yield curve can also be considered only a rough approximation to the correct yield curve. Many attempts have been made to improve on this basic shape and the following sections contain descriptions of a few such attempts. They range from applying well known physical laws and experience from related fields (the granular model, section 2.4.3), to using laboratory results (the modified Coulombic yield curve, section 2.4.4), to using satellite images (the curved diamond, section 2.4.7).

2.4.3 Granular model

A somewhat different approach to the elliptic yield curve was suggested by Tremblay and Mysak (1997), proposing a model based on a granular material rheology. For deformation along a sliding line, the following failure criterion (based on Coulomb's friction law) must be met:

$$\tau_{\mathrm{s}} = -\sigma_{\mathrm{s}} \tan\phi + C, \tag{2.53}$$

where ϕ is the macroscopic angle of friction, τ_{s} and σ_{s} are the shear and normal stresses acting on the sliding plane and C is the cohesive strength.

Tremblay and Mysak (1997) set $C = 0$ arguing that at the coarse resolution their model was to be applied to sea ice has no cohesive strength.

This yield criterion is equivalent to dynamic friction between two dry surfaces where the frictional force is proportional to the normal force. The constant of proportionality is the coefficient of friction $\tan\phi$. For stress ratios $-\tau_s/\sigma_s < \tan\phi$ the ice behaves like an elastic solid and for $-\tau_s/\sigma_s = \tan\phi$ it flows like a fluid. Equation (2.53) can also be written in terms of the stress invariants as

$$\sigma_{II} = -\sigma_I \sin\phi + C'. \tag{2.54}$$

The resulting constitutive law has the same form as the constitutive law in equation (2.34) with $\zeta = 0$ and $P/2$ replaced by P;

$$\sigma_{ij} = 2\eta\dot{\varepsilon}_{ij} - \eta\dot{\varepsilon}_{kk}\delta_{ij} - P\delta_{ij}. \tag{2.55}$$

The value of η, which here should be referred to as the coefficient of friction, is given by

$$\eta = \frac{P\sin\phi}{\dot{\varepsilon}_{II}}. \tag{2.56}$$

The ice pressure $P = -\sigma_I$ is then found by perturbing the last known solution to the momentum equation so that the resulting velocity fulfils the equation:

$$\dot{\varepsilon}_I = \dot{\varepsilon}_{II}\tan\delta, \tag{2.57}$$

where δ is the angle of dilatency. Section 2.4.3 discusses the pressure term solver in more detail. The pressure is therefore only related to ice thickness and concentration through the upper limit set on it;

$$P_{max} = P^* h \exp(C[1 - A]), \tag{2.58}$$

analogously to equation (2.48). Equation (2.57) and the momentum equation are both solved inside a single outer loop, equation (2.57) being solved first. Since there is potentially some difference between the result of the two solutions a larger number of outer loop iterations is needed than when integrating a Hibler-type model. The resulting yield curve is shown in figure 2.2.

Since $\zeta = 0$ the granular material rheology has the form of an incompressible Newtonian fluid with non-linear shear viscosity. Compressibility is however present in the model since the pressure term has a maximum value of P_{max}. For small strain rate values the coefficient of friction, η, must also be set to a constant value η_{max} resulting in a viscous behaviour of the ice under those conditions.

It is worth noting here that Tremblay and Hakakian (2006) showed that using the same ice strength parameter, P^* for the granular model and the ellipse will result in differences in ice strength under isotropic compression.

For given ice strength under isotropic compression, p^*, the ice strength parameter P^* should take the values

$$P^* = p^* \begin{cases} 2/(1+\sqrt{1+1/e^2}) & \text{for ellipse} \\ 2/(1-k_T+\sqrt{(1+1/e^2)(1+k_T)^2}) & \text{for cohesive ellipse} \\ 1/(1+\sin\phi) & \text{for granular model.} \end{cases} \tag{2.59}$$

Note that the eccentricity plays a role here, as well as the angle of friction, ϕ and the cohesion parameter, k_T (see section 2.4.5).

For $e = 2$, $P^*/p^* \approx 0.94$ for the ellipse while for $\phi = 30°$ (as suggested by Tremblay and Mysak, 1997) $P^*/p^* = \frac{2}{3}$, so this is worth considering if the two yield curves are to be compared. Initial tests showed that when comparing different rheologies p^* is the relevant parameter with respect to ridging in the model, not P^*. This scaling is always applied in the model.

We note here also that the modified Coulombic yield curves and the trimmed ellipse (see section 2.4.4, 2.4.6 and 2.4.8) scale like the ellipse (with cohesion) and that the curved diamond (see section 2.4.7) requires no scaling. In the experiments conducted here p^* is set to $p^* = 37.5$ kN/m^2, based on Tremblay and Hakakian (2006), unless otherwise stated.

It was mentioned earlier that the construction of ice pressure in Hibler's model in equation (2.48) can cause ice movement in absence of any (other) forcing. This situation is rectified here since the ice pressure is calculated based on the ice velocities and the angle of dilation. This is probably the most important difference between the two models. Unfortunately this also means increased computation time and complexity in the model code since the ice pressure must be solved iteratively and the pressure and momentum equations must be solved repeatedly until the solution converges. The increased numerical cost is probably the main reason this model has seen much less adoption than the Hibler (1979) one.

Pressure term solver

In the granular model the pressure term is calculated using an iterative solver, not a simple analytical formula as in Hibler (1979). As a result the model has higher computational requirements and worse outer-loop convergence than the Hibler-type models. Following is a short description of the pressure term solver. It differs from the one in Tremblay and Mysak (1997) in that it uses an SOR solver, instead of a Gauss-Seidel method and that the target solution accuracy is variable, similar to the way the momentum equation is solved (see section 2.2.1). Additionally, the C-grid Tremblay and Mysak (1997) use has the velocity points at $i - 1/2$ and $j - 1/2$, but on the current grid these points are at $i + 1/2$ and $j + 1/2$. Tremblay and Mysak (1997) also use the free drift solution as a starting point for their iteration while here we use the solution from the previous time step. This is more

appropriate for the much shorter time step used here. Finally we assume zero degree turning angles, appropriate for a coupled model.

To solve the pressure equation the previous solution (from the previous time step or the previous outer loop iteration) is perturbed until equation (2.57) is fulfilled. In particular we are looking for a perturbed solution $\vec{v}_\mathrm{p} = \vec{v} + \vec{v}'$ and $P_\mathrm{p} = P + P'$ to the momentum equation so that both $\{\vec{v}_\mathrm{p}, P_\mathrm{p}\}$ and $\{\vec{v}, P\}$ are solutions to that equation. Inserting $\{\vec{v}_\mathrm{p}, P_\mathrm{p}\}$ into the momentum equation and assuming the Coriolis terms and frictional terms (i.e. the terms in $\boldsymbol{\nabla \cdot \sigma}$ not dependent on P) are constant we can subtract the unperturbed state giving:

$$\rho_\mathrm{w} C_\mathrm{dw} |\vec{v} - \vec{v}_\mathrm{w}| \vec{v}' = \vec{\nabla} P', \tag{2.60}$$

assuming that $|\vec{v} - \vec{v}_\mathrm{w}| = |\vec{v}_\mathrm{p} - \vec{v}_\mathrm{w}|$. This can then be substituted into equation (2.57) resulting in

$$\vec{\nabla} \cdot \left(\frac{\vec{\nabla} P'}{\rho_\mathrm{w} C_\mathrm{dw} |\vec{v} - \vec{v}_\mathrm{w}|} \right) = \dot{\varepsilon}_\mathrm{II} \tan\delta - \dot{\varepsilon}_\mathrm{I}, \tag{2.61}$$

where $\dot{\varepsilon}_\mathrm{I}$ and $\dot{\varepsilon}_\mathrm{II}$ are calculated using $\vec{v}$.

Rewriting equation (2.61) using finite differences the pressure perturbation can be calculated as

$$P'_{00} = \omega(\dot{\varepsilon}_\mathrm{II} \tan\delta - \dot{\varepsilon}_\mathrm{I}) \left(\frac{1}{\Delta x^2} \left[\frac{1}{\zeta^u_{00}} + \frac{1}{\zeta^u_{-10}} \right] + \frac{1}{\Delta y^2} \left[\frac{1}{\zeta^v_{00}} + \frac{1}{\zeta^v_{0-1}} \right] \right)^{-1}, \tag{2.62}$$

where $\zeta = \rho_\mathrm{w} C_\mathrm{dw} |\vec{v} - \vec{v}_\mathrm{w}|$ with the superscript u and v denoting that ζ is to be calculated in the u and v point, respectively and $\omega \in]1, 2[$ is the over-relaxation parameter. Using $\omega = 1.5$ reduces the number of iterations needed by about factor 10, compared to the Gauss-Seidel solver. Here we've used the same notation as in section 2.2.1, where by $P'_{00} := P'_{i,j}$, $P'_{01} := P'_{i,j+1}$, etc. Note also that the solution must be bounded so that $P_\mathrm{min} \leq P + P' \leq P_\mathrm{max}$, where P_max is calculated using equation (2.58). For cohesive strength (i.e. $\sigma_\mathrm{I} > 0$) one can set $P_\mathrm{min} < 0$, but Tremblay and Mysak (1997) assume $P_\mathrm{min} = 0$.

Once the pressure perturbation has been calculated the velocity perturbation is calculated using equation (2.60), i.e.

$$u'_{00} = \frac{P'_{00}}{\Delta x \zeta^x_{00}} \quad u'_{-10} = \frac{-P'_{00}}{\Delta x \zeta^x_{-10}} \tag{2.63}$$

$$v'_{00} = \frac{P'_{00}}{\Delta x \zeta^x_{00}} \quad v'_{0-1} = \frac{-P'_{00}}{\Delta x \zeta^x_{0-1}}. \tag{2.64}$$

The resulting perturbation quantities are then used to calculate updated pressure and velocity fields for the next step of the iteration; i.e. $\vec{v}^{k+1} =$

$\vec{v}^k + \vec{v}'$ and $P^{k+1} = P^k + P'$. These iterations are continued until the pressure perturbation term becomes sufficiently small. This target is assumed to be $\epsilon_{\mathrm{P}} = P^* \epsilon_{\mathrm{SOR}}$, where ϵ_{SOR} is recalculated after each outer loop iteration (see section 2.2.1).

2.4.4 Modified Coulomb yield curve

We now discuss a model which can be thought of as a combination of the viscous plastic model of Hibler (1979) and the granular model of Tremblay and Mysak (1997). This model uses a so-called modified Coulomb yield curve, first set forward by Hibler and Schulson (2000) when studying anisotropic approaches to sea ice modelling, but later used in a large scale, isotropic model by Heil and Hibler (2002). This yield curve is based on brittle fracture paradigm for sea ice failure on large scale. It can be argued that with this fracture view the behaviour of failure should be similar at small and large scales (Heil and Hibler, 2002, and references therein). Therefore the yield curve of Hibler and Schulson (2000) can be used at large scales, even though it is based on laboratory data.

The curve gives friction-based failure up to a limiting compressive stress while for higher stresses ridging occurs. This limit is set at pure shear deformation, in accordance with the results of laboratory experiments. The yield curve also includes a small amount of tensile stress.

The modified Coulomb yield curve is shown in figure 2.2. Although this curve is referred to as modified Coulombic it can just as well be thought of as a modified ellipse which, when considering the actual formulation, is perhaps a more instructive way of thinking about it.

Consider an elliptic yield curve as described in section 2.4.2. Now demand that for low stress the yield curve be Coulombic, not elliptic. Hibler and Schulson (2000) achieve this by setting

$$\eta = \min(\zeta / e^2, \eta_1), \tag{2.65}$$

where

$$\eta_1 = \frac{P/\alpha - 2\zeta \dot{\varepsilon}_{\mathrm{I}}}{\beta \dot{\varepsilon}_{\mathrm{II}}}, \tag{2.66}$$

with $\alpha = 1.8$ and $\beta = 1.4$. In addition they use a smaller axes ratio of $e = \sqrt{1.91716}$. This gives the desired Coulombic shape for low stress seen in figure 2.2. Additionally, to ensure that there is no stress at zero strain rates Hibler and Schulson (2000) set

$$P' = 2\gamma \Delta\zeta, \tag{2.67}$$

with $\gamma = 0.91$ and replace P with P' in equation (2.34), which then reads

$$\sigma_{ij} = 2\eta \dot{\varepsilon}_{ij} + [\zeta - \eta] \dot{\varepsilon}_{kk} \delta_{ij} - P'/2. \tag{2.68}$$

Since $\gamma < 1$ this also gives cohesive strength under isotropic divergence.

There are no lower bounds for the values of ζ and η, unlike in the elliptic formulation, and the upper bound used is considerably lower or $\zeta_{\max} = (10^6 \text{ s})P$, instead of $\zeta_{\max} = (4 \times 10^8 \text{ s})P$, used for the ellipse. Being relatively new this formulation has seen very little adoption, but it does show promise being numerically efficient like the elliptic formulation, while retaining the physically reasonable Mohr-Coulomb triangle shape for low stress. It does, however, use the same ice pressure parametrisation as the elliptic formulation and is therefore susceptible to problems due to it.

2.4.5 Cohesion

Since the main goal here is to model land-fast ice it is necessary to consider yield curves that describe ice which has some cohesive strength. In the following sections we will consider three yield curves, especially created to test the modelling of land-fast ice. Each one is based to some extent on previously published work, but the modifications made here are aimed at improving the model behaviour when simulating cohesive strength in ice. These yield curves (along with the elliptic yield curve) are used in a realistic setup in chapters 5 and 6.

Cohesion exists in a model whenever the modelled stress lies at a point where σ_1 is positive. As figure 2.2 shows this may happen when using either the elliptic or the modified Coulombic yield curves. In the case of the elliptic yield curve cohesion only exists as long as σ_2 is positive definite; i.e. as long as there is compression along the axis that is orthogonal to the axis of maximum divergence. At isotropic divergence the elliptic yield curve has no cohesive strength. The modified Coulombic yield curve on the other hand also possesses cohesive strength under isotropic divergence.

The elliptic yield curve should therefore be considered a "cohesive yield curve", even though it does not allow for cohesion under biaxial divergence. In fact Dumont et al. (2009) show that the elliptic yield curve can be used to model ice bridges in a limited fashion, precisely because of its cohesive properties.

The granular model can also be easily modified to include cohesion. This is done by allowing P to take on negative values when solving equation (2.57). This results in positive values for σ_I and hence cohesive strength.

The most feasible way of including cohesion under biaxial divergence in a Hibler-type model is probably the one suggested by König Beatty and Holland (2010). They derive a simple formulation which adds cohesive strength, T, to the ellipse used by Hibler (1979), effectively stretching it so that it reaches the positive side of the σ_I axis. The parameter T is then a measure of the cohesive strength under isotropic divergence. Such a shape is attained by simply replacing P in equations (2.42) with $P + T$ and with $P - T$ in

equation 2.34, which then read

$$\zeta = (P+T)/2\Delta \quad \text{and} \quad \eta = \zeta/e^2, \tag{2.69}$$

and

$$\sigma_{ij} = 2\eta\dot{\varepsilon}_{ij} + [\zeta - \eta]\dot{\varepsilon}_{kk}\delta_{ij} - (P-T)\delta_{ij}/2. \tag{2.70}$$

In addition, König Beatty and Holland (2010) assume that the cohesive strength is proportional to the compressive strength and refer to the constant of proportionality as $k_T = T/P$. In their idealised setup König Beatty and Holland (2010) assume that $k_T = 1$, citing Tremblay and Hakakian (2006) who estimate $0.5 \lesssim k_T \lesssim 0.8$.

2.4.6 A flexible modified Coulombic yield curve

The approach of König Beatty and Holland (2010) is interesting in itself, but it also allows for a redefinition of the modified Coulombic yield curve in more flexible terms. The modified Coulombic yield curve may be considered primarily a modification of the elliptic yield curve, replacing the elliptic shape with a linear one for $\sigma_{\mathrm{I}} > -P/2$. To simplify the following we note that equation 2.42 may be rewritten in terms of the invariant stresses and strain rates via equations (2.36), (2.37) and (2.70) as

$$\sigma_{\mathrm{I}} = \zeta\dot{\varepsilon}_{\mathrm{I}} - (P-T)/2 \tag{2.71}$$

$$\sigma_{\mathrm{II}} = \eta\dot{\varepsilon}_{\mathrm{II}}. \tag{2.72}$$

Using this notation it's easy to derive the Coulombic part of the modified Coulombic yield curve as the line (cf. equation (2.53))

$$\sigma_{\mathrm{II}} = -(\sigma_{\mathrm{I}} - T)\sin\phi, \tag{2.73}$$

where ϕ is again the macroscopic angle of friction. Now, since $\sigma_{\mathrm{II}} = \eta\dot{\varepsilon}_{\mathrm{II}}$ we have:

$$\eta_1 = -\frac{(\sigma_{\mathrm{I}} - T)\sin\phi}{\dot{\varepsilon}_{\mathrm{II}}} \tag{2.74}$$

$$= \frac{(P+T)/2 - \zeta\dot{\varepsilon}_{\mathrm{I}}}{\dot{\varepsilon}_{\mathrm{II}}}\sin\phi, \tag{2.75}$$

for the Coulombic part of the yield curve.

Hibler and Schulson (2000) demand that the transition between the elliptic and Coulombic parts of the yield curve takes place at pure shear deformation of the ellipse. In accordance with the normal flow rule the plastic strain rate is normal to the yield curve and since the principle axes of stress and strain rate coincide, pure shear occurs when this normal is parallel to the σ_{II} (and $\dot{\varepsilon}_{\mathrm{II}}$) axis. This happens at the centre of the ellipse, where $\sigma_{\mathrm{I}} = -(P-T)/2$ and $\sigma_{\mathrm{II}} = (P+T)/(2e)$, since e is the ellipse axis ratio.

If we equate this value for σ_{II} with σ_{II} from equation (2.73) and plug in the value for σ_{I} we get

$$\sigma_{\mathrm{II}} = \frac{P+T}{2e} \tag{2.76}$$
$$= -(\sigma_{\mathrm{I}} - T)\sin\phi \tag{2.77}$$
$$= \frac{P+T}{2}\sin\phi, \tag{2.78}$$

which gives

$$e = 1/\sin\phi. \tag{2.79}$$

This also ensures that the yield curve is continuous.

The resulting equations for the shear and bulk viscosities are

$$\zeta = (P+T)/2\Delta \tag{2.80}$$
$$\eta = \min\left(\zeta\sin^2\phi, \frac{(P+T)/2 - \zeta\dot{\varepsilon}_{\mathrm{I}}}{\dot{\varepsilon}_{\mathrm{II}}}\sin\phi\right), \tag{2.81}$$

where

$$\Delta = \sqrt{\dot{\varepsilon}_{\mathrm{I}}^2 + \dot{\varepsilon}_{\mathrm{II}}^2\sin^2\phi}. \tag{2.82}$$

Using this flexible modified Coulombic (FMC) yield curve allows for easily adjusting both the angle of friction and the amount of cohesive strength under isotropic divergence. The yield curve is non-associated for the Coulombic part, with the plastic potential set by the ellipse.

2.4.7 Curved diamond yield curve

A recent addition to the number of possible yield curves is the curved diamond yield curve suggested by Wang (2007). This curve is derived based on observations of so-called linear kinematic features (LKF) and is of special interest here since it includes cohesive strength as a direct result of the methodology used. Wang (2007) shows that the shape of the yield curve can be inferred from the observed angles between LKFs. The resulting shape is a curved diamond (figure 2.3) where

$$\sigma_{\mathrm{II}} = \begin{cases} P^* + \sigma_{\mathrm{I}} & \text{if } -P^* < \sigma_{\mathrm{I}} < \sigma_{\mathrm{IX}} \\ \mu(T-\sigma_{\mathrm{I}})\sqrt{1+\alpha\sigma_{\mathrm{I}}/P^*} & \text{if } \sigma_{\mathrm{IX}} < \sigma_{\mathrm{I}} < 0 \\ T - \sigma_{\mathrm{I}} & \text{if } 0 < \sigma_{\mathrm{I}} < T. \end{cases} \tag{2.83}$$

Here σ_{IX} is the intersection point between the two first contributions and α and μ are constants, derived from the observed angles and the assumed value for T. The values for P^* and T cannot be derived using this method nor the form of σ_{I}, but Wang (2006) assumes $T = P^*/20$, $\alpha = 0.75$ and $\mu = 1$.

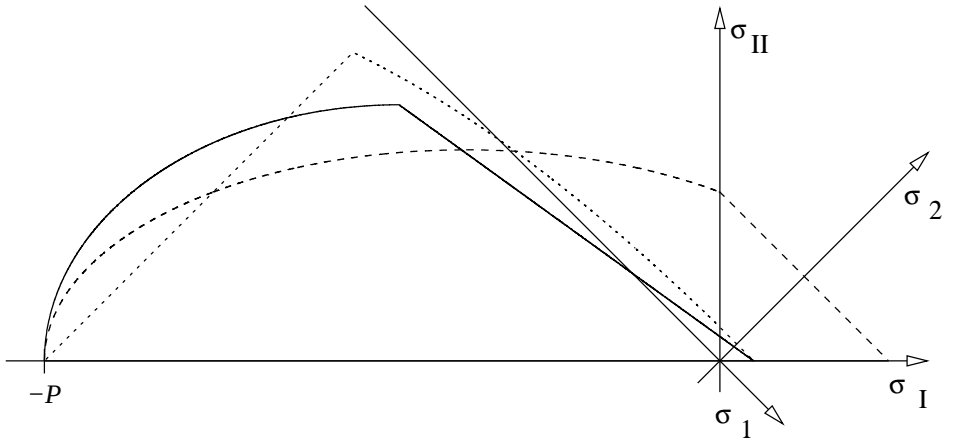

Figure 2.3: The last three yield curves discussed in the text plotted in stress invariant space scaled against P (the principle stress axes are also shown); the FMC yield curve (solid line), the curved diamond yield curve (dotted line) and the trimmed ellipse yield curve (dashed line).

In a later paper Wang and Wang (2009) calculate σ_{I} by using the equations for the elliptic yield curve and assume $e = 1$ (i.e. a circle). They then assume $T = 0$ and use a correspondingly reduced version of equations (2.83). Based on the work of König Beatty and Holland (2010) we can, however, use equation (2.71) to calculate σ_{I}, now including cohesive strength. Equations (2.83) are then used to calculate σ_{II}. The resulting equations for shear and bulk viscosity are then:

$$\zeta = (P + T)/2\Delta \tag{2.84}$$

$$\eta = \sigma_{\mathrm{II}}/\dot{\varepsilon}_{\mathrm{II}}, \tag{2.85}$$

where

$$\Delta = \sqrt{\dot{\varepsilon}_{\mathrm{I}}^2 + \dot{\varepsilon}_{\mathrm{II}}^2}. \tag{2.86}$$

When T is changed the derived parameters α and μ should also change. Wang (2007) states that the slope of the yield curve should be related to the angle between LKFs by

$$\frac{\partial \sigma_{\mathrm{II}}}{\partial \sigma_{\mathrm{I}}} = \tan\beta = \cos 2\theta, \tag{2.87}$$

where β is the slope of the yield curve and 2θ is the angle between two intersecting LKFs. The observed intersection angles 2θ are $0°$, about $90°$, from $120°$ to $160°$ and $180°$. The second line of equation (2.83) is the one containing the constants α and μ and they must be adjusted so that at

$\sigma_{\mathrm{I}} = \sigma_{\mathrm{IX}}$ the slope of the yield curve is $\beta = -26.6°$ and at $\sigma_{\mathrm{I}} = 0$ the slope is $\beta = -43.2°$ (corresponding to $2\theta = 120°$ and $2\theta = 160°$).

To derive the factors α and μ an appropriate initial value is assumed and the intersection point σ_{IX} calculated by equating the first two contributions in equation (2.83). Then α and μ are found by solving the set of equations that results when we assume that

$$\left.\frac{\partial \sigma_{\mathrm{II}}}{\partial \sigma_{\mathrm{I}}}\right|_{\sigma_{\mathrm{I}}=\sigma_{\mathrm{IX}}^{+}} = \cos(120°) \tag{2.88}$$

$$\left.\frac{\partial \sigma_{\mathrm{II}}}{\partial \sigma_{\mathrm{I}}}\right|_{\sigma_{\mathrm{I}}=0^{-}} = \cos(160°). \tag{2.89}$$

This results in a new value for α and μ which results in a new value for σ_{IX}. The final values for α and μ must therefore be found iteratively.

Wang (2007) suggests using $T = P^*/20$, $\alpha = 0.75$ and $\mu = 1$, but more appropriate values for the interval $T \in [0, P^*/20]$ seem to be $\alpha = 0.69$ and $\mu = 0.95$. These give $2\theta \in [119.6°, 120.0°]$ for $\sigma_{\mathrm{I}} = \sigma_{\mathrm{IX}}$ and $2\theta \in [159.0°, 161.8°]$ for $\sigma_{\mathrm{I}} = 0$, using equation (2.87). Setting $\mu \neq 1$ causes a discontinuity at $\sigma_{\mathrm{I}} = 0$, but this can be remedied by setting $\sigma_{\mathrm{II}} = \mu T - \sigma_{\mathrm{I}}$ if $0 < \sigma_{\mathrm{II}} < \mu T$ in equation 2.83. That means that the isotropic cohesive strength is actually μT and not T, but the desired value for μT can easily be found iteratively (see appendix B).

2.4.8 Trimmed ellipse

Finally a new yield curve is suggested which will be referred to as a trimmed ellipse. As the name suggests it is based of the traditional ellipse, but with a small modification for $\sigma_{\mathrm{I}} > 0$.

In section 2.4.5 it was shown how biaxial cohesion can be added to the elliptic yield curve by extending it into the $\sigma_{\mathrm{I}} > 0$ part of the stress plane. It is however not clear that once extended into that part of the plane the shape of the yield curve is correct. To suggest a more appropriate shape the following considerations are offered.

Let us suppose that we are considering only the way a single piece of ice yields. Assuming plasticity we can then argue that the ice will break only once a critical divergent stress is reached. The critical stress along one axis is furthermore independent of the stress exerted on the other axes, given that this stress is less than the critical stress. This means that the yield curve must be a straight line in stress space extending from $\sigma_{\mathrm{I}} = \sigma_{\mathrm{c}}\sqrt{2}$ to $\sigma_2 = \sigma_{\mathrm{c}}$.

Considering now the compression phase, where $\sigma_1 < 0$ we can immediately extend the yield curve so that it is now a straight line extending from $\sigma_{\mathrm{I}} = \sigma_{\mathrm{c}}\sqrt{2}$ to $\sigma_{\mathrm{II}} = \sigma_{\mathrm{c}}\sqrt{2}$. This means that as long as the divergence/-convergence along the y-axis is less than $\pm\sigma_{\mathrm{c}}$ the yield stress for the x-axis

remains the same. This is in fact the same shape as we've already seen in the curved diamond yield curve discussed in the previous section.

What happens for $\sigma_{\mathrm{I}} < 0$ is not immediately clear. The curved diamond yield curve assumes a different shape for $\sigma_{\mathrm{I}} < 0$ than for $\sigma_{\mathrm{I}} > 0$ and this can be interpreted such that the underlying crystal structure breaks when either the divergent or the compressive stress reaches $\pm\sigma_{\mathrm{c}}$. For $\sigma_{\mathrm{I}} < 0$ the ice then retains some of its shear strength, not because of an intact crystal structure, but because of frictional forces (like the ones assumed in the granular model and the modified Coulombic yield curve). The curved part of the curved diamond yield curve may be considered an approximation to a Coulombic yield curve, but the angle of friction is close to 45°, similar to that suggested for the modified Coulombic yield curve.

For the trimmed ellipse a different approach is suggested and, as the name suggests, it is based on the classical elliptic yield curve. We simply add biaxial cohesive strength to the ellipse, as described in section 2.4.5, so that $T = \sigma_{\mathrm{c}}\sqrt{2}$. The axis ratio of the ellipse is then determined so that the combined curve of ellipse and straight line from $\sigma_{\mathrm{I}} = T$ to $\sigma_{\mathrm{II}} = T$ is continuous. This assumes that the crystal structure breaks at $\sigma_1 = -\sigma_{\mathrm{c}}$, but that the frictional forces don't follow a More-Coulomb curve. The resulting yield curve is shown in figure 2.3.

To determine the ellipse axis ratio we note that the equation for an ellipse in $\{\sigma_{\mathrm{I}}, \sigma_{\mathrm{II}}\}$ space can be written as

$$\sigma_{\mathrm{II}} = \pm\frac{b}{a}\sqrt{a^2 - (\sigma_{\mathrm{I}} - x_0)^2}, \tag{2.90}$$

where a and b are the lengths of the major and minor axes and x_0 is the ellipse displacement along the σ_{I} axis. Now $e = a/b$, $a = (P + T)/2$ and $x_0 = -(P - T)/2$ and so we find that (constraining σ_{II} to be positive)

$$\sigma_{\mathrm{II}} = \frac{P}{2e}\sqrt{(1 + k_T)^2 - (2\sigma_{\mathrm{I}}/P + 1 - k_T)^2}. \tag{2.91}$$

We now assume that $\sigma_{\mathrm{II}}(0) = T$ and so

$$\sigma_{\mathrm{II}}(0) = \frac{P}{2e}\sqrt{(1 + k_T)^2 - (1 - k_T)^2} = \frac{P\sqrt{k_T}}{e} \tag{2.92}$$

gives $e = 1/\sqrt{k_T}$ or $e^{-2} = k_T$. The resulting equations for the shear and bulk viscosities are

$$\zeta = (P + T)/2\Delta \tag{2.93}$$

$$\eta = \min\left(\zeta k_T, \frac{(P + T)/2 - \zeta\dot{\varepsilon}_{\mathrm{I}}}{\dot{\varepsilon}_{\mathrm{II}}}\right), \tag{2.94}$$

where

$$\Delta = \sqrt{\dot{\varepsilon}_{\mathrm{I}}^2 + \dot{\varepsilon}_{\mathrm{II}}^2 k_T}. \tag{2.95}$$

From this it is clear that the trimmed ellipse yield curve explicitly assumes $k_T > 0$. In particular demanding that $e = 2$ results in $k_T = 0.25$, which is considerably larger than $k_T = 0.05$ as suggested by Wang (2006). Finally we note that for comparable cohesive strength under isotropic divergence the trimmed ellipse has much lower shear strength than the curved diamond.

Chapter 3

Ideal polynya model

3.1 Introduction

Simple, idealised model setups are often useful when trying to understand the processes behind a given phenomenon. A good example of this is the flux-polynya model suggested by Pease (1987) and the model setup by Bjornsson et al. (2001). In this chapter an idealised polynya model, similar to the one introduced by Bjornsson et al. (2001) is discussed, but the discussion is taken further addressing the importance of non-linear advection terms in the momentum equation, the role of rheology in polynya formation and the way the thickness of newly formed ice is to be parametrised. This material has already been published by the author (Olason and Harms, 2010) and is reproduced here, with only minor modifications.

The model used here is the same as described in chapter 2, except that now the model is coupled to a stationary slab ocean. Cohesion does not play a role in this problem and therefore only the granular model and elliptic and modified Coulombic yield curves are considered. In this chapter p^* is only scaled according to equation (2.59) when using the granular model.

Polynyas and leads are an important part of the climate system at high latitudes. Maykut (1982), for instance, estimates that about 50% of the total atmosphere-ocean heat exchange over the Arctic Ocean in winter occurs through polynyas and leads. During summer, these openings admit shortwave radiation into the ocean, warming it up and thus impacting the heat and mass balance of the ice and ocean (Maykut and Perovich, 1987, Maykut and McPhee, 1995). Arctic polynyas also play a large role in halocline and deep water formation and Winsor and Björk (2000) estimate a mean ice production from all Arctic polynyas of $300\pm30\,\mathrm{km^3\,yr^{-1}}$. The resulting salt flux is about 30% of the estimated flux needed to maintain the halocline.

In terms of general circulation models, polynyas are modelled using dynamic-thermodynamic sea-ice models. This has been done successfully by a number of researchers; e.g. Marsland et al. (2004), Kern et al. (2005) and

Smedsrud et al. (2006). Not all researchers use the same criterion to define a polynya in dynamic-thermodynamic models. The most straightforward approach would seem to be to use ice concentration alone, like Kern et al. (2005). However, Smedsrud et al. (2006) use a combination of ice concentration and thickness and Marsland et al. (2004) use a combination of ice concentration and freezing rate.

This appears to be due to a fundamental difference in the model results of Kern et al. (2005) and Marsland et al. (2004) on one hand and that of Smedsrud et al. (2006) on the other. In the former studies a polynya can be characterised as an area of low ice concentration surrounded by ice of high concentration. In the latter case the polynya is an area of thin ice (but high concentration) surrounded by thick ice.

These differences serve as an incentive to take a closer look at how polynyas form in dynamic-thermodynamic sea-ice models. Highly idealised setups are useful when trying to understand the basic processes involved and so we choose to revisit a study originally made by Bjornsson et al. (2001). In their study, Bjornsson et al. (2001) compared the granular model of Tremblay and Mysak (1997) to the polynya flux model of Willmott et al. (1997) in an idealised basin. In an idealised setup, comparison with measurements is not possible and so the polynya flux model was used to validate the dynamic-thermodynamic model results.

Here we expand on the work done by Bjornsson et al. (2001) and compare the granular model to the more common viscous-plastic model of Hibler (1979) and the lesser known modified Coulombic yield curve by Hibler and Schulson (2000) in a setting similar to that used by Bjornsson et al. (2001). The granular model results are used to assess the outcome from the other two yield curves. Secondly, we consider formulations by Hibler (1979) and Mellor and Kantha (1989) for the thickness of newly formed ice. The former formulation was used by Kern et al. (2005) and Marsland et al. (2004) and the latter by Smedsrud et al. (2006). Finally, we use the collection depth parametrisation of Winsor and Björk (2000) to parametrise the new-ice thickness. Thus we address the important points of a polynya simulation; first the behaviour of the consolidated ice, which is determined by the rheology, and secondly ice formation inside the polynya, determined by the new-ice thickness parametrisation.

The layout of this chapter is as follows: in section 3.2 we discuss polynya formation and how to interpret the results of dynamic-thermodynamic models in light of what we know about polynyas. That section also includes a presentation of the control run by which the following experiments are assessed. In section 3.3 the response of the model using different yield curves is presented. Section 3.4 presents the effects different formulations for the thickness of newly formed ice have on the model results. Section 3.5 contains a discussion of the model results followed by the conclusions of this study.

3.2 Polynyas in a dynamic-thermodynamic model

We will now discuss wind-driven polynyas and how they are modelled using dynamic-thermodynamic sea-ice models. The discussion focuses on understanding the processes involved in polynya formation and how to relate those to the results of the dynamic-thermodynamic model. We find that when it comes to understanding the model behaviour inside the polynya it helps to keep some of the assumptions of the flux polynya models in mind. Polynya flux models are simplified physical models which underline the important processes in polynya formation. They have been proven to be useful in simulating a variety of situations (see e.g. Morales Maqueda et al., 2004). In subsection 3.2.1 we briefly describe the control run used to assess other model results.

Wind-driven coastal polynyas form where the ocean is initially covered by ice and a wind starts blowing off the coast. This causes the ice to move off-shore, opening a polynya at the coast (or fast ice edge). Inside the polynya the ocean is at the freezing point causing frazil ice to form and be herded downstream by the wind and waves. The frazil ice then consolidates at the edge of the initial ice. The polynya remains open as long as the off-shore wind component remains strong enough to maintain it.

The ice in and near a polynya can be divided into three distinct regimes: The thick initial ice, the consolidated ice and the frazil ice inside the polynya. The polynya edge is the interface between the polynya and the consolidated ice. This threefold separation is the basis of flux polynya models. They calculate the location of the polynya edge based on the drift velocity of the consolidated (and thick) ice, the ice formation rate inside the polynya and the thickness of the consolidated ice (H, also referred to as collection depth).

In the first flux polynya model, proposed by Pease (1987), the frazil ice inside the polynya is immediately transferred to the edge of the consolidated ice, where it piles up. The model by Ou (1988), and later models, assume a constant (and finite) velocity for the frazil ice, but this must always be greater than the velocity of the consolidated ice. In reality the frazil ice drifts faster than the consolidated ice because frazil ice, near or at the surface, experiences less water shear stress than the consolidated ice. The water velocity inside the polynya is also different from that under the consolidated ice, but this can be difficult to account for in a simplified setup. Finally the initial ice pack may not drift at the (local) free drift speed, as the wind that creates the polynya is non-uniform and may be weaker further off shore. Islands and other coast lines may also slow down the drift of the initial ice pack.

Polynya flux models focus on the frazil ice representation and the parametrisation of the collection depth. The velocity of the thick initial ice must,

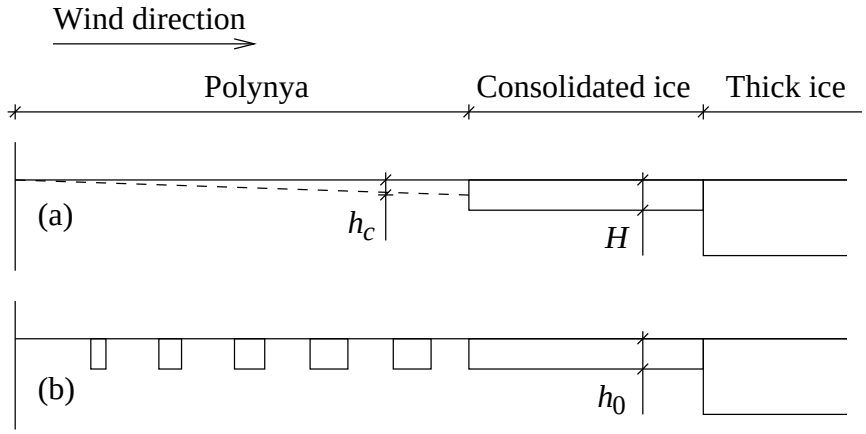

Figure 3.1: Polynya formation in polynya flux models and a dynamic-thermodynamic sea-ice model. (a) In the Pease (1987) model, frazil ice that forms inside the polynya is immediately transported towards the thick ice. There it forms consolidated ice of thickness H. In the Ou (1988) model, the frazil ice has constant (and finite) drift speed inside the polynya and therefore non-zero thickness h_c (dashed line). (b) In a dynamic-thermodynamic sea-ice model newly formed ice is immediately transformed into solid ice of thickness h_0.

however, always be prescribed. Dynamic-thermodynamic models are, on the other hand, designed to model the movement of this thick ice, but they generally do not include any frazil ice parametrisations. When ice forms over open water in dynamic-thermodynamic models solid ice of a predetermined thickness, h_0 (see section 2.3), is immediately formed, more akin to pancake ice than frazil ice.

In a polynya modelled by a dynamic-thermodynamic model the ice in the polynya interior drifts towards the initial ice pack, forming the consolidated ice. The consolidated ice consequently has thickness close to h_0, which, in this particular setup, is then effectively the model's "collection depth". Assuming that the ice in the polynya interior drifts faster than the consolidated ice, like the Ou (1988) model demands, the dynamic-thermodynamic model should also show the three ice regimes the polynya flux models do (see figure 3.1). In addition Bjornsson et al. (2001) showed that the transition from freely drifting ice in the polynya interior to consolidated ice can occur over a few grid cells. This transition region is then analogous to the polynya edge predicted by flux polynya models.

We also note that since the consolidated ice and the ice in the polynya interior are modelled using the same drag coefficients their free drift speed will be the same. Absent any other forcing, or a divergence in the wind forcing, no sharp polynya edge will form. This is because the polynya that

opens up fills with ice drifting at the same speed as the consolidated ice, resulting in linearly increasing ice concentration inside the polynya. Bjornsson et al. (2001) noted this behaviour (see their Fig. 4). In their study a polynya edge forms because the drift of the consolidated ice is slowed down by one of the side walls of their ideal basin. This approach is also used here.

A final point here is that we assume the polynya being modelled to be large enough to cover a substantial number of model grid points. In particular we demand that the model resolve the three ice regimes and the polynya edge. A single grid cell not completely covered with ice may often be interpreted to contain a polynya, especially if the grid resolution is low. In this study, however, we only consider polynyas that are properly resolved by the model grid.

3.2.1 Control run

The model domain is a bay, 135 km long and 75 km wide at 2.5 km resolution (see figure 3.2), similar to the setup Bjornsson et al. (2001) used. At such a high resolution we must assume that on average the ice floes being modelled are no larger than 250 m in diameter. This is because a scale of approximately 10 grain widths can generally be modelled without resolving each individual element using a granular model (Savage, 1998). McNutt and Overland (2003) state that at the multi-floe scale (approximately 2–10 km) sea ice behaves like a granular material, so the granular model should be ideal for a simulation at that scale. We can assume the ice floes in the polynya interior are no larger than pancake ice, which is not much larger than 3 m in diameter. The ice in the polynya interior, and by extension the consolidated ice, is therefore well within the maximum allowed floe size. However, assuming that individual floes are no larger than 250 m in diameter may not always be valid for the thick initial ice, depending on the geographical location of the polynya as well as the time of year. This is only a minor concern for this study since it focuses on the steady state solution where the thick initial ice does not play a role (as it has drifted out of the model domain).

A polynya is created by having a 15 m/s wind blow uniformly at a 30° angle to the direction along the bay. The polynya forms at the inner shore of the bay and the excess ice flows out the open boundary at the mouth of the bay. The atmospheric temperature is kept constant at T_{air}=−20 °C and the oceanic temperature is kept at the freezing point for a salinity of S=32. The water velocity is always zero. The model is initialised with ice concentration A=0.9 and thickness h=1 m. For the solid boundaries, a no-slip condition is used, while for the open boundary zero gradient Neumann boundary conditions are applied to all variables. The Neumann condition is also used for the ice pressure P, which Bjornsson et al. (2001) set to zero at the open boundary. This is done because using the Neumann condition

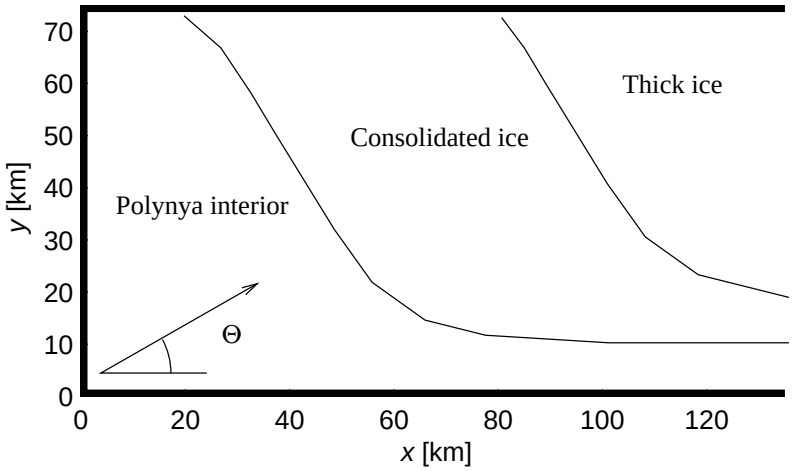

Figure 3.2: The size of the basin (in km) and wind direction during the polynya experiments. The figure also shows the three ice regimes one expects; the polynya interior (where the ice is in free drift), consolidated ice and thick initial ice.

improves the model behaviour near the open boundary by eliminating the excessive ice speed observed there by Bjornsson et al. (2001).

For the ice pressure constants C and P^* in equation (2.48) we use the same values Bjornsson et al. (2001) used; i.e. C=30 and P^*=30 kN/m^2. Bjornsson et al. (2001) showed that these parameters have little effect on the model results using the granular model and we have found the same to be true for the other yield curves. A list of the relevant constants is included in table 3.1.

To illustrate the temporal evolution of the polynya, figure 3.3 shows a Hovmöller diagram of the ice concentration field taken along a section at y=37.5 km. The response to the applied wind stress is immediate and a discernible polynya edge starts to form during the first day of the model integration. After two days the polynya has a clear structure and can be considered fully formed. A practically steady state has been reached after eight days. When the polynya has fully formed a band of large gradient in the concentration field analogous to the polynya edge always exists. For further reference figure 3.4 shows the ice concentration in the basin after eight days of model integration. As figures 3.3 and 3.4 show, the edge in this simulation is at a concentration of between A=0.6 and A=0.9.

Ice formation rates in the model are closely linked to the fractional ice concentration. Ice formation rate for open water is $F(A{=}0){=}13.83$ cm/day. In the polynya interior the ice is between 30 cm and 34 cm thick. If we assume all that ice is 32 cm thick we can calculate the ice formation rate in the polynya interior as a weighted average of $F(A{=}1,\ h{=}32\,cm){=}3.31$ cm/day

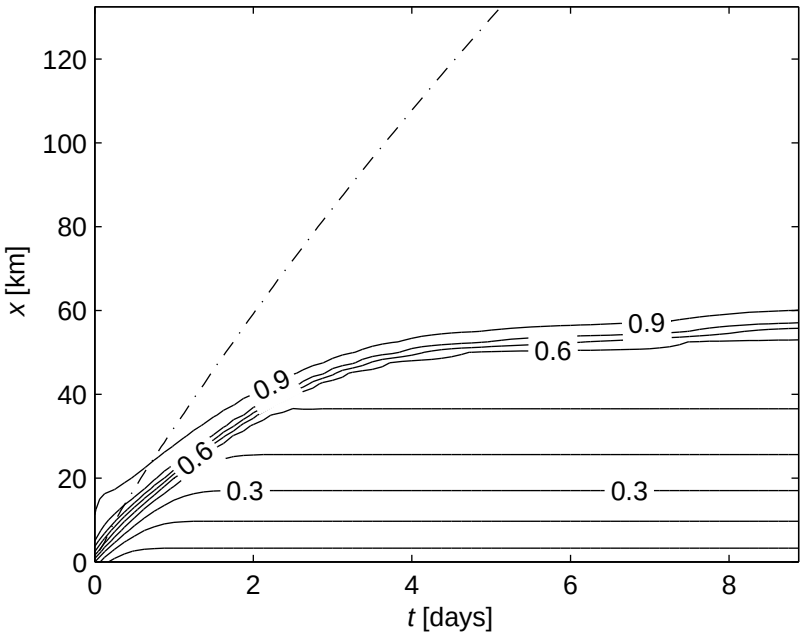

Figure 3.3: A Hovmöller diagram of the ice concentration field (A) in the control experiment taken along a section at y=37.5 km. The vertical axis (x) is the along-channel distance and the horizontal axis (t) is the model time. The dash-dotted line shows the h=1 m isoline separating the thick initial ice and consolidated ice.

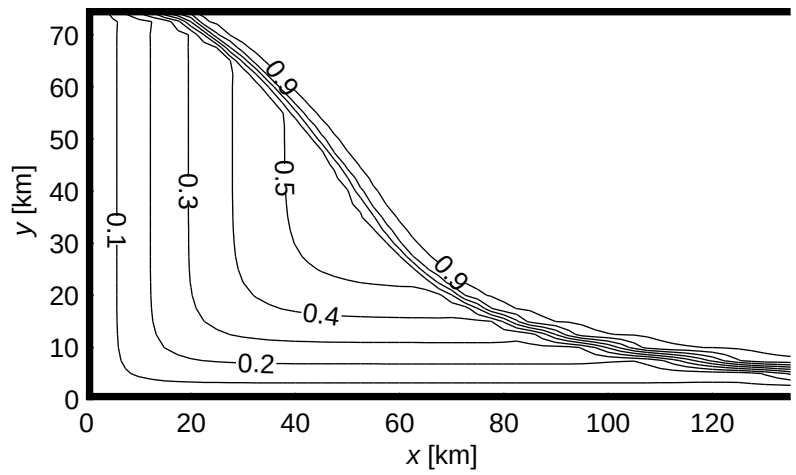

Figure 3.4: Sea-ice concentration in the control experiment (A) after eight days of model integration. The polynya edge is visible as a sharp increase in concentration.

Table 3.1: Main physical parameters and constants used in the simulation.

Variable	Symbol	Value
air drag coefficient	C_{da}	$1.2{\times}10^{-3}$
air temperature	T_{air}	$-20\,^{\circ}\mathrm{C}$
angle of dilatency	δ	$10\,^{\circ}\mathrm{C}$
basin dimensions	L, W	135 km, 75 km
cloud cover	F_{c}	80%
Coriolis factor	f	$1.33{\times}10^{-4}\,\mathrm{s}^{-1}$
ellipse axis ratio	e	2
horizontal resolution	Δx	2.5 km
ice demarcation thickness	h_0	30 cm
ice density	ρ_{i}	$930\,\mathrm{kg/m^3}$
ice strength parameters	C, P^*	30, $30\,\mathrm{kN/m^2}$
internal angle of friction	ϕ	30°
min. viscosity (Hibler)	ζ_{min}	$4{\times}10^8\,\mathrm{kg/s}$
relative humidity	H_{R}	80%
water drag coefficient	C_{dw}	$5.5{\times}10^{-3}$
wind speed, angle	$\lvert\vec{v}_{\mathrm{a}}\rvert$, Θ	15 m/s, 30°

and $F(A{=}0)$; i.e.

$$F = AF(A = 1,\ h = 32\ cm) + (1 - A)F(A = 0). \tag{3.1}$$

This approximation is correct to within 0.05 cm/day for $A{\lesssim}0.8$, but starts breaking down as the consolidated ice gets thicker. Defining the polynya as all points for which $A{<}0.8$ (this choice will be discussed further below), the mean ice formation rate in the polynya is $F{=}11.1$ cm/day after two days and $F{=}10.7$ cm/day after eight days.

According to Ou (1988), ice velocity in the model should fall into two categories; that of free drift in the polynya itself and that of the consolidated ice. In the dynamic-thermodynamic model this velocity change gives the ice drifting in the polynya interior a barrier of slower consolidated ice to pile up against. Figure 3.5 shows the velocity field and speed in the control experiment after eight days. The speed does indeed fall into two categories: The free drift speed $|\vec{v}_{\mathrm{f}}|{=}32.6$ cm/s and the speed of the consolidated ice $|\vec{v}_{\mathrm{c}}|{\lesssim}25$ cm/s, depending on the distance away from the $y{=}75$ km boundary. More importantly the cross channel velocity, v, changes from $v_{\mathrm{f}}{=}15.7$ cm/s to $v_{\mathrm{c}}{\lesssim}3$ cm/s in the consolidated ice. Bjornsson et al. (2001) showed that it is the cross channel velocity that is most important for the size and shape of the polynya. In the polynya interior the ice drifts with the wind but the consolidated ice slides along the $y{=}75$ km boundary with a small cross channel velocity component due to ridging at the boundary.

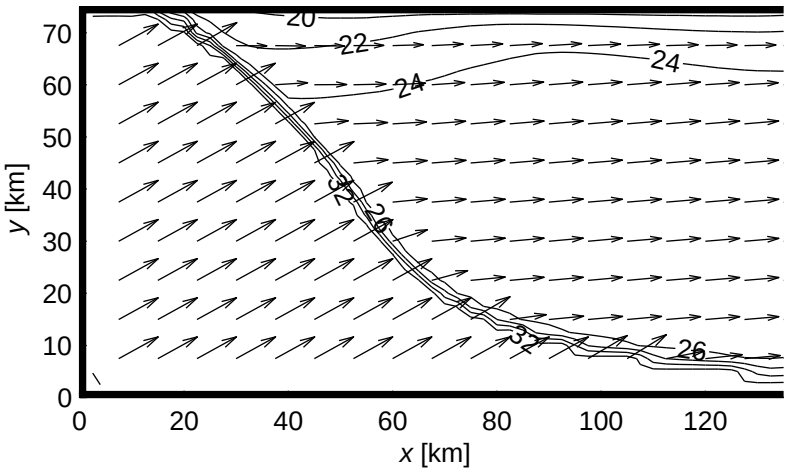

Figure 3.5: Ice velocity ($\vec{v}$) and speed ($|\vec{v}|$) in the control experiment after eight days of model integration. The polynya edge is visible as a sharp decrease in the ice velocity.

This setup exhibits the three fold separation of ice mentioned previously; free drift ice in the interior of the polynya, consolidated ice at the polynya edge and thick initial ice beyond that. This can be seen in the ice concentration field since the concentration is low ($A \lesssim 0.6$) in the polynya interior and high ($A \approx 1$) in the consolidated ice. The transition between the two takes place over approximately 5 grid cells, a region referred to here as the polynya edge. A similar transition is seen in the velocity field; the ice in the interior is in free drift while the consolidated ice drifts slower. The transition between the consolidated ice and the thick initial ice can only be seen in the ice thickness field. The ice in the polynya interior is almost as thick as the consolidated ice so the polynya edge is not apparent in the ice thickness field. In this control run the polynya is most readily defined as an area of low ice concentration and the polynya edge as the area of a large ice concentration gradient.

In the rheologies used here equation (2.48) dictates the ice strength under compression as a function of ice thickness and concentration. When this term is small the rheology term becomes small and the ice is in free drift. Since the ice in the polynya interior is in free drift we propose that the location of the polynya edge, in this particular setup, can be approximated by A=0.8. This is because $P(A{=}0.8)/P(A{=}1) \approx 0.01$ so the rheology will play a negligible role at lower concentrations. This choice is valid for the control run since the A=0.8 contour is within the high gradient region where the polynya edge is found (see figure 3.4). It is also valid for all the following experiments done here, except when using a minimum on the bulk viscosity (ζ) and when using the new-ice thickness parametrisation of Mellor and

Kantha (1989). These two cases will be discussed separately.

3.3 Different yield curves

An important part of the motivation for this study was to compare the results of Bjornsson et al. (2001), using the granular model, to a similar setup using different rheologies. The elliptic yield curve of Hibler (1979) is the most popular yield curve in use today, but it was designed for much lower resolution. It is therefore important to see how it fares in this high resolution setup. The modified Coulombic yield curve was, on the other hand, designed to model ice at high resolution so it will be instructive to see its performance here as well. In this section the focus is on the model response in the consolidated ice, since the rheology does not play a role inside the polynya itself.

In his model Hibler (1979) used a minimum for the bulk viscosity; $\zeta_{\min} = 4 \times 10^8\,\mathrm{kg/s}$ "in order to insure against any non-linear instabilities" noting that that value is "several orders of magnitude below typical strong ice interaction values and effectively yields free drift results" (Hibler, 1979, p. 823). The lower bound should only be necessary when the material derivative is included in the momentum equation (2.3) since in that case having no lower bound will typically result in a noisy solution (Griffies and Hallberg, 2000). Most modern ice models ignore the material derivative and do not include a lower bound on ζ. However, as the resolution increases the material derivative becomes more important. The scaling argument made by Rothrock (1975) shows that the material derivative may need to be included as the shortest significant length scale becomes smaller than about 5 km.

In this idealised setup the material derivative has very little effect on the final solution, regardless of which rheology is used. The difference between the results with and without the material derivative is about 7 mm/s in the grid cells at the x=0 boundary and about 2 mm/s at the y=75 km boundary and at the polynya edge. Everywhere else in the domain the difference is less than 0.1 mm/s. Compared to the free drift speed of $|\vec{v}_\mathrm{f}|$=32.6 cm/s this is small. We also observe no noise, even when the material derivative is included and the lower bound on ζ is set to zero.

Without a lower bound on ζ the results using the elliptic yield curve are nearly identical to those using the granular model. There is a sharp transition from free drift ice to consolidated ice, analogous to the polynya edge, just like in the granular model. This polynya edge forms at nearly the same location as it does in the granular model. Using the modified Coulombic yield curve also gives results very similar to the granular model. This is to be expected, since the modified Coulombic yield curve is in a way a combination of the other two yield curves. The difference between the three model formulations is limited to a small variance in polynya size,

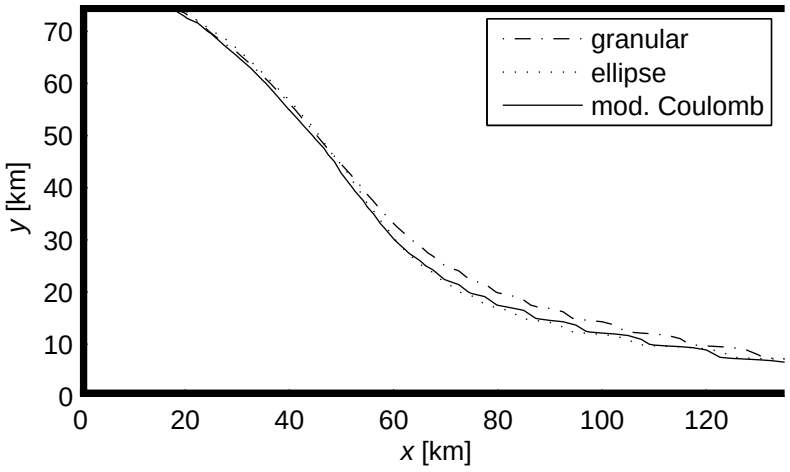

Figure 3.6: The polynya edge (A=0.8) using the elliptic and modified Coulombic yield curves and the granular model after eight model days. The differences between different model formulations are minor.

which as figure 3.6 shows, is due to a shift of the polynya edge by a few grid boxes. In particular, the commonly used elliptic yield curve is sufficient and can be used safely in this context.

Using a minimum on ζ does, however, give considerably different results from the control run. Setting the minimum to $\zeta_{\min}$=4×10^8 kg/s, like Hibler (1979) did, results in a polynya with a very diffuse edge, as figure 3.7 shows. Speed and velocity also fail to meet the criteria for forming a polynya edge; i.e. there is no clear separation between the velocity of the ice in the polynya interior and consolidated ice (see figure 3.7). In addition, the ice in the polynya interior does not flow at a constant speed and its speed is sometimes lower than that of the consolidated ice, which is clearly not plausible. The speed of the ice in the polynya interior when using $\zeta_{\min}$=4×10^8 kg/s is also always lower than it is in the control run. A decrease in the ice concentration is also seen by the y=75 km boundary, contrary to what can be seen in the control run. These effects were noted by Hunke (2001) in a different setup, but that discussion focused on the effects seen at the solid boundary, which will not be discussed further here.

The polynya edge becomes so diffuse because when imposing such a high minimum on ζ, the viscosity is consistently kept at its minimum value for $A \lesssim 0.9$ throughout the simulation. This is because the viscosity is related to the ice pressure via

$$\zeta = P/2\Delta \quad and \quad \eta = \zeta/e^2, \tag{3.2}$$

and the pressure to ice concentration via equation (2.48). The flow where A is sufficiently small is therefore linear viscous, but choosing as a minimum

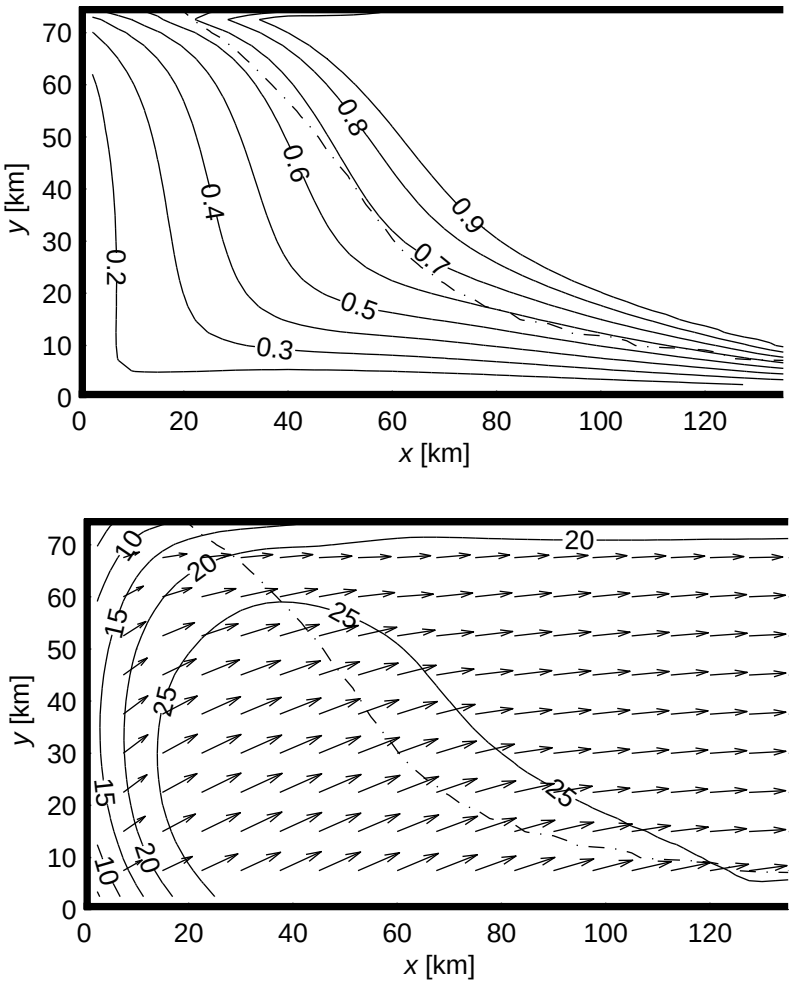

Figure 3.7: Sea-ice concentration (top) and speed and velocity (bottom) using Hibler's original formulation for the elliptic yield curve, after eight days of model integration. Neither figure shows a discernible polynya edge. The dash-dotted line shows the isoline for A=0.8 from the control run.

$\zeta_{\min}$=4×10^8 kg/s does not result in effectively free drift. Lu et al. (1989) also found that this limit was too high compared to measurements.

As previously stated, we observed no non-linear instabilities using $\zeta_{\min} = 0$ kg/s. Some noise is, however, to be expected in a realistic simulation and so a non-zero $\zeta_{\min}$ may be required if one wants to include the material derivative. In that case one would need to choose a low, but non-zero value for $\zeta_{\min}$. The resolution of Hibler's model was 125 km and since viscosity scales with the distance squared, a choice of $\zeta_{\min}$=4×10^4 kg/s seems in order. This yields nearly the same results as with $\zeta_{\min}$=0 kg/s; the largest difference in concentration between the two model runs being ΔA=0.006. The maximum concentration gradient when using $\zeta_{\min}$=0 is $\max(|\vec{\nabla}A|)$=0.230 km^{-1} and it is $\max(|\vec{\nabla}A|)$=0.228 km^{-1} when using $\zeta_{\min}$=4×10^4 kg/s. When choosing larger values for $\zeta_{\min}$, the effects of the capping start to show. For $\zeta_{\min}$=4×10^5 kg/s the maximum gradient is $\max(|\vec{\nabla}A|)$=0.212 km^{-1} and the difference in concentration between that run and the one with zero $\zeta_{\min}$ is ΔA=0.08. For $\zeta_{\min}$=4×10^6 kg/s the maximum gradient is 0.164 km^{-1} and the concentration difference is 0.3.

3.4 New-ice thickness

As we have already seen, the ice rheology affects the initial ice pack and the consolidated ice. The interior of the polynya, on the other hand, is primarily affected by the new-ice thickness parametrisation. This determines the thickness, and thus the concentration of the ice formed inside the polynya.

The most popular method for parametrising the new-ice thickness is probably the one suggested by Hibler (1979) (see section 2.3). Put simply the new-ice thickness is not allowed to drop below a certain minimum, h_0. If the total mass of newly formed ice is not enough to cover the open water fraction of the grid cell at that thickness then the concentration of newly formed ice is adjusted accordingly. If more ice is formed then the new ice is simply thicker than h_0.

The choice of h_0 is not obvious and appears to range from 10 to 50 cm or even more in some cases. Bjornsson et al. (2001) argued for using h_0=30 cm and that is the value used here so far. Their argument is based on the assumption that the ice that forms in the polynya immediately forms pancake ice. However, Bjornsson et al. (2001) state that pancake ice thickness is closer to 10 cm than 30 cm. We therefore include a model run with h_0=10 cm.

The main result of using h_0=10 cm is that with a lower h_0 the polynya fills up much faster. The newly formed ice is thinner, therefore has a larger surface area, which results in faster ice concentration growth in the polynya itself and causes the polynya edge to form closer to the inner shore of the bay than before. The polynya edge is also not as sharp in the concentration field as when using h_0=30 cm. It is, however, still sharp in the velocity field,

as can be seen in figure 3.8.

The mean ice formation rate in the polynya is about 1% lower here than in the control run. The total ice formation is therefore reduced almost only because the polynya is smaller. Using h_0=30 cm gives polynya area of A_p=4.5×10^3 km^2 after eight days, but using h_0=10 cm the polynya area is A_p=2.4×10^3 km^2 after eight days; an approximately 50% reduction in size. Finally, the consolidated ice is thinner since its thickness equals h_0.

The other approach to determining the thickness of newly formed ice described in section 2.3 is the one proposed by Mellor and Kantha (1989). There the thickness of newly formed ice is based on the thickness of the ice already present in the grid cell. Mellor and Kantha (1989) argued that the thickness of newly formed ice should be a quarter of the old ice thickness. This also means that when there is no ice in the grid cell when new ice forms, the ice spreads uniformly over the entire cell, potentially very thinly. A polynya in such a model may therefore be hard to recognise by the change in concentration and researchers using this approach often consider ice below a certain cut-off thickness to represent the polynya. Smedsrud et al. (2006), for instance, use Ah=30 cm for this cut-off thickness.

Using this approach results in a "polynya" that is hardly recognisable in the concentration field, as figure 3.9 shows. Even after eight days there is only a thin sliver of an opening along the x=0 km and y=0 km boundaries and the A=0.8 isoline is a grid box or two away from the shore. More seriously perhaps the velocity field, also shown in figure 3.9, shows no sign of the discontinuity deemed necessary for proper polynya formation. The ice slows down gradually moving away from the x=0 boundary, contrary to our previous assumptions about how a polynya is formed.

Ice thickness near the coast is indeed lower than the initial ice thickness, but as figure 3.10 shows there is no real polynya edge to be found in the ice thickness field. In that respect there is no conceptual difference between using h or Ah. As before the thick initial ice drifts out of the basin, but in this case the ice that replaces it does not have a uniform thickness. It is very thin at the coast with linearly increasing thickness towards the thick initial ice.

We have already mentioned that considerable effort has been put into parametrising the collection depth in polynya flux models. Given the large variation between the results already presented in this section we find it worth considering whether the polynya flux model parametrisations can be applied in the dynamic-thermodynamic model.

The parametrisation by Winsor and Björk (2000) lends itself well to immediate inclusion in the dynamic-thermodynamic model. It is based only on the wind speed and not the polynya width, frazil ice speed or other quantities not accessible to the dynamic-thermodynamic model. By using this parametrisation we aim at improving the modelled consolidated ice thickness and thus also the size of the polynya.

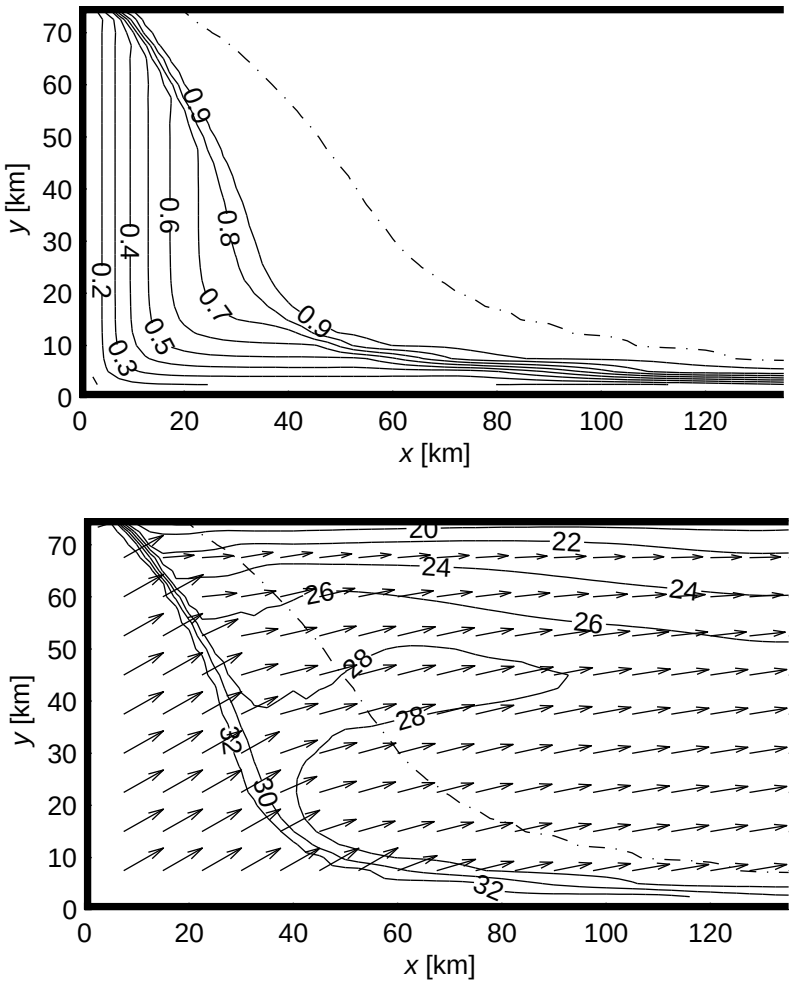

Figure 3.8: The ice concentration (A, top) and speed and velocity ($\vec{v}$ and $|\vec{v}|$, bottom) using h_0=10 cm after eight model days. The resulting polynya is smaller and has a higher ice concentration than the control run. The dash-dotted line shows the isoline for A=0.8 from the control run.

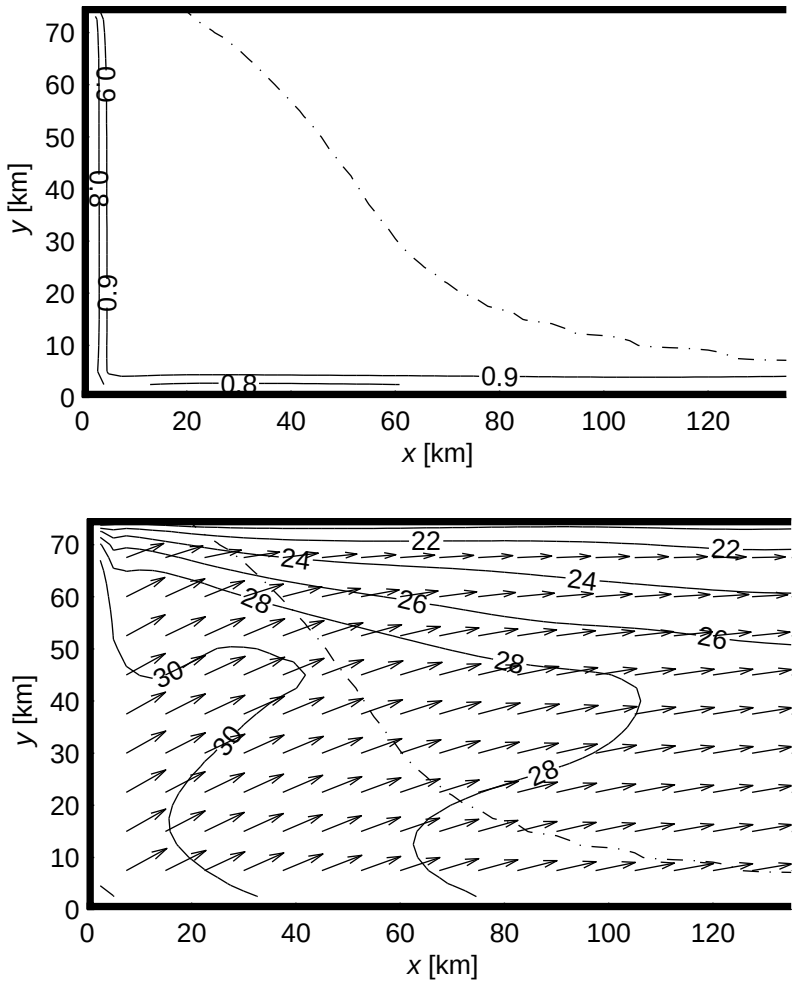

Figure 3.9: The ice concentration (A, top) and speed and velocity ($\vec{v}$ and $|\vec{v}|$, bottom) using the new-ice thickness parametrisation by Mellor and Kantha (1989) after eight model days. The resulting polynya is very small with no discernible edge in the velocity field. The dash-dotted line shows the isoline for A=0.8 from the control run.

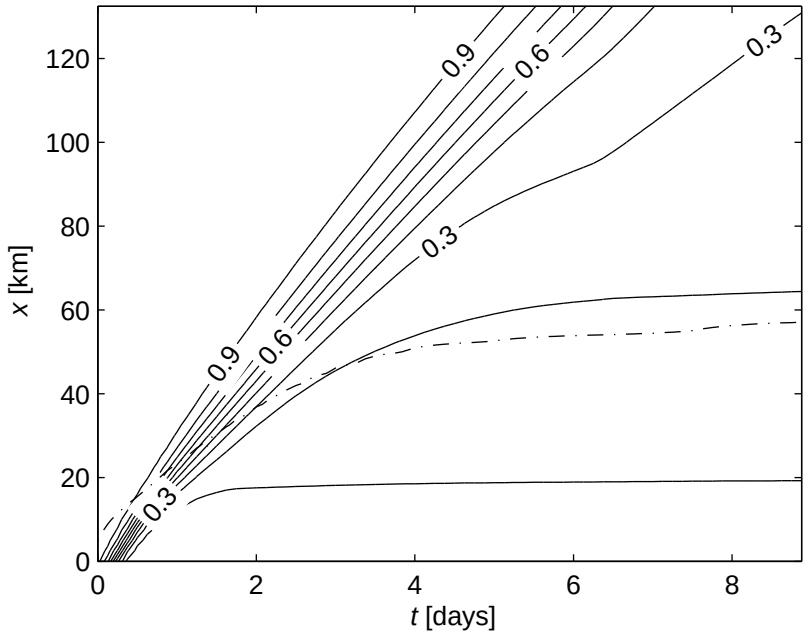

Figure 3.10: A Hovmöller diagram of the ice thickness field (h) using the new-ice thickness formulation by Mellor and Kantha (1989) taken along a section at y=37.5 km. The vertical axis (x) is the along channel distance and the horizontal axis (t) is the model time. The dash-dotted line shows the isoline for A=0.8 from the control run.

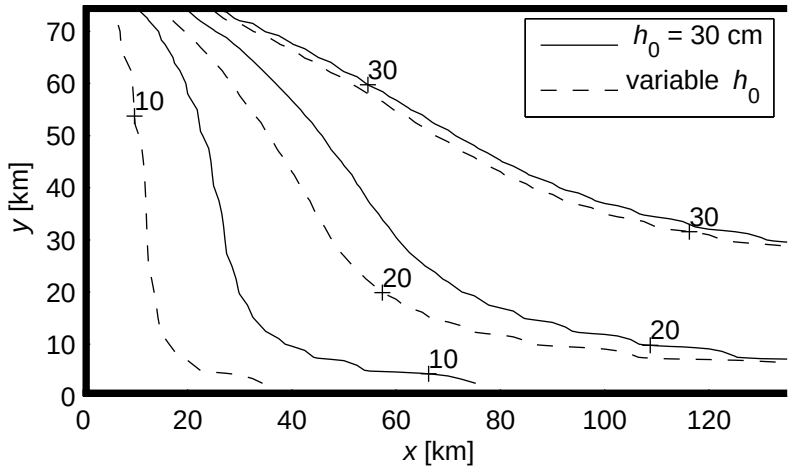

Figure 3.11: The polynya edge after eight days using a constant h_0 and parametrised h_0 according to equation (3.3). A=0.8 is used as a marker for the polynya edge and the edge is plotted for 10, 20 and 30 m/s wind speed.

Winsor and Björk (2000) assumed the collection depth to be a function of wind speed as

$$H = \frac{a + |\vec{v}_\mathrm{a}|b}{c}, \tag{3.3}$$

where $|\vec{v}_\mathrm{a}|$ is the surface wind velocity, a=1 m, b=0.1 s and c=15. In particular, $H\approx$7 cm for $|\vec{v}_\mathrm{a}|$=0 and H=30 cm for $|\vec{v}_\mathrm{a}|$=35 m/s so this parametrisation is well within the range of plausible values for h_0. Equation (3.3) is then used to calculate h_0=H in each grid point.

Using this parametrisation results in smaller polynyas at low wind speeds, compared to h_0=30 cm or larger polynyas at high wind speeds, compared to h_0=10 cm. Figure 3.11 shows the polynya using h_0=30 cm and the parametrisation for the wind speeds 10, 20 and 30 m/s. At lower winds the polynya edge starts to become diffuse, which is to be expected. For further reference figure 3.12 shows the size of the resulting polynya as a function of wind speed. The mean ice formation rate in the polynya increases from F=10 cm/day for $|\vec{v}_\mathrm{a}|$=10 m/s to F=11 cm/day for $|\vec{v}_\mathrm{a}|$=35 m/s and choosing different values for h_0 contributes to about 1% change in the ice formation rate. At the same time the polynya size grows approximately four times as the wind strength grows from 10 m/s to 35 m/s. It is therefore clear that variations in polynya size control the variations in total ice formation in the polynya.

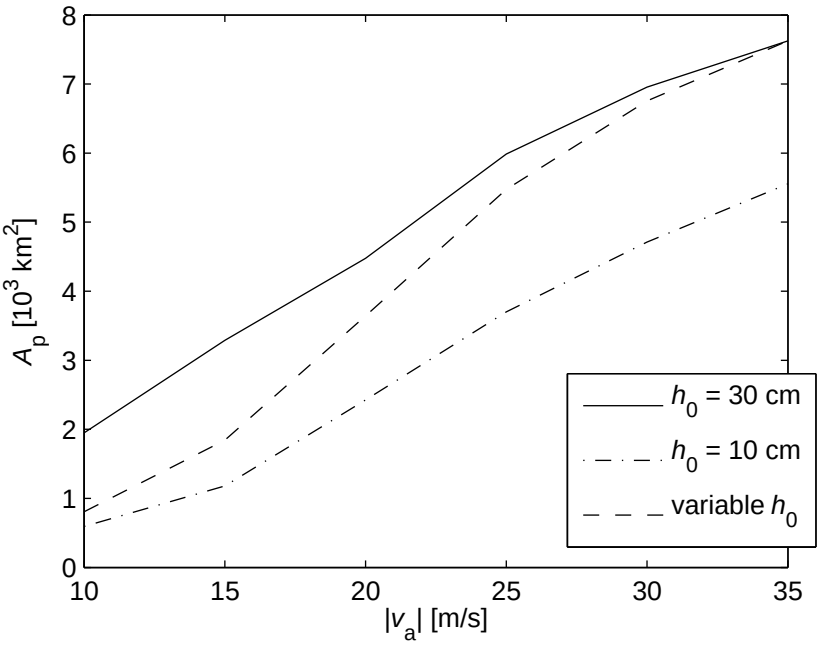

Figure 3.12: The polynya size (A_p) after eight days as a function of wind speed ($|\vec{v}_\mathrm{a}|$). The size is calculated as the sum of the size of all model points where A<0.8.

3.5 Discussion

Bjornsson et al. (2001) have already shown that the granular model can be used to model polynyas in an idealised setting by comparing their results to a polynya flux model. We have shown that this is also the case when using the modified Coulombic yield curve of Hibler and Schulson (2000) and when using the elliptic yield curve of Hibler (1979). This is important since the numerical performance of the granular model is considerably worse than that of the other two models. We find that the granular model requires almost twice the computing time the other two rheologies require. The elliptic yield curve of Hibler (1979) is also already in use in the vast majority of sea-ice models.

All three yield curves give nearly identical results (with the exception of using a capped ζ as discussed below). Looking at the stress states (figure 3.13) we see that when using the granular model the σ_{I} values for points in the consolidated ice are all clustered around $\sigma_{\mathrm{I}}{=}{-}P/1.5$. This means that at these points the ice cover yields or is very close to yielding under compression. When this is the case the behaviour of the ice is controlled by equation (2.48), which is also one of the main equations governing the behaviour of the other two yield curves. The difference between the granular model and the other two is then almost entirely explained by the different formulation of shear strength between the model formulations. As figure 2.2 shows, the granular model and the ellipse have a lower shear strength than the modified Coulombic yield curve, which is why using the modified Coulombic yield curve gives a smaller polynya.

Using the other two yield curves, the stress states are much more evenly distributed along the σ_{I} axis. For the modified Coulombic yield curve the stress states that lie on the Coulombic slope are all inside the polynya while the stress states in the consolidated ice are all on the elliptic part of the yield curve. This happens because in the consolidated ice the divergence ($\dot{\varepsilon}$) is always negative, so according to equation (2.36) $\sigma_{\mathrm{I}}{\leq}{-}P/2$. Using the elliptic and modified Coulombic yield curves therefore yields similar results for the consolidated ice, where both yield curves have an elliptic shape. In the polynya interior the ice is in free drift so the shape of the yield curve has no effect there.

Using a large $\zeta_{\min}$, in particular $\zeta_{\min}{=}4{\times}10^8\,\mathrm{kg/s}$ as Hibler (1979) suggests, does, however, give results that are not plausible. Using this original formulation results in a polynya that is smeared out with no proper edge and a velocity field that has little relation to polynya formation. This happens because the capping of ζ in the model turns the viscous-plastic formulation into a linear viscous model for ice concentration $A{<}0.9$.

Hibler (1979) used the lower bound on ζ to dampen grid scale noise which can arise when the grid Reynolds number constraint is not satisfied.

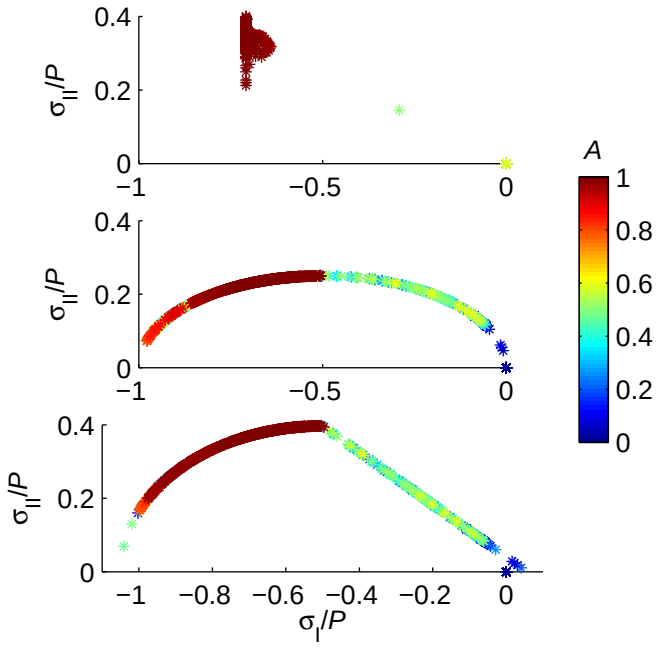

Figure 3.13: Stress states using the granular model (top, σ_{I} scaled according to equation (2.59)), the elliptic yield curve (centre) and modified Coulombic yield curve (bottom) after eight model days plotted in stress invariant space. The colour scale indicates the ice concentration at each point (A) and points with high concentration are drawn on top of those with a lower concentration. Points with high values of A ($A \gtrsim 0.8$) are all located in the region $\sigma_{\mathrm{I}} \leq -P/2$. Points near the open boundary are excluded from the figure.

Considering the limited case of Burger's equation in one dimension:

$$\frac{\mathrm{d}v}{\mathrm{d}t} + v\frac{\mathrm{d}v}{\mathrm{d}x} = A\frac{\mathrm{d}^2 v}{\mathrm{d}x^2}, \tag{3.4}$$

A must be bounded by $A > \frac{1}{2}v\Delta x$ (Griffies and Hallberg, 2000). In free drift and ignoring the sea surface tilt term, the momentum equation becomes Burger's equation and for the one dimensional case $A = \zeta/\rho_\mathrm{i}$. Using the free drift speed of $|\vec{v}_\mathrm{i}|$=32.6 cm/s and Δx=2.5 km the viscosity is bounded by $\zeta > \frac{1}{2}\rho_i|\vec{v}_\mathrm{i}|\Delta x \approx 4\times10^5$ kg/s.

The grid Reynolds number constraint is therefore an order of magnitude larger than our preferred value for a non-zero ζ_min. Since ignoring the material derivative had much less effects on the simulation than using a non-zero ζ_min we conclude that ignoring the material derivative is preferable to including it and a non-zero ζ_min.

With regards to the ice behaviour inside the polynya we considered three ways in which to parametrise the thickness of ice forming over open water. These are the methods suggested by Hibler (1979), Mellor and Kantha (1989) and an adaptation of the collection depth parametrisation by Winsor and Björk (2000). Hibler's method was used when investigating the dynamic aspects (section 3.3) with an ice demarcation thickness h_0=30 cm after Bjornsson et al. (2001). That value may be too high and so we also ran the model using h_0=10 cm.

Using a lower h_0 resulted in a smaller polynya but little change in mean ice formation rates (about 1%). The ice concentration in the polynya interior was higher and as a result the concentration field did not show a sharp polynya edge. The velocity field, on the other hand, still showed a clear discontinuity at the polynya edge. The width of the polynya did decrease, but that was to be expected and can be understood in relation to the Lebedev-Pease width of a polynya (Pease, 1987)

$$L = \frac{HU}{F}, \tag{3.5}$$

where L is the polynya width and HU is the flux of consolidated ice. The collection depth, H, is analogous to h_0 in the dynamic-thermodynamic model. Lowering h_0 from 30 cm to 10 cm results in approximately 1% reduction in the ice formation rate (F). The polynya width is therefore bound do decrease.

Results obtained using the formulation of Mellor and Kantha (1989) were, however, very different from those obtained in the control run. Using Mellor and Kantha's formulation there are two ice regimes; thick ice and thin ice, which may be characterised as nilas. This replaces the threefold separation of thick ice, consolidated ice (of uniform thickness) and frazil/free drift ice, seen in polynya flux models and the control run. The polynya edge is considered to be what separates the consolidated ice and frazil/free drift

ice, but this distinction is lost when using the Mellor and Kantha (1989) approach. The new-ice thickness formulation by Mellor and Kantha (1989) is therefore not suitable for modelling polynyas.

On the whole, the approach by Hibler (1979) is also more reasonable from a physical standpoint. This is because wind and waves, which cannot be resolved by ocean or atmosphere models, will transform the frazil ice in the polynya into pancake ice, similar to the ice formation in that scheme. What is unrealistic about Hibler's approach is that solid ice forms inside the polynya, even where in reality the ice is mainly frazil ice. The thin ice formed using Mellor and Kantha's approach is more akin to grease ice or nilas which form in calmer conditions.

Wind speed is therefore an important factor in determining the new-ice thickness and it is consequently an important part of collection depth parametrisations for polynya flux models. Winsor and Björk (2000) parametrised the collection depth in the Pease (1987) model based only on wind speed and we found that parametrisation easily adoptable for inclusion in the dynamic-thermodynamic model.

Using the Winsor and Björk (2000) parametrisation gives results in the range between the results when using a constant h_0=10 cm and h_0=30 cm. We have already expressed a preference for the Hibler (1979) parametrisation for the new-ice thickness and using the Winsor and Björk (2000) parametrisation enables us to choose a sensible value for h_0. As a result the polynya size should depend on wind strength in a more realistic manner than when using a constant h_0. Using the parametrisation should also give more realistic ice thickness for the consolidated ice.

On a more general note, such a small value for h_0 may not be suitable for models describing the central pack ice as well. In such a situation the approach of Mellor and Kantha (1989) may give better results since the thick pack ice appears to require a larger h_0.

It is trivial to combine all three approaches to new-ice thickness parametrisation discussed here into one:

$$h_0 = \max\left(\frac{h}{\Phi},\ \frac{a + |\vec{v}_\mathrm{a}|b}{c}\right), \tag{3.6}$$

with Φ=4, a=1 m, b=0.1 s and c=15, as before. This approach modifies the previously constant h_0 of Hibler (1979) so that for thick ice the approach of Mellor and Kantha (1989) is used and for thinner ice the parametrisation of Winsor and Björk (2000) is used. Using one value for thick ice and one for thin is appropriate since h_0 is only analogous to the collection depth in a polynya or the marginal ice zone. Where the ice is thicker the ice behaviour should be similar to that described by Mellor and Kantha (1989), given the empirical origin of their formulation.

In our setup the result of equation (3.6) will always be the same as that of equation (3.3) since the ice in the polynya is always thin in the sense that

$h<\Phi(a+|\vec{v}_a|b)/c$. Further testing of this new parametrisation can therefore not be done here but should be carried out in a realistic simulation.

In conclusion we note that in this idealised setup the polynya is best defined as the area where $A<0.8$. This is really the concentration where the ice behaviour starts changing from free drift, for $A\lesssim 0.8$, to being heavily influenced by internal stresses, for $A\approx 1$. This separation is based on equation (2.48) and on the choice of C. The $A=0.8$ isoline is also consistently within the high gradient region for A in all experiments, except when using too high a minimum for the bulk viscosity and when using the new-ice thickness parametrisation from Mellor and Kantha (1989). But both these cases were found to give implausible results.

3.6 Conclusions

We have used an idealised setup to test three different sea-ice rheologies and three different formulations for the thickness of newly formed ice during polynya formation. These tests were done using a dynamic-thermodynamic sea-ice model in an idealised channel, similar to what Bjornsson et al. (2001) did.

We were able to reproduce the results of the granular model using both the modified Coulombic yield curve of Hibler and Schulson (2000) and the elliptic yield curve of Hibler (1979). This is important, since the numerical performance of the granular model is substantially worse than that of the other two models and also since the elliptic yield curve is already in popular use. We also found that including the material derivative and setting a minimum on the bulk viscosity is not a viable alternative to ignoring the material derivative.

The formulation of new-ice thickness suggested by Hibler (1979) turned out to give much better results than that of Mellor and Kantha (1989). Using Mellor and Kantha's formulation failed to give a clear polynya edge, both in the concentration and velocity field. We conclude therefore that this approach does not enable us to properly model polynyas. Hibler's approach, on the other hand, gave a clear separation of the consolidated ice and the polynya itself.

Using Hibler's new-ice thickness parametrisation and any of the rheologies tested here should give realistic results when modelling polynyas. Polynyas that are fully resolved by the model grid can then be recognised as areas of low concentration enclosed by compact ice and/or land. We also suggest using $A<0.8$ as a criterion for low concentration.

Hibler (1979) assumed a constant demarcation thickness (h_0). We suggest, however, using the collection thickness parametrisation of Winsor and Björk (2000) to parametrise h_0. This results in a value for h_0 which is dependent on wind strength and in the range already deemed acceptable for

h_0. As an aside, a combination of this parametrisation with the approach of Mellor and Kantha (1989) is proposed. This should give a parametrisation for h_0 applicable for both the marginal ice zone and the central ice pack.

Chapter 4

The Kara Sea model

4.1 Introduction

Having introduced the ice model and tested it in an idealised setting we will now discuss the model setup in the Kara Sea and some basic thermodynamic and dynamic features it possesses. This chapter is accordingly split into three parts; first is a description of the model area and the applied forcing, then comes a discussion of the thermodynamic properties of the model and last is a discussion of the model dynamics.

In the thermodynamics portion simple dynamics and long run-times are used to investigate the model behaviour with respect to various thermodynamic parameters and settings. The main source for comparison here is satellite data and the observed Kara Sea mean sea-ice concentration. Modelled ice thickness is also considered since the fast-ice strength depends on its thickness. Unfortunately observations of the ice thickness are scarce so no direct comparison is possible. The tests performed show that the model behaviour is robust with respect to reasonable changes in parametrisations and forcing.

The main object of the dynamics portion is to investigate the effects an increased number of outer-loop iterations have on the model results. In particular it is important to know how accurately the velocity field can be modelled, as this helps when determining if the ice is land fast or not. To investigate the behaviour of the solver a variable number of outer-loop iterations is performed and the outer-loop error compared. The computational cost is also considered.

4.2 Model setup

The modelled area covers the Kara Sea, which lies off the Arctic coast of Siberia, between the Laptev and Barents Seas. In particular the Kara Sea lies between Novaya Zemlya, Franz Josef Land, Severnaya Zemlya and the

Siberian coast (see figure 4.1). The modelled area covers all of the Kara Sea and a very small portion of the Barents Sea, west of the Kara Gate. The coupled model permits open boundaries to be placed inside the model domain and such a boundary is placed between Franz Josef Land and the northern tip of Novaya Zemlya and between the islands of Severnaya Zemlya and Malyy Taymyr (dashed lines in figure 4.1).

The Kara Sea has a somewhat unique oceanography in that two very large rivers run into it, the Ob, and the Yenisey. In addition the rivers Pyasina Nadym, Pur and Taz (the last three all run into Ob Bay) all contribute significantly to the freshwater inflow. This inflow is such that the ratio of the mean annual freshwater inflow to the sea's area is 152 cm, the largest of any sea in the World Ocean (Volkov et al., 2002). The waters of the Kara Sea are therefore very fresh, but in addition the Novaya Zemlya prevents much of the Atlantic influences seen in the Barents Sea. The south-western part of the Kara Sea is still warmer and saltier than the rest, in part due to the inflow of Atlantic waters through the Kara Gate. The Ob Bay and Yenisey Gulf are the freshest areas due to the presence of river water. It then extends north and north-east of the river mouths into the southern part Severozemelsky region.

In terms of sea ice the Kara Sea is ice covered most of the year and is normally never completely ice free. According to Volkov et al. (2002) the ice concentration is at a minimum in late August, early September, on average. Ice formation normally starts in the far northern part in early September moving south such that ice formation is more or less only taking place north of Novaya Zemlya by the middle of October. On average the Kara Sea is completely ice covered by late November. Land-fast ice is most prominent in the Severozemelsky region (inside the red rectangle in figure 4.1), but land-fast ice is also an important part of the ice regime in and around Ob Bay and Yenisey Gulf. The formation and evolution of land-fast ice is discussed in detail in chapter 5.

Ice clearance from the Kara Sea begins in the Ob Bay and Yenisey Gulf in May–June. This coincides with the maximum in river runoff due to the spring melt. The discharge of the Yenisey and Ob increases approximately tenfold during May, peaking in early June. From the river estuaries the clearing spreads and by the middle of August most of the ice south of the northern tip of Novaya Zemlya has melted. By late August only the northern most part of the Kara Sea is covered by ice. The remaining ice is normally multi-year ice which is a part of the central Arctic ice massive.

4.2.1 Setup of the coupled model

The ice model introduced in chapter 2 is coupled to the Vector Ocean Model (VOM) developed at the Institut für Meereskunde (see Backhaus, 2008). VOM is a full-fledged primitive equation model with a free surface. It has

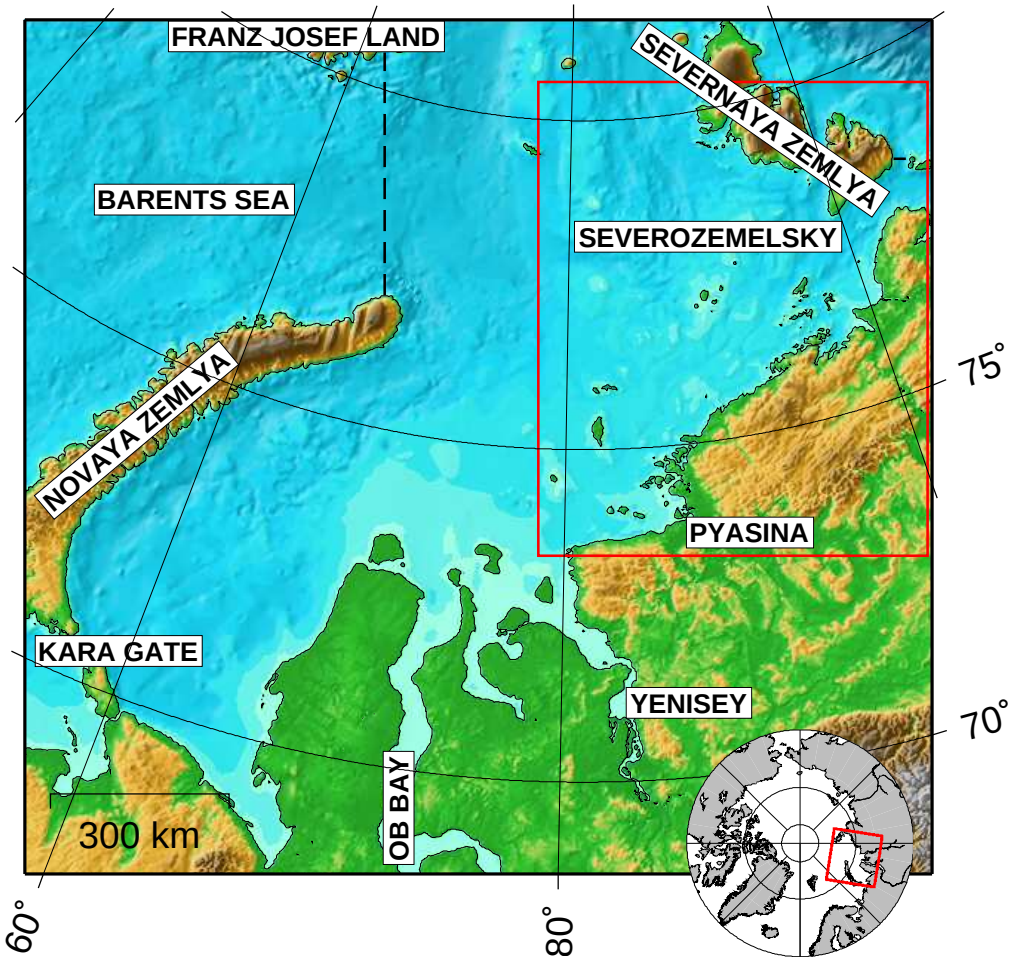

Figure 4.1: A map of the Kara Sea, constrained to the model domain. The red rectangle shows the Severozemelsky region and the dashed line the open model boundary into the Barents Sea.

a novel z-grid which permits variable vertical grid spacing. This allows for better resolution near sharp changes in topography and lower resolution mid-ocean. The coupled model is run at a 10 km horizontal resolution with the appropriate VOM parameters for that resolution (see appendix C). In particular, the surface and bottom grid cells are always 4 m thick with other cells equally thick or thicker. The minimum number of grid cells per column is two and the minimum depth is therefore 8 m.

The extent of the model area is shown in figure 4.1, but the lower left corner of the grid is at 67°3'51"N, 59°24'22"E and the upper right corner is at 79°58'4"N, 113°15'53"E. The model topography is based on the 2.5 km resolution IBCAO (version 1) topography (Jakobsson et al., 2000). The grid is therefore on a polar-stereographic projection, correct at 75°N, but for the current model the grid was rotated such that the y-axis is parallel to the 81st meridian east. The grid was rotated using the `imrotate` command in the MATLAB program, using a bicubic interpolation. The downscaling to 10 km was also done in MATLAB using the `imresize` command with a bicubic interpolation.

Since the minimum model depth is 8 m the VOM gridding routines will treat all cells shallower than 7 m as land (only integer depth values are allowed). In an attempt to produce a more realistic grid in and around the Ob Bay and Yenisey Gulf grid cells shallower than 3 m were set as land while grid cells deeper than that (and shallower than 7 m) were set to 7 m depth. This results in a realistic coast line in the relevant shallow areas.

Some minor manual modifications were made to the resulting grid. The Shokalsky Strait, between the Severnaya Zemlya islands October Revolution Island and Bolshevik Island was closed since it is also closed in the NAOSIM model, which is used to force the lateral boundaries (see section 4.2.2). The extent of the eastern and western open boundaries also had to be adjusted to match the NAOSIM grid. The strait between Belyy island and Yamal peninsula was opened. Finally, single land grid cells were inserted where the Mona, Izvestiy TSIK, Kirova, Voronina and Dlinnyy Islands are located, since they disappeared when regridding the topography. The importance of these islands is discussed in chapter 5.

The ice model itself has already been discussed thoroughly in chapter 2 so only a cursory overview of the model setup will be given here. Unless stated otherwise the thermodynamic growth and melt of the ice is calculated using the three-layer model and variable albedo scheme described in section 2.3. The parametrisation for h_0 described in equation 3.6 is used. When solving the momentum equation the solver described in section 2.2.1 is used, using 500 outer-loop iterations, unless otherwise specified. The number of outer loops is based on the results presented in section 4.4. In some experiments (most notably in section 4.3) the solver from Hibler (1979) is used instead of the one from section 2.2.1. The relevant ice-model parameters are listed in table 4.1.

Table 4.1: Default values of relevant ice-model parameters using the elliptic yield curve.

Variable	Symbol	Value
ice density	ρ_{i}	930 kg/m^3
atmospheric density	ρ_{a}	1.25 kg/m^3
atmospheric drag coefficient	C_{da}	1.2×10^{-3}
water drag coefficient	C_{dw}	5.5×10^{-3}
outer-loop target error	ϵ_{OL}	0.1 mm/s
number of outer loops	n_{OL}	500
ice strength parameters	C, p^*	30, 37.5 kN/m^2
ellipse axis ratio	e	2
minimum viscosity	ζ_{min}	0 kg/s
maximum viscosity	ζ_{max}	$(10^{14}$ s$)P$
new-ice thickness parameter	Φ_F	0.5
lateral melt parameter	Φ_M	4
thermal conductivity of ice	k_{i}	2.03 W/m/K
thermal conductivity of snow	k_{s}	0.310 W/m/K
ocean/ice sensible heat transfer coefficient	C_{oi}	10^{-3}
ice salinity	S_{i}	5 psu
snow density	ρ_{i}	330 kg/m^3
heat capacity of ice	$(\rho c)_{\mathrm{i}}$	1.88 MJ/K/m^3
heat capacity of snow	$(\rho c)_{\mathrm{s}}$	0.690 MJ/K/m^3
volumetric latent heat of fusion for ice	q_{i}	301 MJ/m^3
volumetric latent heat of fusion at ice base	q_{b}	268 MJ/m^3
volumetric latent heat of snow	q_{s}	110 MJ/m^3
ice albedo (constant)	α_{i}	0.64
snow albedo (constant)	α_{s}	0.74
ice albedo (dry, visible)	α_{iv}	0.73
ice albedo (dry, infra-red)	α_{ii}	0.33
snow albedo (dry, visible)	α_{sv}	0.96
snow albedo (dry, infra-red)	α_{si}	0.68
short wave penetration ratio	I_0	0.17

Most of the tabulated parameters have been given values commonly used in the literature and already discussed in chapter 2. The thermodynamic parameters are from Semtner (1976), with the exception of the albedos for the variable albedo scheme which are from Briegleb et al. (2004). The constant ice albedo is the same as Semtner (1976) uses, but the corresponding snow albedo was found through preliminary tuning of the model.

4.2.2 Forcing data

In the current model four main sources of forcing data are used; atmospheric forcing, lateral ocean boundary forcing, tidal forcing and river forcing. The atmospheric forcing is derived from the first NCEP/NCAR reanalysis (Kalnay et al., 1996) providing the model with surface air temperatures (at 2 m), total cloud cover, atmospheric pressure, precipitation, relative humidity and winds (at 10 m). In some simulations the same information was extracted from the ERA-interim reanalysis results (Simmons et al., 2007).

Regridding of the atmospheric data is done using a simple near-neighbour scheme. For each model point the distance d to every data point in the reanalysis results is calculated. A weighted average is then calculated using only forcing data from points within a certain radius R from the model point. For each model point the regridded value is a weighted average of the forcing data with the weight $1/(1 + cd^2/R^2)$. An appropriately smooth output field is obtained using $c = 9$ and $R = 15 \times 10^3$ km$/n_{\text{lat}}$, where n_{lat} is the number of latitude points in the global NCEP/NCAR grid ($n_{\text{lat}} = 73$ or 94, depending on variable). All forcing data is linearly interpolated in time to the model time step at run time.

Oceanic forcing is derived from results from the NAOSIM model (Karcher et al., 2011). The NAOSIM is a high resolution coupled ice-ocean model of the Arctic and North-Atlantic oceans, forced with the same NCEP/NCAR data as used here. The NAOSIM data was used in two ways; as initial conditions and for forcing temperature, salinity and sea surface height on the lateral boundary.

Interpolation of oceanic temperature and salinity is done in two separate steps. First the NAOSIM data is interpolated in the horizontal for each NAOSIM grid level using the same method as described above for the surface forcing. For the vertical interpolation the profile in each column of the VOM model is approximated using a cubic spline and the tracer values at each grid point calculated using it. When the VOM grid reaches deeper than the NAOSIM grid the NAOSIM profile is simply extended using the value from the NAOSIM grid cell closest to the bottom.

The NAOSIM has a rigid lid and so a conversion of the NAOSIM stream function to sea surface height must be made. To do this a geostrophic

equilibrium is assumed such that

$$fu = -g\frac{\partial \eta}{\partial y} \text{ and } fv = g\frac{\partial \eta}{\partial x}, \tag{4.1}$$

where f is the Coriolis factor, u and v mean velocity, g gravity and η surface height. The stream function (ψ) is then defined such that

$$Hu = -\frac{\partial \psi}{\partial y}, \quad Hv = \frac{\partial \psi}{\partial x}, \tag{4.2}$$

where H is the ocean depth. Solving these two gives

$$f\vec{\nabla}\psi = gH\vec{\nabla}\eta. \tag{4.3}$$

Integrating gives, for a constant y

$$\eta(x,y) - \eta(x_0,y) = \int_{x_0}^{x} \frac{f(x')}{gH(x')}\frac{\partial \psi(x')}{\partial x'}dx' \tag{4.4}$$

and a similar formula for constant x. These are solved numerically using

$$\frac{\partial f(x_n)}{\partial x} \approx \frac{f(x_{n+1}) - f(x_{n-1})}{x_{n+1} - x_{n-1}} \tag{4.5}$$

and

$$\int_a^b f(x)dx \approx \frac{(b-a)}{2}[f(a) + f(b)]. \tag{4.6}$$

Finally $\eta(x_0, y_0)$ is set such that the mean sea surface height along all open boundaries is zero for every time step. The VOM model topography (not the NAOSIM topography) is used for H in equation (4.4).

Daily river discharge data for the Ob, Pur, Taz, Yenisey and Nadym rivers was obtained from the Global Runoff Data Centre (GRDC)[1]. Monthly data for Pyasina from June to September as well as the annual average was obtained from the Arctic and Antarctic Research Institute's (AARI) website[2]. The temporal extent of the data is listed in table 4.2. For the GRDC data daily climatological mean values were calculated and used to replace missing data. The monthly AARI data was interpolated to daily values for the summer months with the remainder of the total annual discharge equally distributed over the months for which no data is available. The resulting data was then treated the same as the GRDC data.

River temperatures were calculated based on the T_0 measurement data provided by Lammers et al. (2007)[3]. No temperatures were available for the

[1] Global Runoff Data Centre, 56068 Koblenz, Germany

[2] `http://www.aari.nw.ru/projects/Atlas/Ocean_Summer/digital/runoff/rr_karat.txt`, accessed November 19th 2008

[3] Data obtained from `http://data.eol.ucar.edu/codiac/dss/id=106.233` on February 11th 2011

Table 4.2: The periods for which river runoff data is available from the GRDC and AARI as well as the fraction of data missing from that period.

River	Period	Missing
Yenisey (at Igarka)	1955 to 2003	15%
Ob (at Salekhard)	1954 to 2003	2%
Nadym (at Nadym)	1955 to 1991	5%
Taz (at Sidorovsk)	1962 to 1996	15%
Pur (at Samburg)	1939 to 1991	33%
Pyasina (at Ust-Tareya)	1961 to 1986	two years

Pyasina river so the Pyasina river temperatures were set equal to its nearest neighbour, the Yenisey. The inflow of Ob and Nadym is combined in one in the model and so are the Pur and Taz. Temperature for the combined inflow was calculated as the weighted average of the temperature of the two rivers, weighted with the volume flux.

In general the temperature data is available for every 10 days (three times per month), but missing values were replaced with the climatological mean. During the preprocessing phase the data was linearly interpolated to daily values. All river data is linearly interpolated in time to the model time step at runtime. The climatological river volume flux and temperatures are shown in figure 4.2.

Tidal data comes from the HAMTIDE tidal model (Taguchi et al., 2011)[4]. Tidal amplitude and phase are interpolated at the open boundary using the same technique as for the surface data. The tidal forcing and the NAOSIM sea surface forcing are added up at runtime. Tidal variations in the relevant fast-ice areas are small and little effort was therefore put into investigating tidal influences in the model.

4.2.3 Spin-up

In order to produce reasonable initial temperature and salinity fields for further model runs a cyclic spin-up forcing was created. This is a climatological average of all forcing data, based on the period 1994–2005. An exception to this is the climatological average for the river data, but that is based on all available observations. For the spin-up run the default setup outlined in section 4.2.1 was used, with two exceptions. Firstly one pseudo-time step is used and secondly the maximum and minimum viscosity are set to $\zeta_{\max} = (2.5 \times 10^8 \text{ s})P$ and $\zeta_{\min} = 4 \times 10^8$ kg/s respectively, the same as used by Hibler (1979). These are commonly used values which also give a

[4]see also `http://icdc.zmaw.de/hamtide.html?&L=1`

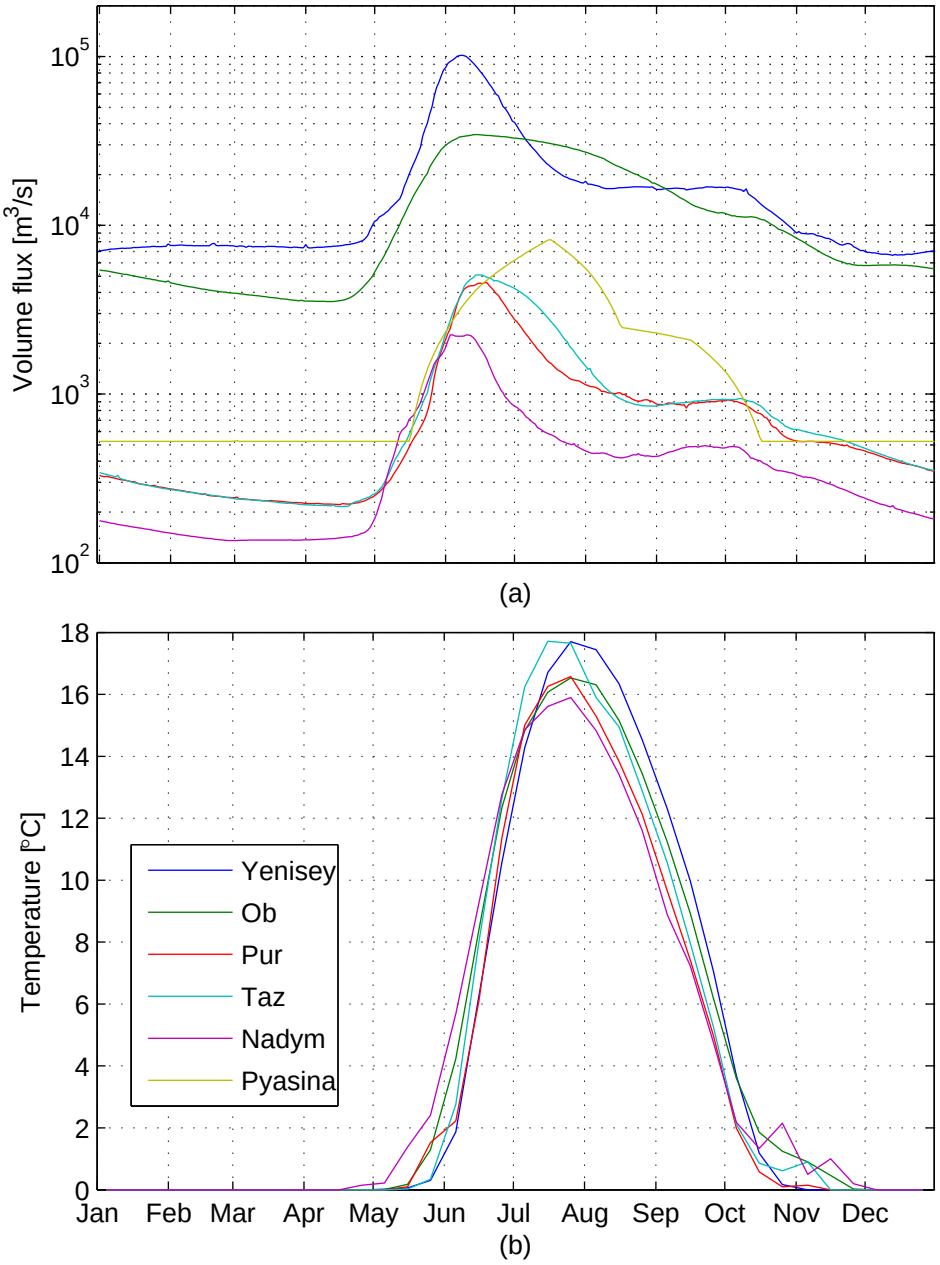

Figure 4.2: Climatological data for the river input used in the model: (a) volume flux and (b) temperature.

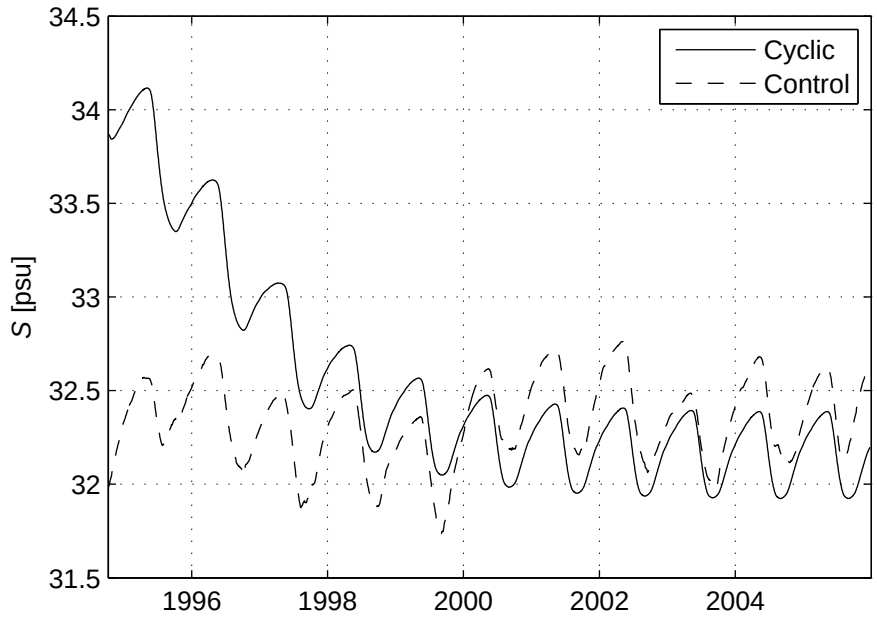

Figure 4.3: Global mean model salinity in the spin-up run. For comparison the dashed line shows the mean model salinity from the control run from section 4.3 and the y-axis is labelled accordingly.

short integration time for the model. In particular using a non-zero minimum viscosity allows us to double the time step size from $\Delta t = 600$ s to $\Delta t = 1200$ s.

Using the NAOSIM temperature and salinity field from October 9^{th} 1994 for initialisation the model was run for 11 years, using the cyclic forcing. After this an approximate cyclic steady state was reached. As figure 4.3 shows this new state has mean salinity that is about 2 psu lower than the NAOSIM mean salinity. This is because the current model employs volume fluxes for the river inflow while the NAOSIM uses salinity restoration. Since approximately half the river flux is just above the freezing point the new ocean temperature is also lower than that of the NAOSIM. The resulting temperature and salinity fields are used as initial conditions for all further simulations, unless otherwise specified.

4.3 Thermodynamics

In this section the model thermodynamics are tested using the same simplified dynamics as for the spin-up run. This reduces the model run-time by

three quarters but does not resolve the ice dynamics very accurately. The shorter run-time does, however, allow us to consider a longer model time period and confirm that the model behaves reasonably on a longer time-scale. To test the thermodynamics the model is integrated from October 9^{th} 1994 to December 24^{th} 2005 covering the last years available at the time from the NAOSIM model. A control run is set up using the NCEP reanalysis for forcing, but otherwise the setup is the same as the one used for the spin-up run described in the previous section.

Satellite observations of the sea-ice concentration are the observations that give the best overall idea of the state of the ice cover in the Arctic. The model data will be compared to the satellite data derived from the Special Sensor Microwave/Imager (SSM/I) brightness temperature and polarisation using the ASI-algorithm (Kaleschke et al., 2001). It provides us with sea-ice concentration at a resolution of 12.5 km, year round for the whole Kara Sea. The most useful variable to consider for a quick overview of the model capabilities is the mean concentration over the entire Kara Sea.

Following is an outline of the different results obtained using the NCEP/-NCAR reanalysis data and ERA-interim data to force the model. The effects of different albedo parametrisations and using different number of thermodynamic layers area also outlined. Finally different parametrisations and parameter choices for lateral melt are tested. This is followed by a comparison of modelled ice thickness and a general discussion of the results.

4.3.1 Comparison with satellite data

Using the Kara Sea mean sea-ice concentration we can quickly compare the control run to observations. Figure 4.4 shows the mean sea-ice concentration in the model area computed from the ASI data, the control run and a run using the ERA-interim reanalysis data instead of the NCEP/NCAR data. The figure shows generally good agreement between model and observations in fall and winter. During winter the absolute difference between observations and model results is nearly always less than 0.1, but the model consistently overestimates the extent of the ice cover when compared to the satellite data. Errors present during fall appear to be primarily caused by erroneous minimum ice extent from the previous summer and are recovered quickly. While the model appears to overestimate the concentration slightly it is probable that the actual concentration is in fact underestimated by the satellite data. This is because the satellite is calibrated for the mean salinity of the Arctic ocean, but since the Kara Sea is fresher the concentration is therefore underestimated.

Larger differences are visible during spring and summer than fall and winter and the two different reanalysis products also give also give considerably different results then. Using the NCEP/NCAR data the model always underestimates the ice cover in summer. This makes little difference when

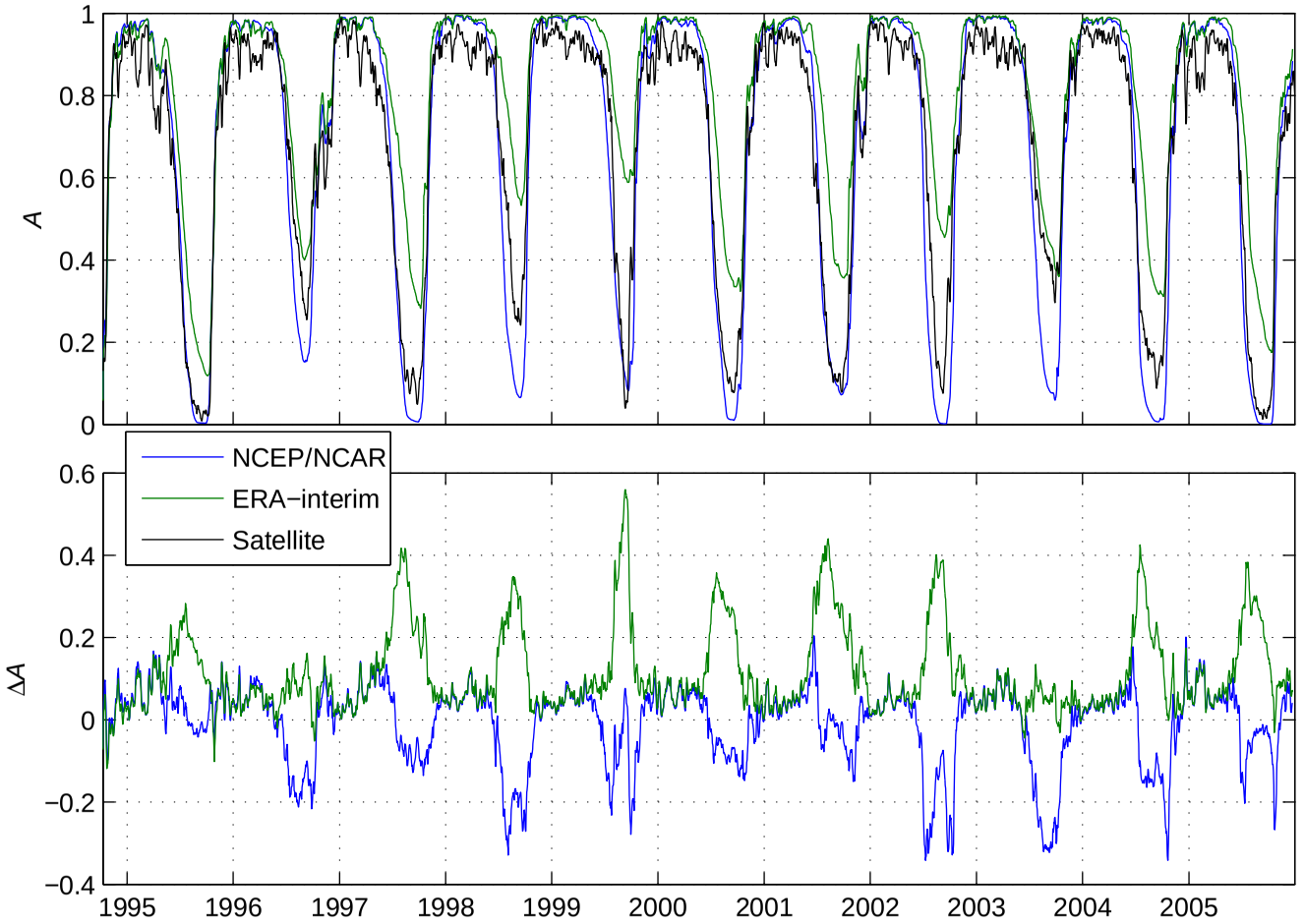

Figure 4.4: The upper panel shows mean sea-ice concentration in the model area modelled using the NCEP/NCAR and ERA-interim reanalysis data compared to satellite data. The lower panel shows the difference between the satellite data and model results.

the observed ice cover is very small at the end of the melt season, but in other years, when the observed concentration is high the difference is also greater. The largest absolute difference in mean ice concentration between satellite and model results using the NCEP/NCAR data is just over 0.3. This occurs in 1998, 2002, 2003 and 2004. For eight out of the eleven summers modelled the absolute difference in concentration becomes greater than 0.2 at some point in time during the summer.

In contrast using the ERA-interim gives an overestimation of the ice extent in summer, mostly to the same absolute magnitude as the NCEP/NCAR underestimation is. So even though the behaviour of the model when using the two different forcing sets differs considerably then the mean error is similar. In particular the root-mean-square error when using the NCEP/NCAR data is 0.10, compared to 0.15 for ERA-interim.

4.3.2 Layer numbers and albedo scheme

In the previous comparison a three-layer Semtner model with variable albedo was used. We will now compare the three-layer model to a zero-layer model with constant and variable albedo. The zero-layer model is known to give less accurate results than the three-layer one (see e.g. Semtner, 1984), but it is nonetheless widely used in the sea-ice modelling community. In particular the zero-layer model is known to give poor results for multi-year ice, but since we primarily have to deal with first year ice here it is worth considering the zero-layer model.

Again the best variable to consider is the mean total ice cover. Figure 4.5 shows the ice cover and model error when compared to the satellite data for the zero-layer model with constant and variable albedo and the three-layer model (the control run). All three model variations give very similar results in fall and winter, with noteworthy differences only appearing in spring and summer.

If we first consider the zero-layer model then there is a clear difference between using a constant albedo and the variable albedo scheme. Using a constant albedo gives clear overestimation of the ice extent, except for the summers of 1998 and 2003, for which the absolute difference between model and observations is always less than 0.1. Using variable albedo, on the other hand always gives a clear underestimation of the ice extent, with the exception of 1995. Using a constant albedo gives, overall better results, with the root-mean-square difference between model results and observations being 0.09 when using constant albedo and 0.12 using variable albedo.

Using the three-layer model with variable albedo gives better results than the zero-layer model with variable albedo. The ice extent is still underestimated in summer, but somewhat less so than when using the zero-layer model. The RMS error for the three-layer model using variable albedo is 0.10.

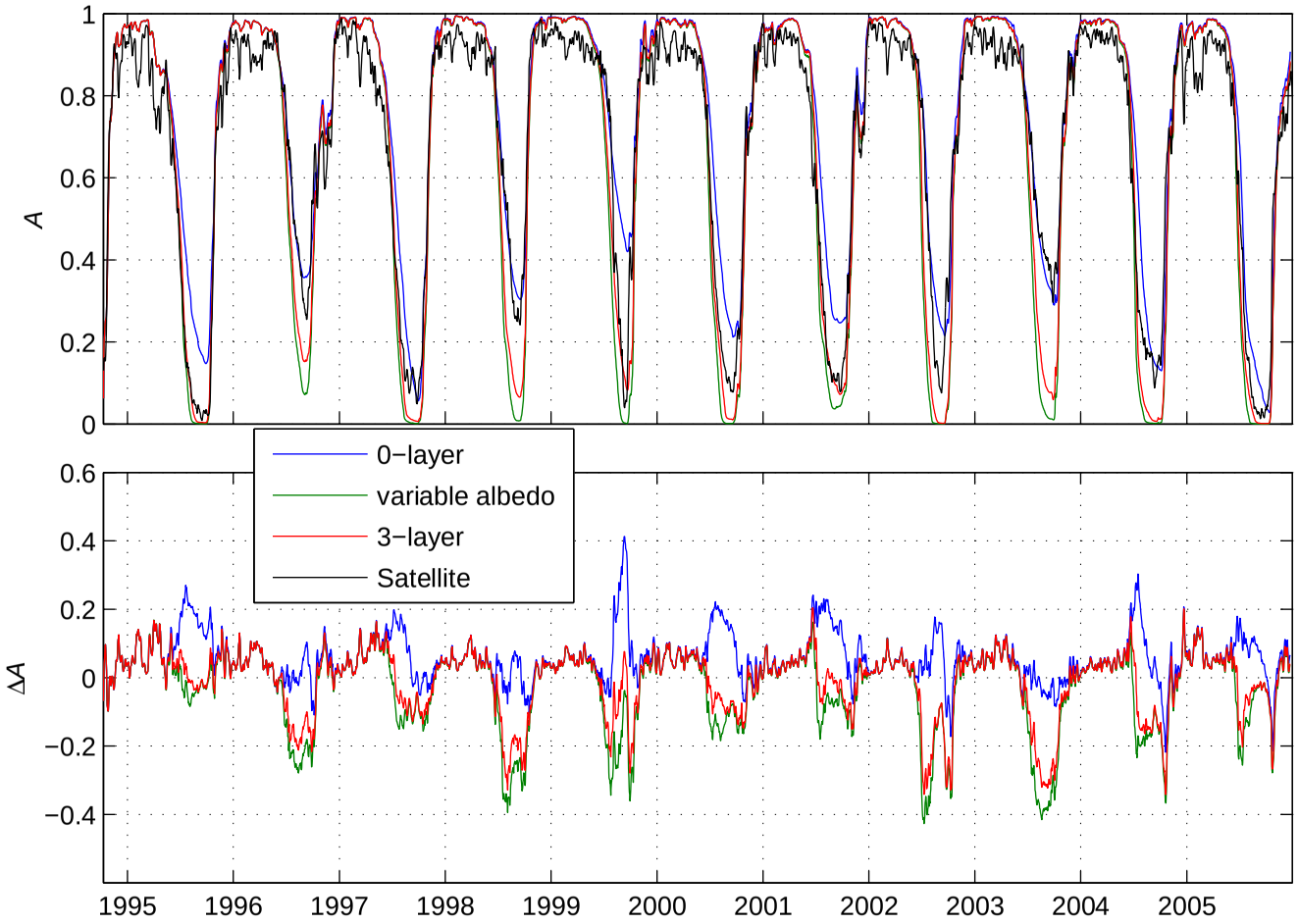

Figure 4.5: The upper panel shows the mean sea-ice concentration in the model area modelled using different albedo and layer settings compared to satellite data. The lower panel shows the difference between the satellite data and model results.

4.3.3 Lateral melt

The Semtner (1976) model addresses melting from the top and bottom of an ice floe, but in addition to that the ice also melts from the sides, termed lateral melt. This portion of the ice melt is not easily modelled based on first principles so simple parametrisations are used. The two approaches implemented here are either to assign a fraction of the basal melt to the lateral melt, or to assume a linear thickness distribution and reduce the ice area accordingly when there is melt at the top or bottom surfaces. The former was suggested by Mellor and Kantha (1989) and the latter by Hibler (1979). The variations used here, where the ocean is allowed to warm above the freezing point in the presence of ice are described in section 2.3.

In terms of mean ice concentration the two approaches by Hibler (1979) and Mellor and Kantha (1989) give very similar results. The RMS error when compared to the satellite data is 0.10 when using Mellor and Kantha's approach and 0.12 using Hibler's. Naturally these differences appear during the melt period.

Another concern is how large a portion of the total melt should be assigned to lateral melt when using the approach by Mellor and Kantha (1989). This amounts to adjusting the parameter Φ_M, which Mellor and Kantha (1989) set at $\Phi_M = 0.5$ (the value also used in the control run). The lower and upper limits for Φ_M are 0 and 1, respectively. If $\Phi_M = 0$ only basal melt will occur and if $\Phi_M = 1$ only lateral melt occurs. In order to test the sensitivity of the model towards changes in Φ_M two decadal runs, each with $\Phi_M = 0.3$ and $\Phi_M = 0.7$ were run. These changes proved to have very limited effects on the mean ice concentration and the RMS error was the same to within 0.002 for all three values of Φ_M tested.

4.3.4 Ice thickness

Ice thickness is of considerable interest in the current context since it is thought to be the main factor determining fast ice strength (see e.g. Divine et al., 2004, and references therein). Unfortunately readily available sea-ice thickness data in the Kara Sea is nearly completely limited to fast ice thickness and these are scarce. The presence of dynamic interactions in the model is likely to cause it to produce thinner ice than it would if no dynamics were involved. Comparing model results (where no fast ice is present) to measured fast-ice thickness can therefore be misleading.

To get some idea of how thick the modelled ice becomes figure 4.6 shows the mean ice thickness, calculated for ice covered cells only. The upper panel shows the mean for the entire model domain and the lower panel shows the mean for the Severozemelsky region, as defined by the red rectangle in figure 4.1. Averages for the NCEP/NCAR data using the zero-layer model with and without variable albedo, the three-layer model (the control run) and

the ERA-interim data are shown.

Comparing the three NCEP/NCAR means shows very little difference between ice thickness depending on the number of layers while the albedo scheme plays a more important role. Using a variable albedo the only notable difference between the zero-layer and three layer models occurs during the melting period. Using the three-layer model slows down the melting, compared to the zero-layer model—much as one would expect given the underlying model physics. Aside from that the difference between the ice thickness modelled using the two model formulations is only a few centimetres.

We've already seen that using the constant albedos prescribed here results in a slower melt than when using the variable albedo scheme. This is also apparent when considering the ice thickness. In particular the summer minimum mean thickness is always some tens of centimetres greater using the constant albedos compared to when using the variable albedo scheme. This can result in a build up of multi-year ice causing the ice in the following winter to be thicker than otherwise. This is most striking in the winter 1999–2000, but can also be seen, to some extent during most of the modelled years.

Adding the ERA-interim results to the comparison shows that changing the forcing can affect the winter ice thickness as well as the summer thickness. Before 1999 the modelled ice is thinner in winter and thicker in summer using ERA-interim. During these years the difference in mean ice thickness can be as much as 20 cm in winter and 50 cm in summer. During the summer of 1999 there's exceptionally little melt modelled using the ERA-interim data. This leads to a build-up of ice and consequently the modelled mean ice thickness is larger for ERA-interim than NCEP/NCAR in the following years.

4.3.5 Summary

This quick overview shows that while the model remains consistent during fall and winter, spring and summer are more problematic. This is not unexpected since the melting period is notoriously difficult to model properly. During it the ice and snow albedo change as the melt sets in. After some time the melt water may gather in ponds on the ice surface, dramatically lowering the albedo and thus accelerating the melt. The formation and drainage of these melt-ponds is extremely difficult to model accurately, but the variable albedo scheme included here is an attempt to give a rough estimation of all these effects. Finally lateral melt also plays a role, but the extent of it is also difficult to estimate.

Given all the unresolved processes involved in the melting of the ice it should come as no surprise that the differences between using different forcing data sets and model formulations are largest in spring and summer.

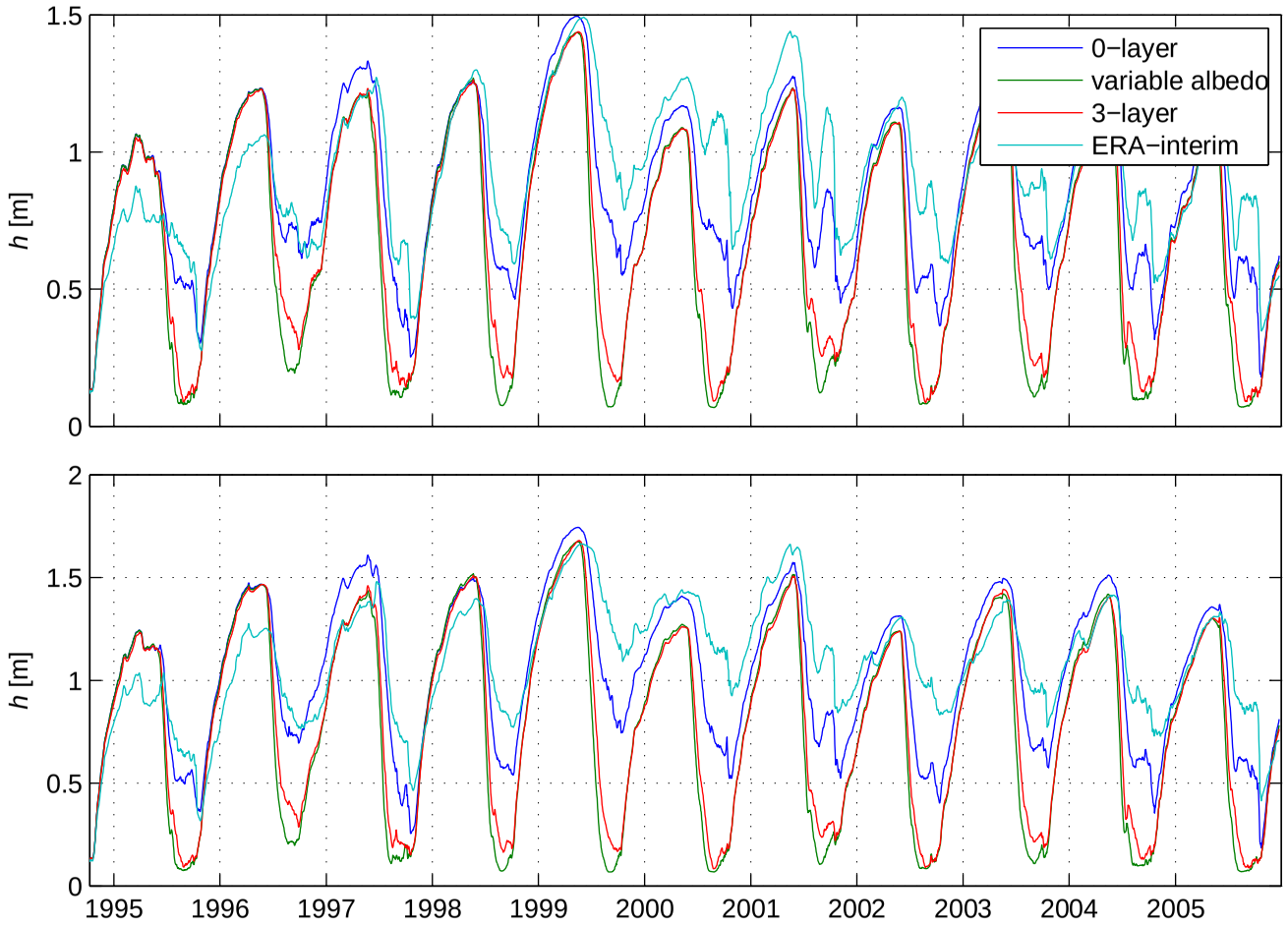

Figure 4.6: The upper panel shows the mean sea-ice thickness in the model area modelled using different albedo and layer settings for the NCEP/NCAR data and the three-layer model with variable albedo for the ERA-interim data. The lower panel shows the same variables with the average constrained to the Severozemelsky region, as defined by the red rectangle in figure 4.1.

Overall using the NCEP/NCAR data leads to an underestimation of the sea-ice extent while using the ERA-interim data leads to an overestimation. These over- and underestimations are of similar absolute magnitude; using the NCEP/NCAR and ERA-interim results in an RMS error of 0.10 and 0.15 respectively when compared to the satellite data. This can be used as a measure of the acceptable variations due to changes in the model parameters.

Parameters that were tested in this section were the surface albedo, the number of layers, the lateral melt scheme and the Φ_M parameter of the Mellor and Kantha (1989) lateral melt scheme. As expected changing the surface albedo has considerable effects on the ice. The mean ice concentration changes considerably in summer depending on the albedo scheme used, but somewhat surprisingly using a constant albedo gives lower RMS error than using the variable albedo scheme. Introducing a three-layer model with variable albedo improves the results compared to the zero-layer model and pushes the RMS error down to the same level as those achieved using the zero-layer model and constant albedo.

Changes in the lateral melt parametrisation may affect similar changes in the RMS error. Replacing the Mellor and Kantha (1989) lateral melt scheme with the one from Hibler (1979) increases the RMS error from 0.10 to 0.12, a similar magnitude as when changing albedo schemes. Changing the Φ_M parameter in the Mellor and Kantha (1989) scheme has, on the other hand a much smaller effect; changing the RMS error by no more than 0.002. The model results are therefore robust with respect to changes in the lateral melt scheme.

Changes to the ice thickness are of interest here since the ice strength depends on its thickness. Differences in ice thickness between the various model runs appear to arise primarily because of differences in the modelled ice extent at the end of the melt season. Using the zero-layer model with constant albedos or the ERA-interim data there is often considerable amount of ice still in the Kara Sea as the melt season ends. This results in thicker ice forming the following winter and the effect is particularly noteworthy in 1999–2000. During that winter the ice in the Severozemelsky region becomes unusually thin in model runs where the ice all melts during the summer. In runs where there's a build-up of multi-year ice the ice thickness is much closer to the average value.

Figure 4.7 goes into more detail showing the maximum mean ice thickness in the Severozemelsky region and the standard deviation thereof for the aforementioned constant and variable albedo runs. Even though the number of samples is statistically very small here we can use the standard deviation as an indicator of what constitutes thin and thick ice in this context. Note in particular that using constant albedo the maximum mean thickness only falls one standard deviation below the mean in 1995 and 2002 while this also happens in 2000 when using the three layer model. The ice can therefore be considered unusually thin in these years. This is particularly interesting

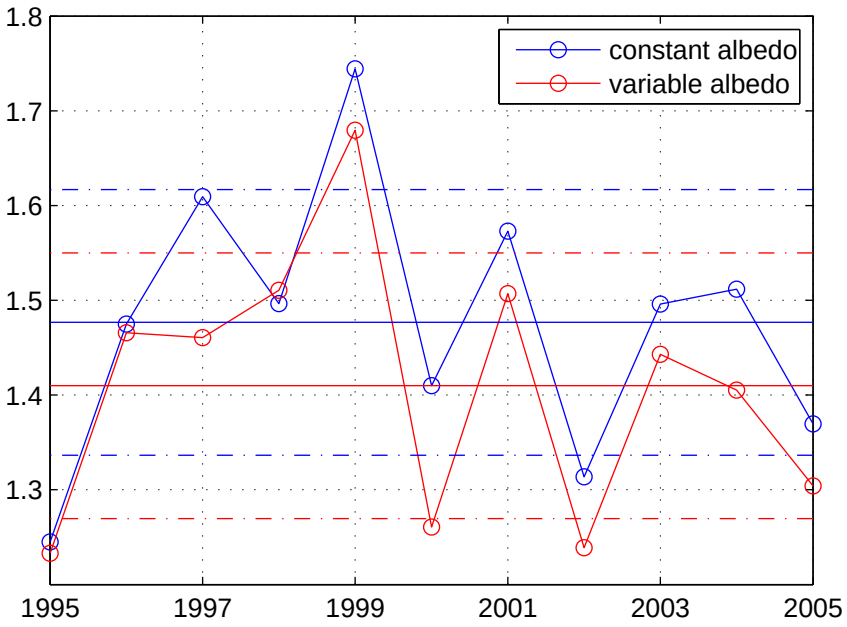

Figure 4.7: The solid lines and circles show the maximum mean ice thickness in the Severozemelsky region while the horizontal solid and dashed-dot lines show the mean and standard deviation respectively.

here because fast ice is observed throughout the winter in 2000, but only for one month in 2002. If ice thickness is the primary factor in deciding whether fast ice forms or not then it is likely that the thicker ice produced when using a constant albedo is more realistic than that produced using the three-layer model. The role of ice thickness on fast-ice formation will be discussed in more detail in chapter 6.

The overall result of these tests is that the model behaviour is robust compared to the quality of the forcing data. The weak link appears to be the albedo scheme and using a constant albedo actually gives lower RMS errors than using variable albedo under the NCEP/NCAR forcing. The significance of this result is diminished when comparing the results from using the ERA-interim data since changing the forcing changes both the sign and the nature of the errors incurred. It would probably be possible to tune the albedo scheme to give better results under the NCEP/NCAR forcing, but this is likely to have an adverse effect on the ERA-interim results. No such tuning was therefore attempted and the model is considered good enough as it is.

4.4 Dynamics

Sea ice modelled in a viscous-plastic model can never be stationary in the presence of applied strain, only move very slowly. It is therefore important to know how accurately the velocity can be modelled so that a sensible separation between fast ice and slowly moving ice can be decided upon. It is also the plastic character of sea ice that gives it cohesion and allows it to remain land fast. It should, therefore, be necessary to iterate the model to a plastic convergence when modelling fast ice.

In his seminal paper, introducing the viscous-plastic model, Hibler (1979) used an SOR-solver to solve the linearised momentum equation. As previously mentioned this results in an erroneous solution since the viscosities used to calculate the velocities were calculated using velocities from the previous time-step. To improve the solution a pseudo time step is used where the momentum equation is re-linearised and solved using the newly calculated velocities. One pseudo time step can also be referred to as two outer loops. Two outer loops are, however, insufficient to achieve a convergent solution and Lemieux and Tremblay (2009) showed that at 10 km resolution somewhere between 200 and 1000 outer loops may be necessary to achieve acceptable convergence.

In the following the convergence properties of the Hibler-type and granular models implemented here are tested. Each model type is tested by varying the number of outer loops from 50 to 500. Convergence is then estimated by considering the outer-loop error and the percentage of grid cells where the outer-loop error falls within a given target. The computational cost of increasing the number of outer loops is also taken into consideration.

4.4.1 The Hibler-type model

In order to asses the performance the Hibler-type model a set of ten 15 month long test runs were run. The setup was the same for each run, except that the number of outer loops was varied from 50 to 500. In other respects the model setup is the same as described in section 4.2.1. It's worth recalling that to try and save some computational time no more outer loops are taken when the outer loop target error ($\epsilon_{OL} < 0.1$ mm/s) is reached. At this point it is assumed that a plastic convergence is reached. Lemieux and Tremblay (2009) use a similar criterion to define what they consider "acceptable convergence".

During these runs the outer-loop error was calculated, as described in section 2.2.1, and written to file. Figure 4.8 shows the percentage of time steps where the outer loop error falls below a given target as a function of the number of outer loops. The target error of 0.1 mm/s is difficult to reach, being reached 19% of the time when using 50 outer-loop iterations, but this ratio becomes 95% at 500 iterations. In comparison the target $\epsilon_{OL} < 1$ mm/s

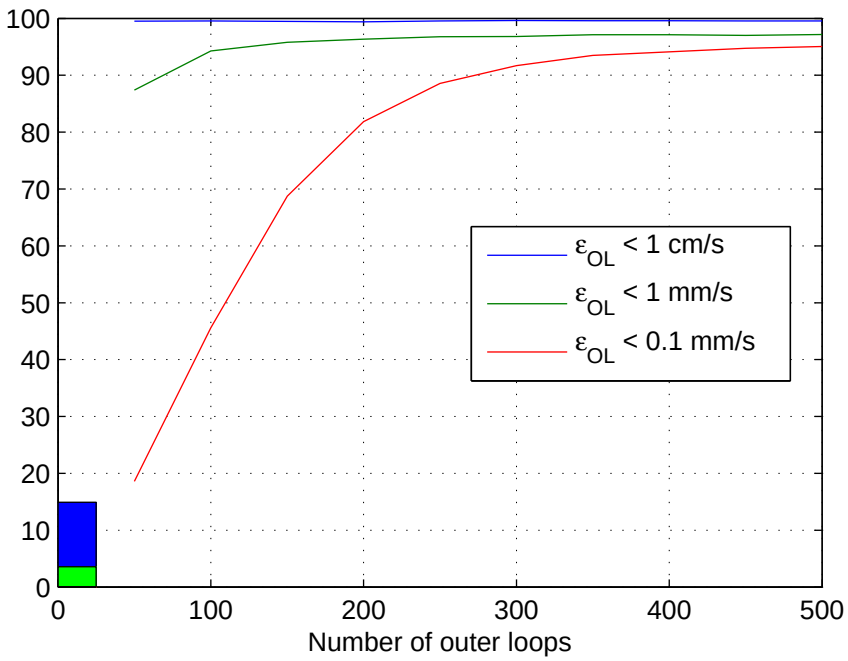

Figure 4.8: The percentage of time steps where the outer loop error falls below a given target as a function of the number of outer loops. The bar in the left corner shows the percentage of time steps where the difference between the results of the two pseudo time steps in Hibler's approach falls below the same targets.

is reached 87% of the time when using 50 outer-loop iterations, 94% of the time when using 100 iterations and 97% of the time using 500 iterations.

The convergence of the model clearly improves with increased outer-loop iterations, but this improvement appears to level off before full convergence is reached. In particular it seems clear that there is little to gain from going beyond 500 outer-loop iterations in terms of the targets $\epsilon_{\mathrm{OL}} < 1$ mm/s and $\epsilon_{\mathrm{OL}} < 0.1$ mm/s. As a further test one run with 1000 outer loop iterations was run. In this run the $\epsilon_{\mathrm{OL}} < 0.1$ mm/s target was reached in only 25 iterations more than when using 500 outer loops, which is 0.04% of the total number of iterations. It seems clear therefore that reaching full convergence at every time step is extremely difficult, using the current model, if at all possible.

On a more positive note figure 4.8 also shows well the vast improvement the current scheme is over the approach of Hibler (1979). Using only a single pseudo time step the change in velocity between the two time steps is never less than 0.1 mm/s. By the same measure the target $\epsilon_{\mathrm{OL}} < 1$ mm/s is reached in 4% of the time steps taken and the target $\epsilon_{\mathrm{OL}} < 1$ cm/s is only

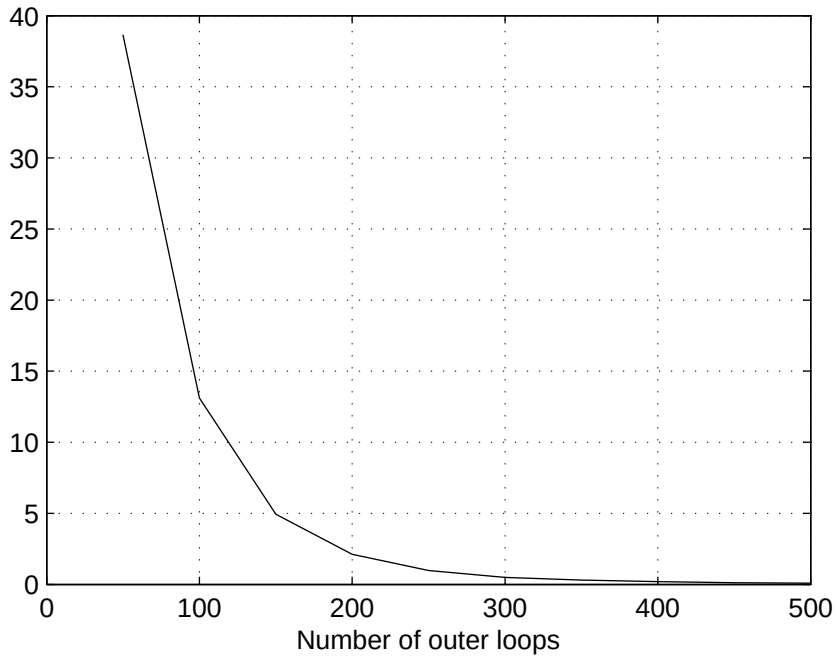

Figure 4.9: The percentage of iterations where more than 1% of the ice covered grid cells have outer-loop errors larger than 0.1 mm/s as a function of the number of outer loops.

reached 15% of the time. In addition to this the maximum velocity difference between using 500 outer loops and one pseudo-time step was calculated for one time step of each modelled day. This maximum difference was always greater than 1 cm.

Lemieux and Tremblay (2009) suggest that if less than 1% of the ice covered grid cells have errors larger than 0.1 mm/s the model should be considered to have converged. This target can also not be reached in every time step using the current model. Figure 4.9 shows that at 50 outer loops 39% of the iterations ended with more than 1% of the ice covered grid cells with errors larger than 0.1 mm/s. This fraction does, however, drop rapidly to 0.09% at 500 outer loops, a total of 57 iterations. Iterating over 1000 outer loops gives little improvement over 500 outer loops. In this case 0.03% of the iterations do not converge, compared to 0.09% using 500 outer loops. Using 500 outer loop iterations we therefore seem to come as close to a complete convergence as reasonably possible with this model.

These good results do come at a steep price, computing time wise. Figure 4.10 shows the time it takes to integrate the model for 15 months on the

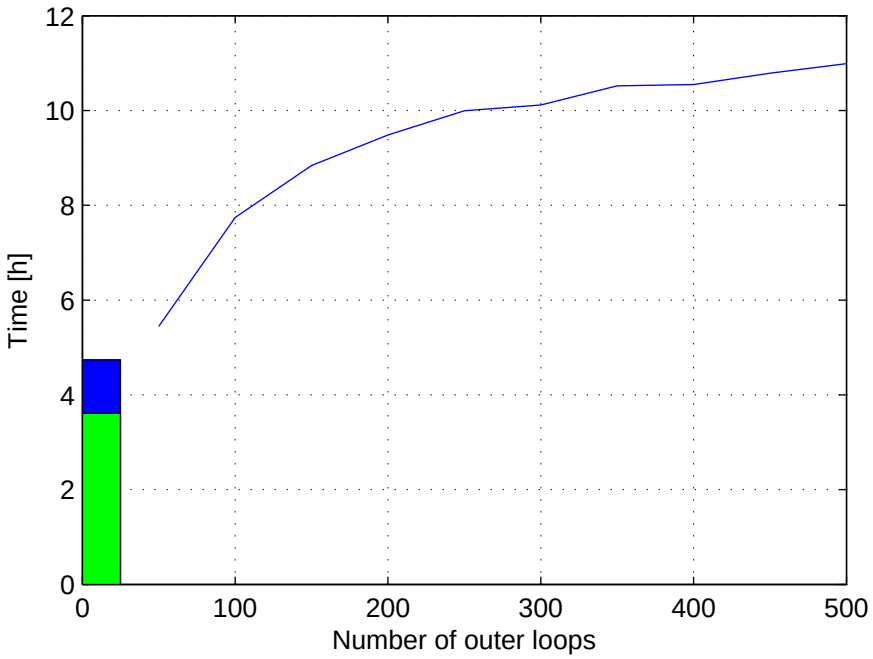

Figure 4.10: The time it takes to simulate 15 model months on the RRZ's Linux cluster. The blue portion of bar in the left corner of the graph shows the time it takes to simulate the 15 months using a single pseudo time step. The green portion shows the time spent in the ocean model.

Regionales Rechenzentrum's Linux cluster computer[5]. It shows that when using Hibler's pseudo time stepping integrating the coupled ice-ocean model for 15 months takes 4.7 hours, while when using 500 outer loops it takes 11.0 hours. This is roughly a doubling of the computing time and as such perhaps not a large sacrifice given how much the results have improved. On the other hand, when using Hibler's pseudo time stepping the ice model takes up 23.8% of the computing time and so the ice model itself takes about 7 times as much computing time with 500 outer loop iterations, compared to using a single pseudo time step. Considering that the number of outer loops increased 200-fold this is perhaps not too bad, but it is clear that reducing the number of outer loops required is essential if we want to iterate the momentum equation to convergence in a more demanding setup. Lemieux et al. (2010) have already indicated a possible way forwards in this regard.

[5]Each computing node as two Intel Xeon E5462 Quad Core CPUs clocked at 2.80 GHz with front side bus speed of 1600 MHz and 16 GB of RAM. When the tests were run only four jobs were assigned to each node since using more than that resulted in a considerable performance degradation. This way the completion of one job has no effect on the runtime of the remaining jobs.

4.4.2 Granular model

So far only the convergence properties of the Hibler-type model using an elliptic yield curve have been considered. There is no reason to assume that the results change much when using a different yield curve and some limited testing indicates this to be true. The granular model, proposed by Tremblay and Mysak (1997) is a different mater, however, since it uses an additional solver to calculate the pressure term. Tremblay and Mysak (1997) note that the introduction of the pressure term solver requires an added number of outer loops compared to Hibler-type models. It is therefore to be expected that the granular model requires more outer loops to reach full convergence.

To test this a set of ten 15 months experiments were carried out in the same manner as before, except now the granular model was used instead of the Hibler-type model. It turns out that the granular model is much further away from reaching a convergence than the Hibler-type model. Figure 4.11 shows the percentage of time steps where the outer loop error falls below a given target, same as figure 4.8 for the Hibler-type model. In this case the target $\epsilon_{\mathrm{OL}} < 1$ mm/s is reached only 22% of the time using 100 outer loops and this result does not improve significantly with increased number of outer loops. The target $\epsilon_{\mathrm{OL}} < 0.1$ mm/s is reached 8% of the time using 100 outer loops and 10% of the time using 500. This is a very small improvement, especially considering that the time required to integrate the coupled model increases almost linearly from 5.1 hours for 50 outer loop iterations to 29.7 hours for 500 outer loops.

The granular model also fails to reach convergence when we consider the fraction of cells with outer-loop errors greater than 0.1 mm/s. At 50 outer loops more than 1% of the grid cells have errors larger than the target error for 87% of the modelled time steps. Using 500 outer loops this fraction falls down to 74%, a substantially worse result than when using the Hibler-type model. It is, therefore, clear that the granular model shows much poorer plastic convergence than the Hibler-type model.

4.4.3 Summary

The results presented for the Hibler-type model show well the limits of the model solver. The tests aimed at reaching "acceptable convergence" or outer-loop error less than $\epsilon_{\mathrm{OL}} = 0.1$ mm/s. This proved impossible to reach at every time step, even using 1000 outer-loop iterations. Using 500 outer loops gave convergence for 95% of the time steps. Increasing the number of outer loops to 1000 improved this percentage by only 0.04 percentage points so it's safe to conclude that at 500 outer-loop iterations the solver performance is close to the optimum, using $\epsilon_{\mathrm{OL}} = 0.1$ mm/s.

Using 500 outer-loop iterations gives much more accurate results than using one pseudo-time step. After one pseudo-time step the changes in

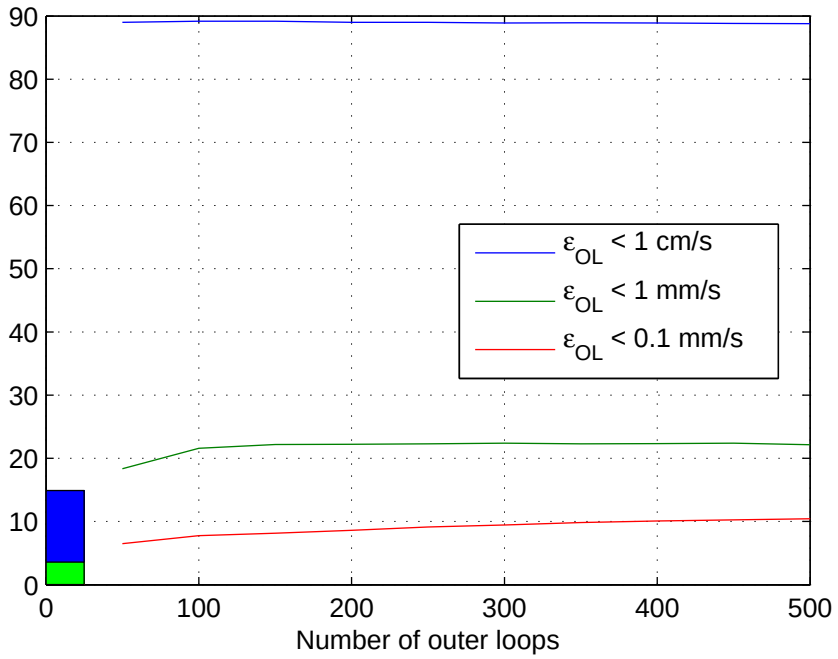

Figure 4.11: The percentage of time steps where the outer loop error falls below a given target as a function of the number of outer loops, using the granular model. The bar in the left corner shows the percentage of time steps where the difference between the results of the two pseudo time steps in Hibler's approach falls below the same targets.

velocity are always greater than 0.1 mm/s, but that limit is reached 95% of the time using 500 outer loops. The improvement is therefore considerable, but full convergence is still not reached 5% of the time. If the convergence criterion is changed to $\epsilon_{\mathrm{OL}} = 0.01$ mm/s the required number of outer loops and time required grows considerably. A test using $\epsilon_{\mathrm{OL}} = 0.01$ mm/s and 1000 outer-loop iterations show that full convergence is only reached 47% of the time in that setup. In addition the model run time is about 34 hours, approximately threefold the runtime when $\epsilon_{\mathrm{OL}} = 0.1$ mm/s and using 500 outer loops. This shows that setting $\epsilon_{\mathrm{OL}} = 0.1$ mm/s and using 500 outer loops gives the best accuracy possible within a reasonable time frame.

The test performed on the granular model showed much worse convergence than that of the Hibler-type model. After 100 outer-loop iterations full convergence was only reached in 8% of the model time steps and 10% of the time after 500 outer loops. Since the improvement in convergence barely grows at all the time it takes to integrate the model increases nearly linearly. Using 500 outer-loop iterations it took almost 30 hours to integrate the 15 model months, compared to 11 hours using 500 outer loops and the Hibler-type model.

In conclusion we note that the experiments performed so far cannot tell us with any certainty what number of outer loops is necessary to model fast ice. The approach taken here will be to iterate the model as close to plastic convergence as is practically feasible and see if this way it is possible to model fast ice. Once the processes involved are better understood it's worth investigating how the model responds to a reduced number of outer loops. This will be done in section 5.3.1.

4.5 Conclusion

This chapter gave a quick overview of the model setup and the forcing data used. In addition two sets of experiments were introduced as a preparation for the following modelling work. Firstly the model response with respect to changes in thermodynamics was considered and secondly the performance of the dynamical solver was investigated.

All the thermodynamical tests showed that the model response is robust with respect to changes in parametrisations. The modelled mean ice concentration compared well with observations with the largest errors present in spring and summer, as expected. Changing the atmospheric forcing from NCEP/NCAR reanalysis data to ERA-interim data changed the sign of the errors, but the root-mean-squared error remained similar. Changes to various thermodynamical parameters produced changes in model output which were much smaller than changes observed when switching from one forcing data set to another. The model therefore produces acceptable results in this respect.

The dynamic tests done focused not on comparison with observations, but rather on determining the solvers capabilities. In particular the relationship between outer-loop convergence and the number of outer loops was investigated. Increasing the number of outer loops reduced the solver error, as expected, but a fully converged solution could not be reached for every time step. The percentage of time-steps where the model error fell below the given target increases rapidly for a low number of outer-loop iterations, but the improvement slows down as the number of outer loops increases.

The dynamical tests determined that when using the Hibler-type model not much is gained by performing more than about 500 outer loop iterations. At this point full convergence is reached 95% of the time. Integrating the ice model with 500 outer-loop iterations takes about 7 times longer than with one pseudo-time step. The integration time of the coupled model is doubled when using 500 outer loops compared to one pseudo-time step.

The granular model showed substantially worse convergence properties with full convergence for only 10% of all time steps at 500 outer-loop iterations. The computational performance of the granular model is also much worse than that of the Hibler-type model. Using 500 outer-loop iterations within the granular model the model integration takes about three times as long as when using the Hibler-type model.

Chapter 5

Fast ice in 1997–98

5.1 Introduction

Land-fast ice is a prominent feature of the Kara Sea ice regime. Mid-winter it is present along the entire Kara Sea coast, but the largest fast-ice extent can be seen between Severnaya Zemlya and the Siberian coast. Volkov et al. (2002) have compiled a comprehensive overview of fast ice formation in the Kara Sea. According to it land-fast ice starts forming in October, December and reaches its maximum width and thickness in April, May. By that time the fast ice boundary tends to follow certain isobaths; between the 10 and 15 m ones in the south-western part of the sea and the 20 and 25 m ones in the north-eastern Kara Sea. A notable exception is the Severozemelsky region (between Severnaya Zemlya and the Taymyr Peninsula) which is typically covered with fast ice during winter, independent of depth. The summer fast-ice breakup usually begins in the last 10 days of June in the south-western Kara Sea while moving east and north the breakup occurs later. In the extreme north-eastern part the last of the fast ice breaks up in mid August, on average.

The extent of the fast-ice cover in the Kara Sea is very variable, especially in the north-eastern part. Divine et al. (2003, 2004) showed that fast ice in the north-eastern Kara Sea undergoes significant seasonal and inter-annual variations. Divine et al. (2005) then showed that this variability in the Severozemelsky region is mostly discrete and that the ice cover in the region primarily occupies one of the three modes shown in figure 5.1. More than one mode may be visible each winter, but there is usually one prevalent mode for the entire winter. These modes can be linked to the prevailing atmospheric circulation patterns (Divine et al., 2005) as well as following a chain of islands in the region, indicated in figure 5.1.

Of these modes the so called S-mode is the smallest, and most common. It extends from Severnaya Zemlya to the Sergey Kirov Islands and from there to Sterlegova Cape (see figure 5.1). The L_1 and L_2 modes can be

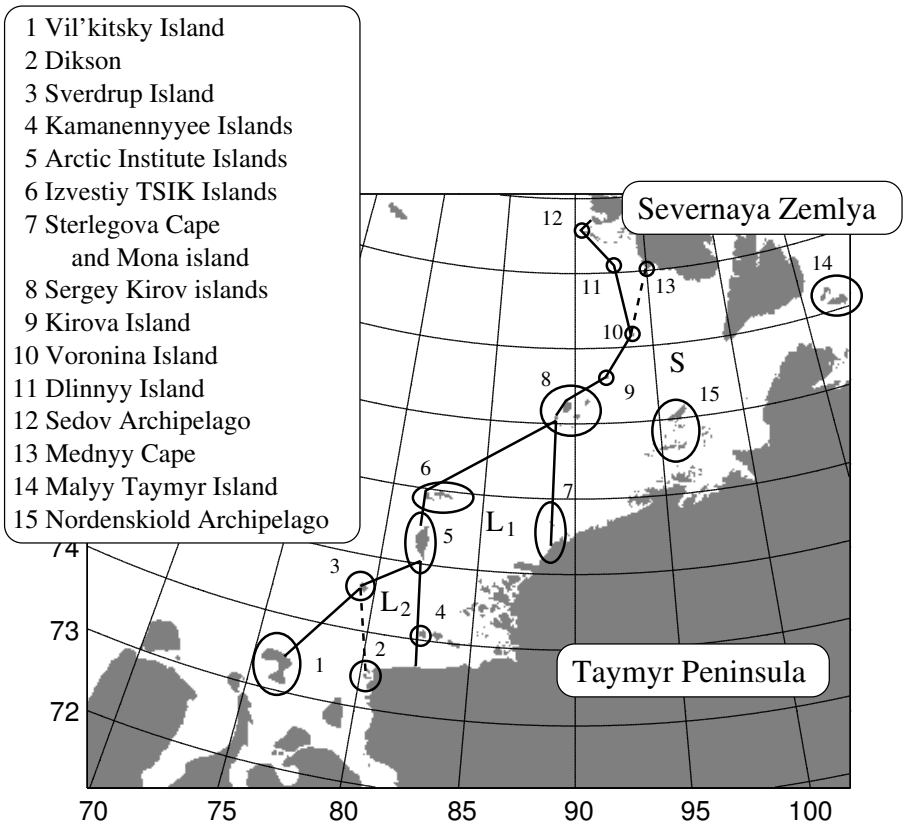

Figure 5.1: The Severozemelsky region. The lines indicate the typical extent of fast ice for S, L_1, and L_2-modes according to Divine et al. (2005), with the dashed lines showing smaller S and L-mode variants. Islands and capes important for the fast ice formation are encircled.

considered extensions of the S-mode and they only form once the S-mode has been established. When in L_1-mode the fast ice extends from the Sergey Kirov Islands to Izvestiy TSIK Islands and the Arctic Institute Islands and from there onto the coast midway between Dikson and the Pyasina delta through the Kamanennyyee Islands. In L_2 mode the fast ice extends from the Arctic Institute Islands to Sverdrup Island and from there to Dikson or Vil'kitsky Island.

In the following it will be shown that much of the land-fast ice formed in the Kara Sea can be modelled in a realistic setup using the viscous-plastic sea-ice model introduced in chapter 2. The common elliptic yield curve is tested along with the granular model and the cohesive yield curves from chapter 2. We also consider how variations of the relevant parameters for these yield curves affect the final solution. For validation the model results are compared to satellite data showing flaw polynya formation and ice charts produced by the Arctic and Antarctic Research Institute (AARI). In the discussion that follows the weak and strong points of the model are considered. In particular it is discussed why some setups give better results than others. An attempt is then made to use this knowledge to better understand how fast ice forms and how best to model it. The effects of using different atmospheric forcing are also discussed. Finally a grounding parametrisation is suggested and model results using it are analysed.

5.2 Observational data

5.2.1 Russian ice charts

The Arctic and Antarctic Research Institute (AARI) and the National Snow and Ice Data Center (NSIDC) have jointly published sea-ice charts produced by the AARI from 1933 to 2006 (Arctic and Antarctic Research Institute, 2007). The charts were produced for safety of navigation in the polar regions and for other operational and scientific purposes. They show ice concentration for multi-year ice, first year ice, new/young ice and land-fast ice. Historically the charts were compiled from many different sources, but the latest charts (i.e. after 1996) are mostly derived form satellite observations. In addition to the satellite observations shipborne observations as well as observations from polar meteorological stations and air reconnaissance flights were used to compile the charts.

Chart coverage and frequency varies, but for most of the series charts were compiled every 10 days during the navigation season, and monthly for the rest of the year. Most of the time a single chart will cover a given 10 day period, i.e. days 1–10, 11-20 of each month and day 21 until the end of the month . Sometimes more than one chart is given for each period, in which case indication is given whether majority of the data in the chart was collected early or late in the observation period. The more recent charts

(i.e. after 1996) usually cover more area than the older ones and are more frequent.

The AARI charts will be our primary source of data for model verification, being the only available fast ice data set for the region. In this particular study the focus will be on a single winter only. This should be chosen from the later part of the data set (i.e. after 1996) since the temporal resolution and the spatial cover is better for that period. We choose to focus on the first full winter in this period; i.e. 1997–98.

5.2.2 Satellite polynya data

The satellite derived polynya data used here is the same as that used in Kern et al. (2005). Open water and thin-ice extent of a polynya is estimated using the Polynya Signature Simulation Method (PSSM) developed by Markus and Burns (1995) and Hunewinkel et al. (1998). The PSSM is based on Special Sensor Microwave/Imager (SSM/I) brightness temperature polarisation ratios at frequencies of 37 and 85 GHz.

This PSSM data is available from the beginning of October through May and as such covers most of the fast-ice period. The SSM/I data come from polar orbiting Defense Meteorological Satellite Program (DMSP) satellites. The data for the Kara Sea for the winter 1997–98 was generally recorded a few hours after midnight or a few hours before noon.

Although the PSSM data does not show fast ice directly, it is useful in this context as it shows clearly flaw polynyas that form downwind of the fast ice. The data therefore affords us a verification of the AARI fast-ice data, when the meteorological conditions are right. This is also the time when it is easiest to check the model results for the presence of fast ice. In addition this data can of course be used to estimate the model's skill in simulating the formation of flaw polynyas.

5.2.3 Overview of the winter 1997–98

Since the focus will now be on the winter 1997–98 this section will consider the atmospheric conditions and observed fast ice in that period. In particular the monthly mean sea level pressure from the NCEP reanalysis data will be used to try and get a clear picture of the atmospheric influence. We will then also consider the AARI ice charts and show how fast ice in the Severozemelsky region forms in winter and breaks up in summer.

Considering first the atmospheric forcing, figure 5.2 shows the monthly mean sea level pressure for the period from December 1997 to July 1998. In December the mean sea level pressure is dominated by a low pressure zone over the central Kara Sea. Since sea ice in free drift drifts approximately along isobars it would seem that the atmospheric pressure in December does not favour fast ice formation in particular, with the ice being herded

away from the Taymyr Peninsula towards Severnaya Zemlya or out into the northern part of the Kara Sea. In January the low deepens and moves just west of Novaya Zemlya resulting in stronger offshore winds of the Taymyr Peninsula. The mean wind direction is such that one would expect fast ice formation, at least in the northern part of the Severozemelsky region, possibly with occasional breakups as the wind blows ice in and out of the region.

February is a period of calm winds in the Severozemelsky region, while in March easterly winds start to blow, growing stronger in April. This period of easterly winds should prevent further fast ice growth and is likely to produce large flaw polynyas of the fast ice. This also coincides with the period of mean maximum fast-ice extent. It turns out that flaw polynyas forming during this period can be seen in the PSSM data discussed earlier. A particularly large flaw polynya forms in the period of April 12–19.

The May average then shows another calm period, which lasts through June. In July a broad high sits in the central Kara Sea resulting in weak onshore winds in the Severozemelsky region. According to Volkov et al. (2002) the Severozemelsky fast ice may start breaking up in June, the last of it breaking up in the middle of August. In June and July of 1998 calm winds blow in the Severozemelsky region and perhaps because of this the fast ice only starts breaking up in the middle of July, that year.

The temporal evolution of the fast-ice cover can be visualized by studying the AARI observations. In figure 5.3 the left panel shows the observation period when stable land-fast ice is first observed and the right panel shows the last observation period in which fast ice is observed in summer. According to the observations fast ice in the Severozemelsky region forms in two discrete jumps in 1997–98. Initially fast ice forms inland of the Nordenskiöld Archipelago during the November 1–10 observation period, growing only slightly after the initial formation. The January 1–10 observation then shows a fully formed S-mode fast ice massive. It is subject to some minor partial breakups and recoveries, but remains, mostly unaltered, until the summer breakup.

Summer breakup of the Severozemelsky fast ice massive occurs in the period from July 11^{th} to August 11^{th}, after which no fast ice is observed in the region. Fast ice in the Vilkitsky Strait breaks up first, followed by the rest of the Severozemelsky fast ice massive offshore off the Nordenskiöld Archipelago. The fast ice inland of the Nordenskiöld Archipelago is the last to break up at the beginning of August, having remained land fast for 9 months.

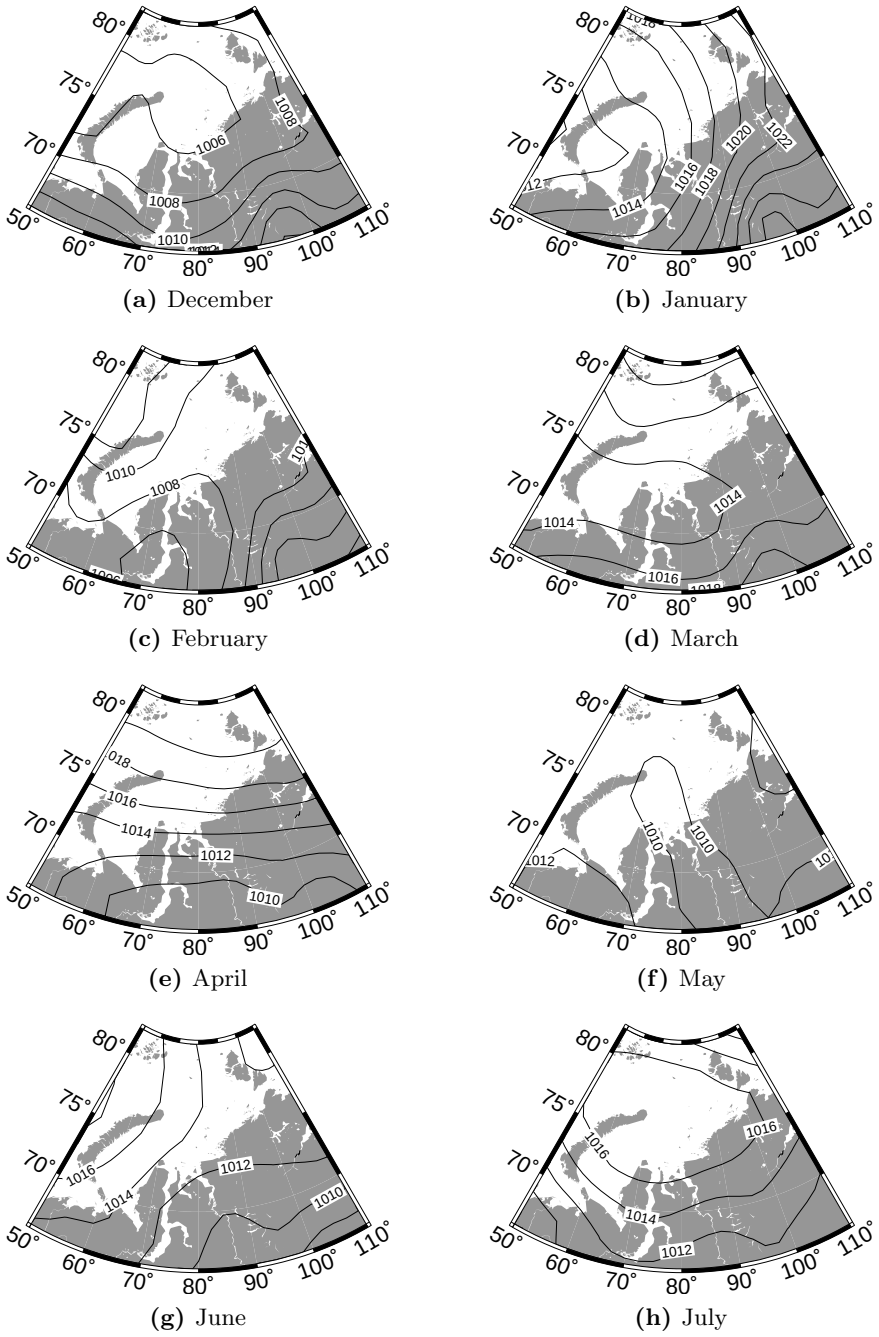

(a) December **(b)** January

(c) February **(d)** March

(e) April **(f)** May

(g) June **(h)** July

Figure 5.2: The monthly mean sea level pressure from December 1997 to July 1998.

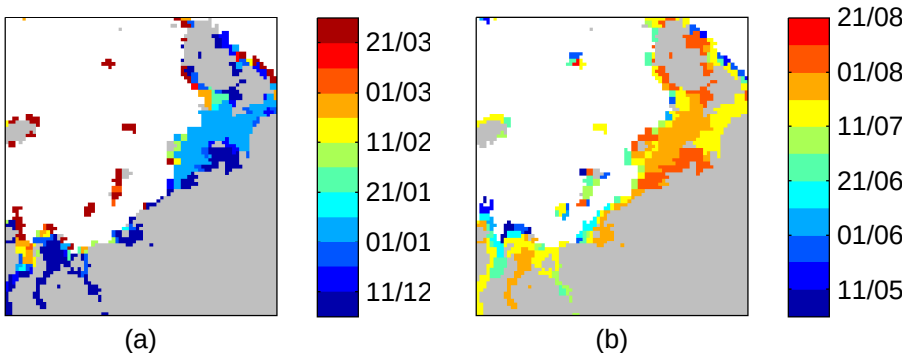

Figure 5.3: The time of onset and break up of fast ice in the Severozemelsky region according to the AARI observations: (a) the observation period when stable fast ice is first observed in winter and (b) the observation period when fast ice is last observed in summer.

5.3 Experiments

In this section a series of experiments using different yield curves are described. These are the elliptic, flexible modified Coulombic (FMC), curved diamond and trimmed ellipse yield curves, in addition to the granular model. For each experiment the model is initialised using the model state of the control run from section 4.3 on October 5$^{\text{th}}$ 1997. On that date the modelled global mean ice concentration is 0.01, close the summer minimum and the role of ice dynamics should therefore be at minimum. All model runs use 500 outer loop iterations, $\zeta_{\min} = 0$ and $\zeta_{\max} = (10^{13}\text{ s})P$, except when stated otherwise. All runs are also forced using the NCEP/NCAR atmospheric reanalysis data, unless otherwise specified.

The results using each model formulation are compared to the observed fast ice extent and breakup times as well as the PSSM polynya data for verification. In this section the tunable parameters of each curve are tuned to give the best correspondence with observations. The results are then discussed in more detail in section 5.4.

5.3.1 Elliptic yield curve

The first yield curve considered is the elliptic yield curve proposed by Hibler (1979), but with the changes in the momentum solver described in section 2.2.1 and using 500 outer-loop iterations. Additionally the maximum bulk viscosity allowed is $\zeta_{\max} = (10^{13}\text{ s})P$. This is considerably larger than the maxima suggested by Hibler (1979) and Hunke and Dukowicz (1997), but it will be shown below that choosing a high maximum on the bulk viscosity is necessary in order to be able to model fast ice. When these settings are

used realistic fast ice appears in the model.

In the control run the yield curve axis ratio is set to $e = 2$ and no biaxial cohesion is included. Having described the results from the control run experiments with variable number of outer loops and variable maximum viscosity are outlined. This is then followed by the results of experiments where the focus is on changes in the ellipse eccentricity and the addition of biaxial cohesion.

Control run

We now consider the well established elliptic yield curve with $e = 2$, using 500 outer loops and $\zeta_{\max} = (10^{13}\text{ s})P$. Aside from the large number of outer loops and large $\zeta_{\max}$ this configuration is the same as what is seen for the vast majority of viscous-plastic models today. It is therefore referred to here as the control run and all other experiments should be considered as an attempt to improve the control run results.

In order to visualise the temporal evolution of fast ice in the model figure 5.4 shows the day on which the land-fast ice becomes stable. The figure is made by walking through the daily model output and noting the date if the ice is moving with a velocity greater than the outer-loop target error $\epsilon_{\text{OL}} = 0.1$ mm/s. This way a map is produced showing the last day on which the ice is mobile. The next day after that is then considered the day on which land-fast ice becomes stable. It is important to consider model output well into the winter to ensure that all fast-ice formation is captured. It is also important to stop the procedure on a day where as much of the drifting ice is moving as possible. When producing figure 5.4 the period from November 1$^{\text{st}}$ through April was considered, ignoring any ice that stops moving after March 31$^{\text{st}}$.

Focusing on the Severozemelsky region we see fast ice formation as early as the beginning of November in Pyasina Bay and inland of the Nordenskiöld Archipelago. This fits well with the AARI observations, but the extent of stable fast ice inland of the Nordenskiöld Archipelago is too small, not reaching the largest of the islands.

According to the AARI observations S-mode fast ice forms in the January 1$^{\text{st}}$–10$^{\text{th}}$ observation period. In the model signs of S-mode fast ice forming can be seen as early as December 18$^{\text{th}}$ and by December 20$^{\text{th}}$ S-mode fast ice is clearly established. It remains mostly stable, with occasional partial breakups until January 24$^{\text{th}}$ when it breaks up completely. On February 3$^{\text{rd}}$ the fast ice appears to have reformed, but it still suffers a partial breakup which is mostly recovered by February 22$^{\text{nd}}$ and a smaller partial breakup recovered by March 4$^{\text{th}}$.

After the partial breakups in March the modelled fast ice remains stable until May 19$^{\text{th}}$, despite a number of storms passing through the region. The best example of this is the period of strong offshore winds in the Severoze-

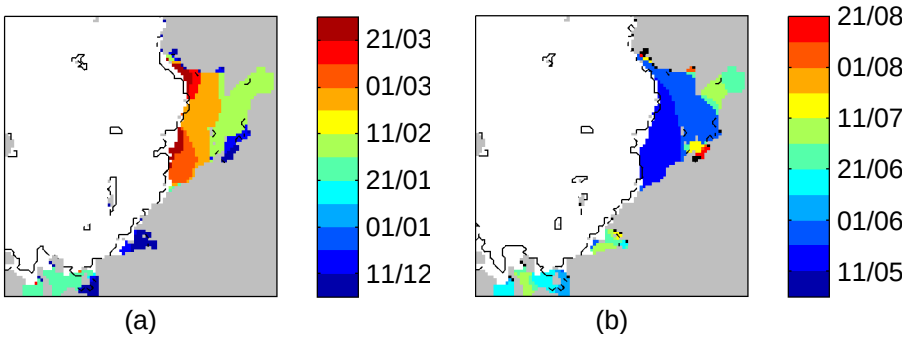

Figure 5.4: Results from the control run: (a) The day land-fast ice becomes stable in winter and (b) the day of (first) fast ice breakup in summer. The solid lines mark the fast-ice extent according to the AARI data for the first observation period in (a) April and (b) May. In the white areas no fast ice is formed and the black patches in panel (b) mark areas of fast ice that survives beyond August 21st.

melsky region from April 9th to 15th. During this time a large flaw polynya opens up which is clearly visible in the PSSM data. This is also clear in the model output, where the thick ice in the western part of the Severozemelsky region breaks apart from the fast ice and new ice forms in the opening. Figure 5.5 shows the modelled ice thickness and ice cover fraction on April 14th, overlaid with the PSSM data.

Comparing the model results with the PSSM data during this period shows generally good agreement between the two. There is clearly a flaw polynya forming in the model and its location is mostly within the area of the observed newly formed ice. An exception is the thick ice modelled between the Arctic Institute Islands and the Taymyr coast where newly formed ice is observed by the satellite. For reference one can assume that PSSM labelled thin ice is not much thicker than about 30 cm, but thicker ice may be reported as thin ice if the concentration is low (Stefan Kern, personal communication).

On May 19th and 21st the modelled S-mode fast ice breaks up completely, but reforms again about a week later. This is followed by a few breakups and reformations, but the final breakup comes on June 23rd, after which fast ice does not appear in the model again during the model run. This final breakup is approximately one month too early, compared to the AARI observations.

It is instructive to consider how the fast ice breaks up in two of the early breakups; from January 20th to 25th and from May 17th to 22nd. Figure 5.6 shows the ice speed as well as the wind during the first period. On January 20th there is a sharp gradient in the ice speed, clearly indicating

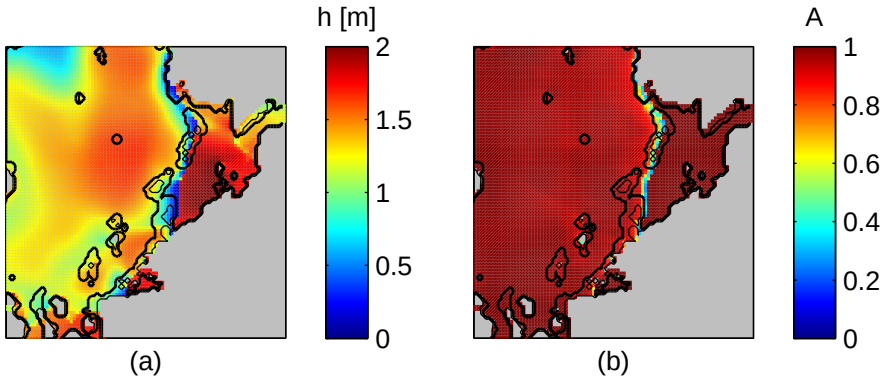

Figure 5.5: Results from the control run: (a) ice thickness (capped at 2 m) and (b) ice fraction. The lines show PSSM data; the thick lines show the extent of newly formed ice and the thin line the extent of open water. The snapshot is taken after the first time step of April 14$^{\text{th}}$.

the fast ice edge. This distinction is clear because of the strong offshore wind blowing almost uniformly in the Severozemelsky region. Some ice movement of $|\vec{v}| \approx 5$ mm/s can already be seen inland of the Sergey Kirov Islands as the fast ice also does not appear to reach those islands completely at this time.

On the following day the low pressure zone that was located in the western Kara Sea has moved onshore near Dikson island causing a divergent wind field in the western part of the fast ice massive. Since the elliptic yield curve only supports very limited cohesion under biaxial divergence the fast ice subjected to the divergent wind stress breaks up. The breakup is probably facilitated by the fact that the fast ice does not reach the Sergey Kirov Islands at the start of the period. This prevents an arch from forming between the Sergey Kirov Islands and Cape Sterlegova, which would presumably strengthen the fast ice.

Following this partial breakup another low pressure zone passes through the Kara Sea on January 23$^{\text{rd}}$, travelling from south-west to north-east. As the low passes north of Severnaya Zemlya the fast ice massive collapses under mostly compressive strain, although shear strain also plays an important role. The breakup is initiated by high shear stress near the Kirova Island, breaking the arch which connects it and Voronina Island. Later it also breaks the arch between the Voronina and Dlinnyy Island. As the low moves north-east the wind turns onshore and the rest of the fast ice collapses under the resulting compressive strain.

The effects of shear strain can be seen more clearly in the May breakup, shown in figure 5.7. In this case the wind stress is always convergent in the

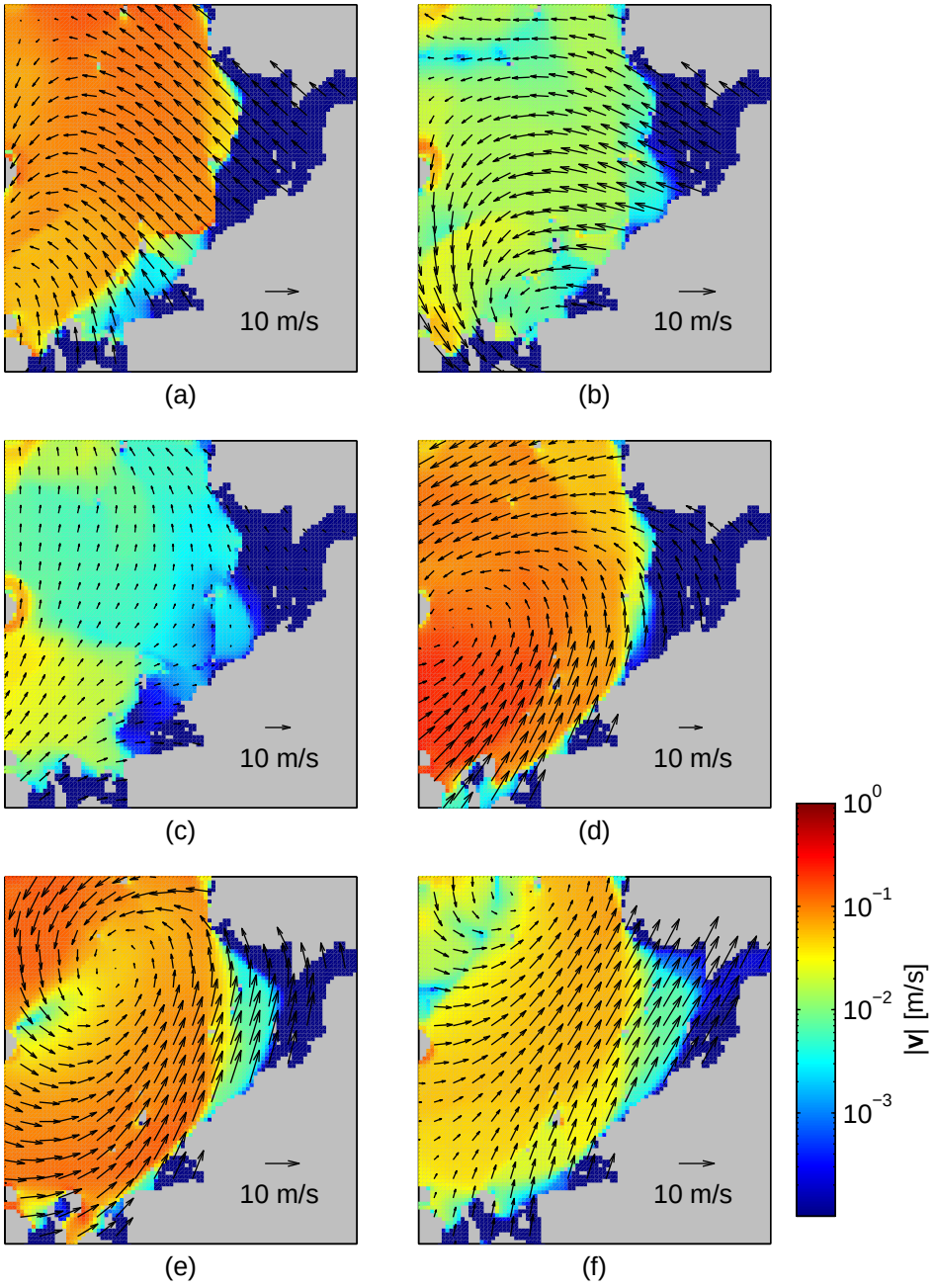

Figure 5.6: The figure shows ice speed in the control run (colour, logarithmic scale) and the applied wind velocity (arrows). Each panel shows the first time step of: (a) January 20$^{\text{th}}$, (b) January 21$^{\text{st}}$, etc.

Severozemelsky region, but it exerts strong shear strain on the ice. This causes a small partial breakup on the 18$^{\text{th}}$ and the rest of the ice to break up on the 21$^{\text{st}}$. The first breakup is initiated when the fast ice breaks away from the Sergey Kirov Islands, but as figure 5.4 shows the fast ice there is never properly established. The fast ice is temporally re-established on the 20$^{\text{th}}$, but the arrival of a second low pressure zone in the region breaks the arch between Voronina and Dlinnyy Islands. Following that the rest of the fast-ice massive then collapses.

From the results presented in this section it is evident that modelling fast ice using the elliptic yield curve is, to some extent, possible. So far a large number of outer loop iterations and a large value for the maximum viscosity have been used, but the following sections go into more detail about the effects of changing these settings. Overall, it seems clear that the modelled ice is weaker than the actual ice, since multiple partial breakups, not observed in the AARI data, have been catalogued here. These modelled breakups last long enough so that they should have been picked up by the observations, were they real.

Number of outer loops

It has already been stated that both the number of outer loops as well as the maximum viscosity should be high, compared to the customary values. Now that it's been shown that fast ice can, to some extent, be modelled using the elliptic yield curve with a large number of outer loops and large maximum viscosity values the effects of these two parameters will be studied in more detail.

Starting with the number of outer loops it is instructive to compare the results from using 500 outer loops to the result when using one pseudo time step. It has already been shown in section 4.4 that using one pseudo time step results in larger outer-loop errors, but we will now consider where these errors are located and if they affect the fast ice formation.

As a concrete example let us consider a snapshot from April 14$^{\text{th}}$. We've seen before that there is a sharp distinction between land-fast ice and drift ice at that time, but with respect to the location of errors the situation is quite typical. Figure 5.8 shows the ice velocity using one pseudo time step and the difference in velocity between using one pseudo time step and using 500 outer-loop iterations. This is the best measure available of the error incurred when using one pseudo time step, compared to a fully converged solution. Note that after this particular time step the solver had reached full convergence in the control simulation; i.e. the outer-loop error was less than $\epsilon = 0.1$ mm/s.

The first thing to note is that we still see some fast ice in the Severozemelsky region, although the total area is only a fraction of the area modelled using 500 outer loop iterations. Using one pseudo time step gives

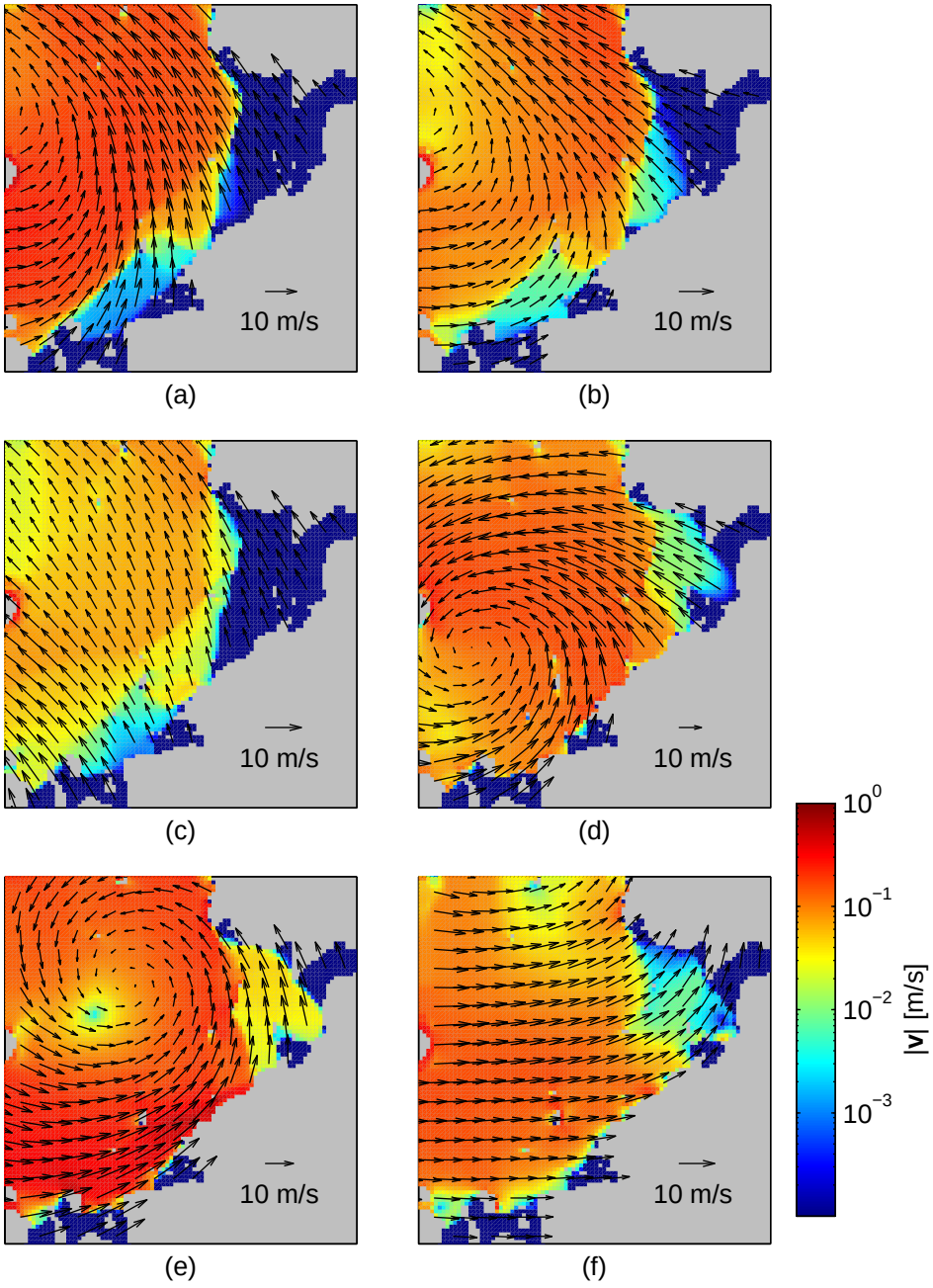

Figure 5.7: The figure shows ice speed in the control run (colour, logarithmic scale) and the applied wind velocity (arrows). Each panel shows the first time step of: (a) May 18^{th}, (b) May 19^{th}, etc.

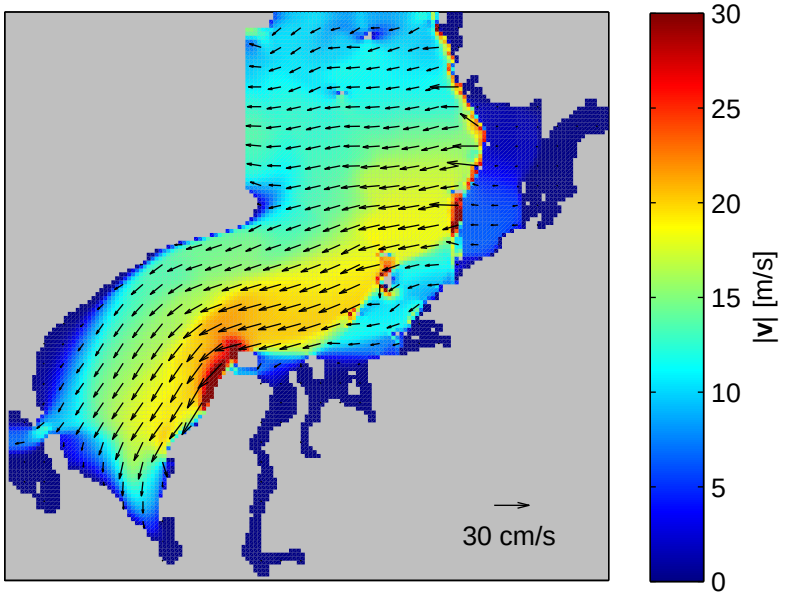

(a)

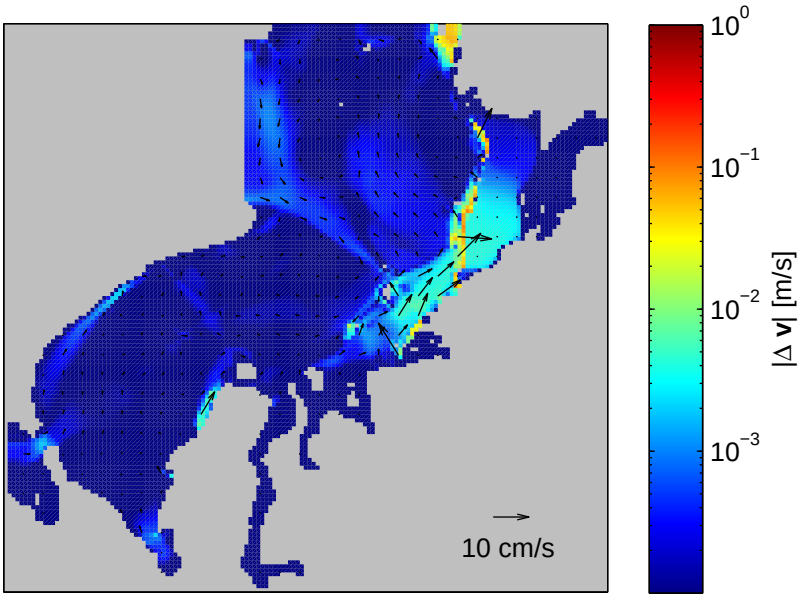

(b)

Figure 5.8: Speed, velocity in the entire model domain using one pseudo-time step: (a) speed and velocity using one pseudo-time step and (b) speed and velocity difference between using one pseudo-time step and 500 outer loops. The snapshot is taken after the first time step of April 14^{th}.

S-mode fast-ice area of $A_S = 35,700$ km^2, while using 500 outer loops gives $A_S = 82,100$ km^2. Both fall short of the observed value of $A_S = 88,800$ km^2, but using 500 outer loops gives a considerable improvement.

The ice velocity is very low in approximately half the S-mode area and we can verify that it's below the target error for 500 outer loops by looking at the model error in the same area (figure 5.8). In the rest of the S-mode area the ice moves at speeds up to 5 cm/s. Taking a closer look at the model errors we see there are two areas where there are considerable errors, while in much of the model domain the error is less than 1 mm/s.

Large errors exist at the fast-ice edge on one hand and inland of a line connecting the Sergey Kirov Islands, Arctic Institute Islands and Vil'kitsky Island, out of Yenisey Bay on the other. The former is the result of a difference in the placement of the fast-ice edge. In the control run the fast ice edge follows the Voronina and Kirova Islands, but using one pseudo time step the ice extends a few grid points beyond the islands. The second error region coincides mostly with the L-mode region. Here the ice speed when using one pseudo time step is approximately half that when using 500 outer-loop iterations. In this region the ice floes through a relatively narrow pass between the Arctic Institute Islands and the mainland. This is an area that was found to be problematic in the control run. Ice would flow too slowly through it causing it to grow too thick and prevent the observed new-ice formation to be properly modelled. Using one pseudo time step this problem is exacerbated with very limited new-ice formation occurring between the Sergey Kirov Islands and Sterlegova Cape (not shown).

Using one pseudo time step does therefore neither give as good fast-ice nor drift-ice results as using 500 outer loops. Having thus shown that using one pseudo time step is not sufficient the question arises of how many outer loop iterations are required to properly model fast ice. To try and answer this figure 5.9 shows the fast-ice area at the start of April as a function of the number of outer loops. The fast-ice area was calculated using the same method as used for making the fast-ice evolution figures. For this comparison the model was run with model time step of $\Delta t = 300$ s as well as $\Delta t = 600$ s (the value used in all other runs).

There is no clear trend to be seen in the figure; rather the model results seem to fluctuate somewhat randomly between $A_S = 67,900$ km^2 and $A_S = 82,800$ km ^{2}. Using 50 outer loops and $\Delta t = 600$ s results in fast-ice area of $A_S = 82,800$ km^2, 700 km^2 more than when when using 500. For intermediary number of loops the fast-ice area fluctuates between 69,300 km^2 and 81,400 km^2. The smallest value simulated here is $A_S = 67,900$ km^2, which occurs for $n_{\mathrm{OL}} = 150$ and $\Delta t = 300$ s. For a larger number of outer loops the model appears to stabilise somewhat, but a jump of 700 km^2 going from 450 to 500 outer loops at $\Delta t = 600$ s indicates that even using such a large number of outer loops the model has not reached a completely stable state. Using a smaller model time step does improve stability at larger n_{OL},

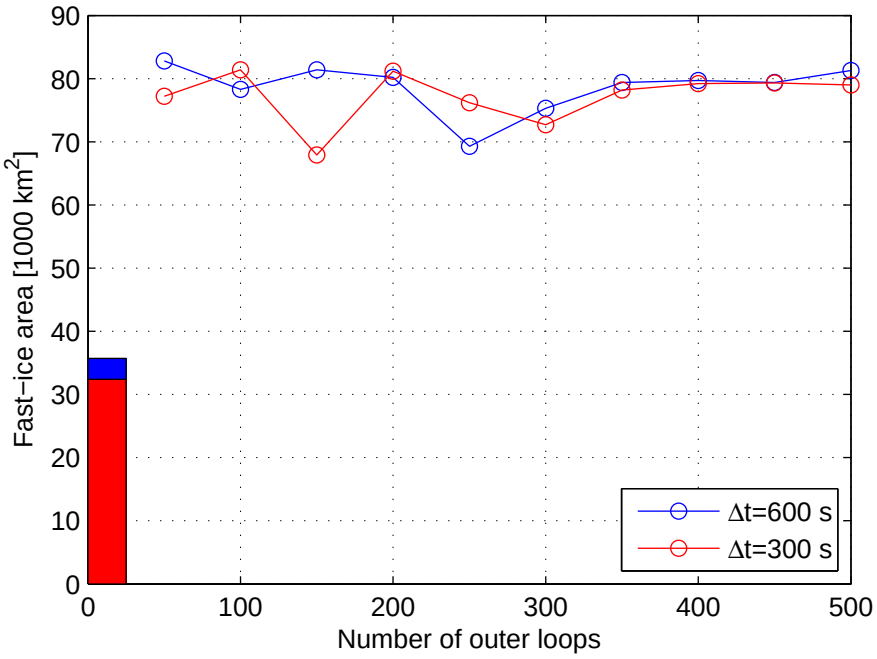

Figure 5.9: Modelled fast-ice area at the start of April as a function of the number of outer loops using two different model time steps. The bar in the left corner shows the fast-ice area modelled using one pseudo time step.

but the random fluctuations remain at low n_{OL}.

The results presented here show that while using one pseudo time step is not a robust method for modelling fast ice, relatively small number of outer loops appear to be sufficient to produce some fast ice. The model appears to stabilise as the number of outer loops grows, but even at $n_{\mathrm{OL}} = 500$ some fluctuations in the fast-ice area remain.

Maximum viscosity

At small strain rates a plastic solution cannot be found and linear viscous deformation takes place, instead of a plastic one. The limit at which this occurs is set by the maximum (bulk) viscosity, $\zeta_{\max}$, which Hibler (1979) set as $\zeta_{\max} = (2.5 \times 10^8 \text{ s})P$. This value was chosen to be large enough to be rarely reached and not to significantly affect the computations (Hibler, 1979). This choice seems to have gone largely unchallenged although Hunke and Dukowicz (1997) chose to use $\zeta_{\max} = (2.5 \times 10^{10} \text{ s})P$ in their elastic-viscous-plastic model. In this section we will examine what value for $\zeta_{\max}$ is suitable for fast-ice modelling.

To accomplish this a set of experiments was run, with the same setup as the control run, except now $\zeta_{\max}$ was changed from $(10^8 \text{ s})P$ to $(10^{17} \text{ s})P$ in steps where $\zeta_{\max}$ was increased by factor 10 for each step. For each experiment the fast-ice extent in April was calculated using the same method as used for making the fast-ice evolution figures. The total fast-ice area is then shown in figure 5.10 as a function of $\zeta_{\max}/P$.

Some fast ice can already be seen at $\zeta_{\max} = (10^8 \text{ s})P$ but as $\zeta_{\max}$ grows the fast-ice extent grows sharply. It plateaus at $A_S \approx 30,000 \text{ km}^2$ for $10^9 \text{ s} \leq \zeta_{\max}/P \leq 10^{11}$ s, but grows again sharply for larger $\zeta_{\max}$, plateauing again at about $A_S \approx 82,000 \text{ km}^2$ at $\zeta_{\max} \approx (10^{13} \text{ s})P$. At $\zeta_{\max} = (10^{16} \text{ s})P$ there is a very slight decline in the modelled fast-ice area. For much larger values ($\zeta_{\max} \gtrsim (10^{20} \text{ s})P$, not shown) the computed ice area starts to oscillate with the oscillations growing larger and more rapid with larger $\zeta_{\max}$. For $\zeta_{\max} \geq (10^{26} \text{ s})P$ the fast-ice area oscillates between $A_S \approx 75,000 \text{ km}^2$ and $A_S \approx 80,000 \text{ km}^2$ for each tenfold increase in $\zeta_{\max}$.

In general it is preferable to keep the maximum viscosity as low as possible, since this makes the equation of motion easier to solve. The lowest feasible value for $\zeta_{\max}$ should therefore be chosen. In this case it is $\zeta_{\max} = (10^{13} \text{ s})P$, giving fast-ice extent close to the observed value of $88,800 \text{ km}^2$.

Modified eccentricity

Dumont et al. (2009) showed that an elastic-viscous-plastic model with the elliptic yield curve can be used to model ice bridges in a limited fashion. They also showed that the ellipse eccentricity plays an important role in

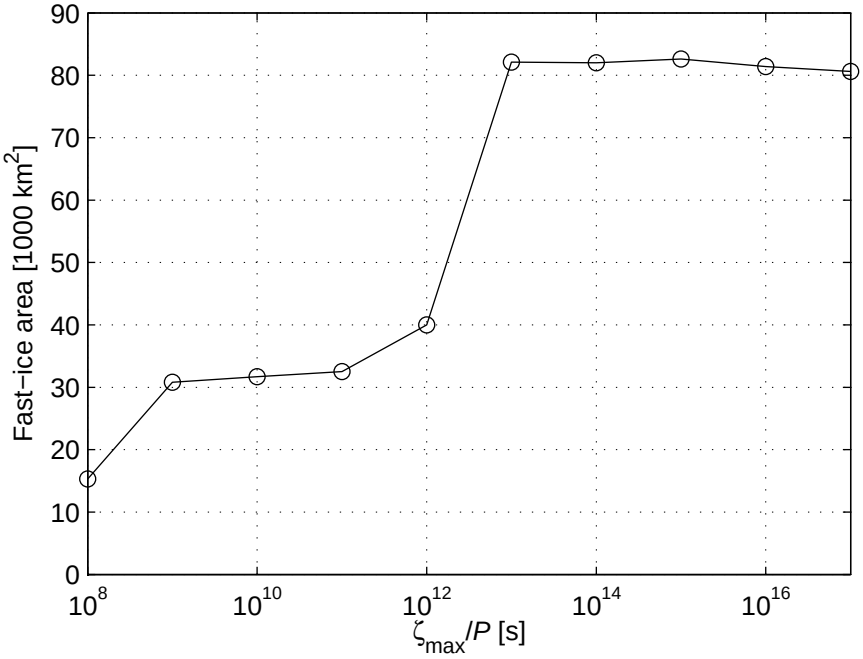

Figure 5.10: Modelled fast-ice area at the start of April as a function of the maximum viscosity ($\zeta_{\max}/P$).

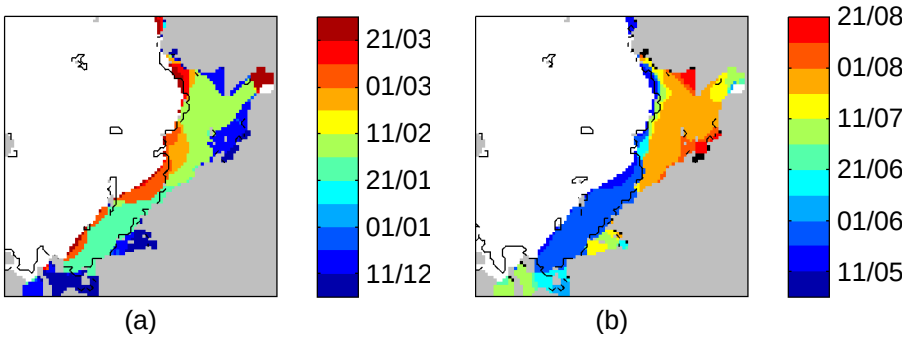

Figure 5.11: Results from using the elliptic yield curve with $e = 1.4$: (a) The day land-fast ice becomes stable in winter and (b) the day of (first) fast ice breakup in summer. The solid lines mark the fast-ice extent according to the AARI data for the first observation period in (a) April and (b) May. In the white areas no fast ice is formed and the black patches in panel (b) mark areas of fast ice that survives beyond August 21$^{\text{st}}$.

such a simulation. Decreasing the axis ratio, e, results in larger uniaxial compressive strength, increasing the potential for arching. In this section the case of smaller axis ratios will be considered.

Testing e from $e = 1.4$ to $e = 1.9$ at intervals of 0.1 shows a marked change related to the change in the yield curve shape. At $e = 1.4$ the ice strength is greatly increased, compared to $e = 2$, resulting in an erroneous L-mode appearing in late January, breaking up in May (see figure 5.11). Using such a small value for e, however, also prevents the May breakup of the S-mode fast ice with most of it breaking up in late July, same as the AARI observations show. On the other hand, the partial breakup in February still occurs with $e = 1.4$. Using $e = 1.5$ does not prevent the May breakup, but still results in an erroneous L-mode.

Taking a closer look at the $e = 1.4$ simulation we now consider the ice thickness and concentration on April 14$^{\text{th}}$, shown in figure 5.12. The modelled flaw polynyas and new-ice formation between the Vil'kitsky and Sergey Kirov Islands coincides with an L_2-mode fast-ice configuration, consistent with the fast-ice extent figure presented before (figure 5.11). This is, however, inconsistent with the PSSM data and AARI observations which clearly shows an S-mode configuration at that time.

A more drastic discrepancy is an unrealistic polynya that opens up in the model. It stretches due north of the Sergey Kirov Islands towards Ushakova island, located at the northern edge of the figure. This large feature should be considered very unrealistic since it is neither observed on this particular date nor any other date covered by the 1997–98 PSSM data. Also, Kern (2008) gives an overview of polynya formation in the Kara Sea during the

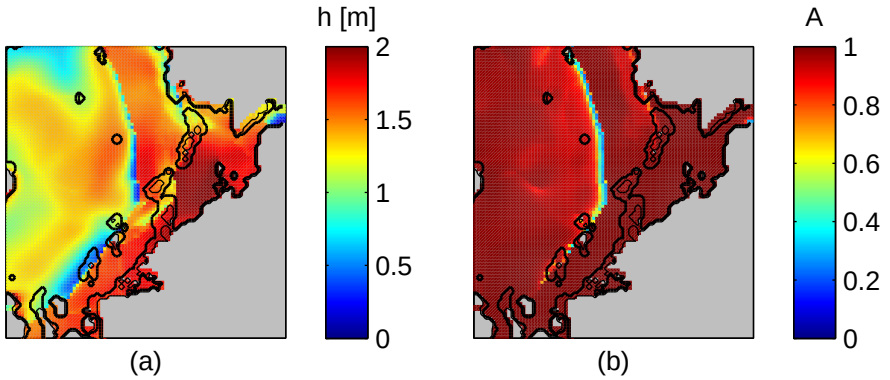

Figure 5.12: Results from using the elliptic yield curve with $e = 1.4$: (a) ice thickness (capped at 2 m) and (b) ice fraction. The lines show PSSM data; the thick lines show the extent of newly formed ice and the thin line the extent of open water. The snapshot is taken after the first time step of April 14^{th}.

years 1979–2003 where the polynya distribution for 1995–2004 is shown in particular (his figure 3). A polynya such as the one discussed here never appears in those figures so it is safe to assume that this feature does not occur in reality.

Decreasing the ellipse eccentricity therefore clearly affects the modelled land-fast ice and decreasing it to $e = 1.4$ prevents the early May breakup. Unfortunately it also affects the drift ice causing more land-fast ice to form than observed. Tuning the ellipse eccentricity therefore presents us with the choice of correctly modelling either the fast-ice extent or the breakup time.

Cohesion under isotropic divergence

The modifications to the elliptic yield curve suggested by König Beatty and Holland (2010) and discussed in section 2.4.5, allow for adding cohesive strength under isotropic divergence to the elliptic yield curve. This is desirable since we can safely presume that real fast ice has cohesive strength under isotropic divergence. Using this approach increasing the cohesive strength under isotropic divergence also increases the uniaxial compressive strength. König Beatty and Holland (2010) assumed the ratio between cohesive and compressive strength to be $k_T = 1$, but initial tests showed that for the current setup k_T should be about an order of magnitude smaller. To test the model response model runs with k_T from $k_T = 0.01$ to $k_T = 0.10$ at intervals of 0.01 were run.

Using a large enough value for k_T can prevent the May breakup, but not the January or February breakups. Figure 5.13 shows the formation date of

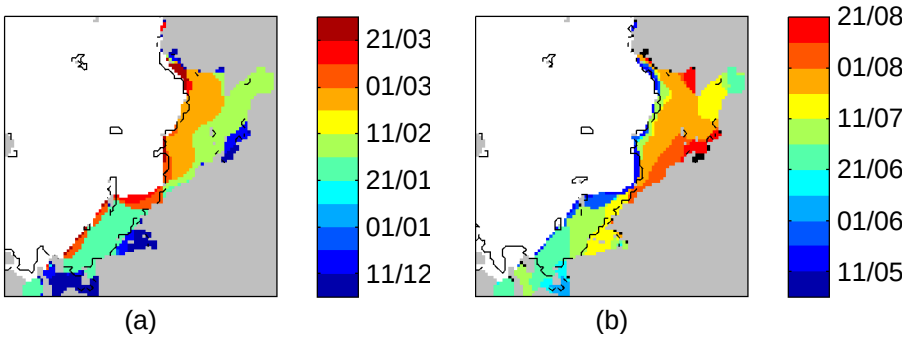

Figure 5.13: Results from using the elliptic yield curve with $k_T = 0.09$: (a) The day land-fast ice becomes stable in winter and (b) the day of (first) fast ice breakup in summer. The solid lines mark the fast-ice extent according to the AARI data for the first observation period in (a) April and (b) May. In the white areas no fast ice is formed and the black patches in panel (b) mark areas of fast ice that survives beyond August 21$^{\text{st}}$.

stable fast ice and the breakup date for a model simulation with $k_T = 0.09$. This is the lowest of the values tested that is large enough to prevent the May breakup. As the figure shows an artificial L-mode appears in the model. Using $k_T = 0.07$ is not large enough to prevent the May breakup, but still large enough to cause an artificial L-mode to appear.

Considering the ice thickness and concentration on April 14$^{\text{th}}$ we see that using $k_T = 0.09$ gives unrealistic results (figure 5.14). A flaw polynya forms along the L-mode boundary between the Vil'kitsky and Arctic Institute Islands. North of that, however, a dramatic change occurs with a polynya opening up stretching practically due north off the fast ice between the Sergey Kirov Islands and the Izvestiy TSIK Islands. This is similar to the erroneous polynya modelled with $e = 1.4$. In order to correctly simulate the polynyas between Severnaya Zemlya and the Sergey Kirov Islands k_T must be set no larger than $k_T = 0.05$. Doing this re-introduces the May breakup.

When adding cohesive strength under isotropic divergence the model therefore suffers in a similar way as when adjusting e. The early breakup in May can be prevented by increasing k, but only at the cost of erroneously producing L-mode fast ice and not simulating drift ice correctly. Simply adding cohesive strength under isotropic divergence in the manner done here does therefore not improve upon the results from the control run.

5.3.2 Modified Coulombic yield curve

In order to try and improve the results of the control run the cohesive yield curves introduced in chapter 2 were tested. First of these is the modified

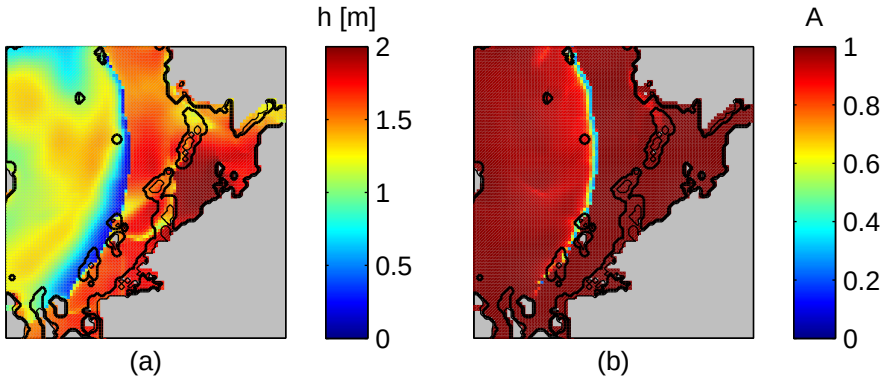

Figure 5.14: Results from using the elliptic yield curve with $k_T = 0.09$: (a) ice thickness (capped at 2 m) and (b) ice fraction. The lines show PSSM data; the thick lines show the extent of newly formed ice and the thin line the extent of open water. The snapshot is taken after the first time step of April 14$^{\text{th}}$.

Coulombic yield curve suggested by Hibler and Schulson (2000) and the flexible variant thereof introduced in section 2.4.6.

In their implementation Hibler and Schulson (2000) used $k_T \approx 0.05$ and $\phi \approx 45°$. These settings do not give enough cohesion to give a realistic amount of fast ice (not shown) and so the FMC was used to test a wider range of parameters. In particular the FMC was tested using $\phi = 30°$ (as suggested by Tremblay and Mysak, 1997) and $\phi = 45°$. Larger values of k_T than the one used by Hibler and Schulson (2000) were also considered.

We first consider $\phi = 30°$. This value gives an axis aspect ratio of 2, the same as used for the ellipse in the control run. We would therefore expect similar results, but larger values of k_T should be required for a fast ice simulation since the Coulombic shape gives smaller uniaxial compressive strength than the elliptic one.

The tests done using $\phi = 30°$ result in fast-ice extent, formation and breakup times similar to those obtained in the control run for $0.15 \leq k_T \leq 0.21$. Larger values of k_T give fewer and smaller partial breakups during the formation phase, but for $k_T = 0.21$ a small fast-ice protrusion extends from the Sterlegova Cape towards the Arctic Institute Islands (see figure 5.15). For $k_T = 0.22$ the normal S-mode fast ice is restored and in addition no May breakup occurs, giving realistic breakup times (see figure 5.16). The realistic breakup time, while still retaining the S-mode is a major improvement from the control run.

Considering the flaw-polynya formation on April 14$^{\text{th}}$ the general trend is for small values of k_T (but $k_T \geq 0.15$ nonetheless) to give more realistic

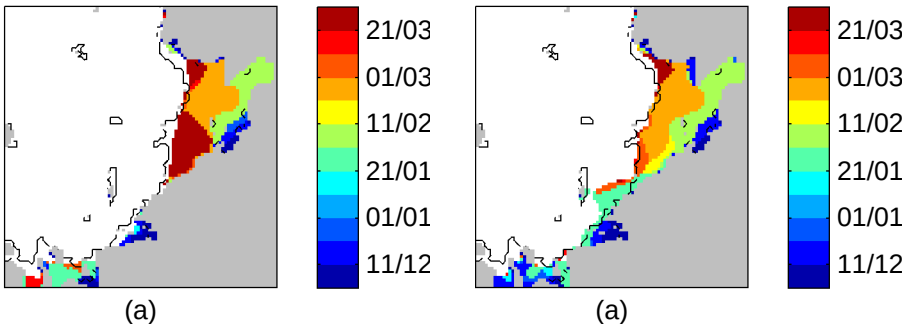

Figure 5.15: Results from using the FMC and $\phi = 30°$. The figure shows the day land-fast ice becomes stable in winter using (a) $k_T = 0.15$ and (b) $k_T = 0.21$. The solid lines mark the fast-ice extent according to the AARI data for the first observation period in April. In the white areas no fast ice is formed.

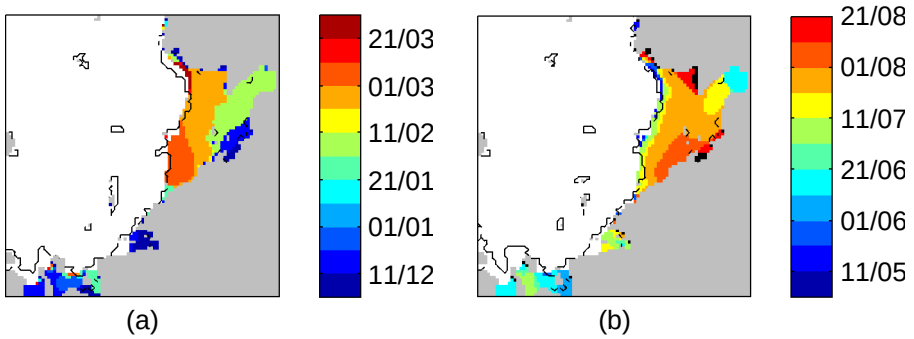

Figure 5.16: Results from using the FMC and $\phi = 30°$ and $k_T = 0.22$: (a) The day land-fast ice becomes stable in winter and (b) the day of (first) fast ice breakup in summer. The solid lines mark the fast-ice extent according to the AARI data for the first observation period in (a) April and (b) May. In the white areas no fast ice is formed and the black patches in panel (b) mark areas of fast ice that survives beyond August 21st.

polynya and new-ice formation, especially inland of the Arctic Institute Islands. Figure 5.17 shows how ice thickness and concentration change when k_T is increased. For $k_T = 0.15$ these fields are very similar to the ones from the control run with realistic polynyas and new-ice formation along the S-mode boundary from Severnaya Zemlya to Sterlegova Cape, but too thick ice inland of the Arctic Institute Islands. The ice inland of the Arctic Institute Islands quickly grows thicker with larger k_T and new ice starts, unrealistically forming offshore off the Arctic Institute and Sverdrup Islands. The S-mode polynyas can still be considered realistic for $k_T = 0.22$

For larger k_T values than the ones already discussed various erroneous fast-ice and polynya patterns can be seen. At $k_T = 0.23$ a polynya forms erroneously extending due north of the Sergey Kirov Islands in a manner very similar that already seen for the ellipse with $e = 1.4$ and $k_T = 0.09$. The ice also breaks up in May again. Larger values still see the model jumping between different states in seemingly random manner, including a formation of the erroneous polynya already described, the formation of either S- or L-modes and with the ice breaking up either in May or late July.

Let us now consider $\phi = 45°$, as suggested by Hibler and Schulson (2000). Using a larger value for ϕ gives a smaller axis aspect ratio, with $\phi = 45°$ resulting in an axis aspect ratio of $\sqrt{2}$. This means that for a given k_T the resulting shear strength and uniaxial compressive strength is larger compared to when using $\phi = 30°$.

Using $\phi = 45°$ realistic fast-ice extent is modelled for $0.10 \leq k_T \leq 0.12$, compared to $0.15 \leq k_T \leq 0.22$ for $\phi = 30°$. For k_T values in this range the fast ice breaks up in late May in the same manner as before (not shown). The fast-ice formation is also interrupted by total and partial breakups in January, February and March, depending on the value chosen for k_T (see figure 5.18).

For $k_T \geq 0.13$ an erroneous L-mode appears in the model, but the May breakup isn't prevented until $k_T = 0.20$. For this value of k_T the S-mode breakup occurs on approximately the right time and in the right manner. The January breakup is also smaller, but still occurs. The downside of choosing this large k_T is the formation of an artificial L-mode (see figure 5.19).

Considering the flaw-polynya formation on April 14^{th} the general trend is the same as for $\phi = 30°$; small values of k_T give more realistic polynya and new-ice formation, especially inland of the Arctic Institute Islands. Figure 5.20 shows how ice thickness and concentration change when k_T is increased. For $k_T = 0.10$ these fields are very similar to the output from the control run with realistic polynyas and new-ice formation along the S-mode boundary from Severnaya Zemlya to Sterlegova Cape, but too thick ice inland of the Arctic Institute Islands. For $k_T = 0.12$ the ice inland of the Arctic Institute Islands has grown thicker and some thinning of the ice offshore off the Arctic

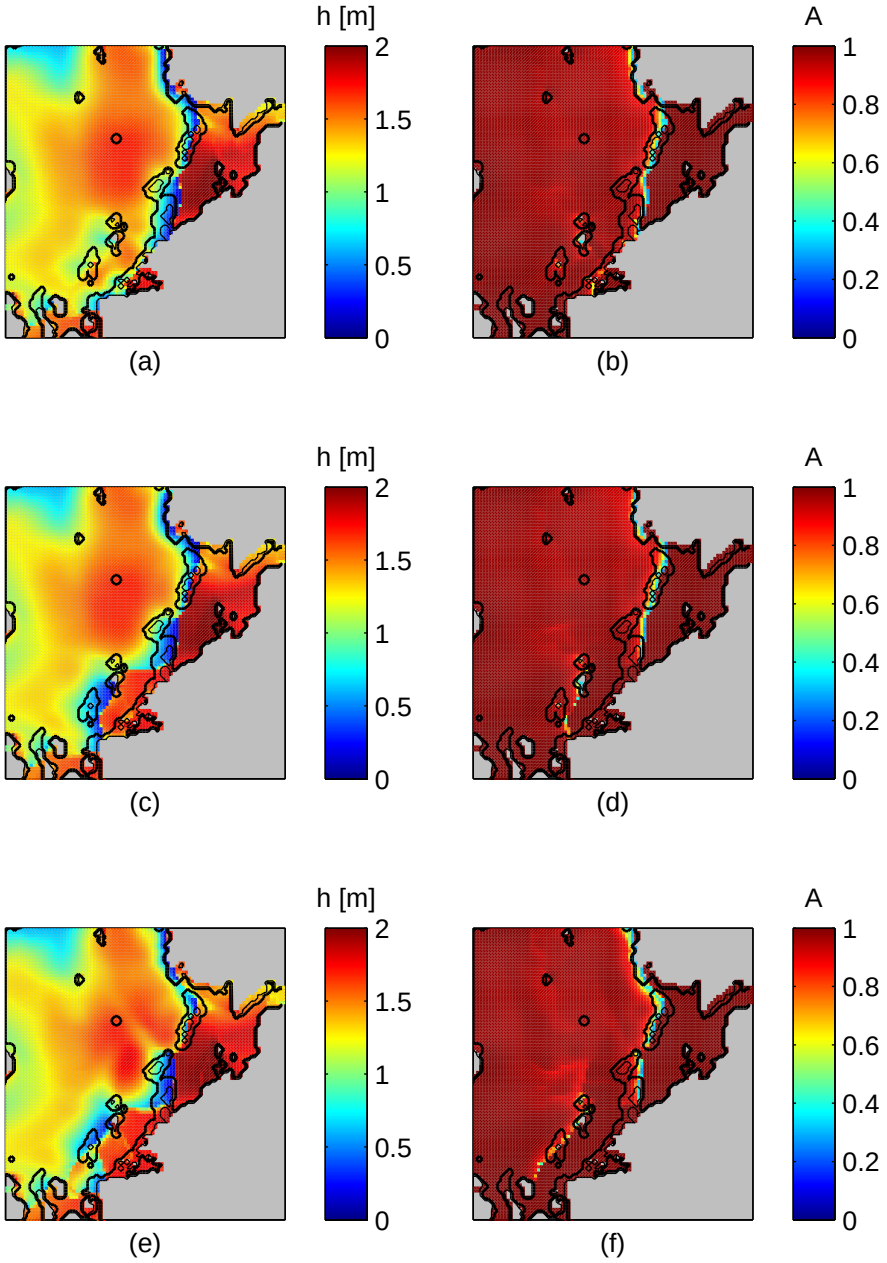

Figure 5.17: Results from using the FMC, $\phi = 30°$: The left column of panels shows ice thickness (capped at 2 m) and the right ice fraction. For the top row of panels k_T was set to 0.15, for the centre row $k_T = 0.17$ and for the bottom row $k_T = 0.22$. The lines show PSSM data; the thick lines show the extent of newly formed ice and the thin line the extent of open water. The snapshot is taken after the first time step of April 14^{th}.

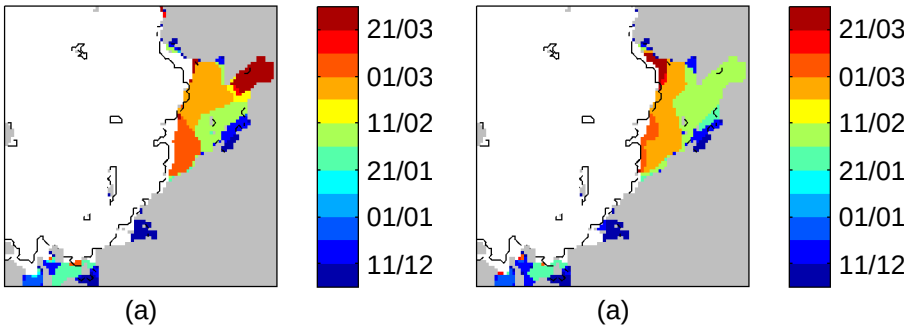

Figure 5.18: Results from using the FMC and $\phi = 45°$. The figure shows the day land-fast ice becomes stable in winter using (a) $k_T = 0.10$ and (b) $k_T = 0.12$. The solid lines mark the fast-ice extent according to the AARI data for the first observation period in April. In the white areas no fast ice is formed.

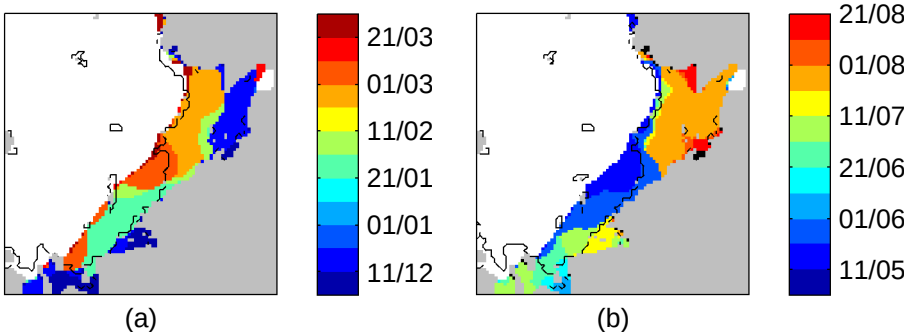

Figure 5.19: Results from using the FMC and $\phi = 45°$ and $k_T = 0.20$: (a) The day land-fast ice becomes stable in winter and (b) the day of (first) fast ice breakup in summer. The solid lines mark the fast-ice extent according to the AARI data for the first observation period in (a) April and (b) May. In the white areas no fast ice is formed and the black patches in panel (b) mark areas of fast ice that survives beyond August 21$^{\text{st}}$.

Institute and Sverdrup Islands can be seen. At $k_T = 0.20$ a polynya opens up erroneously extending north of the Sergey Kirov Islands, as seen before for both the ellipse and FMC with $\phi = 30°$.

In conclusion to this section we note that the results acquired using the FMC are very similar to those acquired using the elliptic yield curve. Using small values for k_T the FMC can be tuned to give results very similar to that of the control run; with respect to polynya locations as well as fast-ice extent and breakup times. Increasing k_T gives increased cohesive strength which can be used to prevent the May breakup and using $\phi = 30°$ and $k_T = 0.22$ prevents the May breakup without producing an erroneous L-mode. This is a major improvement from the previous experiments. Using $\phi = 45°$ the May breakup cannot be prevented without producing an erroneous L-mode and an erroneous polynya north of the Sergey Kirov Islands.

5.3.3 Curved diamond yield curve

The curved diamond yield curve was suggested by Wang (2007) and is based on observations of linear kinematic features of closely packed ice. It was discussed in section 2.4.7. The basic shape of this yield curve, for $\sigma_{\mathrm{I}} > \sigma_{\mathrm{IX}}$ is similar to that of a Coulombic yield curve with $\phi \approx 45°$. However, as figure 2.3 shows, the curved diamond has substantially greater uniaxial compressive strength than the FMC for a given value of k_T.

Calculating ice extent based on the velocity does not yield as clear cut results as before. For $k_T = 0.01$ the S-mode fast-ice area is $A_S = 28,100$ km^2, jumping to $A_S = 53,000$ km^2 for $k_T = 0.02$ and increasing almost linearly to $A_S = 67,600$ km^2 for $k_T = 0.05$ and $A_S = 82,200$ km^2 for $k_T = 0.06$. The total fast-ice area for $k_T = 0.06$ is, however, considerably larger since using this k_T value results in an erroneous L-mode (see figure 5.21). Increasing k_T to $k_T = 0.07$ (figure 5.22) prevents the May breakup that occurs with $k_T = 0.06$ and increasing k_T even further results in an unrealistic fast-ice distribution.

With respect to the polynya formation on April 14$^{\mathrm{th}}$ using $k_T = 0.06$ gives polynyas and new-ice formation along the L-mode border, as expected (figure 5.23). This is not realistic for April 14$^{\mathrm{th}}$, but a similar pattern of polynyas is to be expected when an L-mode occurs. Increasing k_T to 0.07 on the other hand prevents polynyas from forming between the Sergey Kirov Islands and Severnaya Zemlya, with a short polynya stretching north of the Sergey Kirov Islands (figure 5.24). This is similar to the erroneous polynyas already seen for the ellipse and the FMC.

In conclusion the curved diamond yield curve does not appear to deliver results of the same over all quality as the elliptic or FMC yield curves. S-mode fast ice is never formed, only L-mode and when k_T is set large enough to prevent the May breakup a polynya opens up reaching due north of the Sergey Kirov Islands, which is unrealistic.

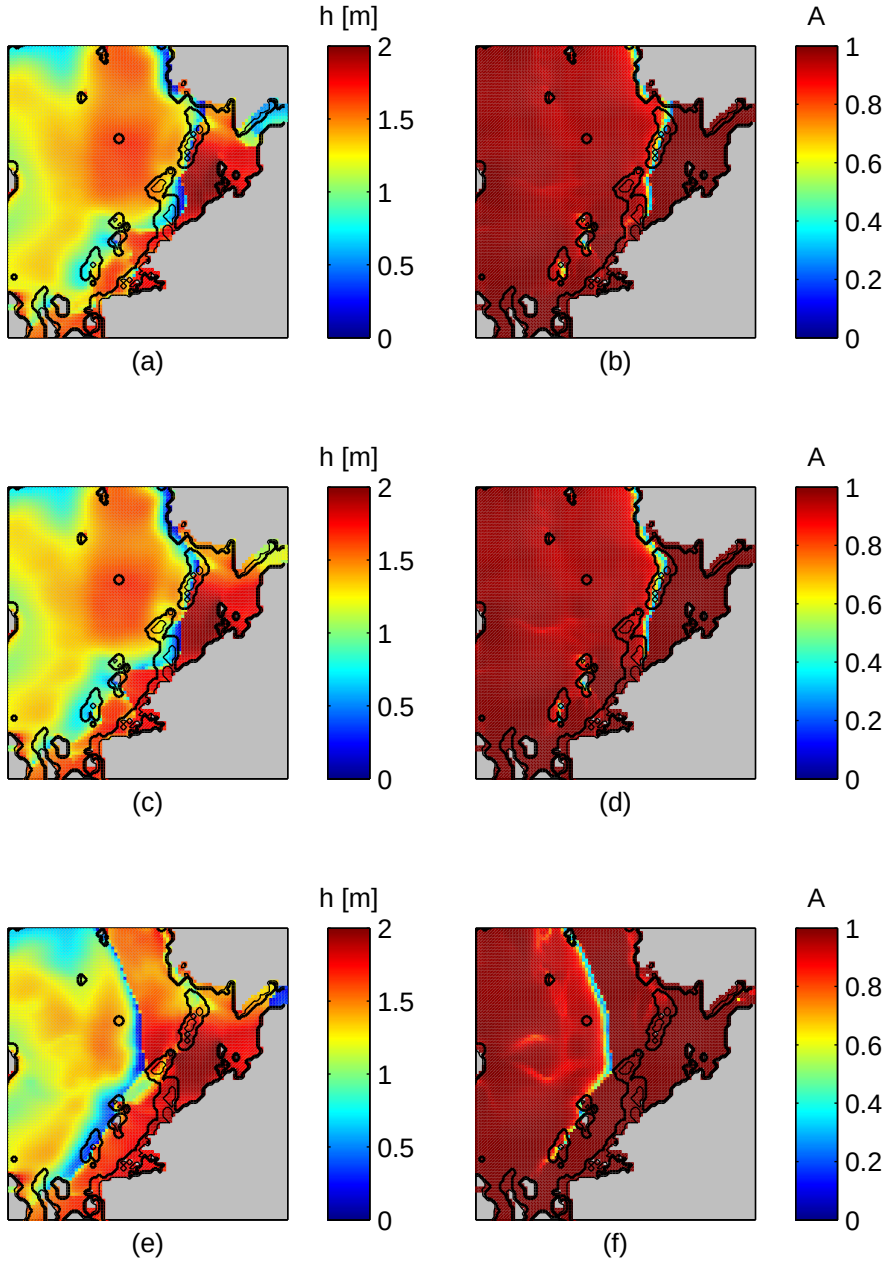

Figure 5.20: Results from using the FMC, $\phi = 45°$: The left column of panels shows ice thickness (capped at 2 m) and the right ice fraction. For the top row of panels k_T was set to 0.10, for the centre row $k_T = 0.12$ and for the bottom row $k_T = 0.20$. The lines show PSSM data; the thick lines show the extent of newly formed ice and the thin line the extent of open water. The snapshot is taken after the first time step of April 14^{th}.

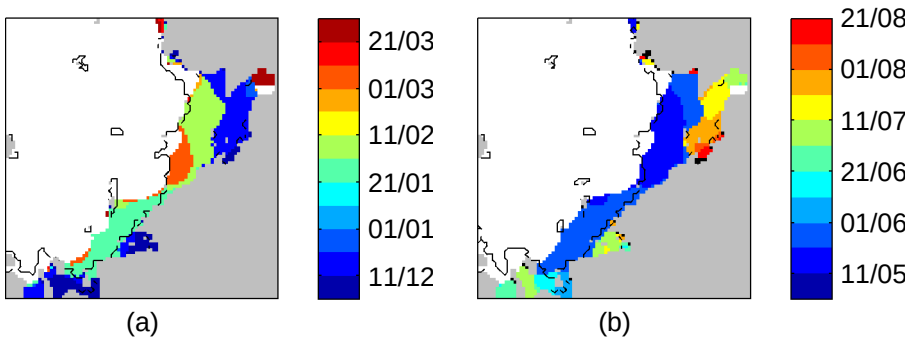

Figure 5.21: Results from using the curved diamond yield curve and $k_T = 0.06$: (a) The day land-fast ice becomes stable in winter and (b) the day of (first) fast ice breakup in summer. The solid lines mark the fast-ice extent according to the AARI data for the first observation period in (a) April and (b) May. In the white areas no fast ice is formed and the black patches in panel (b) mark areas of fast ice that survives beyond August 21$^{\text{st}}$.

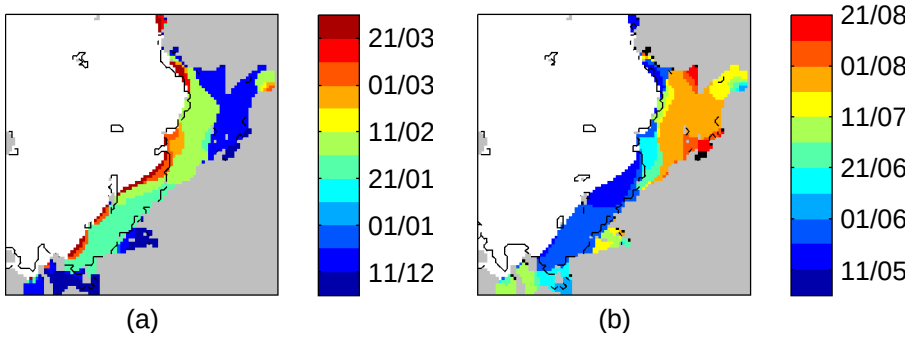

Figure 5.22: Results from using the curved diamond yield curve and $k_T = 0.07$: (a) The day land-fast ice becomes stable in winter and (b) the day of (first) fast ice breakup in summer. The solid lines mark the fast-ice extent according to the AARI data for the first observation period in (a) April and (b) May. In the white areas no fast ice is formed and the black patches in panel (b) mark areas of fast ice that survives beyond August 21$^{\text{st}}$.

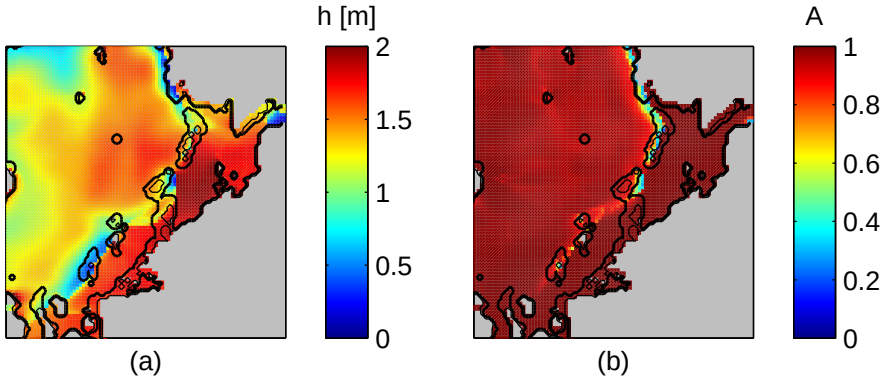

Figure 5.23: Results from using the curved diamond yield curve and $k_T = 0.06$: (a) ice thickness (capped at 2 m) and (b) ice speed (colour, logarithmic) and velocity (arrows). The lines show PSSM data; the thick lines show the extent of newly formed ice and the thin line the extent of open water. The snapshot is taken after the first time step of April 14$^{\text{th}}$.

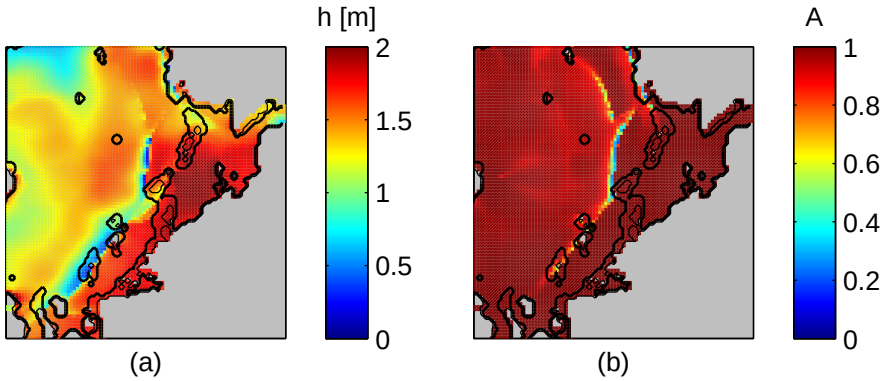

Figure 5.24: Results from using the curved diamond yield curve with $k_T = 0.07$: (a) ice thickness (capped at 2 m) and (b) ice fraction. The lines show PSSM data; the thick lines show the extent of newly formed ice and the thin line the extent of open water. The snapshot is taken after the first time step of April 14$^{\text{th}}$.

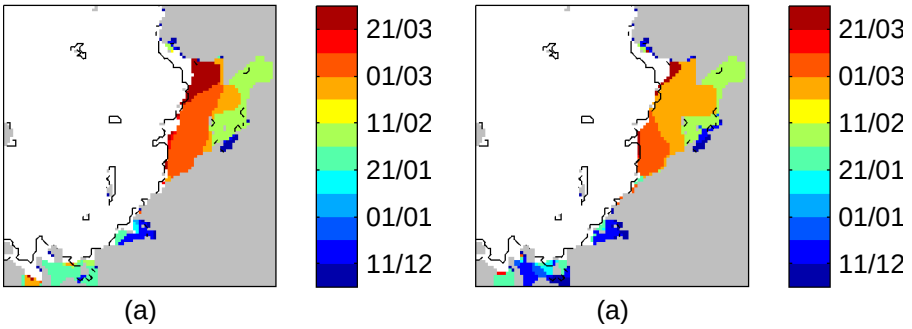

Figure 5.25: Results from using the trimmed ellipse. The figure shows the day land-fast ice becomes stable in winter using (a) $k_T = 0.08$ and (b) $k_T = 0.12$. The solid lines mark the fast-ice extent according to the AARI data for the first observation period in April. In the white areas no fast ice is formed.

5.3.4 Trimmed elliptic yield curve

The trimmed ellipse, introduced in section 2.4.8 is an attempt to refine the behaviour of the elliptic yield curve so that it becomes more physically plausible in the cohesive regime. In this regime it shares some characteristics with the curved diamond. For $\sigma_{\mathrm{I}} > 0$ the trimmed elliptic yield curve has the same shape as the curved diamond, while for smaller values of σ_{I} the elliptic shape is used, giving much less uniaxial compressive strength for the same k_T, compared to the curved diamond. Using $k_T = 0.25$ results in an axis ratio of $e = 2$.

With respect to fast-ice extent the optimal value for k_T lies in the range $0.08 \leq k_T \leq 0.12$ for the current setup. As before an early breakup occurs in May for all values in the range and the timing and manner of that breakup is practically identical to that seen in the control run (not shown). During the freeze-up phase fast-ice growth is interrupted by partial breakups, and as before these are reduced in extent and frequency when k_T is increased (see figure 5.25). At $k_T = 0.13$ the fast-ice area drops from $S_A \approx 82,000$ km^2 for $0.08 \leq k_T \leq 0.12$ to $A_S = 70,300$ km^2. The S-mode is recovered for $k_T = 0.14$, but at $k_T = 0.15$ an erroneous L-mode forms. Setting k_T to $k_T = 0.16$ prevents the May breakup, but at the expense of simulating an unrealistically large fast-ice extent (see figure 5.26).

If we now consider the ice thickness and concentration a similar pattern arises as for the FMC. Lower values of k_T give a better representation of the ice inland of the Arctic Institute Islands with too high values producing an unrealistic polynya stretching due north of the Sergey Kirov Islands (see figure 5.27). The erroneous polynya appears to form for all values of $k_T \geq$

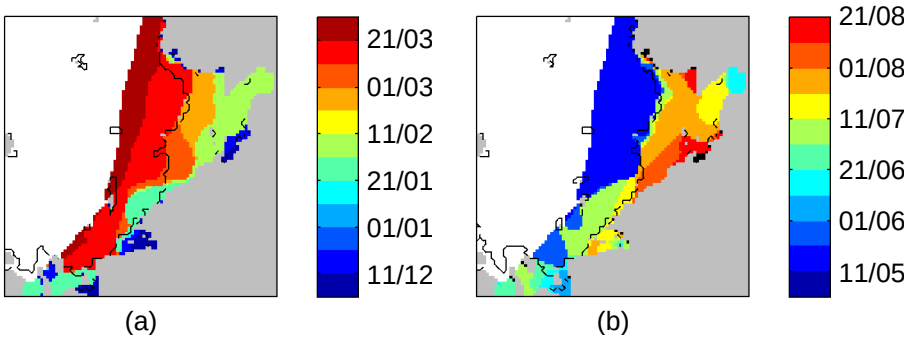

Figure 5.26: Results from using the trimmed ellipse and $k_T = 0.16$: (a) The day land-fast ice becomes stable in winter and (b) the day of (first) fast ice breakup in summer. The solid lines mark the fast-ice extent according to the AARI data for the first observation period in (a) April and (b) May. In the white areas no fast ice is formed and the black patches in panel (b) mark areas of fast ice that survives beyond August 21$^{\text{st}}$.

0.13.

Using the trimmed ellipse improves upon previous results in that when using $k_T = 0.08$ the ice inland of the Arctic Institute Islands is blown offshore causing thinner ice to form where the satellite shows it to be. In contrast no such thinning can be seen using the FMC or in the control run. Overall, the area covered by thin ice is also greater here than in the control run or when using the FMC (see table 5.1).

Using $k_T = 0.08$, the trimmed elliptic yield curve therefore performs very well in simulating drifting ice while the fast ice simulation gives practically the same results as the control run. Larger values of k_T give worse drift ice simulation and for $k_T = 0.13$ an artificial L-mode is modelled. Using $k_T = 0.16$ prevents the May breakup, but also results in an unrealistic fast-ice extent.

5.3.5 Granular model

The granular model was introduced by Tremblay and Mysak (1997) and discussed in section 2.4.3. It uses a Coulombic yield curve and the pressure term is calculated based on the divergence and shear of the flow. Here biaxial cohesive strength has been added to the model by setting $C' = k_T P_{\max}$ in equation (2.53) and allowing for negative pressure ($P = -C'$) in the pressure solver. This produces some fast ice, but the results are far from being as good as those of the control run. The ice extent is much less than that observed and those flaw polynyas that are modelled appear in the wrong places. Changing the maximum viscosity or k_T does not improve the

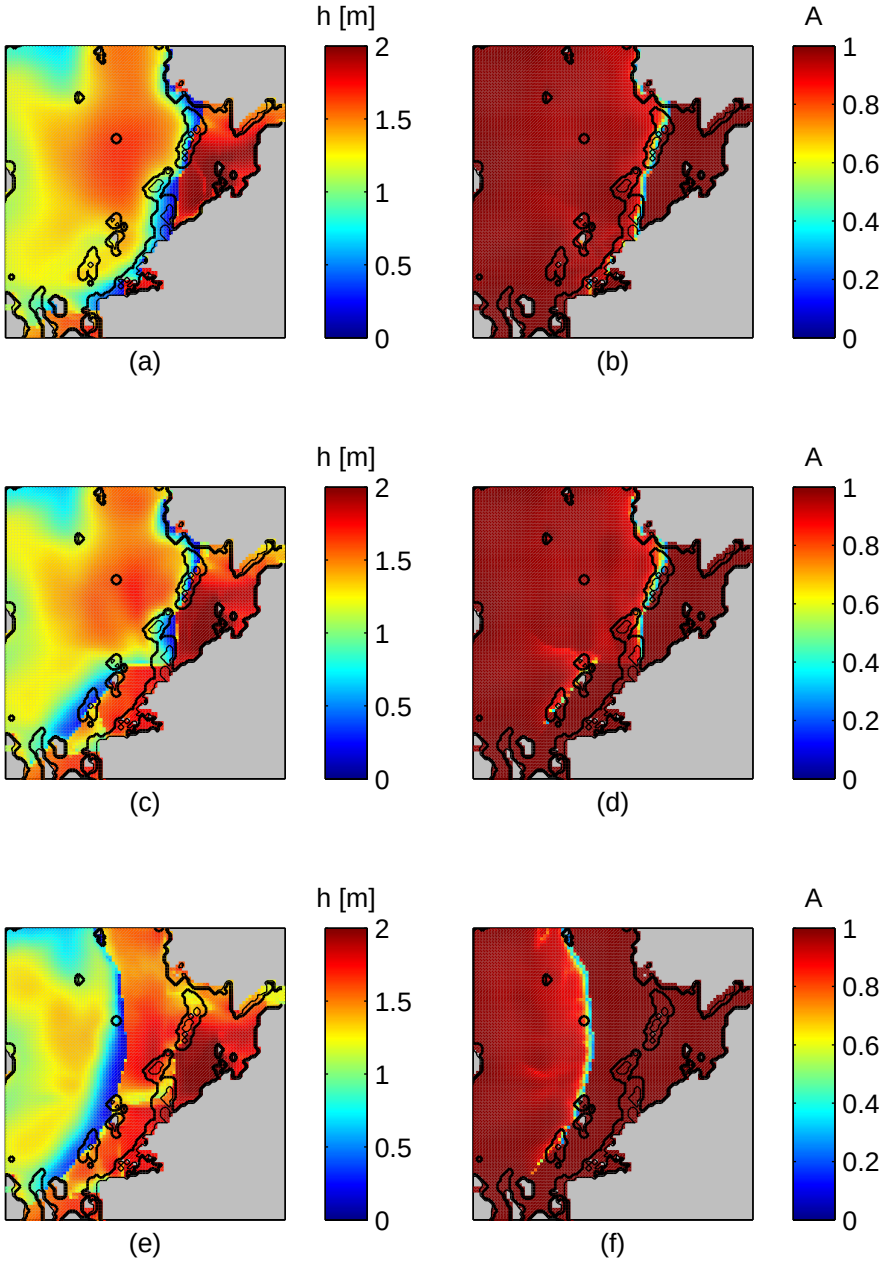

Figure 5.27: Results from using the trimmed ellipse: The left column of panels shows ice thickness (capped at 2 m) and the right ice fraction. For the top row of panels k_T was set to 0.08, for the centre row $k_T = 0.12$ and for the bottom row $k_T = 0.16$. The lines show PSSM data; the thick lines show the extent of newly formed ice and the thin line the extent of open water. The snapshot is taken after the first time step of April 14^{th}.

Table 5.1: The total area of the Severozemelsky flaw polynya new-ice on April 14$^{\text{th}}$. For the PSSM data this is the area of thin ice and open water while the AARI data is the observed young/newly-formed ice from early and late in the April 10$^{\text{th}}$ to 19$^{\text{th}}$ observation period. The modelled new ice is defined to be where $hA \leq 0.5$ m. In addition to the control run yield curves and parameter settings that gave the most plausible polynya locations were chosen.

Observed	
PSSM	28,100 km^2
AARI (early)	24,800 km^2
AARI (late)	21,000 km^2
Modelled	
Control run	12,100 km^2
FMC ($\phi = 30°$, $k_T = 0.15$)	14,200 km^2
FMC ($\phi = 45°$, $k_T = 0.10$)	8,700 km^2
Trimmed ellipse ($k_T = 0.08$)	19,600 km^2

situation.

The reason why the granular model does not produce fast ice in a reliable manner is not entirely clear. It is, however, likely that the poor outer-loop convergence of the model plays a crucial role. We've already seen that a large number of outer loops is needed to produce fast ice in a reliable manner in the Hibler-type model. The assumption to draw from that is that a good plastic convergence is necessary to model fast ice, but this is not present in the granular model. We should therefore not expect to be able to model fast ice in a reliable manner using it.

In terms of fast ice modelling the granular model was not very successful. Given that we've already seen much better results from using the Hibler-type model it is not necessary to discuss the granular model results at length.

5.4 Discussion

The previous section saw different yield curves and parametrisations used to model land-fast ice in the Kara Sea in a realistic setup. Realistic fast-ice extent and polynya formation could be modelled using the commonly used elliptic yield curve, the FMC and the trimmed ellipse. The curved diamond yield curve did not give as realistic fast-ice extent as the others while the granular model proved unsuitable for fast-ice modelling. Realistic breakup times proved difficult to model without sacrificing either the realistic fast-ice extent, the polynya formation or both.

Using the commonly used elliptic yield curve with large maximum viscosity and a large number of outer loops produces realistic fast ice extent and flaw-polynya formation for the winter 1997–98. This was done in the so-called control run. Large maximum viscosity is needed for a fast-ice simulation and using a large number of outer loops improves the stability of the modelled fast ice. This is a noteworthy result since land-fast ice has not been properly simulated before using a dynamic model and in a realistic setup.

Although the control run gives good results it also leaves something to be desired. In particular the ice appears to be too weak; suffering multiple breakups during the freeze-up and breaking up too early in summer. The ice inland of the Arctic Institute Islands is also too thick compared to observations which show new-ice formation to take place there. Additional yield curves were introduced in an attempt to address these problems, but this met with limited success.

None of the setups described succeeded in preventing the freeze-up breakups, while still maintaining a reasonable fast-ice extent at the same time. Preventing the early breakup in May proved a more attainable goal, but preventing that breakup while maintaining the realistic S-mode extent was only possible using the FMC with $\phi = 30°$. New-ice formation inland of the Arctic Institute Islands could in turn only be modelled using the trimmed ellipse. In none of the setups tested were all three features correctly modelled; the fast-ice extent, the breakup time and the new-ice formation inland of the Arctic Institute Islands.

The following discussion will be focused on those yield curves and settings that gave the best results. We will attempt to understand why this is and to better understand what the best approach to model fast ice may be. As an extension to this attempts will be made to improve the results already obtained with these yield curves.

5.4.1 Elliptic yield curve

Starting with the control run we note that it gives quite good results, given the simple form of the yield curve and lack of cohesive strength under isotropic divergence. The main drawback of the results obtained from the control run are the frequent breakups modelled but not seen in observations. Partial breakups may not be unrealistic and according to Volkov et al. (2002) the Severozemelsky fast ice may be subject to partial breakups throughout winter. According to the AARI observations, however, only very small partial breakups occur in the winter 1997–98. The temporal resolution of the AARI charts is only about 10 days and so it is possible that partial breakups may occur and the fast ice re-establish itself in between observations. The modelled partial breakups are, however, usually not recovered so quickly. Another possibility is that the speed limit used in the fast-ice

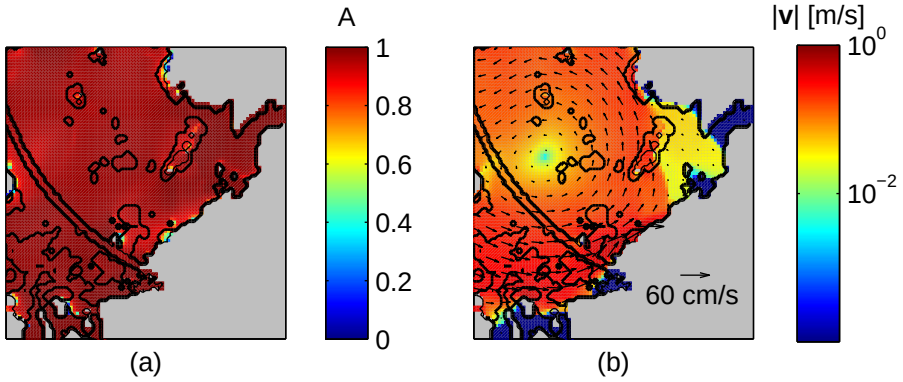

Figure 5.28: Results from the control run: (a) ice fraction and (b) ice speed (colour, logarithmic) and velocity (arrows). The lines show PSSM data; the thick lines show the extent of newly formed ice and the thin line the extent of open water. The snapshot is taken after the first time step of May 22$^{\text{nd}}$. Some ice is erroneously labelled as newly formed in the satellite data due to melt water influences.

detection algorithm is too low causing false breakup reports.

Here the PSSM data can be useful and in particular it shows that on April 22$^{\text{nd}}$ a flaw polynya forms off the fast-ice edge. This demonstrates, without a doubt, that the modelled breakup of the fast ice on that particular date is wrong (see figure 5.28). This date is important since most of the model configurations tested show an early breakup then. Unfortunately not all the partial breakups modelled can be discounted so easily as erroneous, based on the PSSM data. This can only be done if a clear flaw polynya forms and that is not always the case.

Early and partial breakups are therefore a problem, even though the fast ice is recovered. A possibly related problem, perhaps is the early permanent breakup of the ice in the control run. This final breakup occurs little over a month too early. Combined with the fact that the S-mode fast ice is established about a month too late the modelled fast ice season is only about five months compared to about seven months in reality. All in all it would appear that the fast ice is too weak in this simulation.

Given that the fast ice seems too weak it's worth considering changing the ice strength parameter, p^*. In all of the experiments introduced in section 5.3 the mean value from Tremblay and Hakakian (2006) was used, i.e. $p^* = 37.5$ kN/m^2, but the largest value they report as plausible is $p^* = 45$ kN/m^2. With respect to fast ice this is essentially equivalent to lowering the wind drag coefficient, C_{da}, since there is very little water drag present. Using this larger value for p^* does not have a very pronounced effect. The

partial breakups during freeze-up are still present and so is the May breakup.

Setting $p^* = 30$ kN/m^2, the lowest value reported as plausible by Tremblay and Hakakian (2006), gives ice that is too weak to support realistic fast-ice formation. Using this setting the modelled fast-ice area is about half the observed area. This weaker ice does, on the other hand yield to produce realistic new-ice formation inland of the Arctic Institute Islands.

Increasing p^* increases both the ice compressive and shear strength, but increasing only the shear strength turns out to be a more effective way to improve the fast-ice stability. We've discussed how the eccentricity of the ellipse can be changed by changing the parameter e. Using a smaller e increases the shear and uni-axial compressive strength causing the ice to arch more readily. We saw that $e = 1.4$ prevented the May breakup, but unfortunately this also causes an artificial L-mode to form. The L-mode does not form for $e = 1.5$, but the May breakup also occurs then. It is therefore possible that a value $1.4 < e < 1.5$ exists such that the May breakup is prevented and no artificial L-mode forms. Tests varying e by 0.02 in this interval show that this is not so. Using $e = 1.42$ prevents the May breakup, but when e is increased from $e = 1.42$ to $e = 1.44$ the fast ice breaks up in May, but the artificial L-mode still remains.

Uniaxial compressive strength and the related arching therefore clearly plays an important role, but simply adjusting e did not give both realistic fast-ice and drift-ice behaviour. Adding cohesive strength under isotropic divergence can also be used to prevent the May breakup, but the problems encountered are similar. In fact, adding cohesive strength, the way it is done here, also adds both shear and uniaxial compressive strength, so it can be difficult to assess which effects are due to the additional cohesive strength and which are due to the additional uniaxial compressive strength. A test where the uniaxial compressive strength is kept constant as k_T is varied is outlined in the next section.

Despite having its deficiencies the control run does produce realistic fast-ice extent. To our best knowledge, this has not been done before in a realistic setting using a dynamic sea-ice model. The reason fast ice forms is the fact that the elliptic yield curve extends into the $\sigma_2 > 0$ part of the stress space giving it cohesive strength. This is of course the case in nearly all dynamic ice models in use today and what makes the current implementation special is the very large number of outer loops and the large value for the maximum viscosity used.

With respect to the maximum viscosity the value used in nearly all the experiments is $\zeta_{\max} = (10^{13}\text{ s})P$. This results in a realistic fast-ice extent in the control run, with lower values giving less extent and much higher values resulting in some oscillation in the fast-ice area. In order to try to appreciate the role of $\zeta_{\max}$ let us consider the viscous representation of the ice, given simple theoretical arguments.

Suppose that the problem at hand is purely one dimensional; i.e. we

consider only the fast-ice extent along the x-axis. Recall also that setting a maximum on ζ is equivalent to setting a minimum on Δ where $\Delta_{\min}^{-1} = 2\zeta'_{\max}$ and $\zeta_{\max} = \zeta'_{\max} P$. Now consider the behaviour of Δ in one dimension.

Assuming a one dimensional problem the strain-rate invariants become simply $\dot{\varepsilon}_{\mathrm{I}} = \dot{\varepsilon}_{11}$ and $\dot{\varepsilon}_{\mathrm{II}} = 0$ and thus equation (2.42) from section 2.4.2 becomes:

$$\Delta = \sqrt{1 + 1/e^2}|\dot{\varepsilon}_{11}| = \sqrt{1 + 1/e^2}\left|\frac{\partial u}{\partial x}\right|. \tag{5.1}$$

When the ice undergoes viscous creep $\Delta = \Delta_{\min}$. Assuming that the fast ice is modelled as slowly creeping linear viscous material integrating over the fast-ice extent, L we get

$$\Delta_{\min} = \sqrt{1 + 1/e^2}|u(L)|/L, \tag{5.2}$$

assuming no ice motion at the coast; i.e. $|u(0)| = 0$. Using this equation we can set $\Delta_{\min}$ so that the maximum ice velocity in viscous creep and at the fast-ice edge is equal to the target outer-loop error, ϵ_{OL}.

So far we have set $\epsilon_{\mathrm{OL}} = 0.1$ mm/s and inserting this for $u(L)$ into equation (5.2) and assuming $L = 100$ km we get $\Delta_{\min} = 10^{-9}$ s^{-1}. This is equivalent to setting $\zeta'_{\max} = 5 \times 10^8$ s, so for the fast-ice edge to move no faster than 10^{-4} m/s when all the ice is flowing viscously $\zeta'_{\max}$ must be set no larger than this. This is twice the value Hibler (1979) used but almost two orders of magnitude smaller than that used by Hunke and Dukowicz (1997). If the Severozemelsky fast ice is all in the viscous state then this should be a sufficiently large value for $\zeta_{\max}$.

The optimal modelled value is therefore about five orders of magnitude larger than that which the theoretical calculations suggest. This can be interpreted such that under high wind stress the fast ice is not in viscous flow, but rather very slow plastic deformation. This is supported by figure 5.29, which shows that, on April 14$^{\mathrm{th}}$ in most of the Severozemelsky fast ice the bulk viscosity is less than $\zeta_{\max}$.

The physical interpretation of this is that under these circumstances the ice in the Severozemelsky region is not a single unmoving fast-ice massive, but rather undergoes some cracking and ridging under the applied strain. This is not unreasonable and compares well with the description of the fast-ice behaviour in the area given by Volkov et al. (2002). The maximum viscosity then needs to be set high enough to capture this behaviour, rather than trying to simulate the fast ice as an extremely highly viscous fluid. Another possible interpretation is that the viscous approximation is simply wrong and that raising $\zeta_{\max}$ simply prevents it from influencing the model too much.

Varying the number of outer loops also affects the modelled fast-ice extent, but the response is not as clear-cut as when modifying $\zeta_{\max}$. Using just one pseudo time step did give some fast ice, but the fast-ice area modelled in this manner was just under half the observed area. Using more than

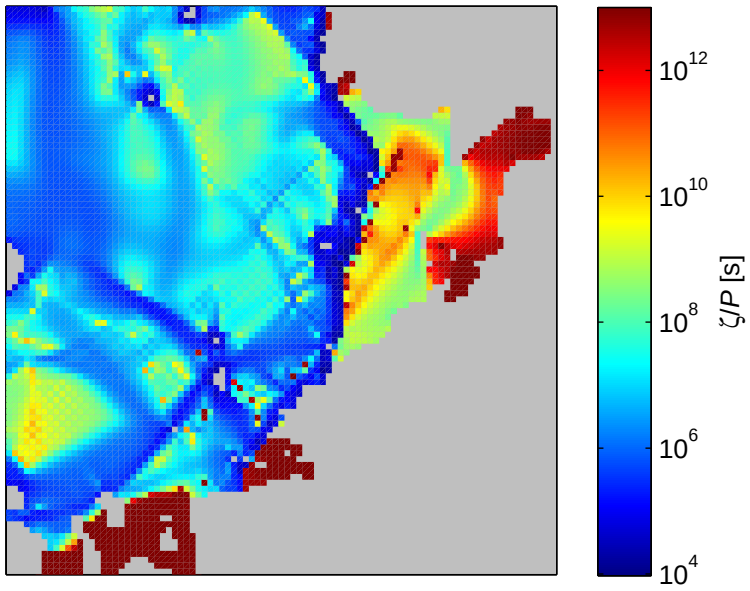

Figure 5.29: Bulk viscosity over ice pressure in the control run. The viscosity is capped so that $\zeta/P \leq 10^{13}$ s and therefore where $\zeta/P = 10^{13}$ s the ice behaves like a linearly viscous fluid. The snapshot is taken after the first time step of April 14^{th}.

50 outer-loop iterations gives reasonable fast-ice area, but with a notable dip at 250 and 300 outer loops. In general more fluctuations appear in the modelled fast-ice area for a small number of outer loops than for a large one. Some instability is, however, still present at 500 outer loops. Using a smaller model time step a similar pattern can be seen. This gives a strong indication that the fluctuations should, in general decrease with a larger n_{OL} and a more accurate solution of the momentum equation.

A possible explanation for this is that the model equations have multiple solutions. Hunke (2001) has demonstrated that for an idealised case multiple solutions to the viscous-plastic equations exist. Multiple solutions were also observed by Lemieux and Tremblay (2009) who found that multiple solutions may appear if the tanh-form for $\zeta_{\max}$ is not used (see equation (2.50)) and the constant of proportionality between the outer-loop error and the linear solver error is too small (α, see section 2.2.1). In our model the tanh-form is used, which, according to Lemieux and Tremblay (2009) should prevent multiple solutions from appearing. The parameter α is, however, smaller than recommended by Lemieux and Tremblay (2009) simply because the SOR-solver is not as capable as the GMRES-solver they use. This could be causing multiple solutions to appear here.

Another possible explanation is that the erratic behaviour comes about because the momentum solver does not reach the converged solution in every time step. In section 4.4 we saw that even when using 500 outer loops the solver does not reach the convergent solution in 5% of the modelled time steps. Each time the solver misses the converged solution in this manner the model diverges from the path a fully converged model would take. The number of such bifurcations decreases as n_{OL} is raised, but even at $n_{\mathrm{OL}} = 500$ the model does not reach full convergence in each time step.

Bifurcations like these can occur in essentially all numerical models, but are usually much too small to be of any importance. In this case, however, they do appear to cause considerable differences in the predicted fast-ice area, particularly using a small number of outer loops. Using larger n_{OL} the modelled fast-ice area appears to be more stable, but fluctuations in it are not completely eliminated. This could be due to the fact that the model still does not reach convergence in 5% of the modelled time steps, or about 5500 times during the whole simulation.

Another possibility still is that the target error used is too large. The target error is the convergence criterion used in that if the difference between the velocities after two consecutive outer loops is less than the target error the solver is considered to have converged. Here the target error was $\epsilon_{\mathrm{OL}} = 0.1$ mm/s. In section 4.4 this was found to be the smallest target error possible from a practical stand point, but it is also the limit suggested by Lemieux and Tremblay (2009). If it is not small enough then the solution the solver returns is never the converged one and this may cause apparently spurious bifurcations when changing n_{OL}. This is probably not the case here

since using large values for n_{OL} clearly reduces fluctuations in modelled fast-ice area. If the fluctuations were due to too large target error only, increasing n_{OL} should only give minor improvements. Using a different model time step should also result in different model behaviour, but this is also not the case.

All the same, this raises the question of how small ϵ_{OL} should be. Since the current model cannot handle values much smaller than $\epsilon_{\mathrm{OL}} = 0.1$ mm/s we must content ourselves with an educated guess. The best guess is probably based on the calculations in section 5.3.1. There a relationship between $\Delta_{\min}$ and the creep speed of ice in linear-viscous creep was demonstrated. Assuming the speed at the edge of a 100 km fast ice block to be of the order 0.1 mm/s gave $\Delta_{\min} = 10^{-9}$ s. This is about four orders of magnitude smaller than what experiments with the model indicated to be applicable for fast ice simulations.

Let us now assume that $\zeta_{\max} = (10^{13}\ \mathrm{s})P$, as indicated by the model experiments in section 5.3.1. This is then equivalent to assuming $\Delta_{\min} = 5 \times 10^{-14}$ s and using equation (5.2) this gives $|u(L)| = 4 \times 10^{-9}$ m/s, for $L = 100$ km. If we wish to accurately predict all ice movements where plastic interactions dominate this is probably the accuracy to aim for. Using a larger value for $\zeta_{\max}$ would then require an even smaller target error and vice versa. It should be noted though that assuming $L = 100$ km is probably an overestimation. It has already been shown that under certain circumstances the extent of the fast ice that can be modelled as linear viscous is much smaller. On the other hand using $L = 10$ km, which is probably an underestimation, gives $|u(L)| = 4 \times 10^{-8}$ m/s. This is still well outside the range of possible ϵ_{OL} for the current model.

Another way to look at the question of what value for ϵ_{OL} should be chosen is to consider the strain rates in relationship to Δ and $\Delta_{\min}$. The viscous-plastic material has two phases; a linear viscous one and a non-linear plastic one. For large strain rates the material is plastic, but when the strain rates become so small that $\Delta \leq \Delta_{\min}$ a phase transition occurs and it becomes linear viscous. If all the ice were in the linear viscous phase the Coriolis term would be the only non-linear term in the momentum equation. Ignoring it, the phase transition at $\Delta = \Delta_{\min}$ therefore gives an indication for how accurately the momentum equation needs to be solved; it can simply be assumed that the outer-loop iterations must continue until changes in Δ between successive iterations becomes smaller than $\Delta_{\min}$ or some fraction thereof. This method has not been tested, but it is likely to be at least as demanding on the outer-loop solver as choosing as small ϵ_{OL} as suggested earlier.

Assuming that this relationship between maximum viscosity and target error hold we can try to understand the fluctuations seen for large maximum viscosities noted in section 5.3.1. Assuming that a certain minimum ϵ_{OL} is required to accurately model all plastic interactions means that if the maximum viscosity is raised the target model error must conversely be

lowered so that all plastic interactions continue to be accurately modelled. Here only the maximum viscosity was raised while the target error remained unchanged. This means that there are more and more errors appearing in the calculations of the plastic interactions as the maximum viscosity gets higher, increasing the chances that one of them cause a large bifurcation in the model.

The erratic behaviour for large maximum viscosity can therefore be considered to support the supposition of a relationship between maximum viscosity and minimum target error. The relative stability of the model at large n_{OL} on the other hand show that the target error used here is small enough so the relationship between maximum viscosity and minimum target error appears to be weak. Finally the theoretical arguments offered indicate that the target error would have to be much smaller, in contradiction with the observed stability of the model. This is probably another failure of the linear-viscous assumption in that the ice cannot be assumed to behave correctly when in the linear-viscous state. The maximum viscosity should therefore be be set high enough to prevent the viscous limit from playing a large role in the simulation. If this is the case the maximum viscosity cannot be used to estimate ϵ_{OL}, as done previously. The role of the maximum viscosity and the applicability of the linear-viscous approximation in general therefore needs more closer consideration, but this will not be done here.

5.4.2 The cohesive yield curves

Having discussed results obtained using the elliptic yield curve we now turn to the more realistic cohesive yield curves; the modified Coulombic, curved diamond and trimmed ellipse. Previous results suggest that the uniaxial compressive strength and/or other forms of cohesive strength should be larger than in the control run. Using the parameter values suggested by their authors the modified Coulombic yield curve gives low uniaxial compressive strength and the curved diamond yield curves give higher uniaxial compressive strength compared to the control run. They should, however, both give a more realistic description of the ice behaviour for positive σ_1, than the ellipse.

Using the original form of the modified Coulombic yield curve gave very little fast ice extent and it was necessary to switch to the FMC to get a reasonable extent. With the correct tuning this yield curve can be used to reproduce and improve upon the results of the control run. Using $\phi = 30^\circ$ and large enough values for k_T it is possible to prevent the May breakup, while maintaining correct fast ice extent. The downside is that the ice inland of the Arctic Institute Islands becomes unrealistically thick. Correctly simulating the fast-ice breakup time is still a major improvement on the control run. This good result is, however, only reached for a narrow k_T interval making it somewhat suspect. Using the FMC and $\phi = 30^\circ$ realistic

S-mode fast ice is simulated for $0.15 \leq k \geq 0.22$, but the May breakup does not occur for $k_T = 0.22$. For $k_T \geq 0.23$ unrealistic ice formations are observed in the model results.

The fast ice modelled using the curved diamond yield curve turned out to be much more sensitive to changes in k_T than when using the FMC. Using $k_T = 0.06$ gives realistic fast-ice extent, but $k_T = 0.05$ gives fast-ice area approximately half the S-mode area while using $k_T = 0.07$ produces an erroneous L-mode. In addition the drifting ice is not as well simulated as in the control run or when using the FMC.

Finally the trimmed ellipse gives the best drift-ice results of the rheologies tested here. It can be tuned to give the same fast-ice area as the control run, but at the same time it gives a better representation of the drifting ice. The area of newly formed ice is larger than in any other setup tested and new-ice formation is seen inland of the Arctic Institute Islands, contrary to the other setups. Both should be considered an improvement in the model performance.

Despite having had considerable success in modelling fast ice so far the main problem remains of simultaneously simulating realistic polynyas, fast-ice extent and formation and breakup times. The elliptic, FMC and trimmed elliptic yield curves can all be tuned to capture two of these three features, but not all three at the same time. Only the FMC can be tuned to model a realistic breakup time and S-mode fast ice (instead of L-mode), but this does not allow for a realistic simulation of the ice inland of the Arctic Institute Islands. The ice behaviour there is only realistically simulated using the trimmed ellipse, but this is done at the cost of not correctly simulate the breakup times. In the following we will first consider what happens in the pass inland of the Arctic Institute Islands. The focus is then shifted to the early breakup that occurs in May.

Focusing on what happens in the pass between the Arctic Institute Islands and the Taymyr coast we now consider the modelled stresses for the FMC using $\phi = 30^\circ$ and $k_T = 0.15$ and 0.22. These settings are the ones that gives the best simulation (using the FMC)) of the ice in the pass between the Arctic Institute Islands and the coast ($k_T = 0.15$) and the setting that prevents the May breakup ($k_T = 0.22$). To demonstrate the role of cohesive stresses figure 5.30 shows the second principle stress (σ_2) on April 14^{th} for the FMC using $\phi = 30^\circ$ and the two values for k_T considered here. The second principle stress is a good measure of how important cohesion is in the model since cohesion occurs only for $\sigma_2 > 0$.

First of all figure 5.30 shows that the stress in the fast ice is overwhelmingly cohesive but compressive in the rest of the ice cover. The figure also shows that using small k_T no cohesion is present in the Arctic Institute Islands Pass while using the larger value for k_T introduces cohesive stress there. It can be argued that it's the uniaxial compressive strength that matters, rather than k_T or some other parameter, by considering the first

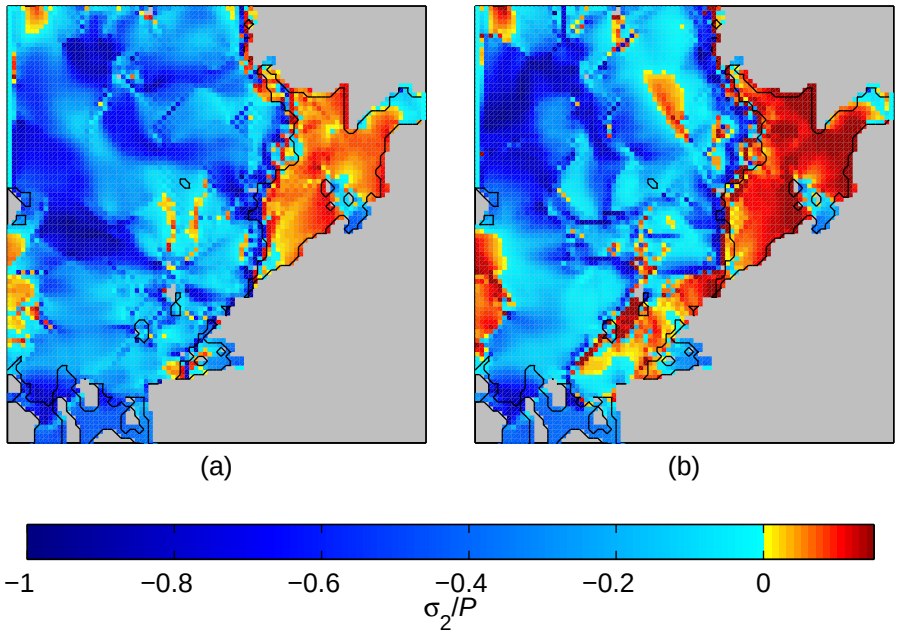

Figure 5.30: The second principle stress (σ_2) on April 14$^{\text{th}}$ for the FMC using $\phi = 30°$ and (a) $k_T = 0.15$ (b) $k_T = 0.22$.

principle strain rate axis.

Since the principle stress and strain rate axes coincide the first principle strain rate ($\dot{\varepsilon}_1$) gives the minimum normal strain acting on the ice. A negative $\dot{\varepsilon}_1$ therefore means that there is compressive strain rate orthogonal to the direction of the largest divergent strain rate. Consider now the case of a converging channel, as studied by Dumont et al. (2009). If the ice flows through the convergence zone $\dot{\varepsilon}_1$ must always be negative where the channel converges, as long as the external forcing only acts along the channel. This is also the case even if the external forcing were to cause divergent strain rates along the flow direction.

On April 14$^{\text{th}}$ $\dot{\varepsilon}_1$ is always negative in the region inland of the Arctic Institute Islands. In other words; the ice is being compressed against the Arctic Institute and Sverdrup Islands as it drifts south-west along the Taymyr Peninsula. Now, if the uniaxial compressive strength, σ_{uc} is large the ice will not yield as it is blown against the islands and so a blockage forms. Weaker ice on the other hand yields allowing it to drift to the south-west as well. It should therefore be kept in mind that tuning of σ_{uc} depends entirely on the forcing that's applied to the model. Wind speed as well as the strength of the ocean currents and the thickness of the ice all influence the resulting tuned value for σ_{uc}.

Using a given forcing it should, however, be possible to select a known good value for σ_{uc} and keep it constant in order to simulate the ice flow in the Arctic Institute Islands Pass properly while adjusting k_T to prevent the May breakup. Either the elliptic or the FMC yield curve can be used adjusting and e or ϕ to achieve the right value for σ_{uc} for a given value of k_T. Both yield curves were tested in this manner, returning the same basic result that this is not a feasible approach[1]. Even if σ_{uc} is kept constant at a known good value then increasing k_T will not prevent the May breakup without also producing an erroneous L-mode. The L-mode then forms, not by arching in the Arctic Institute Islands Pass, but rather because the tensile strength is enough to extend the fast ice from the arch between Sterlegova Cape and the Sergey Kirov Islands.

It is therefore clear that a larger value for σ_{uc} is needed to prevent the May breakup than that which allows for a realistic ice flow through the Arctic Institute Islands Pass. This is consistent with our earlier results where setting k_T (and thus σ_{uc}) large enough to prevent the May breakup invariably caused blockage or fast ice formation in the Arctic Institute Islands Pass. The conclusion to draw from this is that, all things being equal, realistic breakup times and ice behaviour in the Arctic Institute Islands Pass cannot be modelled, both at the same time during this particular winter by tuning the yield curve. Some other model or forcing modifications are therefore needed the most interesting of which are discussed in relation to the early breakup covered in the following section.

Using too large k_T normally does not only cause an erroneous L-mode to form but also an unrealistic polynya between Sergey Kirov and Ushakova Islands. The polynya also forms because σ_{uc} is too large. On April 14^{th} the flow of ice between Sergey Kirov and Ushakova Islands is convergent, which means that when σ_{uc} is set large enough cohesive forces slow down the flow, causing the polynya to form. Were the model forcing different so that the flow were not convergent the polynya would not form, regardless σ_{uc}. The same can be said for the formation of the erroneous L-mode. If we, however, assume that the model forcing is good enough then it is clear that adjusting the yield curve is not sufficient to explain why the correct breakup times cannot be modelled without introducing the aforementioned model artefacts.

A number of model parameters and assumptions may be responsible for our inability to prevent the May breakup. One of these may be related to the relationship between the ice pressure, P and the ice concentration, A and the relationship between P and the ice cohesive strength. In particular we note that the difference in cohesive strength between fast ice and drift ice can be expressed such that for $A = 1$ the cohesive strength should be large, but for $A \lesssim 1$ it should be small. This is of course the same kind of

[1]The equations used to calculate σ_{uc} are derived in appendix D

behaviour as described by equation (2.48) for the compressive strength. The cohesive strength is related to the compressive strength through the yield curve so changing the dependence of the compressive strength on A changes the dependence of the cohesive strength on A. This is done by changing the parameter C in equation (2.48).

In the simulations introduced in section 5.3 $C = 30$ was used, while Hibler (1979) used $C = 20$. Using the latter value means that at $A = 0.95$ the ice strength has fallen by one e-folding scale compared to the strength at $A = 1$; i.e. $P(A = 0.95)/P(A = 1) = \exp(1)$. To test the effects of changing C simulations were run using the FMC, curved diamond and trimmed ellipse yield curves tuned to give correct breakup times. In addition C was set to $C \in \{33, 50, 100, 200, 1000\}$, the values for which the ice strength has fallen by one e-folding scale at $A \in \{0.97, 0.98, 0.99, 0.995, 0.999\}$, compared to $A = 1$. The objective is to decrease the shear and uniaxial compressive strength in the Arctic Institute Islands Pass without affecting the S-mode fast ice.

The effect of raising C appears, however, to be opposite of that hoped for. Raising C weakens the fast ice without significantly easing the flow through the Arctic Institute Islands Pass. One way to interpret this is that the ice strength shouldn't change when its slightly cracked, but that large leads will weaken it quickly. This behaviour could be parametrised by changing equation (2.48) for P so that it reads:

$$P = P^* h \min[1, \exp(-C[1 - A - D])]. \tag{5.3}$$

The parameter D parametrises the separation between "small cracks" and "large leads". However, since raising C did not improve the flow through the Arctic Institute Islands Pass nothing much seems gained by testing this formulation. Further changes to the ice pressure formulation should be based on the physical properties of the ice, but these were not attempted here.

It is also possible that the shear and compressive strength respond differently to changes in concentration. This means, in essence that the shape of the yield curve is a function of the ice concentration. For example the curved diamond shape may be valid for large A while the trimmed ellipse becomes valid at lower values. At present it is not clear precisely what the relationship between concentration and yield curve shape should be and no attempts were made to establish one.

Another possibility is that the air drag coefficient is different over drift ice compared to fast ice. This may be because the stability of the atmosphere is different over fast ice compared to the stability over drift ice. Atmospheric stability affects the ice-atmosphere drag, although it's not immediately clear how large this effect is with respect to fast ice. In the current model atmospheric stability plays no role in determining the drag coefficient, which is simply constant.

A difference in drag between fast ice and drift ice can also come about because of form drag experienced by the drift ice and not fast ice. The effects of form drag is an active research area (see e.g. Stössel and Claussen, 1993, Lüpkes and Birnbaum, 2005), but form drag has not been incorporated into the current model. Further research into the effects atmospheric stability and form drag has on fast ice modelling is needed, but would be outside the current scope.

As a quick test of the effects of atmospheric drag a series of tests were run using the trimmed ellipse, $k_T = 0.8$ and $10^3 C_{\mathrm{da}} = 0.1, \ldots, 1.0$. At $C_{\mathrm{da}} = 0.5 \times 10^{-3}$ the summer breakup was correctly timed, but an erroneous L-mode does form. The modelled polynyas are also much smaller than those observed. The previous experiments used $C_{\mathrm{da}} = 1.2 \times 10^{-3}$, so the ratio is 42%. This shows that that the strength of the drift ice should be about half that of the fast ice if we expect to be able to simulate both accurately at the same time.

According to Guest and Davidson (1991) very smooth first year ice without pressure ridges has $C_{\mathrm{da}} = 1.5 \times 10^{-3}$, first year pack ice has $C_{\mathrm{da}} = 2.0 \times 10^{-3}$ and first year ice in the marginal ice zone averages $C_{\mathrm{da}} = 3.1$. Wave affected first year ice has $C_{\mathrm{da}} = 4.2 \times 10^{-3}$. If we were, based on this to assume $C_{\mathrm{da}} = 1.5 \times 10^{-3}$ for fast ice then, using the ratio found above C_{da} for the drift ice would be $C_{\mathrm{da}} = 3.6 \times 10^{-3}$. This value is within the given range for wave affected first year ice, a category that is meant to describe ice in the marginal ice zone. It is therefore not likely that variations in C_{da} alone can account for our inability to model both fast ice and drift ice at the same time.

It is also possible that the ocean drag coefficient is wrong. We've seen that it's possible to tune virtually all the yield curves to give approximately right breakup times, but this almost always comes at the cost of producing erroneous L-mode fast ice and erroneous polynya formations. The conclusion drawn was that the ice uniaxial compressive strength was too high, but it is also possible that the oceanic drag is too large, slowing down the drift ice and giving an erroneous result. Changing the ocean drag coefficient should have no effect on the fast ice, but a similar effect as having a different atmospheric drag coefficient over fast ice vs. drift ice.

In the experiments run so far the oceanic drag coefficient has been $C_{\mathrm{da}} = 5.5 \times 10^{-3}$. To test the effects of lowered ocean drag simulations were run using the FMC, curved diamond and trimmed ellipse yield curves tuned to give appropriate breakup times and with[2] $C_{\mathrm{da}} = \{1, 2, 3, 5\} \times 10^{-3}$. If the ocean drag coefficient used so far is indeed too high using a lower drag coefficient should allow realistic thorough flow through the Arctic Institute Islands Pass without affecting the S-mode fast ice. The tests done do, how-

[2]Given the measurements of Langleben (1982), Pease et al. (1983), Shirasawa (1986) and Wamser and Martinson (1993) 10^{-3} is a low value for C_{da}

ever, not show this. Although the ice is clearly affected by changing C_{da}, lowering it does not ease the flow through the Arctic Institute Islands Pass.

Finally the role of tides has not been investigated here. The tidal forcing used here provides lower tidal amplitude than that observed and so tidal effects are likely to be underestimated. Tides may still have an effect, e.g. by breaking up the ice in the Arctic Institute Islands Pass.

Moving away from the ice model it self we now come back to the possibility that errors in the atmospheric forcing cause the observed model shortcomings. The NCAR/NCEP data has very low resolution compared to the features being modelled. In particular orographic effects from surrounding islands and mountains may be important to the fast ice formation, while being unresolved by the forcing data. In the model snow also simply piles up until the melt sets in, while in reality snow may be blown off the ice. This can affect the ice albedo as well as its thickness due to the insulating effects of snow. Any effects the flaw polynyas may have on the atmosphere area also not resolved. The higher resolution ERA-interim data set was therefore tested and will be discussed in more detail below (section 5.4.3).

The low resolution, in particular can be seen to have considerable effects on the ice and snow thickness at the southern coast of Severnaya Zemlya. Figure 5.31 shows the ice and snow thickness shortly before the May breakup where the ice is thinner and the snow thicker near the Severnaya Zemlya compared to the rest of the S-mode area. In most of the S-mode area the ice thickness is $h \gtrsim 2$ m, while north of the Voronina Island and south of Severnaya Zemlya it is $h \approx 1.4$ m. The figure also shows overlaid the land mask from the NCEP/NCAR reanalysis and that clearly shows that the thin ice/thick snow occurs where the land mask protrudes into the ocean. It therefore seems very likely that the modelled ice is erroneously thin in this area.

It is easy to simply stop the simulation shortly before the May breakup, increase (manually) the thickness of the thin ice and the resume the calculation. If this error were crucial to the May breakup such an intervention into the model integration could prevent it. Setting the ice thickness to $h = 2$ m, similar to the rest of the S-mode ice, does not prevent the breakup using those yield curves and settings that give reasonable ice behaviour in the Arctic Institute Islands Pass. Previously the ice would in fact start breaking up where it is erroneously thin, but using this correction it starts breaking up near the Sergey Kirov Islands instead. The erroneous ice thickness does therefore affect the ice, but not to the extent that it explains the May breakup.

5.4.3 ERA-interim forcing

So far the NCAR/NCEP reanalysis data has been used to force the model. This data set covers an extensive period of time and is as such suitable to

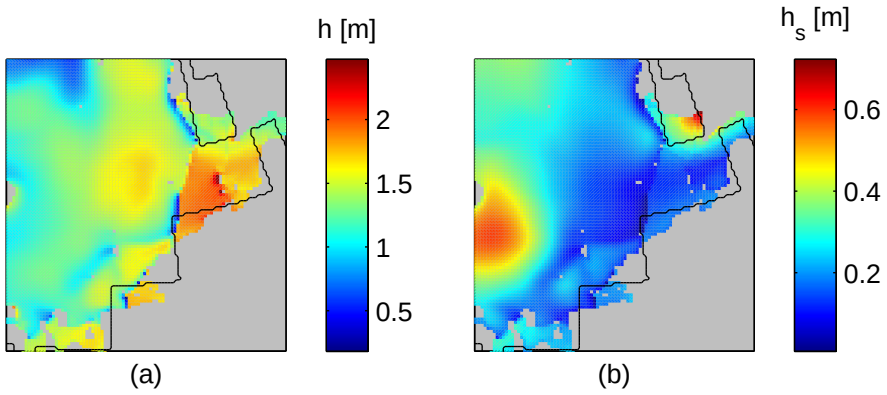

Figure 5.31: Results from the control run: (a) ice thickness and (b) show thickness. The lines show the NCEP/NCAR land mask. The snapshot is taken after the first time step of May 3rd.

investigate long term trends and changes. The spatial resolution is, however, only about 2.5°, which in the Kara Sea equals about 95 × 280 km. It is therefore worth considering a higher resolution forcing and here the ERA-interim reanalysis data set is chosen. The ERA-interim reanalysis is available from 1989 onwards and has a spatial resolution[3] of about 0.5°, which in the Kara Sea equals about 19 × 56 km. In addition this allows us to better judge the effects "reasonable changes" in the forcing terms may have on the model results. To avoid going into the same amount of detail as before only the FMC with $\phi = 30°$ and trimmed ellipse were tested using the ERA-interim reanalysis. These yield curves arguably gave the best results using the NCEP/NCAR forcing and it is reasonable to assume that they should perform well using ERA-interim as well.

The most remarkable result of the ERA-interim runs was that both yield curves required considerably higher cohesive strength under isotropic divergence in order to produce realistic fast ice, compared to the runs using the NCEP/NCAR forcing. Using the same criterion as before the FMC gave the best fast ice results with $0.32 \leq k_T \leq 0.38$, compared to $0.15 \leq k_T \leq 0.22$ using the NCEP/NCAR forcing. Using the trimmed ellipse the best results were obtained using $0.16 \leq k_T \leq 0.23$, compared to $0.08 \leq k_T \leq 0.12$ using the NCEP/NCAR forcing.

The reason for this appears to be twofold. Firstly the wind in the Severozemelsky region, during this period is consistently about 30% stronger in the ERA-interim reanalysis compared to NCEP/NCAR. Comparing the two for the entire model domain shows the ERA-interim winds to be 20%

[3] At the time these experiments were conducted access was restricted to the publicly available downscaled version. This version has been downscaled to 1.5°.

stronger in that area. No comparison was made on a larger scale. Such systematic differences in wind forcing affect the fast ice modelling in three ways; through the cohesive strength parameter k_T, the compressive strength parameter p^* and through the wind drag coefficient C_{da}.

The wind drag and ice strength parameters have so far been considered constants. The wind drag coefficient is at best a very roughly determined figure and can probably be assumed to be the same for the two reanalysis data sets. To determine p^* when using the ERA-interim reanalysis one should repeat the analysis of Tremblay and Hakakian (2006) using the ERA-interim winds instead of the NCEP/NCAR ones. If the two reanalysis give globally consistent results the resulting value for p^* should be the same, and this has been assumed so far. This is not necessarily correct and it is possible that the ERA-interim mean wind speed is larger, simply because of the difference in resolution. Whether the difference in wind stress is local or global it is clear that using winds from different reanalysis products can give very different results.

In addition to changes in wind stress the snow fall in the ERA-interim reanalysis is also considerably greater than that in the NCEP/NCAR results. The difference in modelled snow thickness on the Severozemelsky fast ice massive is about 10 cm in middle of April or about 50%. This causes the ice to grow slower using the ERA-interim data and in the middle of April the difference in modelled ice thickness is about 30 cm or 15%. The difference in ice thickness between using the ERA-interim and the NCEP/NCAR forcing is greatest early in the season, but becomes less as the ice grows thicker. These differences are consistent south of Voronina Island, but it has already been shown that the NCEP/NCAR forcing may not be valid between it and Severnaya Zemlya. Differences in other forcing variables appear to have negligible effects on the ice thickness.

Using ERA-interim reanalysis therefore gives thinner and consequently weaker ice. This means that the cohesive strength needs to be increased even further when using the ERA-interim data in order to get realistic fast-ice results. Considering this we can immediately see that a 30% increase in wind stress should be compensated by about 70% increase in the tensile strength (since the wind speed is squared when calculating the wind stress). A 15% decrease in ice thickness should be compensated by a 15% increase in the tensile strength. Combining the two gives a 85% estimated increase to k_T needed for the ERA-interim data compared to NCEP/NCAR when focusing on getting the April fast-ice formation right. This is close to the increase in k_T needed in the model. In addition to average changes in wind strength and ice thickness spatial and temporal differences between ERA-interim and NCEP/NCAR may also play a role. These can affect the fast ice simulation in non-trivial ways, which may invalidate this simple estimate.

When using properly tuned cohesive strength the two yield curves give qualitatively similar results using ERA-interim compared to NCEP/NCAR.

In all cases good agreement between model and observations is seen at the height of the fast ice season, while the breakups during freeze-up and the early breakup in May as well as the ice in the Arctic Institute Islands Pass remain a problem. Using the NCEP/NCAR forcing the FMC could be tuned to give both correct breakup times and fast-ice extent, but this was not the case with the ERA-interim and the FMC gives, overall worse results using the ERA-interim than with the NCEP/NCAR forcing. In contrast the results using the trimmed ellipse remain similar using the ERA-interim compared to the NCEP/NCAR forcing. Using low k_T the fast-ice extent and the ice in the Arctic Institute Islands Pass can be realistically simulated, but the early breakup in May remains a problem.

These limited tests with the ERA-interim data show no clear benefits from using it over the NCEP/NCAR data. The only clear improvement is that the ice thickness north of Voronina Island is more realistic using the ERA-interim, but this does not appear to affect the fast-ice simulation. The tests do, however, show that using a different set of forcing conditions requires a recalibration of the model. The most important factor there is the difference in wind stress and we can conclude that some work may be needed for a more thorough recalibration. A comparison should also be made between the reanalysis results and available observational data, but this is outside our scope here.

As an side note it is worth mentioning that the modelled ice thickness using NCEP/NCAR and the ERA-interim forced model give acceptable results compared to the measurements provided by Polyakov et al. (2003)[4]. They provide maximum fast ice thickness at Sterlegova Cape, which in 1998 is 1.82 m. The modelled maximum in that area is just over 2.0 m using the NCEP/NCAR data and just under 2.0 m using the ERA-interim forcing. According to the Polyakov et al. (2003) data the mean maximum fast ice thickness from 1936 to 2000 is 193 cm and the standard deviation is 27 cm. Both model results are therefore within the acceptable range, even if they are too large for the given year. In both cases runs with correct breakup times were used since the maximum fast-ice thickness occurs after the erroneous May breakup. For the NCEP/NCAR forcing this is reached on June 5$^{\text{th}}$, but on June 28$^{\text{th}}$ when using the ERA-interim forcing.

We can conclude that due to the sensitivity of the land-fast ice to external forcing it is vital to use good forcing data for a fast-ice model. It would, in particular be interesting to see if a coupled ice-ocean-atmosphere model would give substantially better results than the current setup.

[4]Data available from `http://people.iarc.uaf.edu/~igor/research/ice/ice_arctic_seas.tar` as of January 5$^{\text{th}}$ 2011

5.4.4 Grounding parametrisation

According to Volkov et al. (2002) there are two basic mechanisms at work when land-fast ice forms in the Kara Sea. One is the anchoring of fast ice on islands, which has been our main topic so far and the other is anchoring on grounded pressure ridges. To fully model the grounding process an additional shear term would need to be included in the momentum equation, describing the interaction between ice and ocean floor. Such a term would require making assumptions about the coefficient of friction between the ice and ocean floor and assumptions about the shear strength of the grounded keel would also have to be made. In addition a good sub-grid scale parametrisation for the ridging process, giving the depth of the ridge keel and the area of contact with the ocean floor would be needed.

We are unaware of a functioning grounding parametrisation built upon the principles described above. The building blocks for such a scheme could be an advanced multi-category ice model and the data from ridge grounding studies (e.g. Mahoney et al., 2007). Building such a scheme is, however, outside the scope of this study and in stead a very simple scheme is suggested to test the possible effects grounding may have on the stability of the fast ice.

In Volkov et al. (2002) it is noted that the fast ice appears to mostly follow isobaths; the 10–15 m isobath in the south-western Kara Sea and the 20–25 m isobath in the north-eastern Kara Sea. In our simulation the ice thickness in the south-western Kara Sea is about 1–1.5 m and about 2–2.5 m in the north-eastern Kara Sea. A very simple grounding scheme would therefore require all ice that is thicker than one tenth of the ocean depth to become stationary. Lieser (2004) implemented such a scheme and reported good results using it in the Laptev Sea.

This scheme can be generalise slightly by allowing the constant of proportionality in the linear approximation to vary such that ice of thickness h becomes stationary when

$$h\Gamma \geq H, \tag{5.4}$$

where Γ is the constant of proportionality and H is the ocean depth. In addition ice is allowed to flow into a grid cell where this inequality holds, but not out of it. This simulates ridging that may occur because of the presence of grounded ice.

Aside from the physical reasons already mentioned for considering a grounding scheme the results already obtained indicate that such a scheme may improve the results. For most of the Severozemelsky region the 25 m isobath is close to the shore, compared to the model resolution. An exception to this are the shallows around the Sergey Kirov Islands. There an area about 18 times the area of the islands themselves lies above the 25 m isobath. This also happens to be an area where the ice extent in the control run and trimmed ellipse run with $k_T = 0.08$ (see figures 5.4 and 5.25) is too small. In

general too little fast ice appears around the Sergey Kirov Islands when the cohesive strength is small and the ice inland of the Arctic Institute Islands is realistically modelled. Using a grounding parametrisation may be a good way to correct the fast-ice extent around the Sergey Kirov Islands without increasing the cohesive strength.

The grounding scheme in equation (5.4) was tested with the trimmed ellipse with $k_T = 0.08$. Without the grounding scheme it shows too little fast ice extent around the Sergey Kirov Islands, while giving good results inland of the Arctic Institute Islands. Using the grounding scheme can increase the fast-ice extent around the Sergey Kirov Islands, but setting $\Gamma = 10$ gives too large fast ice extent. Testing Γ in the range $1 \leq \Gamma \leq 10$ in steps of one shows that the grounding scheme has no considerable effect until Γ reaches $\Gamma = 5$. For lower values the ice is grounded in the Pyasina Bay and around the Nordenskiöld Archipelago, but not near the Sergey Kirov Islands. For $\Gamma = 5$ and $\Gamma = 6$ grounding near those islands occurs and consequently the fast-ice extent becomes more realistic there (see figure 5.32 and 5.33). At $\Gamma = 7$ grounding near Sverdrup Island causes the ice inland of it and the Arctic Institute Islands to grow unrealistically thick and become land-fast producing an erroneous L-mode. The realistic range for Γ in this setup is therefore $4 < \Gamma < 7$.

Given that the average ice thickness in the Severozemelsky region is between 2 and 2.5 m this range of Γ assumes grounding where the ocean depth is between 8 and 18 m. This is quite shallow, given that the minimum ocean depth in the model is 8 m, with minimum level thickness[5] of 4 m. Using the grounding scheme gives very good results compared to the PSSM data (see figure 5.33), but does not alter the breakup times already established for the trimmed ellipse.

These results show that pressure ridge grounding may play an important secondary role when modelling land-fast ice in shallow areas. We will also see that the grounding scheme is very important in the multi-year runs performed in the next chapter. Further more they also indicate how sensitive the modelled ice may be to inaccuracies in the model topography. When using $\Gamma = 7$ the ice is grounded around Sverdrup Island, with grounded ice in six grid points south of the island, which is represented by one grid point in the model. The six grounded grid points are sufficient to severely slow down the ice flow between the islands and the coast causing thick ice to build up upstream. Since the grounding scheme uses the ocean model grid to determine depth the grounding may depend on the vertical resolution of the ocean model.

Although the grounding scheme used here is very simplistic these results

[5]The level thickness can vary because of the uneven horizontal spacing implemented in VOM. However, in shallow areas, where the ocean depth is only a few multiples of the minimum level thickness all levels have the minimum thickness.

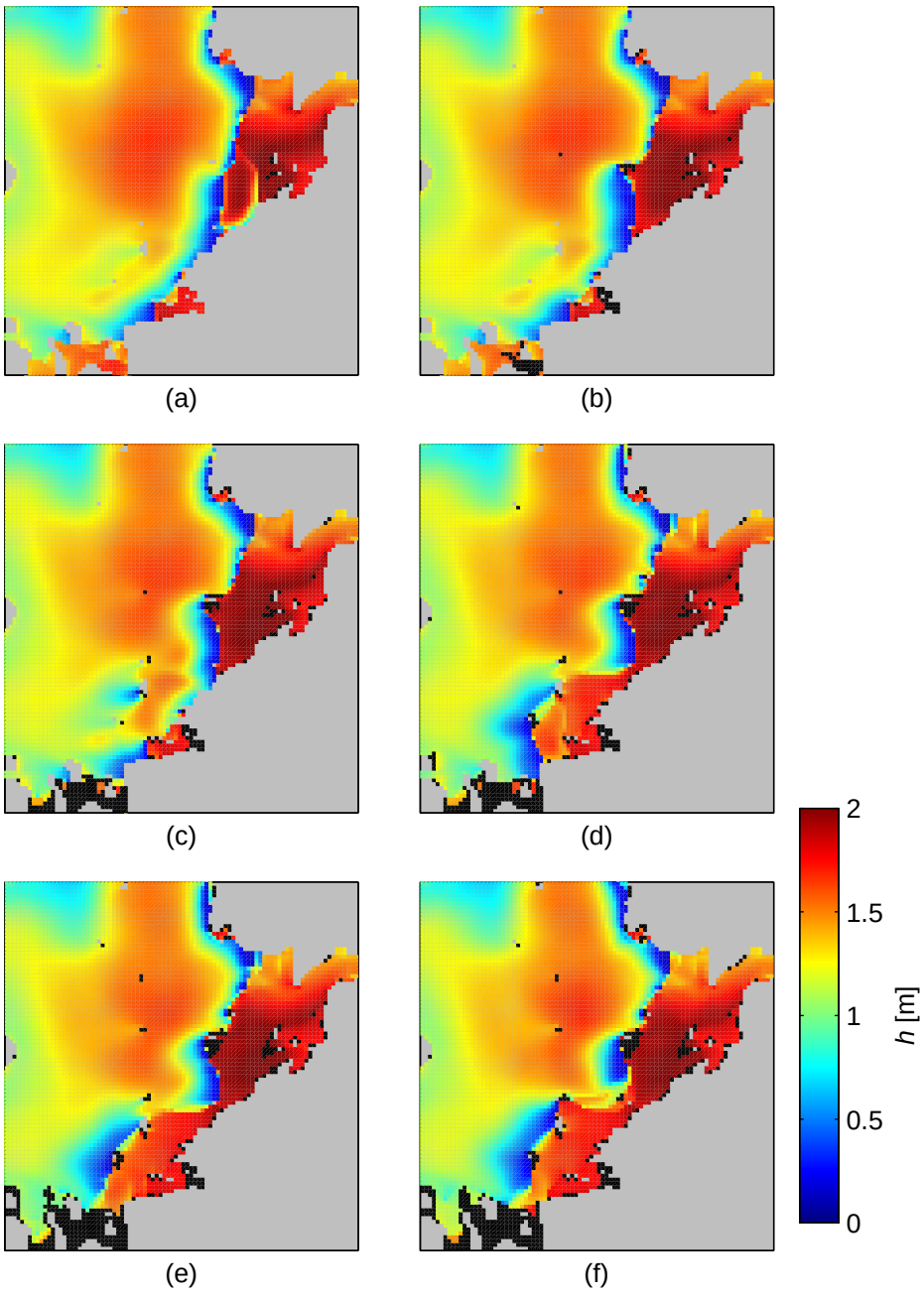

Figure 5.32: Results from using the trimmed ellipse with $k_T = 0.08$ and the grounding scheme with (a) $\Gamma = 4$, (b) $\Gamma = 5$, etc. The figure shows ice thickness (capped at 2 m) where grid cells with grounded ice are masked with black. The snapshots are taken after the first time step of April 14^{th}.

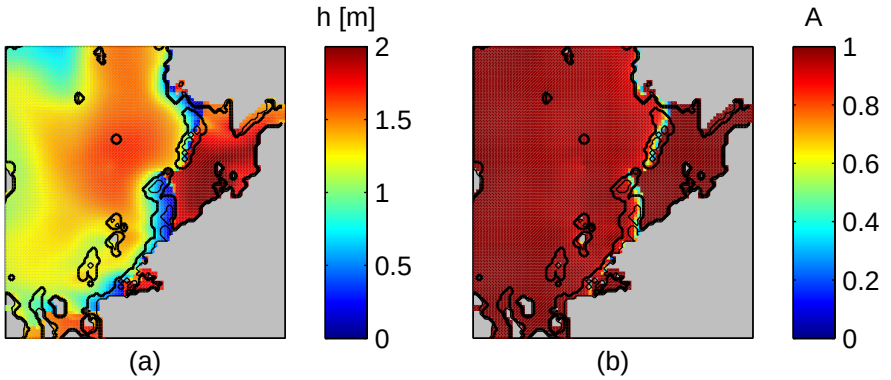

Figure 5.33: Results from using the trimmed ellipse with $k_T = 0.08$ and the grounding scheme with $\Gamma = 5$: (a) ice thickness (capped at 2 m) and (b) ice fraction. The lines show PSSM data; the thick lines show the extent of newly formed ice and the thin line the extent of open water. The snapshot is taken after the first time step of April 14$^{\text{th}}$.

can be used to infer the importance of grounding, both in modelling and reality. Further work is needed to create a more physically plausible grounding scheme. This would help with both modelling efforts and our understanding of the behaviour of the fast-ice cover.

5.5 Conclusion

In this chapter it has been shown that much of the land-fast ice formed in the Kara Sea can be modelled in a realistic setup using a viscous-plastic sea-ice model. A number of different viscous-plastic yield curves were considered along with variations in the relevant parameters. Finally a very simple ice grounding parametrisation was introduced.

The model described in chapter 2 was set up for the Kara Sea using the same basic parameters as described in chapter 4. This means, in particular that the NCEP/NCAR reanalysis results were used to force the model throughout, except in section 5.4.3 where the ERA-interim reanalysis was used. All the yield curves introduced in chapter 2 were tested along with the granular model. The granular model did not produce realistic fast ice, but all the yield curves used with the Hibler-type model could be tuned to do so. The FMC and trimmed ellipse yield curves were considered to give the best result, but the traditional ellipse also gave good results.

In addition to testing different yield curves two other model parameters were tested; the maximum viscosity and the number of outer loops. The maximum viscosity sets the limit for which the model material stops behav-

ing as a plastic and becomes linearly viscous. It is also the viscosity of the linearly viscous material. The number of outer loops is the number of linearisations and linear solves the non-linear solver attempts before aborting and using the best available solution. If at any point the maximum velocity difference between two consecutive outer loops (linear solves) is less than a given target error the solution is considered converged.

The main conclusion to draw from this chapter is that it is possible to model fast ice using a viscous-plastic model. In order to do this it proved necessary to use much larger maximum viscosity than commonly used. The recommended value was found to be $\zeta_{\max} = (10^{13}\text{ s})P$, instead of the traditional value of $\zeta_{\max} = (2.5 \times 10^{8}\text{ s})P$. In addition using a large number of outer loop iterations is also recommended, although varying the number of outer loops did not give as clear results as changing the maximum viscosity. The yield curves tested could all be tuned to produce fast ice, although some gave more realistic results than others.

Varying the maximum viscosity from $\zeta_{\max} = (10^{8}\text{ s})P$ to $(10^{13}\text{ s})P$ gives a continuous increase in the fast-ice extent reaching a maximum for $\zeta_{\max} = (10^{13}\text{ s})P$. For higher values the fast-ice area remains quite stable, but the start of a slow oscillation in the fast-ice area can already be seen at $\zeta_{\max} = (10^{16}\text{ s})P$. These oscillations should not present a problem here given how slow they are and that they only start to become apparent at very large values for $\zeta_{\max}$.

More erratic changes in the fast-ice area are, however, visible when changing the number of outer loop iterations from $n_{\text{OL}} = 50$ to $n_{\text{OL}} = 500$. A large number of outer loop iterations appears to be necessary to give consistent results, but no rigid limit was suggested. The best way to improve the stability of the modelled fast-ice area appears to be to improve the convergence properties of the solver. Currently it converges in 95% of the modelled time steps, but increasing this to 100% would probably eliminate the observed fluctuations. Decreasing the target error may also improve the model stability. In both cases a completely new solver is required.

Despite these problems it was found that most of the yield curves tested could produce realistic fast ice at the height of winter. The most realistic results were found using the traditional elliptic yield curve, the FMC and the trimmed ellipse. These yield curves could all be adjusted to produce realistic fast ice extents and drift-ice behaviour, but only the trimmed ellipse gave realistic drift-ice behaviour in the Arctic Institute Islands Pass and realistic fast-ice extent at the same time. They could also all be adjusted to give realistic fast-ice breakup times, but only the FMC could be adjusted to give realistic breakup times and fast-ice extent at the same time.

The main difficulties in obtaining a realistic model response were unrealistic breakups during formation in winter, too thick ice in the Arctic Institute Islands Pass and too early breakup of the fast ice in summer. The reason behind the breakups during formation is at this point not clear, although it

is possible that the ice forms too slowly in fall. The poor drift-ice behaviour in the Arctic Institute Islands Pass was resolved when using the trimmed ellipse, which has the lowest shear strength. Too high shear strength when using the other yield curves could be the reason why ice tends to build up in the pass. It is also possible that the wind in the pass is poorly represented or that higher resolution is necessary to resolve the dynamics in the pass properly.

Finally the modelled fast ice invariably breaks up in May not July as observed. This can be prevented, but usually at the cost of large errors in the drift-ice behaviour. The notable exception to this was using the FMC with $\phi = 30^\circ$ and $k_T = 0.22$, but changing k_T by 0.01 gave different results, so this is probably not very robust. A number of possible reasons behind this early breakup were suggested, including erroneous atmospheric or oceanic drag, incorrect ice pressure parametrisation and errors in the atmospheric forcing itself. No conclusive reason for the early breakup was found.

A very simple grounding scheme was also suggested where by the ice becomes grounded when its thickness reaches a given fraction of the ocean depth. The inclusion of this scheme did improve the model results in some cases, but did not allow the proper modelling of all three aspects mentioned above, at the same time. This shows that grounding plays a secondary role to the ice cohesive strength, increasing the size and strength of the arch footers which keep the fast ice in place. Grounding does not appear to be very important for fast-ice formation in 1997–98, while the following chapter will show it to be more important in other years.

Tests using the ERA-interim reanalysis results as forcing data showed the considerable sensitivity these simulations have to the applied forcing. The cohesive strength of the ice had to be increased by about 100% when using the different forcing. This is mostly due to an approximately 30% increase in the mean Severozemelsky wind strength of ERA-interim compared to NCEP/NCAR. Differences in snowfall and thus ice thickness also played a role. In order to successfully model fast ice one must therefore carefully tune the model to the given forcing data.

In this chapter it has been shown that land-fast ice in the Kara Sea can be modelled using a viscous-plastic model. Some modifications to the model had to be made; most importantly the viscous limit had to be raised, but changes to the momentum solver and yield curves were also important. So far the model has only been tested for the winter 1997–98, but in the following chapter longer time periods will be modelled. Despite modelling only one winter the work done in this chapter has highlighted the capabilities and weaknesses of the viscous-plastic model. The importance of ice cohesion vs. pressure ridge grounding for fast-ice formation was also underlined improving our understanding of how fast ice forms.

Chapter 6

Decadal experiments

6.1 Introduction

Having shown that fast ice can be modelled to a certain extent in one particular year the model will now be tested over a longer time period. The periods chosen here are 1967–74 and 1998–2005. During these periods a large and small average fast-ice extent was observed, respectively. Both computational and time restraints prevent us from going into the same sort of detail here as in the previous chapter. Therefore two of the most successful yield curves were chosen for an initial set of experiments. Comparing the model results to observations only the fast-ice extent, formation and breakup times will be considered.

The tests performed here show that simply using the best setups from the previous chapter is insufficient. The reason for this is that the role of pressure ridge grounding was underestimated in the previous chapter and in order to get acceptable results the grounding scheme had to be included. Using the flexible modified Coulombic (FMC) yield curve with the grounding scheme gives good overall results with reasonable fast-ice extent modelled every year, save one. These good results show that the model can be used to model fast ice on a longer time scale. The model results are then used to infer a critical thickness for fast-ice formation; the thickness the ice needs to reach before fast ice will form. This is of some interest when considering fast-ice presence in warmer or cooler climates than the current one.

In the following an overview of the available observations is first given. These are the sea-ice charts produced by the Arctic and Antarctic Research Institute (2007). Section 6.3 then outlines the results from the eight different experiments performed using the model. These cover the two time periods and yield curves, as already mentioned. This is followed by a discussion of the results. In it the relatively poor model performance in the initial experiments is linked to underestimating the importance of ice grounding. By including the grounding scheme the results are improved dramatically.

A discussion of the critical formation thickness and the role of ice-ocean interaction as also included.

6.2 Observations

The most useful set of observations is again the ice charts compiled by the Arctic and Antarctic Research Institute (2007), introduced and used in the previous chapter. These are available from 1933 to 1992 and 1997 to 2006, of which the years 1967–74 and 1998–2005 overlap with the temporal range of the current model.

To offer a quick overview of the fast-ice characteristics during the more recent period figures 6.1 and 6.2 map the observation period when fast ice becomes stable and when it breaks up, respectively. The method used to produce these figures is the same as used for 1998 earlier. As before these figures offer only a quick overview, since they only capture fast ice that is land-fast during April. This means in particular that land-fast ice that breaks up before April 1st is not shown and ice that becomes land fast after April 1st is also not shown. This is only a minor concern here since the prevailing trend is for the fast-ice extent to increase in January, February and March and decrease in June, July and August.

Summarising what can be seen in the figures it is first of all clear that the year 2002 is special in that fast ice only forms very close to the shore and no S-mode fast ice can be seen. S-mode fast ice was observed in January, but is not shown in the figure since it breaks up before April 1st. This has been noted before and according to Divine et al. (2005) 2002 is the only year this happens during the entire span of the AARI observations. The years 1998 and 2003 only S-mode ice forms, while in 1999–2001 and 2005 L_1-mode forms and in 2004 L_2 mode forms. In general the S-mode forms in early January. The L-mode then forms either simultaneously with the S-mode or in late March. The breakup of the S and L_1 modes always occurs in late June or in July, but in 2004 the L_2 extension breaks up in late May, having been land-fast since late March.

The earlier time period considered here, 1967–74 is more problematic since the temporal resolution of the observations is much worse. During winter and early spring only monthly observations are available and they only begin in February. This means that the onset of fast-ice formation is lost. In late spring and summer the observations are, however, mostly every 10 days so the breakup times should be reliable. For this period only the breakup is therefore considered (see figure 6.3).

During the period 1967–74 an L-mode is always present during the height of winter except in 1968 and 1972 when only an S-mode is present. Only in 1971 and 1974 do the L and S-modes break up at the same time, all other years the L-mode breaks up first. The L-mode normally breaks up in late

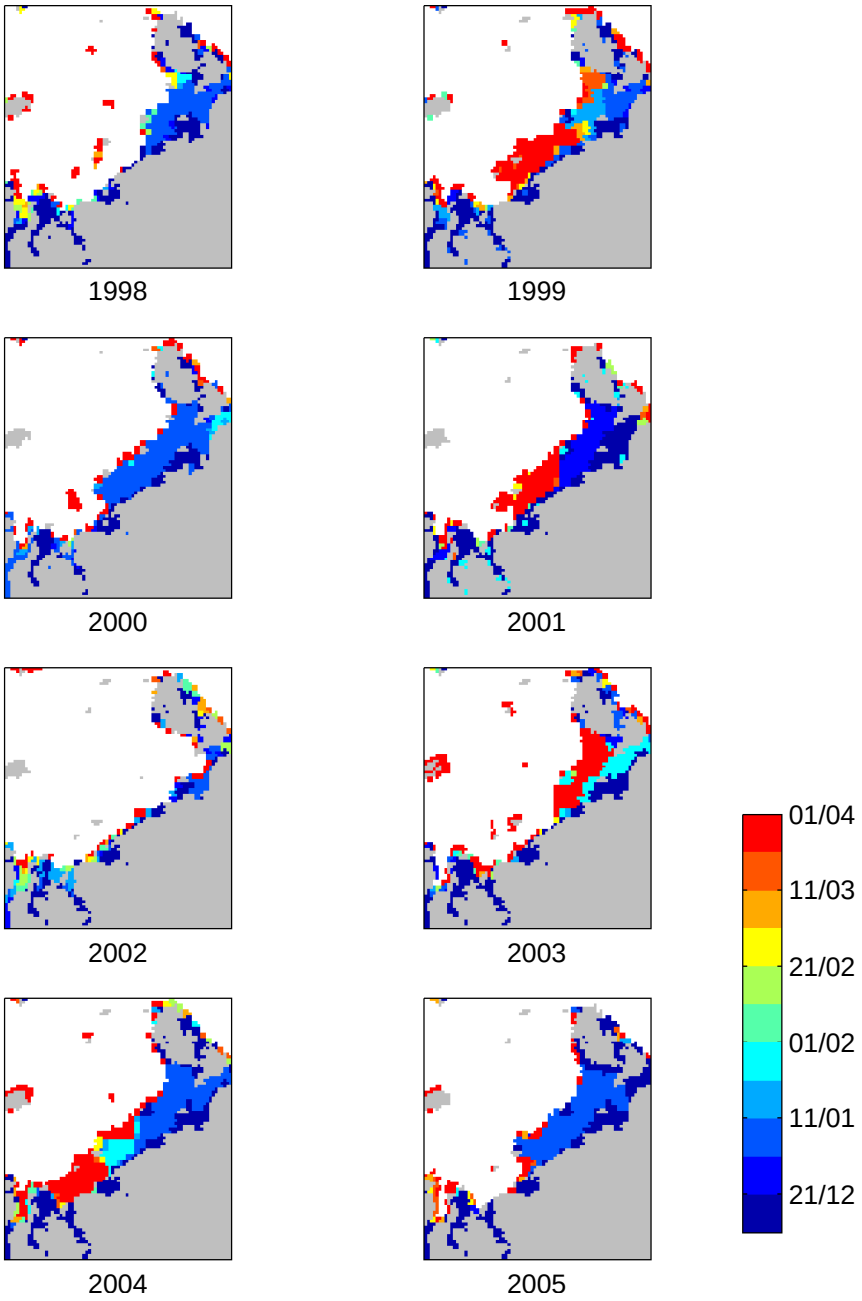

Figure 6.1: The observation period when stable fast ice is first observed in winter in the Severozemelsky region, according to the AARI observations.

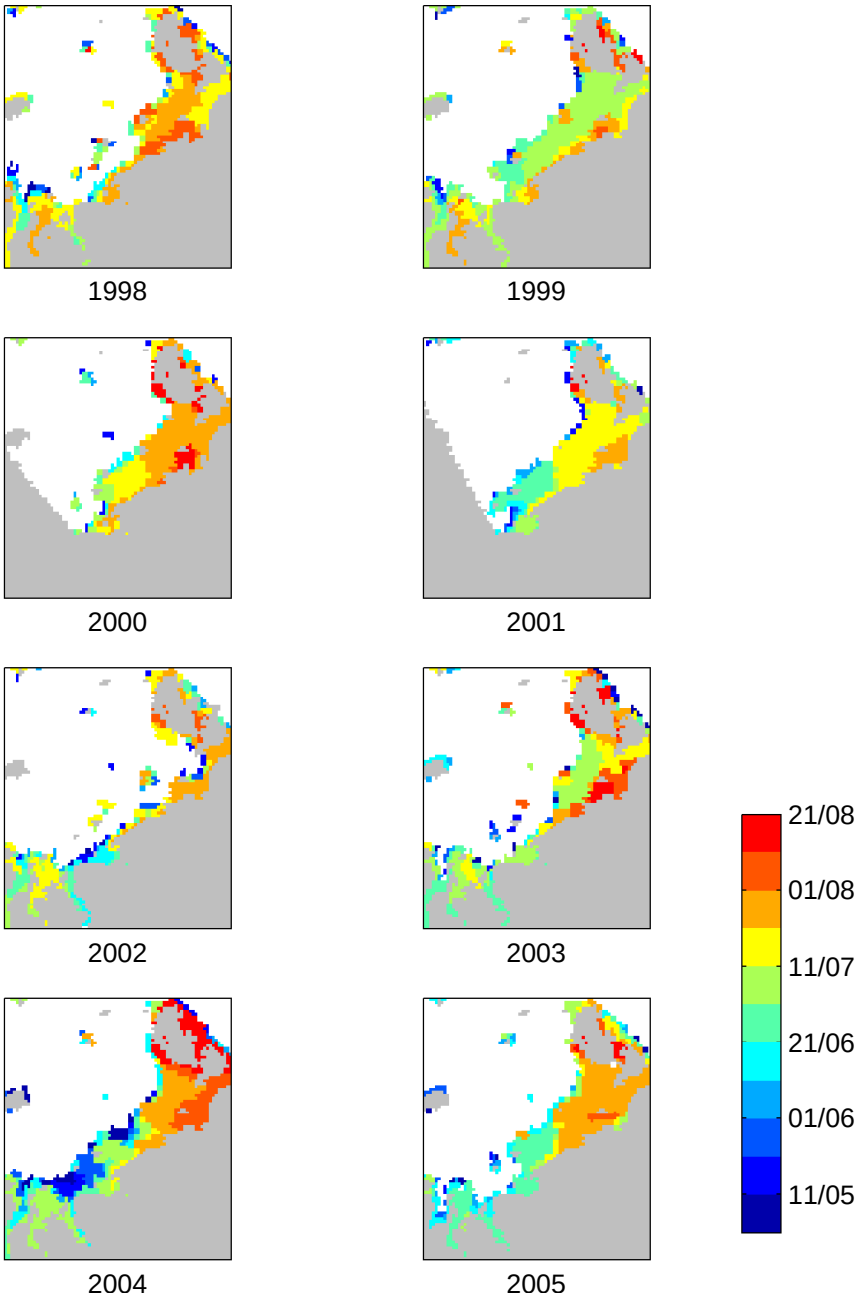

Figure 6.2: The observation period when fast ice is last observed in summer in the Severozemelsky region, according to the AARI observations

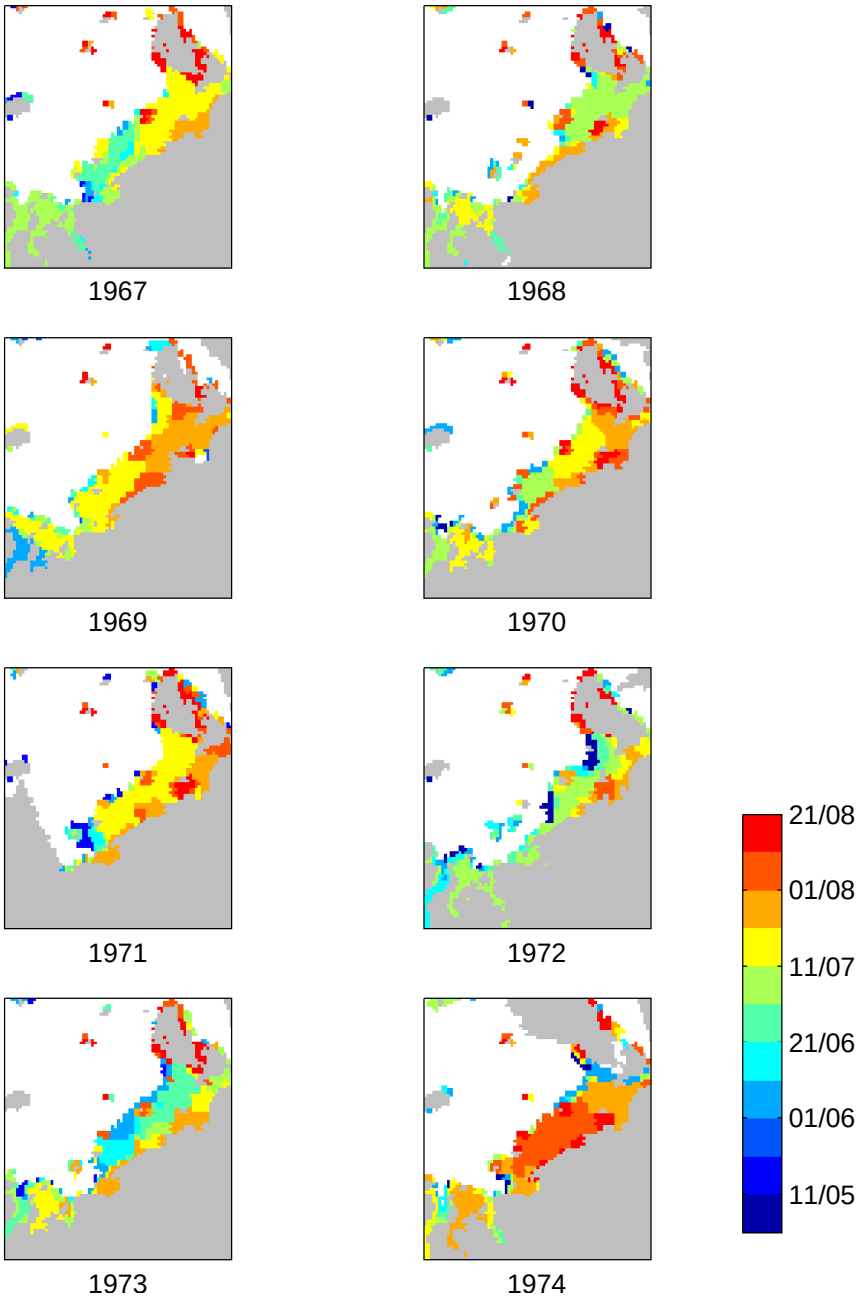

Figure 6.3: The observation period when fast ice is last observed in summer in the Severozemelsky region, according to the AARI observations

June, early July while the S-mode breaks up about a month later. In the eight year period considered here L-mode forms during 6 winters, compared to 5 winters in the 1998–2005 period.

Finally a minor discrepancy in figure 6.3 should be noted. In the panel for 1974 the L-mode is shown to break up after the first observation period in August, but the S-mode breaks up after the last observation period in July. This would mean that the S-mode breaks up before the L-mode, but this is in fact almost certainly not the case.

What happens is that during the last observation period of July the observations show an L-mode, but for the following observation (in the first period of August) no data is available for the S-mode area. That observation still shows the L-mode portion of the fast ice massive. In the observation following it, the one covering August 11^{th} to 20^{th} both the S- and L-modes have broken up leaving only traces of fast ice along the coast. Strictly speaking the last observation period where S-mode fast ice was observed is there fore the period of July 21^{st} to 31^{st}, but given the dynamics involved and the results of Divine et al. (2005) it is safe to assume that the S-mode does not break up before the L-mode, but rather at the same time.

6.3 Experiments

In order to test the model response over a longer time period two time periods were chosen using two different yield curves, a total of four experiments. As mentioned previously the two time periods are 1998–2005 and 1967–74, but in both cases the model was spun up for three years, the runs starting from the climatological average in fall 1994 and 1963 respectively. During the spin-up full ice dynamics and cohesive yield curves are used which means, in particular that the winters of 1997–98 simulated here should not necessarily be identical to those simulated in the previous chapter.

The two time periods were chosen to represent two extremes with respect to fast-ice extent, based on the results of Divine et al. (2003, 2004). The late 1960s and early 1970s were a period of large average fast-ice extent while the late 1990s and early 2000s were a period of comparatively small extent. Having tuned the model for the winter of 1997–98 it is also interesting to see how it fairs during the 1960s and 1970s. In particular, if the ice is thicker during the earlier period the fast ice should also be more stable and easier to reproduce in the model.

The two yield curves chosen were the FMC with $\phi = 30^\circ$ and $k_T = 0.22$ and the trimmed ellipse with $k_T = 0.08$ and the grounding scheme with $\Gamma = 5$. This setup of the FMC gives correct breakup times and fast-ice extent, but too thick ice in the Arctic Institute Islands Pass. The setup chosen for the trimmed ellipse does not give correct breakup times, but instead offers a realistic simulation of the ice in the Arctic Institute Islands

Pass. The two setups represent two extremes; the FMC giving strong ice while using the trimmed ellipse results in weak ice compared to other realistic setups.

In the following sections the results from the different experiments are introduced. First the results using the FMC for 1998–2005 are described followed by the results for the same setup, only using the trimmed ellipse and grounding scheme instead of the FMC. Section 6.3.3 then discusses the time period of 1967–74. To avoid going in to the same amount of detail as before only the fast-ice extent and evolution will be compared to observations, not the polynya formation. These results are then discussed in more detail in section 6.4. We will, in particular see how the relatively poor results achieved here can be attributed to underestimating the importance of ice grounding.

6.3.1 Flexible modified Coulombic yield curve

In the previous chapter it was shown that using the FMC yield curve with $\phi = 30^\circ$ and $k_T = 0.15$ produced both realistic breakup times and fast-ice extent for 1998 using the initial conditions imposed there. Figures 6.4 and 6.5 show that this is not the case here. Now, in 1998 the early part of the freeze-up phase is similar to that modelled previously (see figure 5.16), but in late March an erroneous L-mode becomes stable. This did not happen before. In addition to this both the L- and S-modes break up in late May here, but in the earlier experiment the S-mode survived until July. The only difference in the experimental setup between this simulation of the winter 1997–98 and the one discussed in the previous chapter is the initial conditions.

Out of the eight years considered here only in 2001 and 2002 is the modelled fast-ice extent reasonably close to the observed extent. In 2002 almost no fast ice is observed and the model does capture this, although the modelled fast-ice extent is somewhat larger than the observed one. In 2001 an L-mode is observed, which is mostly captured by the model. In addition to this an S-mode is modelled in 2000 and 2004, but an L-mode was observed in those years. In 1999, 2003 and 2005 the modelled fast ice occupies neither an S- nor L-mode. In 2001 and 2002 the fast-ice extent is therefore correct, while in 1998, 2000 and 2004 fast ice is present in the model, but in the wrong mode. This leaves the years 1999, 2003 and 2005, during which the modelled fast-ice extent is unrealistic.

With respect to formation and breakup times the freeze-up phase generally shows the same unrealistic breakups and reformations as observed before. The breakup generally occurs too early. The only year that shows correct formation times is 2004, although the modelled ice extent is an S-mode while the observed one is an L-mode. The S-mode correctly forms during the last ten days of December, but the L-mode either does not form or breaks up again before April 1$^{\text{st}}$. The most westerly portion of the S-

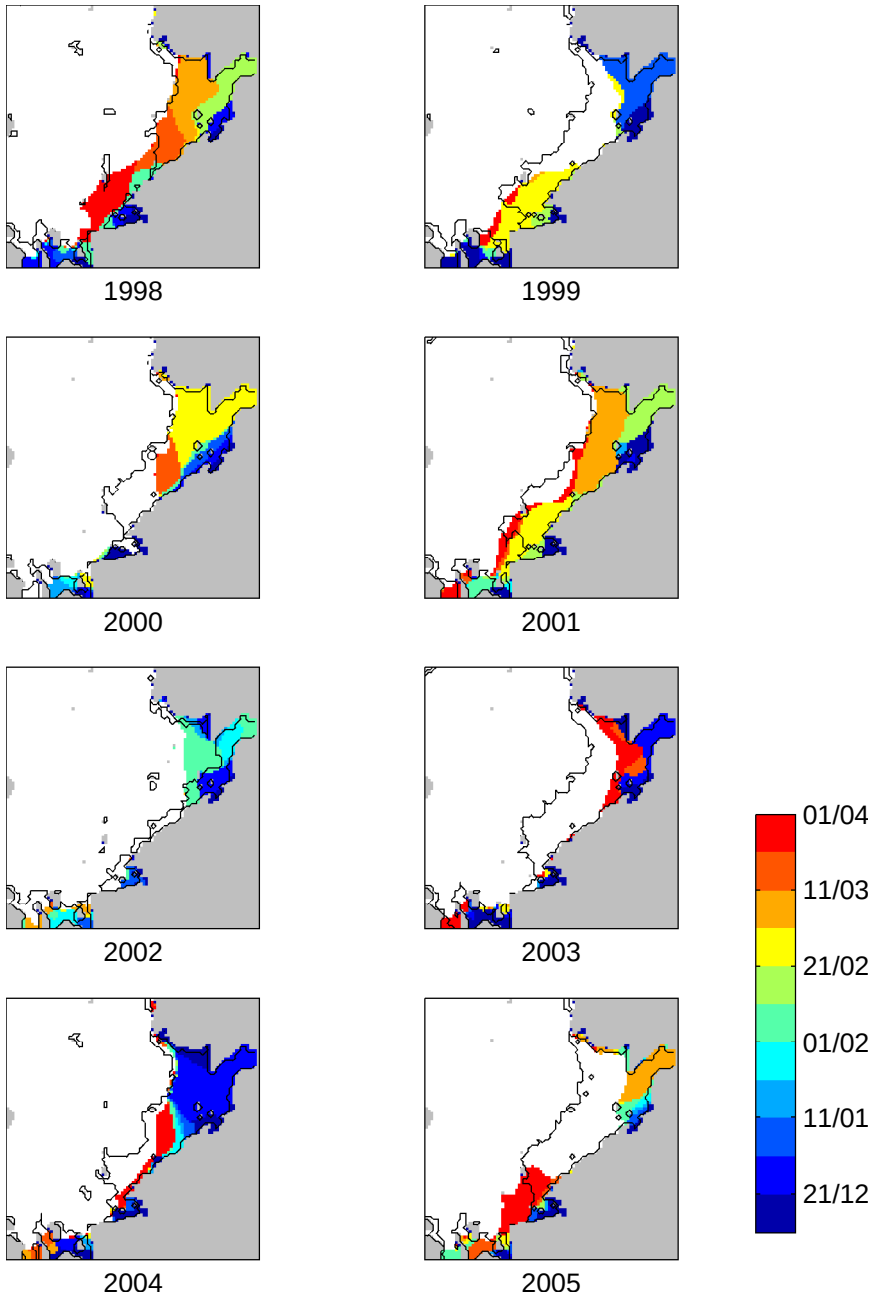

Figure 6.4: The day land-fast ice becomes stable in winter during the years 1998–2005 using the FMC. The solid line marks the fast-ice extent according to the AARI data for the first observation period in April. In the white areas no fast ice is formed.

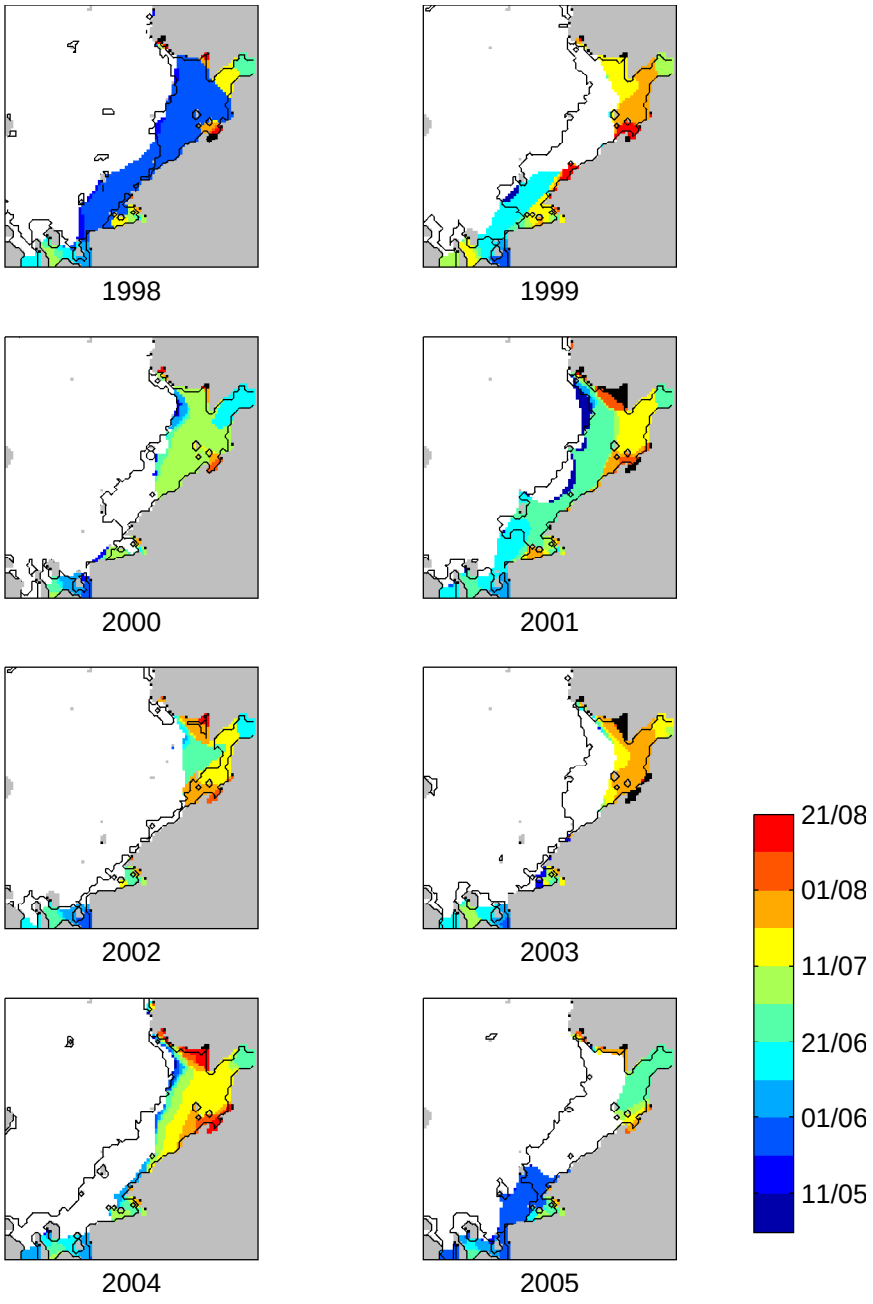

Figure 6.5: The day land-fast ice breaks up in summer during the years 1998–2005 using the FMC. The solid line marks the fast-ice extent according to the AARI data for the first observation period in May. In the white areas no fast ice is formed and the black patches mark areas of fast ice that survives beyond August 21st.

mode also suffers a few partial breakups and reformations in January and then again in March. The breakup in 2004 is also well timed; occurring in the middle of July, approximately ten days early compared to the observations.

6.3.2 Trimmed ellipse

In chapter 5 the trimmed ellipse was found to give the best results with respect to drifting ice in the Arctic Institute Islands Pass and polynya formation. The fast-ice extent was also accurately modelled, but the breakup time was not. Using the grounding scheme further improved the polynya simulation. The trimmed ellipse is of interest here, even though the quality of the polynya simulation will not be considered specially. This is because the trimmed ellipse offered stable fast ice at lower uniaxial compressive strength than the other yield curves. The fast ice is therefore weaker and in particular weaker than when using the FMC. In the experiments discussed here the cohesive strength under isotropic divergence was set to $k_T = 0.08$ and the grounding parameter to $\Gamma = 5$, as per the results of the previous chapter.

Unlike the FMC the trimmed ellipse gives nearly identical results for the winter 1997–98 here compared to the results from section 5.4.4 (see figures 6.6 and 6.7). The modelled fast-ice extent follows the S-mode outline correctly, but multiple partial breakups occur during the freeze-up and the fast ice breaks up too early in summer.

Using the trimmed ellipse an L-mode is never modelled, but an S-mode is modelled in 1998, 2001 and 2005. In 2001 and 2005 an L-mode is observed, so 1998 is the only year the model captures the right fast-ice mode. In 2002 fast ice is only modelled inland of the Nordenskiöld Archipelago, but observations show it to block the Vilkitsky strait as well. The remaining years (1999, 2000, 2003 and 2004) the modelled fast ice unrealistically occupies none of the predefined modes.

During the freeze-up every modelled year shows unrealistically late breakups compared to the observations. The breakup time is also incorrectly simulated for all the years. The breakups in 2001 and 2005 are still better timed than that in 1998, which occurs two months too early. In 2001 the modelled ice breaks up about 20 days too early and in 2005 it breaks up about 10 days early, with a partial breakup 30 days too early. Overall the results using the trimmed ellipse and the grounding scheme are decidedly worse in the years 1999-2005 than in 1998, for which the model was tuned.

6.3.3 The winters of 1967–74

The second time period considered here is 1967–74, a period when the mean winter fast-ice extent has been shown to be larger than otherwise (Divine et al., 2003, 2004). During this time period the AARI ice charts do not properly cover the freeze-up phase and so we will focus on the April extent

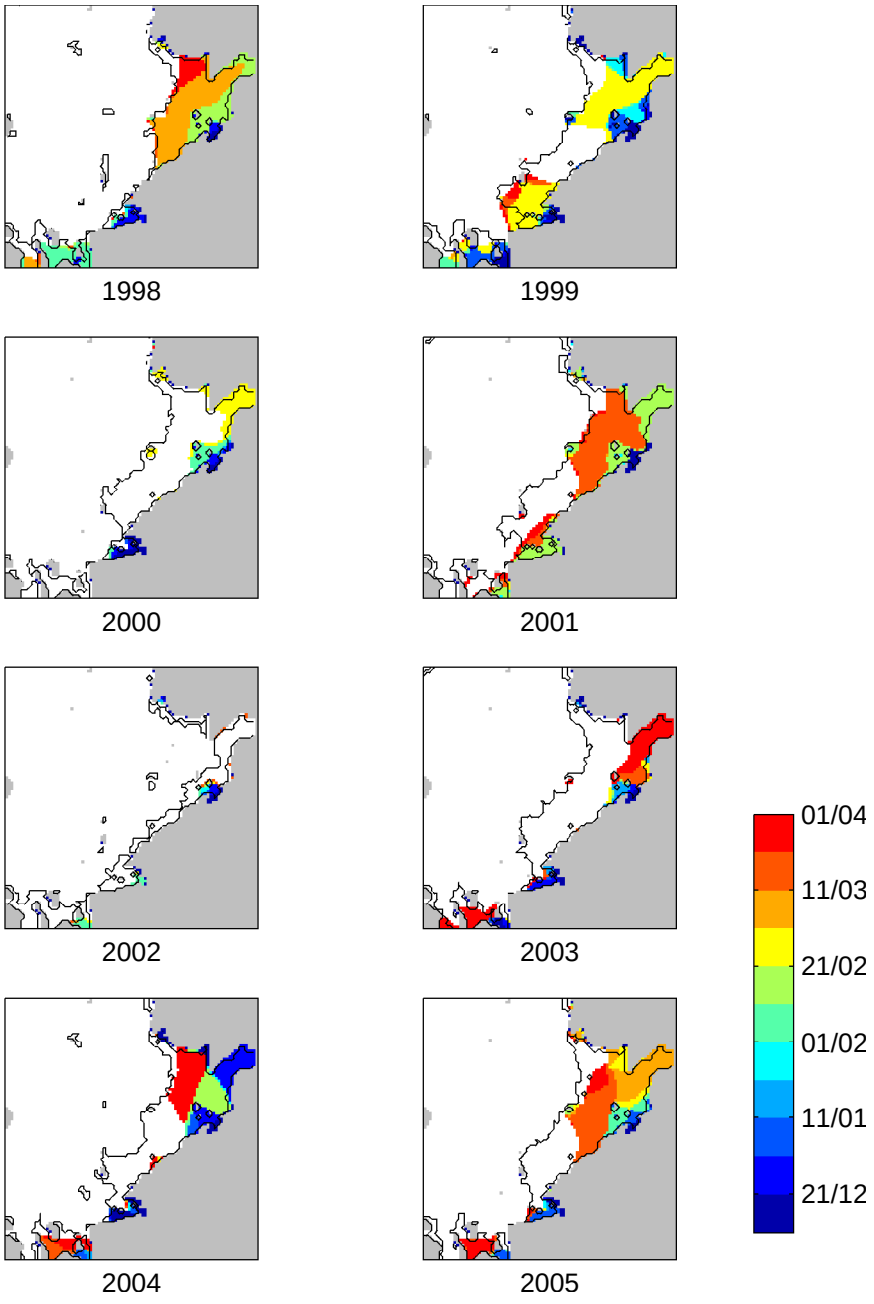

Figure 6.6: The day land-fast ice becomes stable in winter during the years 1998–2005 using the trimmed ellipse and grounding scheme. The solid line marks the fast-ice extent according to the AARI data for the first observation period in April. In the white areas no fast ice is formed.

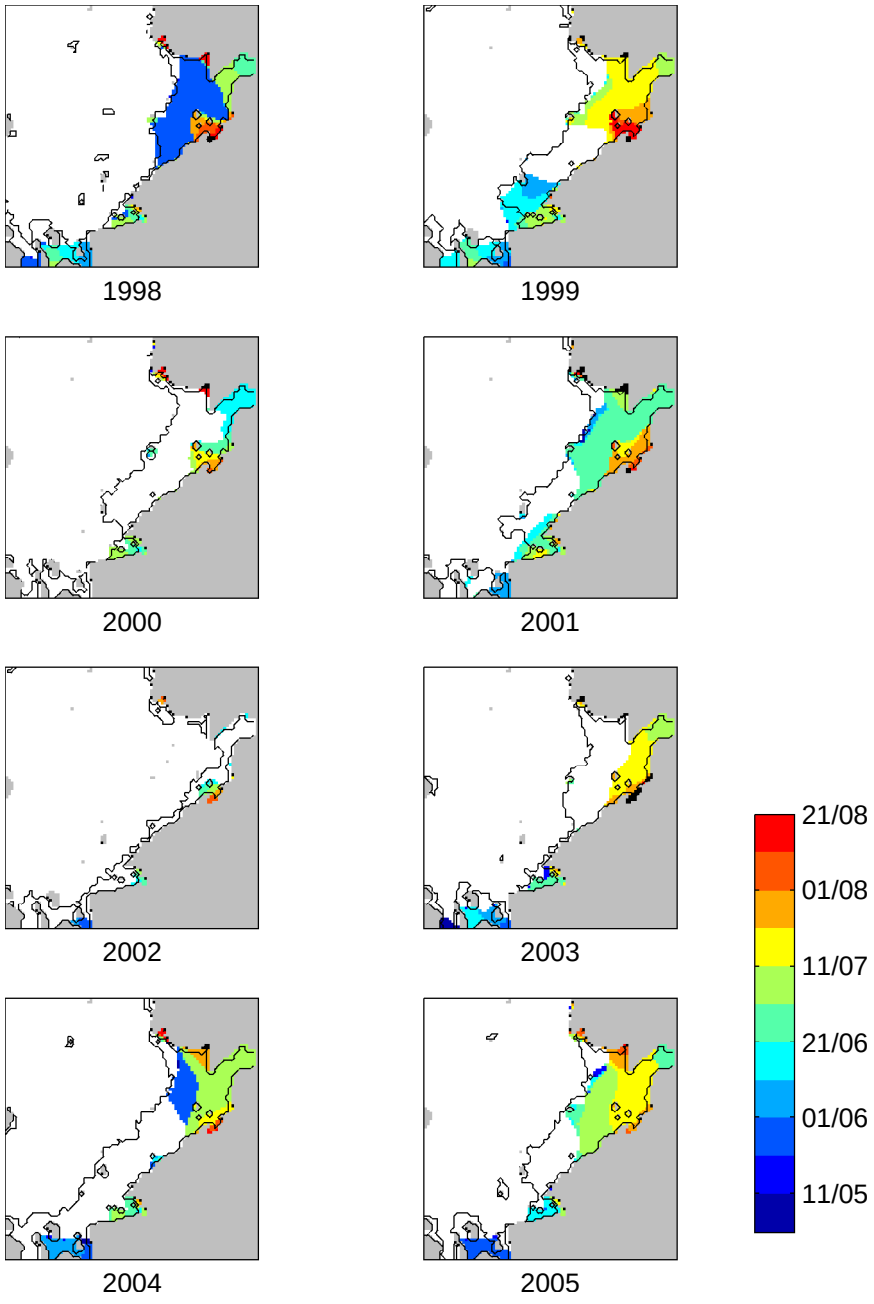

Figure 6.7: The day land-fast ice breaks up in summer during the years 1998–2005 using the trimmed ellipse and grounding scheme. The solid line marks the fast-ice extent according to the AARI data for the first observation period in May. In the white areas no fast ice is formed and the black patches mark areas of fast ice that survives beyond August 21st.

and breakup times here.

Starting with the FMC the model only produces accurate results for 1969 (see figure 6.8). This year an L-mode is observed in April and also produced in the model. According to the observations the L-mode breaks up during the July 11^{th} to 20^{th} observation period with the S-mode breaking up during the following observation period. In the model both the L- and S-modes break up during the July 11^{th} to 20^{th} observation period leaving only the fast ice in the Vilkitsky strait to break up in the following observation period. The modelled fast-ice extent during the July 21^{st} to 31^{st} observation period is therefore too small, but the breakup times are otherwise correct.

In 1970, 1971 and 1973 an S-mode forms in the model but an L-mode is observed. In 1971 the modelled ice actually forms a sort of a broken L-mode with an S-mode and a block of fast ice between the Arctic Institute Islands, Sverdrup Islands and the coast. The fast ice that is observed between the Arctic Institute and Sergey Kirov Islands is not captured in the model. The fast ice inland of the Arctic Institute Islands breaks up in early May along with half the S-mode fast ice. The S-mode presumably reforms and the rest of it breaks up during the July 11^{th} to 21^{st} observation period, the same period S-mode (and L-mode) fast ice is last observed in 1971.

The modelled breakup time of the S-mode in 1970 is mostly correct, although the ice inland of the Nordenskiöld Archipelago does survive longer than observed. In 1973 the fast ice is observed to break up unusually early or in the last observation period of June. The model does not capture this early breakup and in it the fast ice breaks up about a month later. The remaining years (1967, 1968 and 1974) the modelled fast-ice extent is always less than the S-mode extent.

The trimmed ellipse gives weaker ice than the FMC, even with the grounding scheme. This means in particular that the L-mode that forms in 1969 breaks up too early and is smaller than when using the FMC (see figure 6.9). The breakup of the S-mode portion of the ice is similar to that modelled with the FMC. The fast-ice extent is also smaller during the other model years, but in 1971 the S-mode is more stable using the trimmed ellipse and the grounding scheme. Using the trimmed ellipse an L-mode is only modelled in 1969 and an S-mode only in 1971. During all other years the fast-ice extent is less than that of the S-mode. The trimmed ellipse, therefore, clearly gives worse results than the FMC for this time period.

6.4 Discussion

Considering the results of these experiments there are two main results that warrant further discussion. First of all is the overall poor ability of the model to simulate realistic fast ice for other years than that of 1998, for which it was tuned. This will be shown to be the result of underestimating

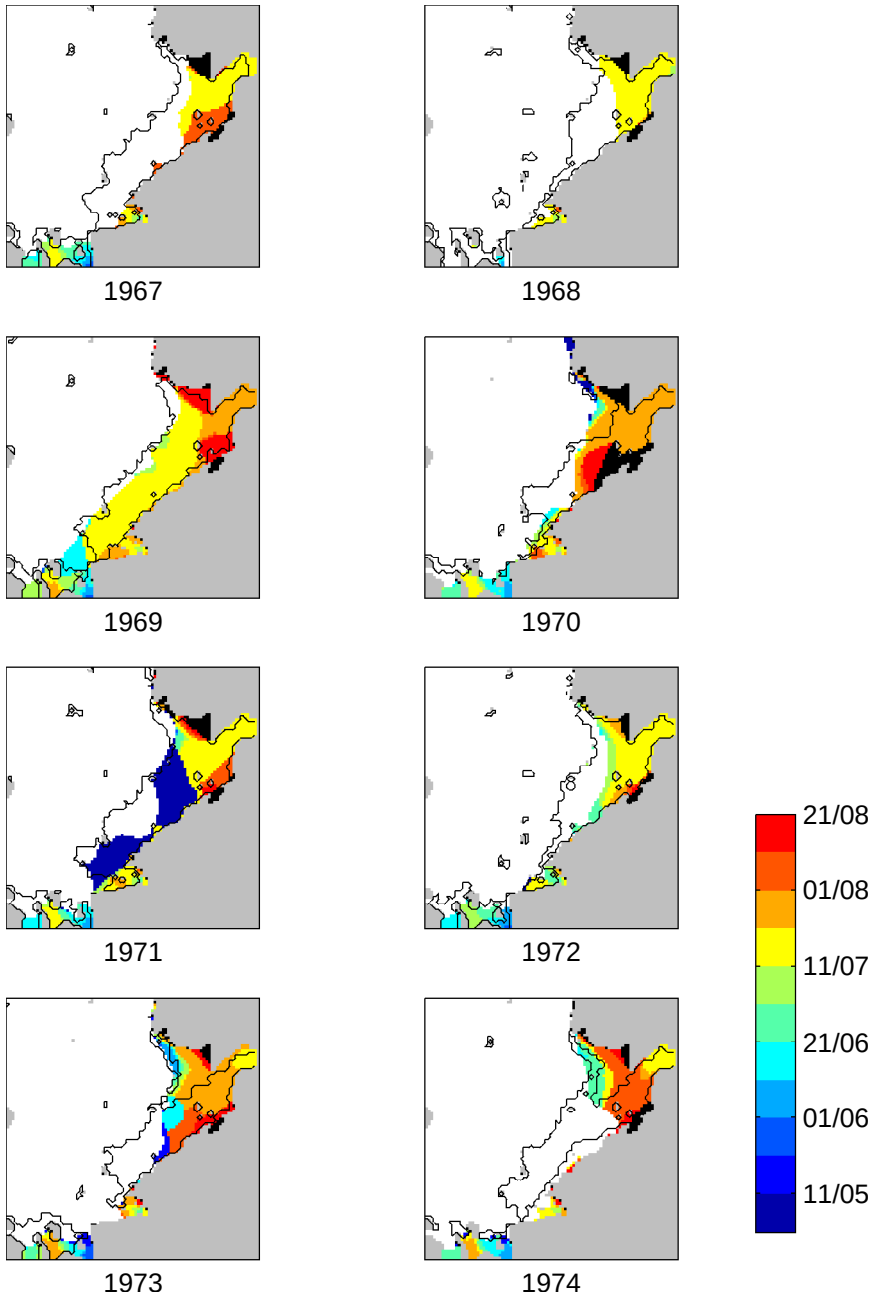

Figure 6.8: The day land-fast ice breaks up in summer during the years 1967–74 using the FMC. The solid line marks the fast-ice extent according to the AARI data for the first observation period in May. In the white areas no fast ice is formed and the black patches mark areas of fast ice that survives beyond August 21st.

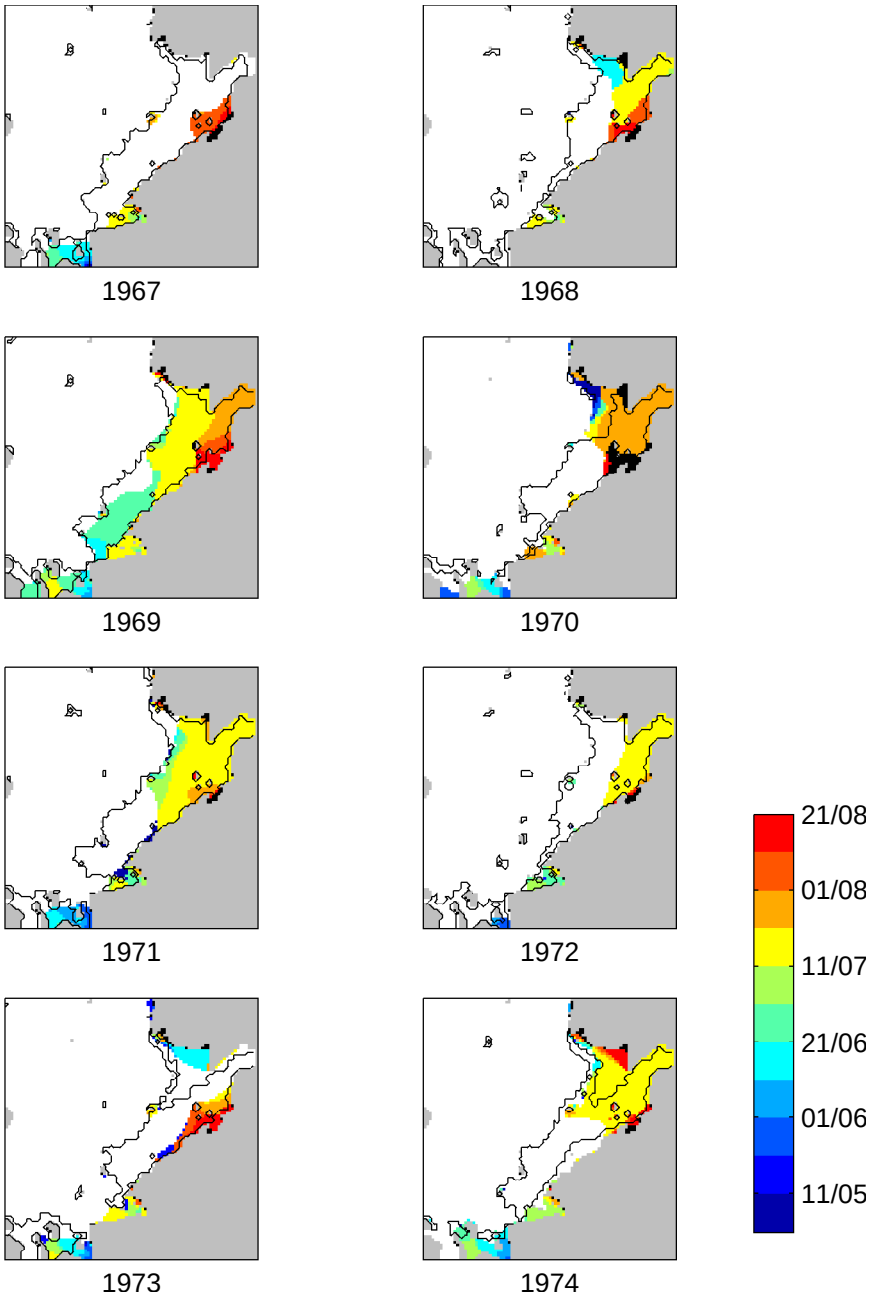

Figure 6.9: The day land-fast ice breaks up in summer during the years 1967–74 using the trimmed ellipse and grounding scheme. The solid line marks the fast-ice extent according to the AARI data for the first observation period in May. In the white areas no fast ice is formed and the black patches mark areas of fast ice that survives beyond August 21st.

the role of ice grounding. It is also interesting to see that the fast-ice extent modelled here for 1998 using the FMC is substantially different from that modelled in the previous chapter. This raises questions about the effects the land-fast ice has on the ocean and the land-fast ice's sensitivity to the oceanic forcing.

In this section three topics will be discussed; ice strength, critical ice thickness and ice-ocean interaction. In the section on ice strength we discuss the fact that the modelled ice appears to be too weak. To solve this the FMC is used along with the grounding scheme and increased maximum viscosity. This approach gives much better results than those already introduced. In the following section these improved results are then used to give an estimate of the minimum ice thickness needed for fast ice to form. Finally the influences of the cohesive yield curves on ice-ocean interaction are discussed.

6.4.1 Ice strength

Let us first consider the reason behind the relatively poor results shown in section 6.3, compared to those of the previous chapter. First of all the problem is clearly that the ice is too weak. Using the FMC, which gives stronger ice than the trimmed ellipse, too little fast ice is modelled for 12 out of the 16 years considered here. Only in 1998 is the modelled fast-ice extent considerably larger than the observed one. In 1969 and 2001 the modelled fast-ice extent is similar to the observed one while in 1970, 1971, 1973, 2000 and 2004 an L-mode is observed at the height of winter, but the model simulations result in an S-mode.

When judging the model's performance in these longer runs three basic criteria should be considered. Firstly one should consider if the model produces realistic fast ice at all; i.e. either an S- or an L-mode should form, in keeping with the general characteristics of the fast-ice cover. In this respect the FMC succeeds in nine out of sixteen modelled years. The second criteria is that of inter-annual variability; i.e. whether the right mode is modelled at the right time. In this respect the model fairs much worse, giving the correct result for only three years out of sixteen. Finally formation and breakup times should be considered, but these times proved difficult to model in the previous chapter. Only in 2004 does the model reproduce the observed formation times[1]. In addition the breakup times are modelled within some 10 days of the observed date during three model years; 1969, 1970 and 2004.

If the ice is simply too weak then tuning the yield curve or changing it should have a positive effect. This could give unrealistic results for 1998, but a set of parameters should be found that would maximise the number of years that give correct fast-ice extent. Such an exercise is very costly, both

[1] Formation times cannot be deduced for the earlier period; 1967–74

with respect to time and computing resources and so it is not undertaken here.

It is, however, possible to test a different year from 1998 and to do this the suite of experiments performed in the previous chapter was re-run for the winter 1998–99. As before the model was started in fall and initialised using the model state from the simplified-dynamics control-run described in section 4.3. Using the elliptic yield curve and $e = 1.4$, $k_T = 0.09$ or $k_T = 0.10$ gave correct fast-ice extent and good breakup times. The other yield curves did not give realistic fast-ice extent for the values tested and no further effort was made to adjust them, since using more cohesive strength is known to cause unrealistic drift-ice behaviour. Unfortunately, using the ellipse with such a small value for e or large for k_T is also known to cause unrealistic drift-ice behaviour.

In order to try and increase the ice strength through other means tests were performed using the FMC and the parameter settings used in section 6.3.1, together with the grounding scheme and increased maximum viscosity. For 1999 including the grounding scheme (with $\Gamma = 5$) stabilised the fast ice so that an L-mode is modelled, but an L mode was also observed for the height of the fast-ice season. Increasing the maximum viscosity to $\zeta_{\max} = (10^{17}\text{ s})P$ did not have a marked effect. This value is four orders of magnitude larger than the optimal value found in section 5.3.1 and nine orders of magnitude larger than the value used by Hibler (1979). Given the results of section 5.3.1 it is unlikely that using a larger value will improve the model performance.

Given these results two additional runs were performed for the period 1998–2005 using the FMC. In one the grounding scheme, with $\Gamma = 5$ was used and in the other the maximum viscosity was set to $\zeta_{\max} = (10^{17}\text{ s})P$, in addition to using the grounding scheme. Here the non-linear nature of the model again becomes apparent since the results of the long-term run are not the same as that of the shorter test performed before. When modelling the winter 1998–99 only, an L-mode was modelled using either $\zeta_{\max} = (10^{13}\text{ s})P$ or $\zeta_{\max} = (10^{17}\text{ s})P$. In the long term run, where the model is spun up using the cohesive yield curve, an L-mode is only modelled in 1999 when the maximum viscosity is set to $\zeta_{\max} = (10^{17}\text{ s})P$. In all other years the difference between the two runs is minimal. Based on this a run was performed for 1967–74 using the grounding scheme and $\zeta_{\max} = (10^{17}\text{ s})P$. The results from these runs are shown in figures 6.10–6.13.

The results using the FMC, with the grounding scheme and increased maximum viscosity are markedly better than those presented earlier. For the sixteen years considered here either an S- or an L-mode is modelled for fifteen. This leaves out the year 2002 when no S-mode ice is observed. That year the modelled ice is smaller than the S-mode, but larger than the observed extent (see figures 6.10 and 6.11). Overall the basic fast-ice behaviour is therefore well captured.

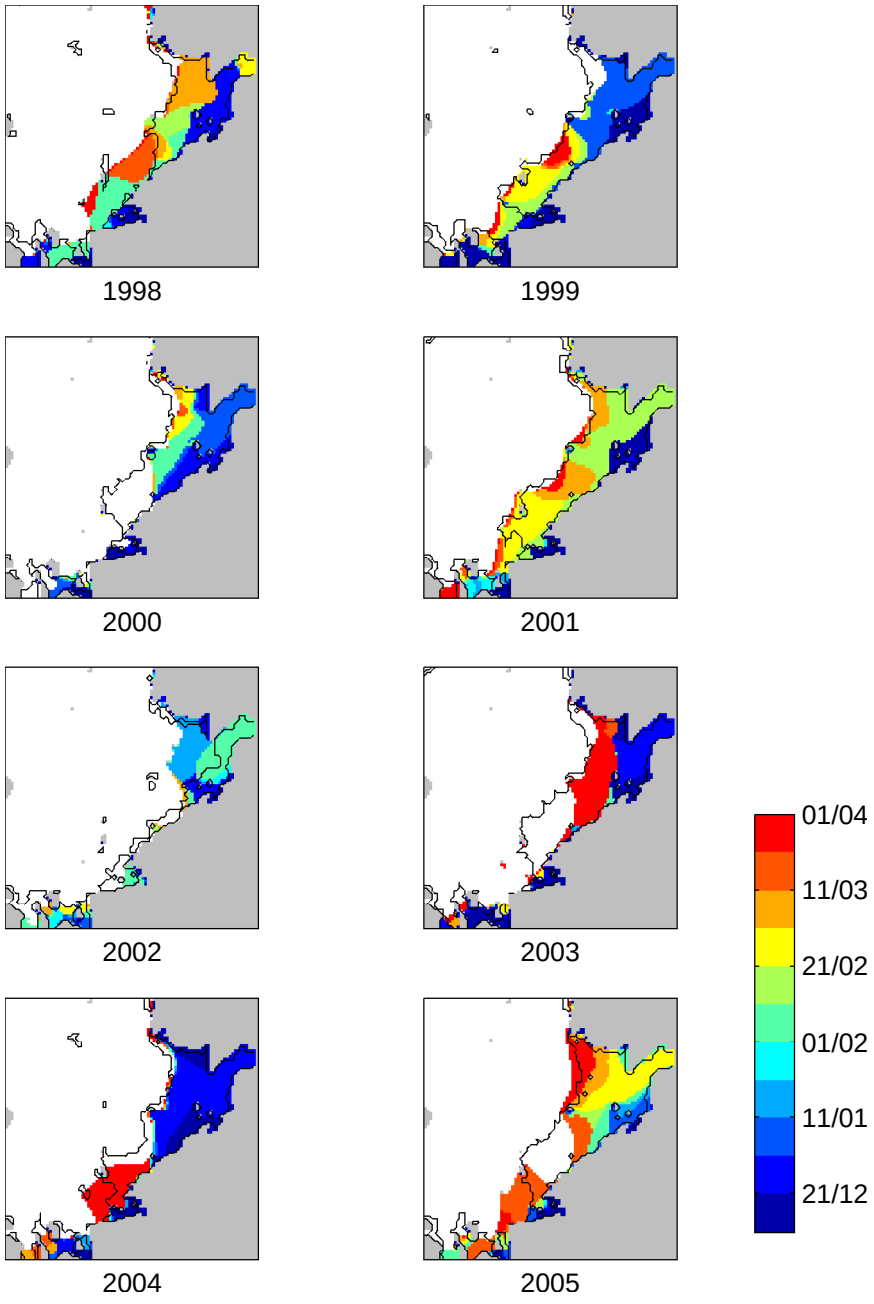

Figure 6.10: The day land-fast ice becomes stable in winter in 1998–2005 using the FMC with increased maximum viscosity and using the grounding scheme. The solid line marks the fast-ice extent according to the AARI data for the first observation period in April. In the white areas no fast ice is formed.

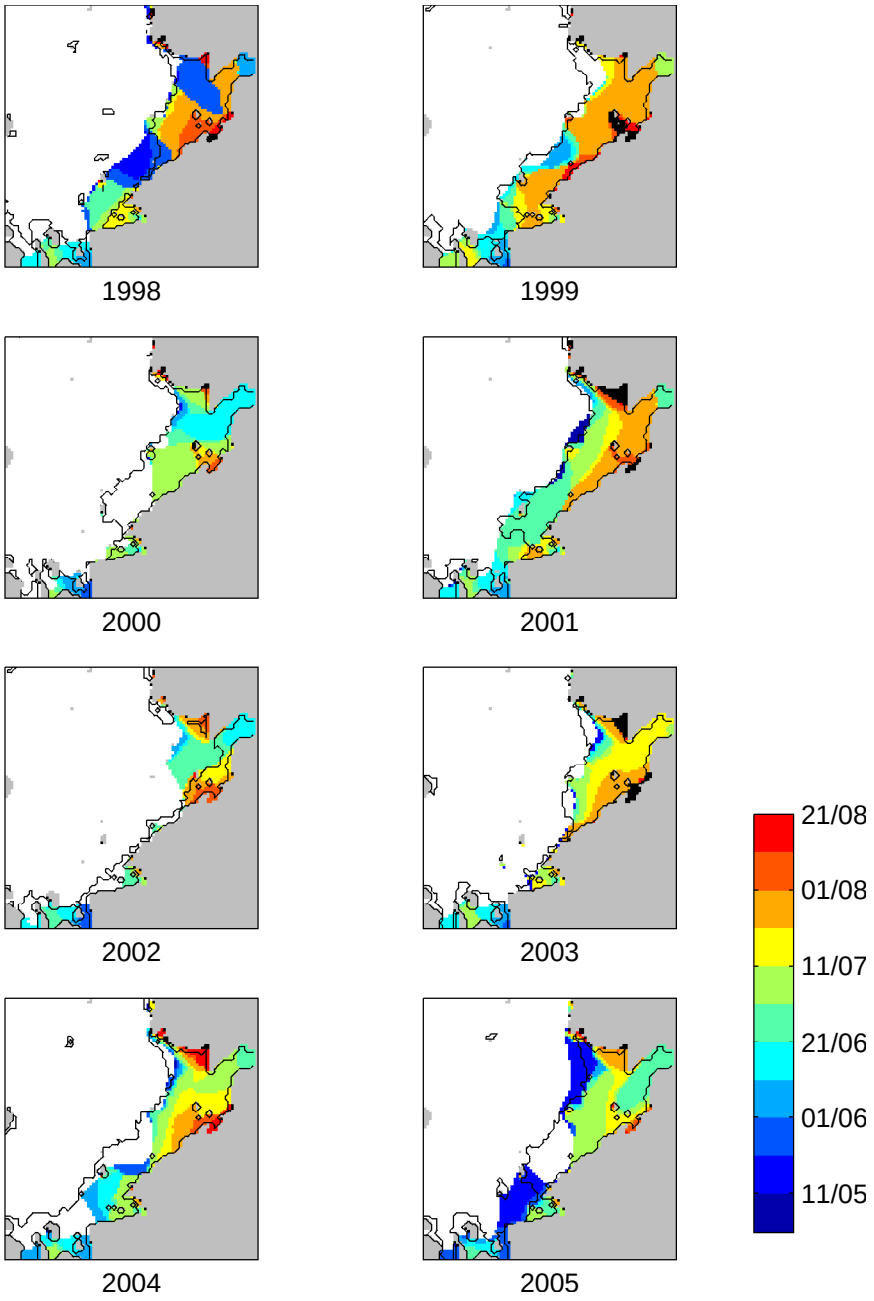

Figure 6.11: The day land-fast ice breaks up in summer in 1998–2005 using the FMC with increased maximum viscosity and using the grounding scheme. The solid line marks the fast-ice extent according to the AARI data for the first observation period in May. In the white areas no fast ice is formed and the black patches mark areas of fast ice that survives beyond August 21st.

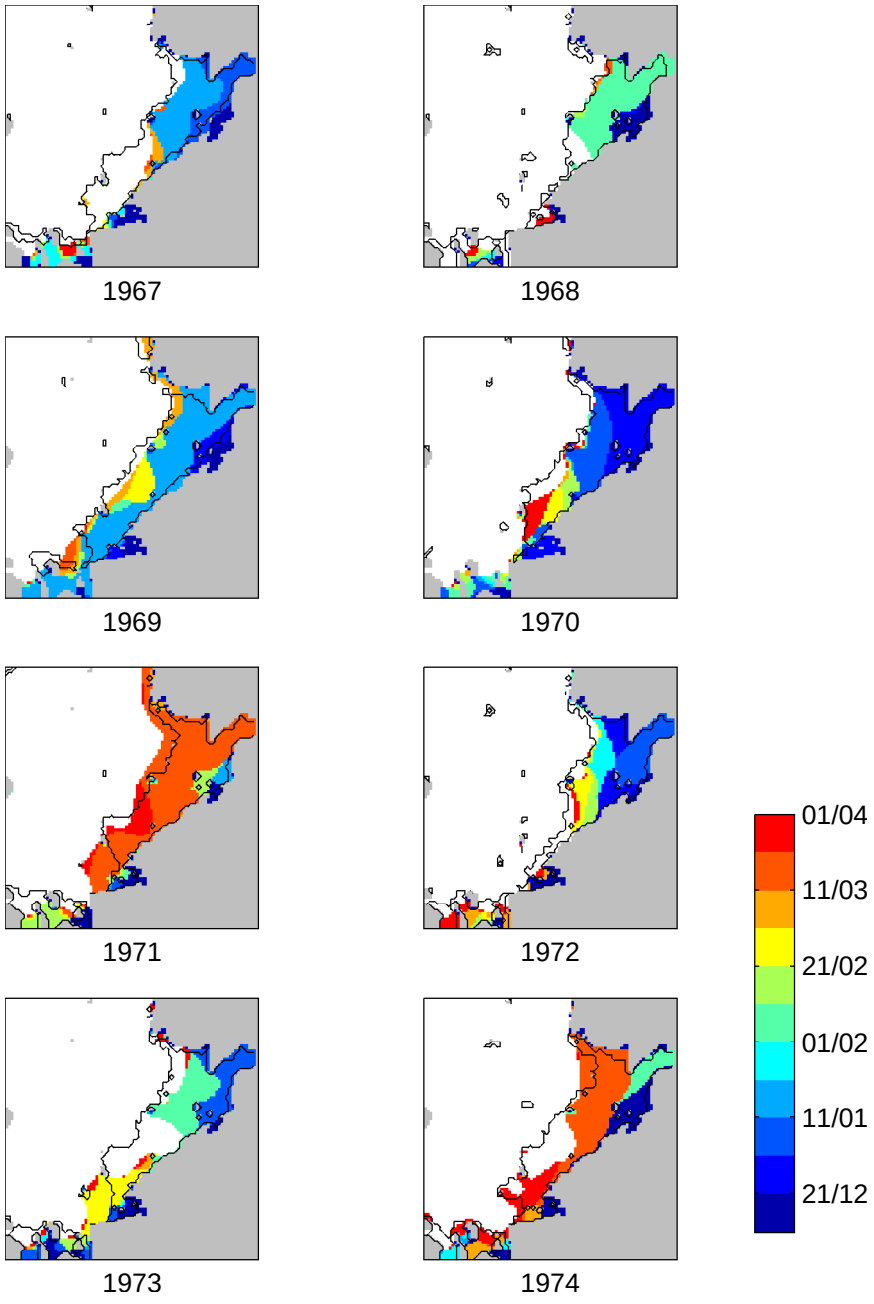

Figure 6.12: The day land-fast ice becomes stable in winter in 1967–74 using the FMC with increased maximum viscosity and using the grounding scheme. The solid line marks the fast-ice extent according to the AARI data for the first observation period in April. In the white areas no fast ice is formed.

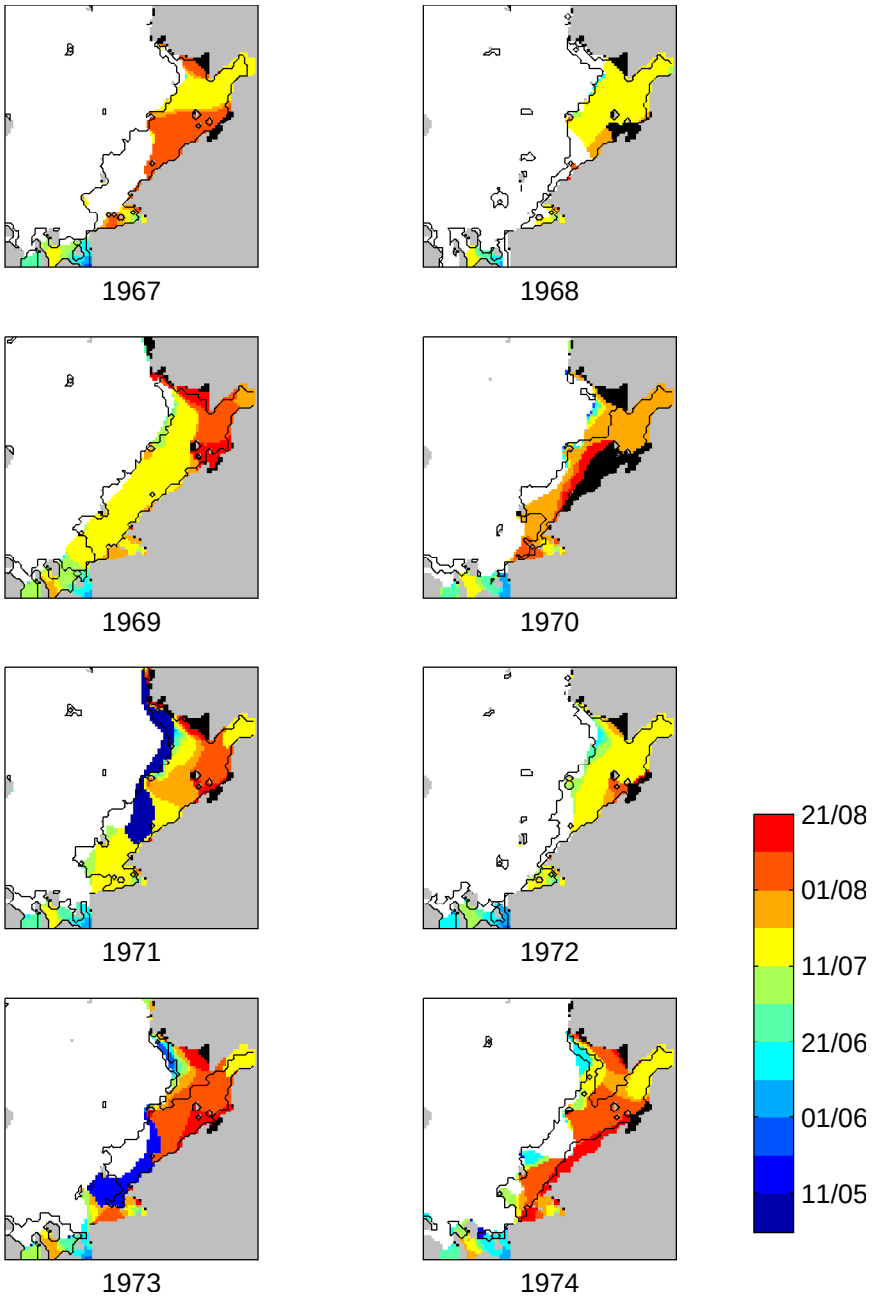

Figure 6.13: The day land-fast ice breaks up in summer in 1967–74 using the FMC with increased maximum viscosity and using the grounding scheme. The solid line marks the fast-ice extent according to the AARI data for the first observation period in May. In the white areas no fast ice is formed and the black patches mark areas of fast ice that survives beyond August 21st.

The inter-annual variability is not captured as well by the model. Out of the sixteen years the correct mode is modelled for seven, which is still a marked improvement compared to three years earlier. Finally the right formation times (to within about 10 days) are modelled in 1999 (S-mode only), 2003 and 2004, but the correct breakup time is never really captured in the 1998–2005 period. Despite this the modelled breakup is only in 1998 more than a month off and in that year it is only a partial breakup that occurs early. In 1967–74 the correct breakup time is captured by the model in 1968, 1969, 1972 and 1974 a considerably better performance than in the period 1998–2005. In 1967–74 the formation time was not observed.

To conclude it is clear that using the grounding scheme and increased maximum viscosity greatly improves the model results. Here the grounding scheme is a vital part of the fast-ice formation, but in the previous chapter its role appeared to be minimal. The grounding of pressure ridges therefore appears to increase the stability of the fast-ice massive and clearly deserves a closer look.

These new results open the doors to further investigations into various topics, but these are mostly outside the current scope, but in the following section the idea of a critical thickness will be addressed. There an estimate is given for the minimum ice thickness needed to support fast-ice formation. Should such a critical thickness exist then knowing it can give an indication of whether the Severozemelsky fast ice can be expected to be present in a future warmer climate.

6.4.2 Critical thickness

These improved results can now be used to try and estimate a critical thickness, h_c for fast-ice formation in the Severozemelsky area. The idea is that a certain critical ice thickness must be reached in order for the ice to become land fast. This thickness is independent of the time period; during colder years the ice will grow faster and simply become land fast earlier. It is, on the other hand almost certainly dependent on location.

Using the algorithm developed to track the temporal evolution of the fast-ice cover in the model it is trivial to track the thickness dependence as well. The modified program simply registers both the time of formation or breakup and the ice thickness when this occurs. In this manner a map can be produced showing the ice thickness in each model point when the ice becomes land fast and when it breaks up. Figures 6.14 to 6.17 show such maps for the FMC with the grounding scheme and increased maximum viscosity. The figures show considerable spatial variability in h_c during the fast-ice formation phase, especially in 1998–2005. The breakup thickness is less varied. This is a result of the partial breakups and reformations seen during the formation phase, a feature of the model not seen in the observations. The modelled breakups tend to be more uniform with all of

the fast-ice massive collapsing at the same time under the applied wind stress.

The incorrect model behaviour during the formation phase can be due to dynamical or thermodynamic problems in the model. If the cause is predominantly dynamical then the ice thickness is correct, but the formation time is wrong because the ice is too weak. The algorithm proposed here would therefore overestimate the critical thickness since the fast ice becomes stable some time after it has reached the critical thickness. If the cause is primarily due to thermodynamical problems then the ice thickness is wrong, but the breakup time is wrong precisely because the ice thickness is wrong. The proposed algorithm would therefore give the right critical thickness. For the breakup the same is true; i.e. if the thermodynamics are wrong then the critical thickness is still right and if the dynamics are wrong then the critical thickness will be overestimated.

A more useful way of looking at the formation and breakup thickness is to consider a histogram of the recorded thickness. Figure 6.18 shows four such histograms; for h_c during fast-ice formation and breakup in 1967–74 and 1998–2005. To exclude fast-ice formation in the river estuaries only points north of Dickson are considered. Due to temporal and spatial variations in ice thickness and wind strength one would expect a histogram of h_c to show an approximately normal distribution around a given mean $\bar{h}_c$, which would then be the critical mean thickness in the Severozemelsky region.

The two histograms for the breakup period show just such a behaviour with $\bar{h}_c = 117$ cm for 1967–74 and $\bar{h}_c = 116$ cm for 1998–2005. The standard deviation is 37 cm and 36 cm respectively. During the formation phase in 1967–74 the histogram is approximately normally distributed as well, but the mean is considerably higher with $\bar{h}_c = 143$ cm and standard deviation of 33 cm. The histogram distribution for the formation phase in 1998–2005 is much flatter than the others, more reminiscent of a smoothed step-function than a normal distribution. This is consistent with the gradual build up of fast ice seen in these years and the probability distribution function (pdf) is therefore most likely a combination of two normal distributions; one centred around h_c when fast ice starts forming and the other around h_c when the fast ice is fully formed. The first coincides approximately with h_c retrieved from the breakup periods while the other coincides with h_c retrieved from the formation period in 1967–74.

The difference in $\bar{h}_c$ for the breakup and formation times is most likely a testimony of the difference in atmospheric conditions during the two periods. The fast ice is broken up by cyclones and in the Arctic winter cyclones are more intense than summer ones (see e.g. Sorteberg and Walsh, 2008). The fast ice can therefore remain thinner in summer without breaking up, compared to winter.

There is also a telling difference between the pdf for formation in 1967–74 and 1998–2005. In 1967–74 the distribution is close to normal because

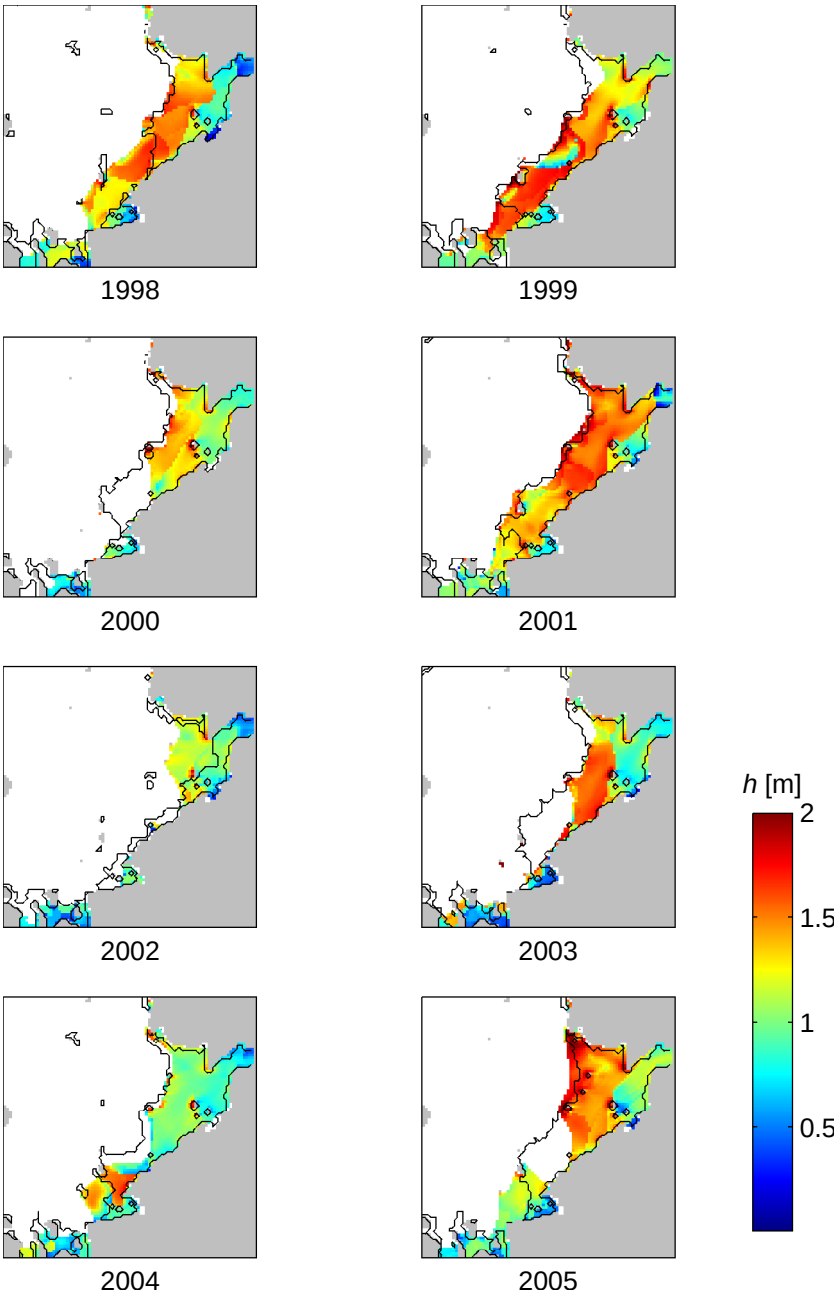

Figure 6.14: The ice thickness when the fast ice becomes stable in winter during the 1998–2005 period. The solid line marks the fast-ice extent according to the AARI data for the first observation period in April. In the white areas no fast ice is formed.

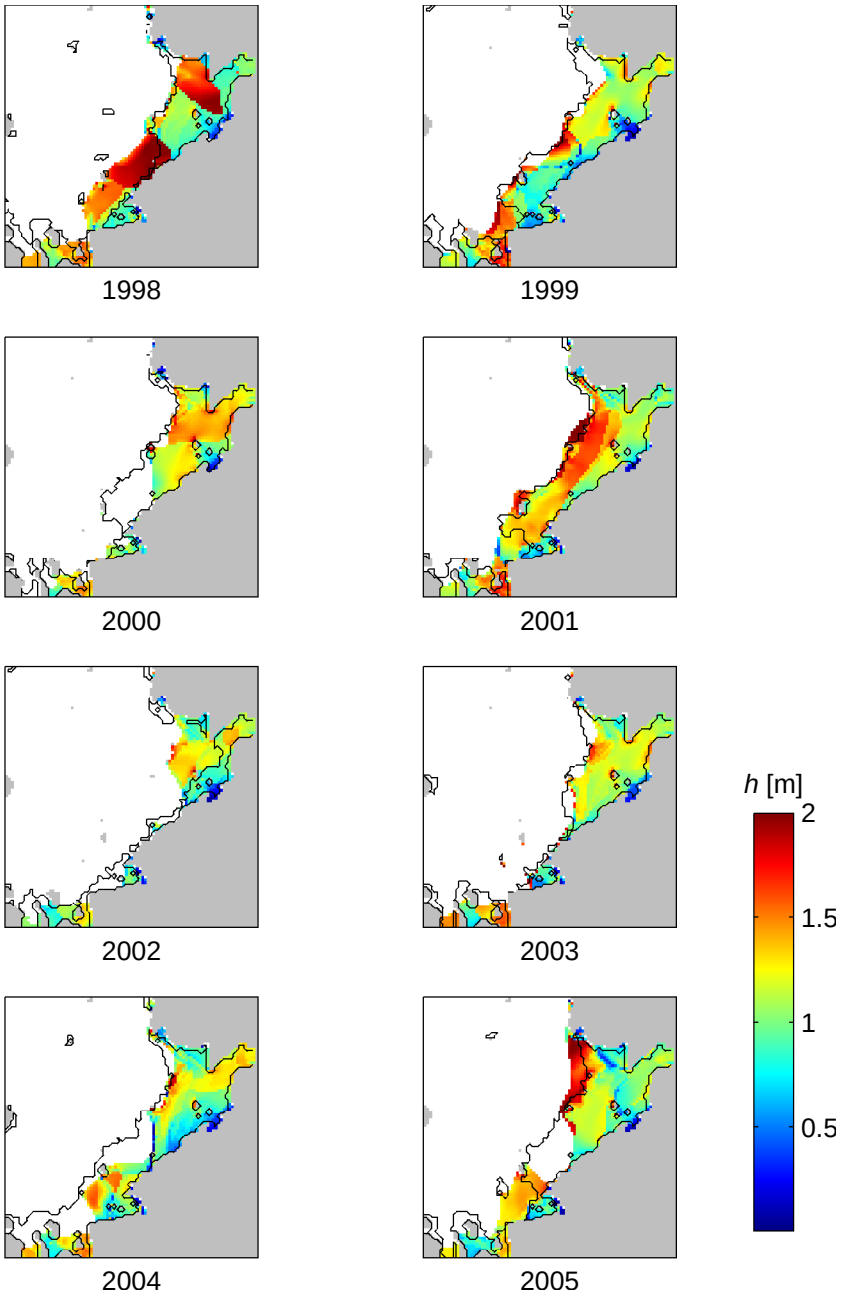

Figure 6.15: The ice thickness when the fast ice breaks up in summer during the 1998–2005 period. The solid line marks the fast-ice extent according to the AARI data for the first observation period in May. In the white areas no fast ice is formed.

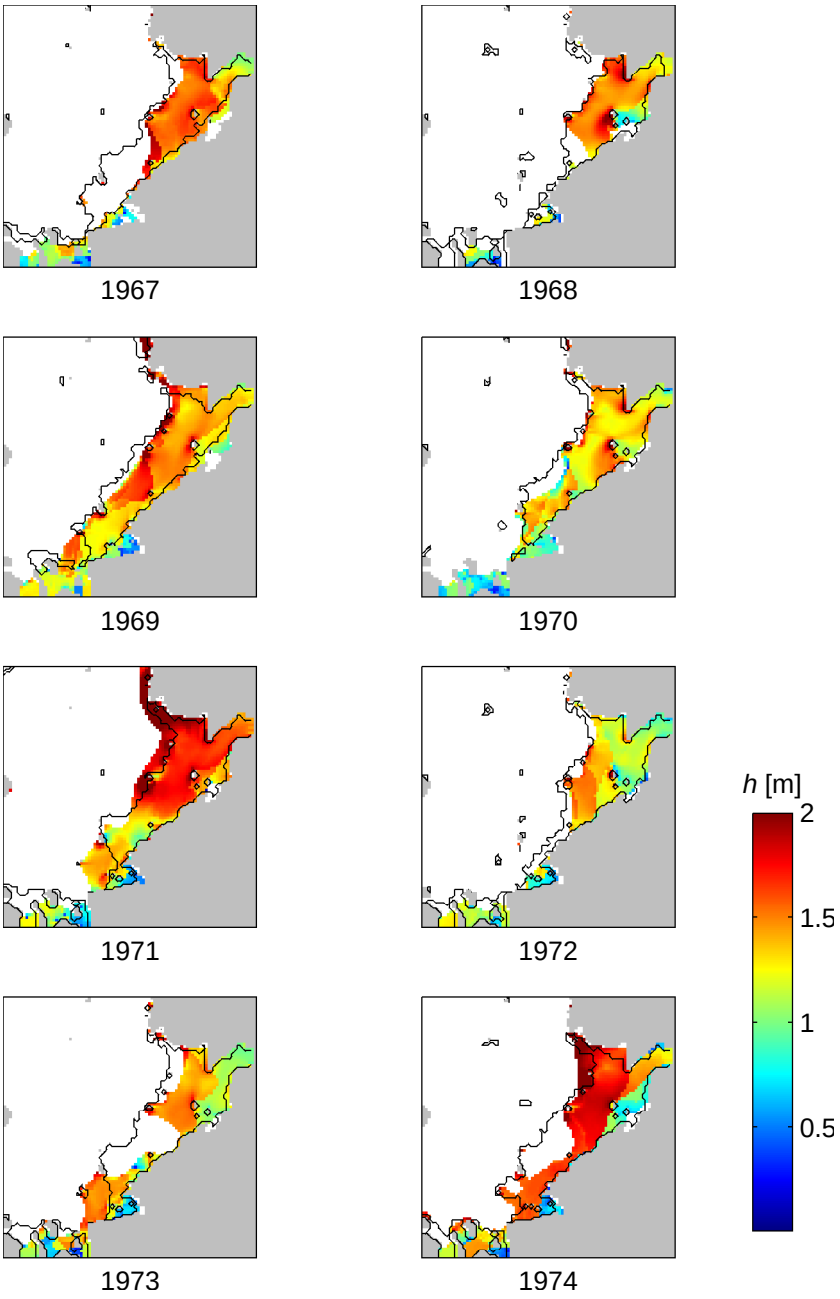

Figure 6.16: The ice thickness when the fast ice becomes stable in winter during the 1967–74 period. The solid line marks the fast-ice extent according to the AARI data for the first observation period in April. In the white areas no fast ice is formed.

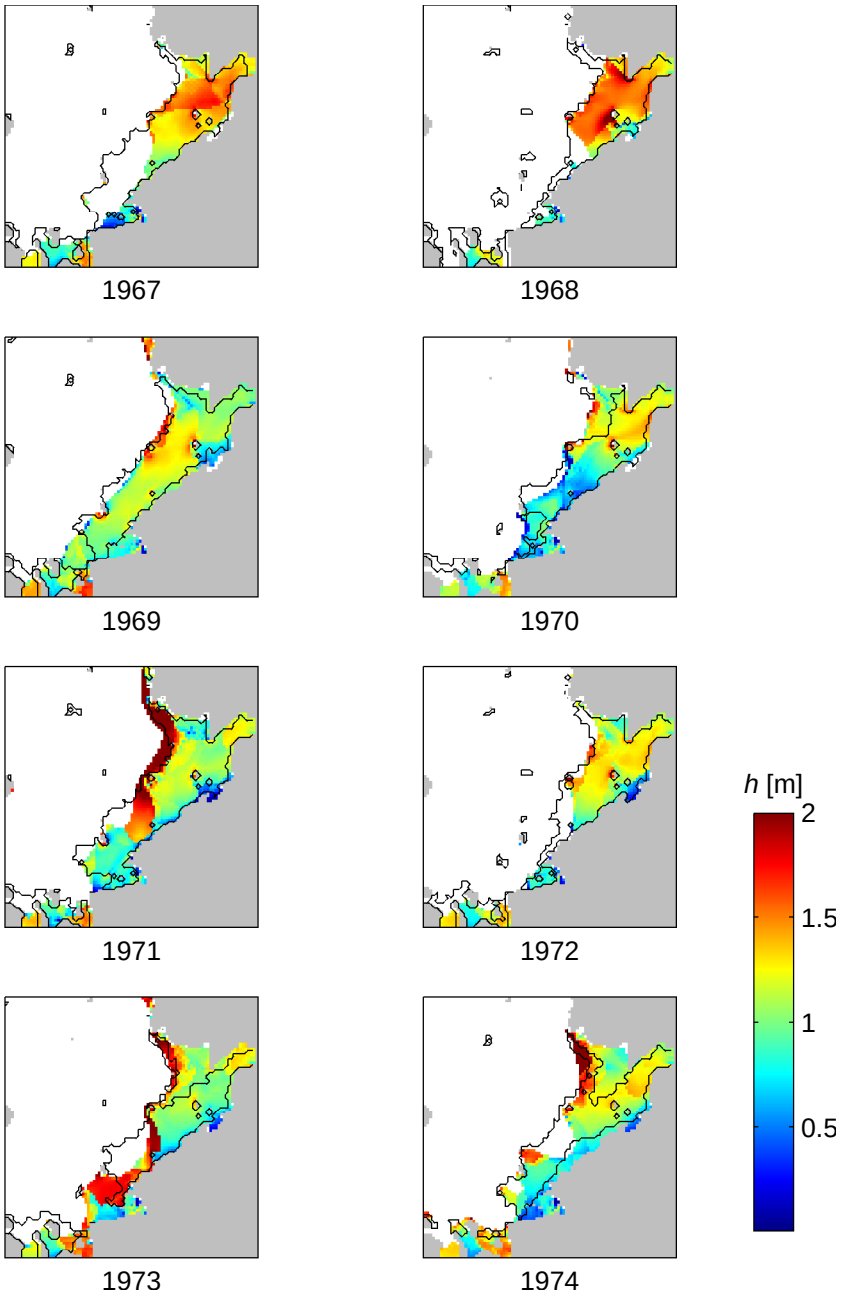

Figure 6.17: The ice thickness when the fast ice breaks up in summer during the 1967–74 period. The solid line marks the fast-ice extent according to the AARI data for the first observation period in May. In the white areas no fast ice is formed.

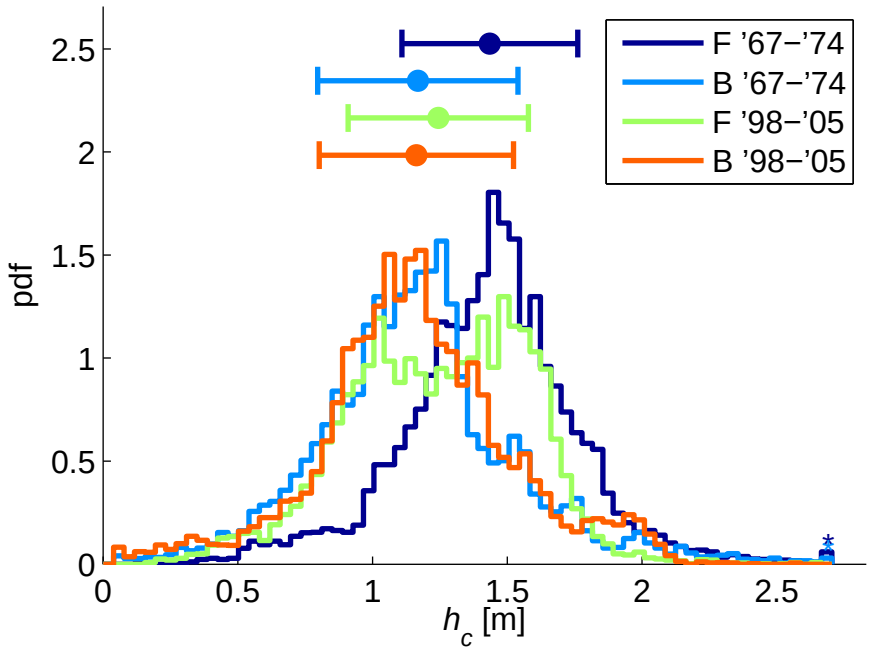

Figure 6.18: Histograms of ice thickness when the fast ice first becomes stable in winter (F) and when it breaks up in summer (B), during the two time periods: 1967–74 and 1998–2005. The mean value and standard deviation are also indicated on the graph.

the fast ice does not suffer large partial breakups before eventually becoming stable. In 1998–2005, however, large and multiple partial breakups during the formation phase cause change the pdf. In 1967–74 a considerable amount of multi-year ice forms in the Severozemelsky region which has the effect that the ice grows thick rapidly in fall, compared to 1998–2005 where little multi-year ice forms. The rapid ice growth therefore prevents the multiple partial breakups otherwise modelled.

This indicates that the ice growth in fall 1998–2005 is not rapid enough. One mechanism that may speed up the ice formation in fall, but may be underestimated in the model is surface layer stratification. In the Severozemelsky region the ice cover only breaks up in summer, when surface wind mixing is at a minimum. According to Volkov et al. (2002) this causes a thin (5–10 m) surface layer of fresh and cold water to form. If freezing begins again shortly after the ice melts (as is usually the case in the Severozemelsky region) this fresh and cool surface layer may accelerate the initial ice growth. River water may also play a similar role, but it is both warmer and unlikely to reach the S-mode area (see Volkov et al., 2002). On the face of it this effect would appear to be only minor since the energy released when ice forms is much greater than that released when cooling the same amount of water by a few degrees. It could, however, suffice to cause a full ice cover to form earlier. This would greatly reduce the short-wave penetration into the ocean and thus accelerate the ice growth. The overall impact of this requires a more detailed investigation.

The histograms in figure 6.18 leave us with three possible values for $\bar{h}_c$; $\bar{h}_c = 117$ cm, based on the pdf for both breakup periods, $\bar{h}_c = 143$ cm, based on the pdf for the ice formation in 1967–74 and $\bar{h}_c = 125$ cm, based on the pdf for all four breakup and formation periods. The first is useful if we want to have an idea of how much ice must remain in the Severozemelsky region after the summer melt in order for the ice to remain land-fast all year round. For comparison in 1967–74 the mean ice thickness in the S-mode region in summer was about 50 cm in the model (see figure 6.19). It would therefore require considerably harsher climate than the current one for the ice to remain land fast all year round.

The critical thickness based on the formation period in 1967–74 is an indicator of the ice thickness necessary to initiate fast-ice formation. This is $\bar{h}_c = 143$ cm, 25 cm thicker than $\bar{h}_c$ based on the breakup periods. It is relevant for considerations of future warmer climates where the ice may not always reach the critical thickness. For comparison the S-mode average ice thickness (see figure 6.19) reaches the critical formation thickness for every year modelled here.

In 1998–2005 the maximum ice thickness is normally some 40 cm more than this critical thickness. Two notable exceptions are 2002 and 2005 when the maximum ice thickness is 19 and 25 cm larger than the critical thickness, respectively. In 2005 an L-mode was observed, but an S-mode modelled. In

2002 S-mode fast-ice was only observed in January, with stable fast ice only present along the shore throughout the winter. The modelled fast-ice extent is larger than the observed one, but still less than the S-mode. The lack of stable S-mode ice in 2002 therefore appears to be the result of both thin ice and strong winds. In addition it is possible that the model overestimates the ice thickness. In 2005 the ice on the other hand does grow thick enough to form stable fast ice, but it is also likely that the model underestimates the ice thickness in that year.

One should not directly compare the date the S-mode mean ice thickness reaches the critical threshold with the onset of stable fast-ice formation each year. The former is based on a long time average while the latter depends on the ice thickness as well as the strength and timing of passing cyclones. All the same, there is still some correlation between the two. In 1967–74 the ice grows thick quicker than in 1998–2005 and reaches $\bar{h}_c$ sooner. The fast ice also becomes stable sooner in 1967–74 than in 1998–2005 (see figures 6.10 and 6.12). A longer time series would be needed to make a statistical comparison.

Calculating the critical thickness based only on the formation period in 1967–74 is arguably suspect since the formation period in 1998–2005 gives a different result. It was argued that since the model behaviour during the formation period is more realistic in 1967–74 the period 1998–2005 should be discarded. This, however, leaves us with only eight modelled winters, which is a small number to base any statistical analysis on. Using all four formation and breakup periods gives the largest number of estimates for h_c and therefore a more reliable statistic. The resulting pdf is close to the normal distribution, with a coefficient of determination $R^2 = 0.98$. For comparison the pdfs in figure 6.18 have a determination coefficient in the range $R^2 \in [0.89, 0.93]$, when compared to the normal distribution.

6.4.3 Ice-ocean interaction

Finally, an interesting point to note is the difference between the modelled fast-ice extent using the FMC now and in the previous chapter. In chapter 5 using the FMC with $\phi = 30°$ and $k_T = 0.22$ gave S-mode fast ice with correct breakup times. Here the same settings give wrong extent and wrong breakup times. The only difference between the two setups are the initial conditions; the spin-up for chapter 5 was done using simplified dynamics while here the full dynamics were used for the entire run.

Although the difference in the fast-ice extent in these two runs is noteworthy then the difference in ice thickness and concentration is not. In early January the difference in thickness in the Arctic Institute Islands Pass is of the order of centimetres. These differences are seen where ridges and leads form; i.e. there is no particular area where large differences occur. In the decadal run in February arches start forming between Sverdrup Island and

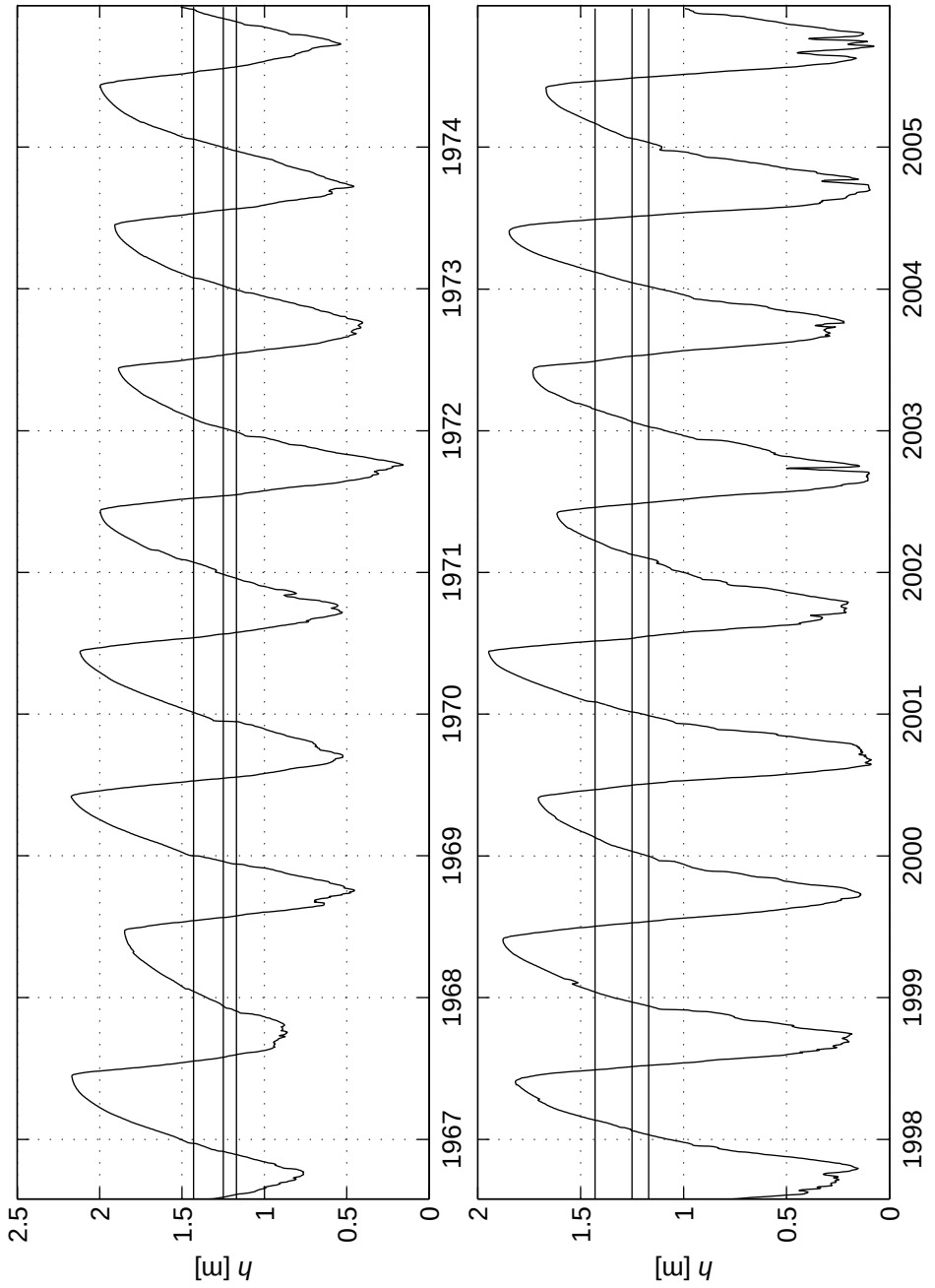

Figure 6.19: Mean ice thickness in the S-mode region using the FMC, grounding scheme and increased maximum viscosity. The upper panel shows the years 1967–74 and the lower 1998–2005. The three horizontal lines indicate the three values for the critical thickness mentioned in the text; $\bar{h}_c = 117$ cm, $\bar{h}_c = 125$ cm and $\bar{h}_c = 143$ cm.

Dikson and Sverdrup and Sergey Kirov Islands. Such arches do not form when the model is initialised using simple dynamics. The difference in ice thickness between the runs is still only a few centimetres, despite the arches forming. Following the formation of these arches the two models diverge. Where the arches form the ice becomes land fast, while in the other model the ice remains mobile.

This apparently drastic response to a minor perturbation in ice thickness underlines the non-linearity of the model. A perturbation of a few centimetres is enough to push the model from an S-mode state to an L-mode one. This also goes to show how close the settings used for the FMC are to an L-mode branch. In chapter 5 we saw that increasing k_T by 0.01 pushed the model into an L-mode state, and this small perturbation seems to have done the same.

Following this it is worth our while to take a cursory look at the oceanic response to different ice mechanics. Comparing the control run from section 4.3, which uses simplified dynamics to the results from the decadal experiments presented here gives some interesting results. Comparing, in particular the surface salinity at the summer ice minimum shows that using the FMC (with the grounding scheme and increased maximum viscosity) the ocean surface is saltier (see figure 6.20). At first this would seem counter intuitive. Using the full dynamics and the cohesive yield curves fast ice forms, decreasing the atmosphere-ocean heat and freshwater exchange. The ocean surface should therefore be fresher, not saltier.

The fast ice does indeed have this effect which can be verified in a simple experiment. Using the simple dynamics setup from section 4.3 the AARI observations were assimilated into the model by simply arresting all ice movement where fast ice was observed. This rather crude data assimilation shows that if the only change in the ice were the inclusion of fast ice then the ocean under that ice would indeed be fresher (see figure 6.21).

Using the full dynamics and cohesive yield curves therefore introduces a source of salinity for the ocean. This source can only be increased ocean-atmosphere exchange so one must conclude that the full dynamics cause larger leads to open, compared to the simplified dynamics. Such behaviour is to be expected from a cohesive material, but the full influence of this behaviour will not be studied further here.

6.5 Conclusion

In this chapter the model parametrisations tested for 1998 in the previous chapter were used in longer runs. Initially two yield curves were tested during two time periods, with further runs performed based on the results of the initial experiments. The yield curves tested were the FMC and trimmed ellipse, tuned such that the former gave relatively strong fast ice and the

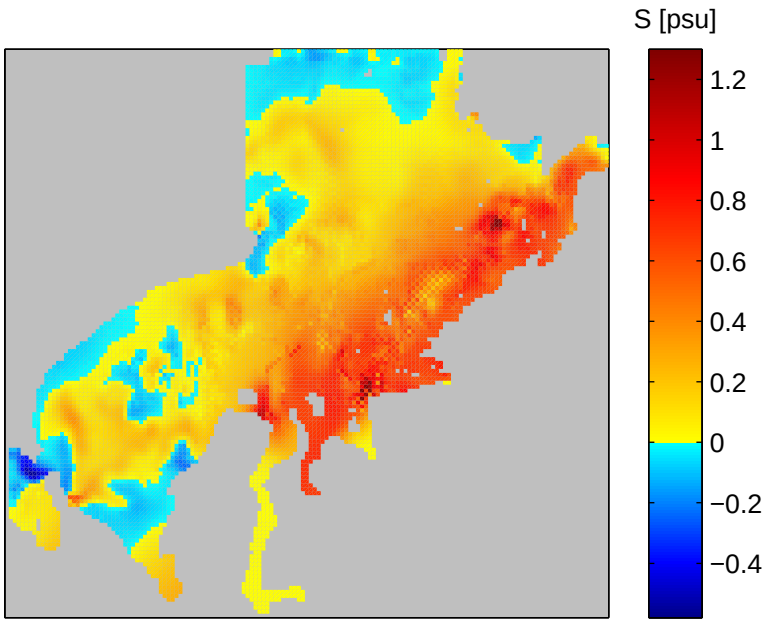

Figure 6.20: Ocean surface salinity using simplified dynamics subtracted from the salinity using the FMC with the grounding scheme and increased $\zeta_{\max}$. The figure shows the entire model domain after the first time step of October 5^{th}, 1998.

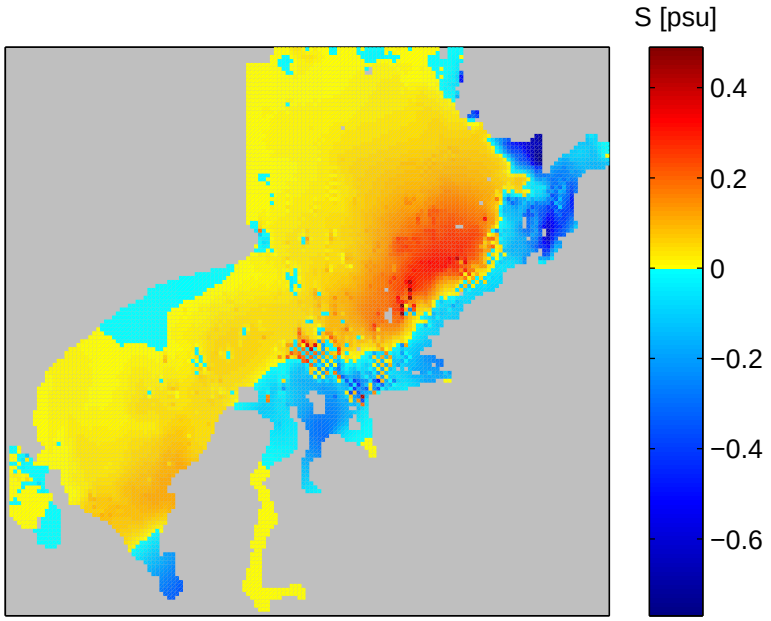

Figure 6.21: Ocean surface salinity using simplified dynamics subtracted from the salinity using the assimilated AARI fast-ice observations. The figure shows the entire model domain after the first time step of October 5^{th}, 1998.

latter relatively weak. The time periods were 1967–74 and 1998–2005; with relatively large fast-ice extent being observed in the former and relatively small extent observed in the latter.

The main result of these initial tests was that the modelled ice was too weak to produce realistic land-fast ice every year modelled. The FMC gives stronger ice than the trimmed ellipse resulting in better results in general, but these were still wanting. Because of this some further tests were performed using increased ice strength for the winter 1998–99. The best result was obtained using the FMC as before but with the grounding scheme and an even larger increase in maximum viscosity than that introduced in the previous chapter.

When judging the model's performance in these longer runs three basic criteria should be considered. Firstly one should consider if the model produces realistic fast ice at all; i.e. either an S- or an L-mode should form, in keeping with the general characteristics of the fast-ice cover. In this respect the FMC, with the grounding scheme and increased maximum viscosity succeeds in fifteen out of sixteen modelled years. The year when the model fails is 2002, when S-mode fast ice was only observed briefly in January. The model overestimates the fast-ice extent that year, but without producing S-mode fast ice.

The second criteria is that of inter-annual variability; i.e. whether the right mode is modelled at the right time. In this respect the model does not fair as well, giving the correct result for seven years out of sixteen. Finally formation and breakup times should be considered and here the correct values were modelled for four years out of eight observed formation periods and four out of sixteen observed breakup periods.

The basic fast-ice formation process does therefore seem to be captured quite well by the model, while seasonal and inter-annual variability is not. In order to capture the formation process properly it was still necessary to use the grounding scheme and very large values for the maximum viscosity. The grounding scheme, as it stands is very simplistic and needs considerable improvement. The success this simple scheme has here does, however, indicate that the grounding process is quite robust. This makes it feasible to work on an improved grounding scheme since it can be expected not to be very sensitive to parametrisations.

The fact that such large maximum viscosity was required raises doubts about the applicability of the viscous approximation, in this context. It is clear that the land-fast ice does not undergo creep flow, at least not at any meaningful speed. Using $\zeta_{\max} = (10^{17}\text{ s})P$, as was done here would result in the creep flow speed of $v = 10^{-13}$ m/s at the edge of a 100 km fast-ice massive (see section 5.4.1). This is about 1 μm per year, a speed that has no real meaning in the present context. It is, in particular an intriguing question how well an elastic-plastic model (as per e.g. Coon et al., 1974) would perform, compared to the viscous-plastic one. Implementing such a

model is, however, well outside our scope here.

The failure to properly capture formation and breakup times (i.e. seasonal variability) as well as inter-annual variability can be, at least in part due to short comings in the model forcing. With respect to the inter-annual variability the NCEP/NCAR reanalysis could simply not be capturing the variability of the system. A further step would be to test different reanalysis products and compare to the NCEP/NCAR forced results. The reanalysis should also be compared to observations. Further improvements could possibly be made by using a coupled ocean-ice-atmosphere model.

Regarding formation times it was suggested that the ice simply did not grow rapidly enough in fall. Too slow ice growth would lead to a gradual increase in the overall ice strength and therefore a gradual increase in the fast-ice area. This would then also affect the ice thickness and strength in summer, when the fast ice breaks up. It was also suggested that proper modelling of the stratification due to melt water and possibly river run-off could increase the ice growth rate in fall. A more thorough investigation is, however, needed into the importance of this process.

Having established the reliability of the model its results were used to give estimates of the critical thickness for fast-ice formation in the Severozemelsky region. The critical thickness (h_c) is the thickness the ice needs to reach for fast ice to form and remain stable under normal atmospheric and oceanic conditions. The three estimates given were based on the thickness of the ice when fast ice forms in the model, when it breaks up and based on both the formation and breakup periods.

Interestingly the critical thickness for breakup was smaller than that for formation; $\bar{h}_c = 117$ cm for breakup vs. $\bar{h}_c = 143$ cm for formation. The reason behind this difference is that winter cyclones are more intense than summer cyclones and the fast ice can therefore become thinner in summer before breaking up. These estimates include the breakup thickness for both 1967–74 and 1998–2005, but only the formation thickness for 1967–74. This was done because the formation thickness in 1998–2005 appeared to be spread between the two values of $\bar{h}_c$ already mentioned. It was suggested that this happens because the ice growth in fall is too slow during the latter time period.

The formation critical thickness is then the thickness the ice needs to reach for the fast ice to become stable during winter. It is of particular interest when considering fast-ice presence in warmer climates. The breakup critical thickness on the other hand gives the limit below which the ice must melt before the ice breaks up. That is of interest when considering cooler climates when the ice may have remained land-fast all year round.

Taking the mean of h_c over all modelled formation and breakup periods gave $\bar{h}_c = 125$ cm, with a standard deviation of 37 cm and $R^2 = 0.98$, compared to the normal distribution. From a statistical point of view this should be the most dependable value. It gives the mean critical thickness

based on all the cyclones that may break up the ice, independent of their intensity.

In order to give some perspective for the given values for the critical thickness they were compared to the mean S-mode ice thickness during the two time periods. The mean ice thickness grew to be greater than the critical formation thickness for all the modelled years. It was, however, clear that the ice in 1967–74 was both thicker and reached the critical thickness sooner. The modelled ice did reach the critical formation thickness in 2002, but in that year S-mode fast ice was only observed in January. It is therefore likely that the very early breakup of fast ice in 2002 was due to both unusually thin ice and unusually strong winds. The modelled mean ice thickness was lowest in 2002 of all the modelled years.

Finally an interesting side effect of the cohesive yield curves was discovered. When using the cohesive yield curves the surface salinity in the ocean model was larger than when using the simplified dynamics. The difference was only about 0.5 psu at the end of the melt season, but the signal appears to be robust. The reason for this must be that when using the cohesive yield curves the leads that form are larger, increasing the ocean-atmosphere interaction.

The main result of this chapter is that using a cohesive yield curve (i.e. the FMC) with improved dynamics, high maximum viscosity and the grounding scheme, fast ice can be modelled on a longer time scale. The model captures the basic formation mechanisms, but some improvements are needed to capture the temporal variability observed. Improvements may be needed in the oceanic and atmospheric forcing to achieve this. As it stands the model can still give valuable insights into the nature of the Severozemelsky fast-ice massive, and in particular the conditions needed for it to form in the first place.

Chapter 7

Conclusion

This thesis presents a coupled ice-ocean model, capable of producing realistic land-fast ice. The model is based on the well known viscous-plastic formulation first suggested by Hibler (1979), which is the basis for the vast majority of sea-ice models currently in use. Neither Hibler's original model, nor any of its derivatives are, however, able to produce realistic land-fast ice and therefore some further development of the model was required. This is the first time land-fast ice has been modelled in a realistic setting using a dynamic sea-ice model.

The ice model used here was written to be coupled onto the Vector Ocean Model (see chapter 2). The ice model was designed to be simple and easy to implement allowing time to be spent on those model features deemed most important for a fast-ice simulation. Thus the model was initially very similar to that written by Hibler (1979); it used two ice classes only (ice and open water), an elliptic yield curve, an SOR solver for the momentum equation with a single pseudo-time step and zero-layer Semtner (1976) thermodynamics with constant albedos. Improvements made to this model were essentially twofold: New yield curves were introduced and an improved pseudo-time stepping scheme was implemented (referred to as the outer-loop solver).

The new yield curves were introduced in order for the model to reproduce the cohesive strength present in sea ice. Land-fast ice has been shown to be attached to grounded pressure ridges in many cases. In the Kara Sea, however, the ice remains land fast in regions where the ocean depth is too great for pressure ridges to be grounded. An additional mechanism is thus needed to explain why the ice remains land fast and this was assumed to be ice cohesive strength.

In addition, the solver for the momentum equation needed improvement. With the traditional approach of on pseudo-time step errors of the order of 1 cm/s were often present in the velocity field. Errors of such a magnitude could cause the fast ice to break up, even though it should not. The velocity

field also needs to be accurately predicted since the modelled fast ice should move very slowly. In section 4.4 it was shown that the new solver reaches a much more accurate solution. More work is, however, needed to improve the solver, which is both slow and not as accurate as aimed for.

Other improvements were also made. The zero-layer model was replaced with a three layer model using variable albedos. This improved the simulation of the Kara Sea ice cover (see section 4.3) yet did not have a large impact on the modelled ice thickness. The formation of new ice in polynyas was studied in chapter 3 where improvements were made to the parametrisations for newly formed ice. An appropriate scheme for lateral melt had also to be chosen to prevent the fast ice breaking up at the onset of melt. Finally a very simple grounding scheme was implemented whereby the ice is assumed to be stationary if it grows thicker than a certain fraction of the ocean depth (section 5.4.4).

Chapters 3 and 4 outlined various tests performed on the model before the actual fast-ice simulations were done. The former outlined an idealised study on polynya formation. It showed that the formation process is mostly independent of rheology, but underlines the importance of the new-ice formation parametrisations. Chapter 4 introduced the realistic Kara Sea model and outlined two sets of tests performed; one dynamic and the other thermodynamic. The dynamic tests were performed to investigate the performance of the outer-loop solver and establish the accuracy to which the ice velocity field could be modelled.

The thermodynamic tests were based around a model setup with simplified dynamics (i.e. a single pseudo-time step and elliptic yield curve) and some changes in the thermodynamic parameters of the model. The modelled Kara Sea ice cover, using NCEP/NCAR and ERA-interim reanalysis data as forcing was compared to satellite observations. In addition the influence of a number of (mostly) thermodynamic parameters was tested. The effects of changing these parameters were found to be less than those seen when using different forcing data sets. While NCEP/NCAR data gave marginally better results than ERA-interim data, the model tended to underestimate summer ice extent using NCEP/NCAR data while the extent of summer ice was overestimated using ERA-interim data.

Having introduced the model and done preliminary testing chapters 5 and 6 present the two main fast-ice experiments done here. First, the model is used to simulate the winter 1997–98, testing all the yield curves implemented in the model as well as the importance of the outer-loop solver, the limit for transition between viscous and plastic behaviour and the grounding scheme. The model results were compared to observations showing both fast-ice extent and the locations of flaw polynyas.

The main results of these first tests were that it is indeed possible to model land-fast ice using a viscous-plastic model. To achieve this it was crucial to increase the maximum viscosity parameter $\zeta_{\max}$. This parameter

sets the limit between linear viscous and plastic response of the model material. Using high maximum viscosity the ice remains plastic under smaller strain rates and is more viscous in the linear viscous phase.

It was shown that using the traditional value for $\zeta_{\max}$ amounted to trying to simulate the Kara Sea fast-ice massive as a single block of linearly viscous fluid, when moderate wind stress was applied. This did not work and realistic fast ice only formed once $\zeta_{\max}$ had been increased by five orders of magnitude. Using such a high value for $\zeta_{\max}$ the fast ice was in (slow) plastic deformation under moderate wind stress.

This raises questions about the applicability of the viscous approximation for small strain rates. Using such a large value for $\zeta_{\max}$ also means that the speed of the creep flow the ice undergoes is of the order of 10^{-9} m/s or about 1 cm a year. This is such negligible speed as to be meaningless in the current context. Since lowering the contribution from the viscous part of the model improves the results it could be interesting to replace the viscous behaviour with elastic, as per e.g. Coon et al. (1974). Presumably an elastic-plastic model would be a more accurate description of sea ice and it would be interesting to see if such a model performed better than the viscous-plastic one.

The yield curve shape was also found to play a role when modelling fast-ice. The exact shape did not appear to be of great importance as long as the yield curve gave enough cohesive strength so that fast ice could be produced. The model behaved in general as one would expect with respect to cohesive strength; small cohesion gave little or no fast ice, intermediate values gave realistic fast ice and large values gave too much fast ice and unrealistic drift-ice behaviour. Realistic fast-ice extent could be produced using most of the yield curves and within a limited range of ice cohesive strength.

While the flexible modified Coulombic (FMC) yield curve could be tuned to produce both realistic fast ice extent and breakup times ice drift in the narrow Arctic Institute Islands pass was too slow. The trimmed ellipse produced more realistic flow in the pass yet lead to erroneous timing of the fast-ice break up. These two yield curves present both the best results obtained and also two extremes; the FMC could be tuned to give realistic results under high cohesive strength while the trimmed ellipse permitted less cohesive strength for realistic results.

In addition to testing different model parametrisations a small set of tests using the ERA-interim data were performed. These dramatically underlined the model's sensitivity to wind stress. In the fast-ice region of the Kara Sea the mean wind strength in the ERA-interim reanalysis is 30% greater than that of the NCEP/NCAR reanalysis. The ice also grew to be some 15% thinner when using the ERA-interim reanalysis, compared to using NCEP/NCAR data. As a result the ice cohesive strength had to be increased by about 100% when using the ERA-interim reanalysis, compared to when

using NCEP/NCAR data.

Finally a grounding scheme for pressure ridges was suggested and tested. It did not prove to have considerable effects on the fast-ice extent or stability. Using the trimmed ellipse (which gave the weakest fast ice) the grounding scheme did improve the model results around the Sergey Kirov Islands, but the overall impact of the scheme was deemed small. This impact turned out to be much greater in the other years modelled in the chapter that followed.

After tuning the model for the winter 1997–98 longer time periods were modelled in chapter 6. For these runs the time intervals 1967–74 and 1998–2005 were chosen, as these periods represent a maximum and minimum in the observed fast-ice extent, respectively. Only two yield curves were tested initially; the FMC and the trimmed ellipse yield curves found to give the best results in the previous chapter.

Results from the initial tests were not promising; a fact later attributed to the underestimation of ice grounding. Realistic fast ice, i.e. L or S-mode was modelled in nine out of sixteen modelled years using the FMC and only in three years using the trimmed ellipse. The parameters fitting to model the year 1998 did therefore not give nearly as good results for the long term run. It was clear, in particular that the modelled fast ice was much too weak.

Based on these results some tests were performed with increased ice cohesive strength for the winter 1998–99. These showed that increasing the cohesive strength could not improve the fast-ice results without resulting in a highly unrealistic drift-ice simulation. Application of the grounding scheme greatly improved the stability of the fast-ice sheet so that using the FMC, parametrised as before, and the grounding scheme together gave realistic results. Increasing the maximum viscosity by another four orders of magnitude improved the results still further. The grounding scheme proved much more important here than in the previous chapter which clearly shows that pressure ridge grounding is an important secondary process in fast-ice formation.

Using the FMC with the grounding scheme and increased maximum viscosity, realistic fast ice was modelled in 15 out of 16 model years. In the remaining year, 2002, S-mode fast ice is only observed in January. This is the only year in the observational record where this happens, all other years show S-mode ice present from January through May. While the model fails to fully capture this extreme event the modelled fast-ice extent in 2002 is still less than in any of the other modelled years.

Basic fast-ice formation mechanisms therefore appear to be well captured while temporal variability is lacking. Even though an S or an L-mode was always modelled (except in 2002) the right mode was not necessarily modelled at the right time. The observed mode was modelled during seven of the sixteen modelled years. Formation and breakup times were also not captured very well, with the formation modelled correctly in four out of

eight[1] observed years and breakup in four out of sixteen.

These shortcomings in temporal variability can be due to errors in the model itself or to some extent errors in the forcing. It is not unlikely that the incorrect inter-annual variability is due, at least in part, to errors in the NCEP/NCAR based forcing, but this has yet to be investigated. With respect to formation times it was shown that the rapid initial ice growth in fall in 1967–74 relative to 1998–2005 resulted in more realistic formation times. It was suggested that the ocean model's inability to resolve the near-surface stratification of the ocean could slow down initial ice growth. The proper modelling of this stratification requires much higher vertical resolution than is currently feasible. Further investigation into the effects of near-surface stratification is therefore indicated.

One of the aspects of fast-ice formation the model allows us to investigate further is the existence of a critical formation thickness. It can be assumed that fast ice can only form once the sea ice reaches a certain minimum thickness, termed the critical thickness of fast-ice formation. The most sensible value for critical thickness is both a spatial and temporal average. The spatial average was taken over the entire fast-ice extent and the temporal average takes into account the inter-annual variability in cyclone intensity.

The model results strongly indicated that such a critical thickness exists with the mean critical thickness of $\bar{h}_c = 125$ cm. It was also shown that the critical thickness retrieved during fast-ice formation was greater than that retrieved during break up. This can be explained by the fact that winter cyclones are on average more intense than summer cyclones. It was also shown that the fast ice grew notably thicker in 1967–74 than in 1998–2005, but the 1998–2005 ice always grew thicker than the mean critical thickness. Should the ice continue to grow thinner fast-ice less winters will become a regular occurrence. No attempt was made to estimate when this might occur.

Overall the model effectively reproduces the fast-ice extent in the Kara Sea. This is a major achievement since fast ice has never before been modelled in a realistic setting based on the model material properties. Key to this success are increased maximum viscosity, modified yield curve, increased solver accuracy for the momentum equation and a simple grounding scheme. It was shown that fast ice can be modelled using a basic cohesive Coulombic yield curve, but that the viscous approximation is insufficient to describe fast ice. By using very large maximum viscosity the viscous approximation is effectively avoided. A better approach could be to replace the viscous response with an elastic one. The need for a grounding scheme underlines the importance of pressure ridge grounding as a secondary process in fast-ice formation.

[1]The formation time was not observed during the 1967–74 observation period

The results obtained here give us insight into the nature of land-fast ice, its formation and the forces that hold it together. The ability to model fast ice opens up new avenues of research in areas where fast ice plays a role in atmospheric, oceanographic, biological or economic context. It would be particularly interesting to see how the model performs in other locations, such as the Laptev Sea or the Canadian Arctic Archipelago. Large expanses of fast ice form in the Laptev Sea and since it forms over shallower waters grounding may be more important there than in the Kara Sea. In the Canadian Arctic Archipelago static arching is likely to play a large role in the ice dynamics and it would be interesting to see how the model proposed here would behave in those circumstances. Finally Zhang and Rothrock (2005) have shown that increasing the cohesive strength affects the ice behaviour on the pan-Arctic scale, an effect that could be investigated further with the current model.

On a more model-oriented note certain aspects of today's ice models have been brought into focus. It was shown that the common viscous-plastic model could be used to model land-fast ice, something that has not been done before. From a purely physical stand point one would expect that changing the yield curve should be enough to create a material that gives land-fast ice, yet this was shown to be insufficient. To produce fast ice the outer-loop solver had to be improved and the viscous limit had to be increased significantly.

Improving the outer-loop solver is a question of improving numerics, something that still requires considerable work. Deciding on the viscous limit, however, concerns one of the basic assumptions of the viscous-plastic model; that sea-ice undergoes creep flow. The results presented here indicate that the creep flow speed is so small as to be meaningless in this context. This offers two possibilities; either to use the current viscous-plastic approach with arbitrarily high maximum viscosity or replace the viscous response with a different one, e.g. elastic. The former would probably require some improvement in the model numerics, but the resulting model would be an essentially purely plastic model. The latter was done by Coon et al. (1974) and then abandoned in favour of the viscous-plastic model. It would be possible to either revisit the work of Coon et al. (1974) and attempt improvement or opt for a different approach, e.g. the elastic-brittle model proposed by Girard et al. (2011).

Appendix A

A note on spelling

The word combinations sea ice, fast ice, land-fast ice and the alike require different forms of hyphenations depending on their role in a sentence. When used as a noun "sea ice" and "fast ice" remain unhyphenated, while they must be hyphenated when used as adjectives. Consider for instance: "Fast ice remains attached to the shore" vs. "the fast-ice edge follows a chain of islands". In the former sentence "fast ice" is a noun and thus not hyphenated but in the latter it is an adjective and hyphenated.

In the phrase "land-fast ice" the words "land-fast" act as an adjective describing the ice and are therefore hyphenated. One could, for example use the phrase "land-fast-ice cover" instead of simply "fast-ice cover", requiring two hyphenations. This is not aesthetically pleasing and is consequently not done here.

Appendix B

Solver for the curved diamond yield curve equations

In order to find the parameters α and μ in equation 2.83 based on a given value for k_T the following Mathematica program was used. It assumes the equation has been rewritten as

$$\sigma_{\mathrm{II}}/P^* = \begin{cases} 1 + \sigma_{\mathrm{I}}/P^* & \text{if } -1 < \sigma_{\mathrm{I}}/P^* < \sigma_{\mathrm{IX}}/P^* \\ \mu(k_T - \sigma_{\mathrm{I}}/P^*)\sqrt{1 + \alpha\sigma_{\mathrm{I}}/P^*} & \text{if } \sigma_{\mathrm{XI}} < \sigma_{\mathrm{I}} < 0 \\ \mu k_T - \sigma_{\mathrm{I}} & \text{if } 0 < \sigma_{\mathrm{I}}/P^* < \mu k_T. \end{cases} \tag{B.1}$$

The algorithm assumes that $2\theta = 120°$ for $\sigma_{\mathrm{I}} = \sigma_{\mathrm{XI}}$ and $2\theta = 160°$ for $\sigma_{\mathrm{I}} = 0$. Given a value for μk_T (the variable kinit in the code) it calculates α, μ, σ_{XI} (the variable x in the code) and k_T (the variable k in the code).

```
b = D[μp(kp − σp)Sqrt[1 + αpσp], σp]
sf[μ_, α_, k_, σ_]:=ArcCos[b/.{μp → μ, αp → α, kp → k, σp → σ}]/Degree;
α = 0.75;
μ = 1;

kinit = 0.05;
kerr = 1;
While [kerr > 10^−7,
  k = kinit/μ;
  err = 1;
  While [err > 10^−7,
    σx = Solve[σ + 1 == μ(k − σ)Sqrt[1 + ασ], σ][[1]];
    x = σ/.σx;
    sol = Solve[{sf[m, a, k, 0] == 160., sf[m, a, k, x] == 120.}, {m, a}][[−1]];
    aerr = Abs[α − a/.sol];
```

merr = Abs[$\mu - m$/.sol];
err = Max[aerr, merr];
α = Re[a/.sol];
μ = Re[m/.sol];];
kerr = Abs[μk − kinit];]
$\{\alpha, \mu, x\}$
αr = Round[α, 0.001];
μr = Round[μ, 0.001];
$\{\alpha$r, μr, $k\}$
$\{$sf[μr, αr, k, 0], sf[μr, αr, k, x]$\}$

Appendix C

VOM runtime parameters

When the VOM model is run it reads in the `guide_vom` file containing the time step size, grid size and other parameters. For the sake of completeness this file is included here.

```
../
10
 600.   10.e+3   10.e+3   0.1          DT   DX   DY DTE (ice model elastic time step) (note: dx,dy either in
    meters or in minutes !!!)
 2.5e-3   3.2e-6 1.0                  RBOT  WLAM  slip_seabed (seabed friction, wind-stress coefficient)
 73.00000   -77.00000    0.5          REFLAT REFLON EQUATOR_DIST   (values in degrees)
 1 10000   0.5   1.0                  AHNULL AHMAX  AH_KH SLIP (KH=AH * AH_KH)
 0.50    50.0                        RETARD(hrs) MIXLEN Kochergin Parameters
 300.e-4   0.1e-7    0.5              VISMAX VISMIN SCHMIDT-NO ==> Kv = SMI_NO * Av
 0.5   1.53   1.e-6 100               PIMP, OMEGA, EPSILON, MAXITR (SOR parameters)
 0.5   1.e-6 1.e-8   0.5   1.0   1   PIMP_MOM MOM_EPS TS_EPS PIMP_TS   HAS_WEIGHT HAS_STEPS
 1.8d0 32.5d0 0.d0 0.d0 0.0 0.0       TINIT SINIT (initial homogeneous T,S), TREF,SREF (reference-T,S),
    relax_t,relax_s
 0.0 0.0                   SCAL_INIT (initial value for scalar tracer), SCAL_REF (reference-value for tracer)
 0.0 0.0 0.0 0.0 0.0                  WX, WY, QSURF Steric height grads (x,y)
 10 6.0                               NFORC_RMP [days], ROUGHNESS_HOURS
 1997   09 28 00 0000                 START-TIME: YEAR, MONTH, DAY, HOUR, SECONDS
 1998   12 26 00 0000                    END-TIME:    YEAR, MONTH, DAY, HOUR, SECONDS
 1440 40320 50   1                 DATOUT WARMOUT DUMPOUT  (units: minutes) output, warmstart, Dump, MOD_WRITE_CNT
 1.00                             ZFAC amplification factor for ASCII-output of ==> ZETA
ft     EXTERNAL_GRID, READ_LAT_LON          external grid projection=T: then dx,dy are expected in minutes,
   READ_LAT_ON=T: latitude and longitude read from vom_input/grid_{lat,lon}.dat - only if EXTERNAL_GRID=F.
tf     CORIOLIS, F_PLANE                    t ==> coriolis-rotation desired, f-plane desired
ftf    NLM_UPS, NLM_SVU, NLM_J7             Momentum-Advection (UPStream, selective upstream SVU, or J7)
ttf    TS_INPUT, PROGNO, PRESSURE           t ==> TS_INPUT data available, otherwise use TINIT, SINIT (above)
ftf    AH_LARGE, AH_SCALS, DIFF_DISSIPATION   large stencil AH; hor. diffusion for scalars
   DIFFERENTIAL_DISSIPATION
f      SCALAR_TRACER                        SCAL_TRACER desired
tt     SURFLUX, ICE_MODEL                 SURFACE_FLUXES (via bulk formulae) desired, ICE-MODEL desired
f      SW_PENETRATION                      penetration of SHORT WAVE radiation into water column desired
ffff   ADJUST_N, _S, _W, _E                ==> open boundary adjustment desired
tff    BINOUT, ASCOUT, DUMP                output options (binary, zeta as ascii, ascii-dump)
```

```
tff    RESTART, WARM, CLIMYEAR          write warm-start fields; read warm-start fields
ftt    XMINIT,RUN_TIDE,AVG_TIDE           t ==> output files named in hours AND minutes, 0: only hours
1                                       NSTEPS (keep 1 to deal with start-date and end-date)


Info about VOM (Vector Ocean Model) parameters in this file:

=============================================================
 DATA
=============================================================

PATHDIR          1st line: name of VOM data directory (make sure that line covers 80 characters !!!)

DT            time-increment [s]
DX DY         space-increments  [m] if(ext.grid=f) or ['] min if(ext.grid=t)

RBOT          bottom friction parameter [-]
WLAM          drag coefficient of wind stress [-]
G             earth acceleration [m**2/s]

REFLAT           reference latitude for LAT/LON grid, and/or for Coriolis (f-plane) [ ]
REFLON           reference longitude for LAT/LON grid [ ]
EQUATOR_DIST     distance from equator where coriolis rotation is switched off [ ]

AHNULL           min horizontal turb. exchange coefficient [m**2/s**2]
AHMAX         max horizontal turb. exchange coefficient [m**2/s**2]
AHCONVECT
AH_KH
SLIP          boundary condition for lateral turb. exchange at coast [-]
              SLIP=1  ==> full-slip
              SLIP=0  ==> semi-slip
              SLIP=-1 ==> no-slip
```

```
RETARD              time coefficient [hour]
MIXLEN              factor for mixing length in Kochergin scheme [m]
MODE_ADJUST         setting for type of convective adjustment scheme [-]
                  MODE_ADJUST= 1 ==> careful  convective adjustment by ==> ADJUST
                  MODE_ADJUST= 0 ==> brutal   convective adjustment by ==> ADJUST
                  MODE_ADJUST=-1 ==> convective adjustment by increased mixing ==> TURBULENCE

VISMAX              max eddy viscosity [m**2/s**2]
VISMIN              min eddy viscosity [m**2/s**2]
SCHMIDT-NO          relation factor for eddy diffusivity Kv = SMI_NO * Av [-]

PIMP                   Cranck-Nicholson pointer for implicit scheme of SSE [-]
OMEGA                  Relaxation parameter for ==> SOR scheme
EPSILON             Desired Accuracy (Error) of Iteration of SSE
MAXITR              max number of iteration [-]
MODITR
LEFT_UNFROZEN       percentage of [%]
UPDATE_PRESSURE        [timesteps]

PIMP_MOM         Cranck-Nicholson pointer for implicit scheme of momentum [-]
TS_EPS              Desired Accuracy (Error) of Iteration of temperature and salinity [-]
PIMP_TS             Cranck-Nicholson pointer for implicit scheme of temp. and sal. [-]
HAS_WEIGHT          (central differences) 0.0 < HAS_WEIGHT < 1.0  ( upstream acheme) [-]
HAS_STEPS           number of steps with reduced time increment [-]

TINIT            initial homogeneous temperature [C]
SINIT            initial homogeneous salinity [psu]
TREF             reference temperature [C]
SREF             reference salinity [psu]

SCAL_INIT           initial homogeneous tracer concentration [%]
```

```
SCAL_REF        reference concentration of tracers [%]

WX,WY                east, north components of constant wind [m/s]
QSURF           surface energy flux [W/m**2]
Steric height grads tilt of sea surface [m/m]

NFORC_RMP            ramp forcing for cold start [days]

START-TIME        year,month,day,hour if XMINIT=f; day,hour,seconds if XMINIT=t []
END-TIME         year,month,day,hour if XMINIT=f; day,hour,seconds if XMINIT=t []

DATOUT              time increment of ascci and binary output [timesteps]
WARMOUT             time increment of warmstart output [timesteps]
DUMPOUT             time increment of dump output [timesteps]  !!!! large output !!!!
LTUNE_SOR           SOR iteration [timestep]

ZFAC            amplification factors for zeta [-]
```

LOGICALS

```
EXTERNAL_GRID         t ==> external grid projection, then dx,dy are expected in minutes

CORIOLIS            t ==> coriolis-rotation desired
F_PLANE                   t ==> coriolis-rotation on F_PLANE desired

NLM_UPS               t ==> Momentum-Advection (UPStream)
NLM_J7                t ==> Momentum-Advection (J7)
SOLVER                t ==> hybrid Gauss solver; f ==> chessboard solver
```

```
TS_INPUT          t ==> TS_INPUT data available, f ==> use TINIT, SINIT
PROGNO              t ==> run T,S in prognostic mode, f ==> diagnostic mode
PRESSURE          t ==> density depends on pressure

AH_LARGE          t ==> apply the hybrid Laplacian Diffusion operator, which uses the +/-2 stencil
AH_SCALS          t ==> apply (optional) horizontal diffusion to scalar fields

SCALAR_TRACER       t ==> scalar tracer will be computed
SOR_FREEZE          t ==> freezing algorythm will be used

SURFLUX             t ==> SURFACE_FLUXES (via bulk formulae) desired
ICE_MODEL           t ==> ICE-MODEL desired

SW_PENETRATION      t ==> penetration of SHORT WAVE radiation into water column is desired

ADJUST_N, _S, _W, _E t ==> open boundary adjustment desired

BINOUT              t ==> binary data output desired
ASCOUT              t ==> ascii zeta output desired
DUMP              t ==> ascii column-wise dump desired

RESTART               t ==> re-start option desired
WARM                  t ==> warm-start desired
CLIMYEAR          t ==> 30 days per year; f ==> realistic year

XMINIT                t ==> output files are named in hours and minutes; f ==> year,month,day,hour
RUN_TIDE          t ==> tidal forcing will be prescribed
AVG_TIDE          t ==> velocities are averaged over a tidal period

NSTEPS              1 to deal with start-date and end-date
```

Appendix D

Equations for uniaxial compressive strength

The uniaxial compressive strength for a given yield curve (σ_{uc}) is the value of σ_2 for which $\sigma_1 = 0$ for that particular curve. For the flexible modified Coulombic yield curve σ_{uc} can be found using some simple trigonometric identities.

Figure D.1 shows the relevant portion of stress space in which a Coulombic yield curve has been drawn. The angle between the Coulombic slope and the σ_{I} axis is α where $\tan\alpha = \sin\phi$ andϕ is the internal angle of friction. The angle between the yield curve and the σ_1 axis is β and the angle between the σ_1 and σ_{I} axes is 45°.

Using the sine rule the distance between the origin and the intersection between the yield curve and the σ_1 axis, in stress invariant space is

$$\sigma'_{\text{uc}} = k_T \frac{\sin\alpha}{\sin(45^\circ - \alpha)}. \tag{D.1}$$

Using some trigonometric identities this can be rewritten to

$$\sigma'_{\text{uc}} = k_T\sqrt{2}\frac{\sin\phi}{1-\sin\phi}. \tag{D.2}$$

Now σ'_{uc} is not the yield curve's uniaxial compressive strength because that is measured in principle stress space which is derived from stress invariant space through rotation and scaling. To recover the actual uniaxial compressive strength we note that

$$\sin 45^\circ = \frac{\sigma_{\text{uc}}}{2\sigma'_{\text{uc}}}, \tag{D.3}$$

giving the uniaxial compressive strength as

$$\sigma_{\text{uc}} = 2k_T\frac{\sin\phi}{1-\sin\phi}. \tag{D.4}$$

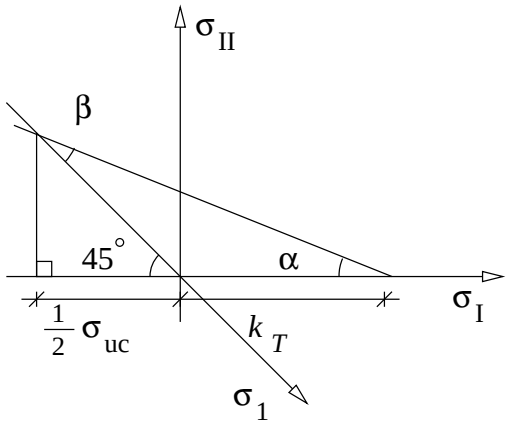

Figure D.1: The relevant portion of stress invariant space showing a Coulombic yield curve, the σ_1 axis and the relevant angles and distances.

When scaling with respect to p^* $\sigma_{\rm uc}$ needs to be divided by $1+\sin\phi$ (see equation (2.59)).

To find $\sigma_{\rm uc}$ for the elliptic yield curve it is probably best to solve the equation $\sigma'_2=0$ where $\sigma'_2=\sigma'_{\rm I}-\sigma'_{\rm II}$, resulting in $\sigma'_{\rm I}=\sigma'_{\rm II}$. The relationship between $\sigma_{\rm I}$ and $\sigma_{\rm II}$ is a simple ellipse and so this becomes

$$\frac{1}{2e}\sqrt{(1+k)^2-(2\sigma'_{\rm I}+1-k)^2}=\sigma'_{\rm I}. \tag{D.5}$$

The solution to this equation is

$$\sigma'_{\rm I}=\frac{-1}{1+e^2} \tag{D.6}$$

and so

$$\sigma_{\rm uc}=-2\sigma'_{\rm I}=\frac{2}{1+e^2}. \tag{D.7}$$

The scaling with respect to p^* is accomplished by dividing this result with $(1+\sqrt{1+1/e^2})/2$ (see equation (2.59)).

If we include cohesion under isotropic divergence the equations become more complicated. The elliptic relationship then becomes

$$\frac{1}{2e}\sqrt{(1+k)^2-(2\sigma'_{\rm I}+1-k)^2}=\sigma'_{\rm I} \tag{D.8}$$

and the final solution is

$$\sigma_{\rm uc}=\frac{1-k+\sqrt{1+k\,(2+4e^2+k)}}{1+e^2}. \tag{D.9}$$

The scaling with respect to p^* is achieved by dividing this result by $(1-k+\sqrt{(1+1/e^2)(1+k)^2})/2$. Replacing e with $1/\sqrt{k}$ gives the uniaxial compressive strength for the trimmed ellipse.

Bibliography

Arctic and Antarctic Research Institute (2007). *Sea ice charts of the Russian Arctic in gridded format, 1933-2006*. Boulder, Colorado USA: National Snow and Ice Data Center. Edited and compiled by V. Smolyanitsky, V. Borodachev, A. Mahoney, F. Fetterer, and R. Barry.

Backhaus, J. (2008). Improved representation of topographic effects by a vertical adaptive grid in vector-ocean-model (VOM). Part I: Generation of adaptive grids. *Ocean Model. 22*(3-4), 114–127.

Barry, R., R. Moritz, and J. Rogers (1979). Fast ice regimes of the Beaufort and Chukchi Sea coasts, Alaska. *Cold Reg. Sci. Technol. 1*(2), 129–152.

Bitz, C. and W. H. Libscomb (1999). An energy-conserving thermodynamic model of sea ice. *J. Geophys. Res. 104*(C7), 15669–15677.

Bjornsson, H., A. Willmott, L. Mysak, and M. Morales Maqueda (2001). Polynyas in a high-resolution dynamic-thermodynamic sea ice model and their parameterization using flux models. *Tellus 53A*, 245–265.

Briegleb, B., C. Bitz, E. Hunke, W. Lipscomb, M. Holland, J. Schramm, and R. Moritz (2004, June). Scientific description of the sea ice component in the community climate system model, version three. NCAR Technical Note NCAR/TN-463+STR, National Center for Atmospheric Research, Boulder, Colorado.

Bryan, K., S. Manabe, and R. Pacanowski (1975). A global ocean-atmosphere climate model. Part II. The oceanic circulation. *J. Phys. Oceanogr. 5*(1), 30–46.

Connolley, W., J. Gregory, E. Hunke, and A. McLaren (2004). On the consistent scaling of terms in the sea-ice dynamics equation. *J. Phys. Oceanogr. 34*(7), 1776–1780.

Coon, M., G. Maykut, R. Pritchard, D. Rothrock, and A. Thorndike (1974). Modeling the pack ice as an elastic-plastic material. *AIDJEX Bulletin 24*, 1–105.

Divine, D. V., R. Korsnes, and A. P. Makshtas (2003). Variability and climate sensitivity of fast ice extent in the north-eastern Kara Sea. *Polar Res. 22*(1), 27–34.

Divine, D. V., R. Korsnes, and A. P. Makshtas (2004). Temporal and spatial variation of shore-fast ice in the Kara Sea. *Cont. Shelf. Res. 24*(15), 1717–1736.

Divine, D. V., R. Korsnes, A. P. Makshtas, F. Godtliebsen, and H. Svendsen (2005). Atmospheric-driven state transfer of shore-fast ice in the north-eastern Kara Sea. *J. Geophys. Res. 110*(c9), C09013.

Dumont, D., Y. Gratton, and T. E. Arbetter (2009). Modeling the dynamics of the North Water polynya ice bridge. *J. Phys. Oceanogr. 39*(6), 1448–1461.

Ebert, E. and J. Curry (1993). An intermediate one-dimensional thermodynamic sea-ice model for investigating ice-atmosphere interactions. *J. Geophys. Res. 98*(C6), 10085–10109.

Feltham, D., N. Untersteiner, J. Wettlaufer, and M. Worster (2006). Sea ice is a mushy layer. *Geophys. Res. Lett. 33*, L14501.

Feltham, D. L. (2008). Sea ice rheology. *Annu. Rev. Fluid. Mech. 40*, 91–112.

Girard, L., S. Bouillon, J. Weiss, D. Amitrano, T. Fichefet, and V. Legat (2011). A new modeling framework for sea-ice mechanics based on elasto-brittle rheology. *Ann. Glaciol. 52*(57), 123–132.

Goldstein, R. V., N. N. Osipenko, and M. Leppäranta (2004). On the shape of the fast ice - drift ice contact zone. *Geophysica 40*(1–2), 3–13.

Griffies, S. M. and R. W. Hallberg (2000). Biharmonic friction with a smagorinsky-like viscosity for use in large-scale eddy-permitting ocean models. *Mon. Weather. Rev. 128*(8), 2935–2946.

Guest, P. and K. Davidson (1991). The aerodynamic roughness of different types of sea ice. *J. Geophys. Res. 96*(C3), 4709–4721.

Günzel, S. (2003). *Entwicklung eines thermo-hydrodynamischen Eismodells mit Anwendung auf die Ostsee*. Ph. D. thesis, Universität Hamburg.

Heil, P. and W. D. Hibler, III (2002). Modelling the high-frequency components of Arctic sea ice drift and deformation. *J. Phys. Oceanogr. 32*, 3039–3057.

Hibler, W., J. Hutchings, and C. Ip (2006). Sea-ice arching and multiple flow states of Arctic pack ice. *Ann. Glaciol. 44*, 339–344.

Hibler, III, W. (1979). A dynamic thermodynamic sea ice model. *J. Phys. Oceanogr. 9*(4), 815–846.

Hibler, III, W. and E. Schulson (2000). On modeling the anisotropic failure and flow of flawed sea ice. *J. Geophys. Res. 105*(C7), 17105–17120.

Hibler, III, W. and J. Walsh (1982). On modeling seasonal and interannual fluctuations of Arctic sea ice. *J. Phys. Oceanogr. 12*(12), 1514–1523.

Hunewinkel, T., T. Markus, and G. Heygster (1998). Improved determination of the sea ice edge with SSM/I data for small-scale analyses. *IEEE T. Geosci. Remote. 36*(5), 1795–1808.

Hunke, E. and J. Dukowicz (1997). An elastic-viscous-plastic model for sea ice dynamics. *J. Phys. Oceanogr. 27*(9), 1849–1867.

Hunke, E. C. (2001). Viscous-plastic sea ice dynamics with the evp model: Linearization issues. *J. Comput. Phys. 170*(1), 18–38.

Huwald, H., L.-B. Tremblay, and H. Blatter (2005). A multilayer sigma-coordinate thermodynamic sea ice model: Validation against Surface Heat Budget of the Arctic Ocean (SHEBA)/Sea Ice Model Intercomparison Project Part 2 (SIMIP2) data. *J. Geophys. Res. 110*(C5), C05010.

Idso, S. B. and R. D. Jackson (1969). Thermal radiation from the atmosphere. *J. Geophys. Res. 74*(23), 5397–5403.

Ip, C. F., W. D. Hibler, III, and G. M. Flato (1991). On the effect of rheology on seasonal sea-ice simulations. *Ann. Glaciol. 15*, 17–25.

Jakobsson, M., N. Cherkis, J. Woodward, R. Macnab, and B. Coakley (2000). New grid of Arctic bathymetry aids scientists and mapmakers. *Eos. Trans. AGU 81*(9), 89.

Kaleschke, L., C. Lupkes, T. Vihma, J. Haarpaintner, A. Bochert, and J. Hartmann (2001). SSM/I sea ice remote sensing for mesoscale ocean-atmosphere interaction analysis. *Can. J. Remote. Sens. 27*(5), 526–537.

Kalnay, E., M. Kanamitsu, R. Kistler, W. Collins, D. Deaven, and L. Gandin (1996). The NCEP/NCAR 40-year reanalysis project. *B. Am. Meteorol. Soc. 77*(3), 437–471.

Karcher, M., A. Beszczynska-Möller, F. Kauker, R. Gerdes, S. Heyen, B. Rudels, and U. Schauer (2011). Arctic ocean warming and its consequences for the Denmark Strait overflow. *J. Geophys. Res. 116*(C02037), C02037.

Kern, S. (2008). Polynya area in the Kara Sea, Arctic, obtained with microwave radiometry for 1979-2003. *IEEE Geosci. Remote. S. 5*(2), 171–175.

Kern, S., I. Harms, S. Bakan, and Y. Chen (2005). A comprehensive view of Kara Sea polynya dynamics, sea-ice compactness and export from model and remote sensing data. *Geophys. Res. Lett. 32*(15), L15501.

König Beatty, C. and D. M. Holland (2010). Modeling landfast sea ice by adding tensile strength. *J. Phys. Oceanogr. 40*(1), 185–198.

Lammers, R., J. Pundsack, and A. Shiklomanov (2007). Variability in river temperature, discharge, and energy flux from the Russian pan-Arctic landmass. *J. Geophys. Res. 112*(G4), G04S59.

Langleben, M. (1982). Water drag coefficient of 1st-year sea ice. *J. Geophys. Res. 87*(NC1), 573–578.

Lemieux, J.-F. and B. Tremblay (2009). Numerical convergence of viscous-plastic sea ice models. *J. Geophys. Res. 114*, C05009.

Lemieux, J.-F., B. Tremblay, J. Sedláček, P. Tupper, S. Thomas, D. Huard, and J.-P. Auclair (2010). Improving the numerical convergence of viscous-plastic sea ice models with the Jacobian-free Newton-Krylov method. *J. Comput. Phys. 229*(8), 2840–2852.

Lieser, J. L. (2004). *A Numerical Model for Short-term Sea Ice Forecasting*. Ph. D. thesis, Universität Bremen.

Liu, W. T., K. B. Katsaros, and J. A. Businger (1979). Bulk parameterization of air-sea exchange of heat and water vapor including the molecular constraints at the interface. *J. Atmos. Sci. 36*, 1722–1735.

Lu, Q.-M., J. Larsen, and P. Tryde (1989). On the role of ice interaction due to floe collisions in marginal ice-zone dynamics. *J. Geophys. Res. 94*(C10), 14525–14537.

Lüpkes, C. and G. Birnbaum (2005). Surface drag in the Arctic marginal sea-ice zone: A comparison of different parameterisation concepts. *Bound.-Lay. Meteorol. 117*, 179–211.

Mahoney, A., H. Eicken, and L. Shapiro (2007). How fast is landfast sea ice? A study of the attachment and detachment of nearshore ice at Barrow, Alaska. *Cold Reg. Sci. Technol. 47*, 233–255.

Manabe, S., K. Bryan, and M. Spelman (1979). Global ocean-atmosphere climate model with seasonal-variation for future studies of climate sensitivity. *Dynam. Atmos. Oceans. 3*(2-4), 393–426.

Markus, T. and B. Burns (1995). A method to estimate subpixel-scale coastal polynyas with satellite passive microwave data. *J. Geophys. Res. 100*(C3), 4473–4487.

Marsland, S., N. Bindoff, G. Williams, and W. Budd (2004). Modeling water mass formation in the Mertz Glacier Polynya and Adélie Depression, East Antarctica. *J. Geophys. Res. 109*, C11003.

Maykut, G. and M. G. McPhee (1995). Solar heating of the Arctic mixed layer. *J. Geophys. Res. 100*(C12), 24691–24703.

Maykut, G. and D. Perovich (1987). The role of shortwave radiation in the summer decay of a sea ice cover. *J. Geophys. Res.-Oceans 92*(C7), 7032–7044.

Maykut, G. A. (1982). Large-scale heat exchange and ice production in the central Arctic. *J. Geophys. Res. 87*(C10), 7971–7984.

Maykut, G. A. and N. Untersteiner (1971). Some results from a time-dependent thermodynamic model of sea ice. *J. Geophys. Res. 76*(C6), 1550–1575.

McNutt, S. and J. Overland (2003). Spatial hierarchy in Arctic sea ice dynamics. *Tellus 55*(2), 181–191.

McPhee, M. (1975). Ice-ocean momentum transfer for the AIDJEX ice model. *AIDJEX Bulletin 29*, 93–111.

Mellor, G. L. and L. Kantha (1989). An ice-ocean coupled model. *J. Geophys. Res. 94*(C8), 10937–10954.

Millero, F. (1978). Freezing point of seawater. In *Eighth Report of the Joint Panel on Oceanogrpahic Tables and Standards*, Number 28, Annex 6 in UNESCO Technical Papers in Marine Sciences, pp. 35 pp. Paris: UNESCO.

Morales Maqueda, M., A. Willmott, and N. Biggs (2004). Polynya dynamics: A review of observations and modeling. *Rev. Geophys. 42*, RG1004.

Olason, E. and I. Harms (2010). Polynyas in a dynamic-thermodynamic sea-ice model. *The Cryosphere 4*(2), 147–160.

Ou, H. (1988). A time-dependent model of a coastal polynya. *J. Phys. Oceanogr. 18*, 584–590.

Pease, C. (1987). The size of wind driven polynyas. *J. Geophys. Res. 92*, 7049–7059.

Pease, C., S. Salo, and J. Overland (1983). Drag measurements for 1st-year sea ice over a shallow sea. *J. Geophys. Res. 88*(NC5), 2853–2862.

Polyakov, I., G. Alekseev, R. Bekryaev, U. Bhatt, R. Colony, and M. Johnson (2003). Long-term ice variability in Arctic marginal seas. *J. Climate. 16*(12), 2078–2085.

Press, W. H., S. A. Teukolsky, B. P. Flannery, and W. T. Vetterling (1992). *Numerical Recipes in FORTRAN: The Art of Scientific Computing*. New York, NY, USA: Cambridge University Press.

Rothrock, D. (1975). Steady drift of an incompressible Arctic ice cover. *J. Geophys. Res. 80*(3), 387–397.

Savage, S. (1998). Analyses of slow high-concentration flows of granular materials. *J. Fluid. Mech. 377*, 1–26.

Semtner, A. (1976). Model for thermodynamic growth of sea ice in numerical investigations of climate. *J. Phys. Oceanogr. 6*(3), 379–389.

Semtner, A. (1984). On modeling the seasonal thermodynamic cycle of sea ice in studies of climatic-change. *Climatic change 6*(1), 27–37.

Shirasawa, K. (1986). Water-stress and ocean current measurements under 1st-year sea ice in the Canadian Arctic. *J. Geophys. Res.-Oceans 91*(C12), 14305–14316.

Simmons, A., S. Uppala, D. Dee, and S. Kobayashi (2007). ERA-Interim: New ECMWF reanalysis products from 1989 onwards. *ECMWF Newsletter* (110), 25–35.

Smedsrud, L., W. Budgell, A. Jenkins, and B. Adlandsvik (2006). Fine-scale sea-ice modelling of the Storfjorden polynya, Svalbard. *Ann. Glaciol. 44*, 73–79.

Sorteberg, A. and J. Walsh (2008). Seasonal cyclone variability at 70 degrees N and its impact on moisture transport into the Arctic. *Tellus A 60*(3), 570–586.

Stössel, A. and M. Claussen (1993). On the momentum forcing of a large-scale sea-ice model. *Clim. Dynam. 9*, 71–80.

Taguchi, E., D. Stammer, and W. Zahel (2011). Inferring deep ocean tidal energy dissipation from the global high-resolution data-assimilative HAMTIDE model. Manuscript submitted for publication.

Tremblay, L.-B. (1999). A comparison study between two visco-plastic sea-ice models. *Lect. Notes. Phys. 533*, 333–352.

Tremblay, L.-B. and M. Hakakian (2006). Estimating the sea ice compressive strength from satellite-derived sea ice drift and NCEP reanalysis data. *J. Phys. Oceanogr. 36*(11), 2165–2172.

Tremblay, L.-B. and L. Mysak (1997, November). Modeling sea ice as a granular material, including the dilatancy effect. *J. Phys. Oceanogr. 27*, 2342–2360.

Ukita, J. and D. Martinson (2001). An efficient adjustable-layering thermodynamic sea-ice model formulation for high-frequency forcing. *Ann. Glaciol. 33*, 253–260.

Volkov, V. A., O. M. Johannessen, V. E. Borodachev, G. N. Voinov, L. H. Pettersson, L. P. Bobylev, and A. V. Kouraev (2002). *Polar Seas Oceanography: An integrated case study of the Kara Sea*. London: Springer.

Wamser, C. and D. Martinson (1993). Drag coefficients for winter Antarctic pack ice. *J. Geophys. Res. 98*(C7), 12431–12437.

Wang, K. (2006). Pack ice as a two-dimensional granular plastic: a new constitutive law. *Ann. Glaciol. 44*, 317–320.

Wang, K. (2007). Observing the yield curve of compacted pack ice. *J. Geophys. Res. 112*(c5), C05015.

Wang, K. and C. Wang (2009). Modeling linear kinematic features in pack ice. *J. Geophys. Res. 114*(c12), C12011.

Washington, W., A. Semtner, C. Parkinson, and L. Morrison (1976). Development of a seasonal change sea-ice model. *J. Phys. Oceanogr. 6*(5), 679–685.

Weaver, J. (1951). The ice of sea in the North American Arctic. In V. Stefansson (Ed.), *Encyclopedia Arctica*, Volume 7. New York: The Stefansson Library.

Webster, N. and J. McKechnie (Eds.) (1979). *Webster's new twentieth century dictionary of the English language* (second ed.). William Collins Publishers, Inc.

Willmott, A., M. Morales Maqueda, and M. Darby (1997). A model for the influence of wind and oceanic currents on the size of a steady state latent heat coastal polynya. *J. Phys. Oceanogr. 27*, 2256–2275.

Winsor, P. and G. Björk (2000). Polynya activity in the Arctic Ocean from 1958 to 1997. *J. Geophys. Res. 105*(C4), 8789–8803.

Woods Hole Oceanographic Institution (2010, September). Arctic Model Intercomparison Project: Surface stress. `http://www.whoi.edu/page.do?pid=30576`.

World Meteorological Organization (1970). *WMO sea-ice nomenclature*. Geneva, Switzerland: Secretariat of the World Meteorological Organization.

Zhang, J. and D. Rothrock (2005). Effect of sea ice rheology in numerical investigations of climate. *J. Geophys. Res. 110*(C8), C08014.

Zyryanov, D. and R. Korsnes (2003). A numerical model for simulation of sea ice destruction due to external stress in geoscale areas. In H. Konietzky (Ed.), *Numerical modeling in micromechanics via particle methods: proceedings of the 1st International PFC Symposium, Gelsenkirchen, Germany, 6-8 November 2002*, pp. 29–36. Balkema.

Acknowledgements

I would like to thank my supervisors, Lars Kaleschke and Ingo Harms, for their help and support. I would especially like to thank Ingo Harms for his help with various practical matters as well as his help with this thesis. Thanks are also due to Stefan Heitmann, Michael Karcher, Dirk Notz, Bruno Tremblay, Jan Backhaus, Udo Huebner and Halldór Björnsson for their help and interest in this project at its various stages. Finally I would like to thank my wife, Agnes Vogler, for her support and friendship. This project was funded by the DFG under HA 3166/2-1 "STARBUG".